Deep Super-resolution Microscopy:
Novel Developments and Optimisations

Sohaib Abdul Rehman

Jesus College
University of Cambridge

This dissertation is submitted for the degree of
Doctor of Philosophy

March 2019

Declaration

I hereby declare that this dissertation is the result of my own work and includes nothing which is the outcome of work done in collaboration except as declared in the Preface and specified in the text. It is not substantially the same as any that I have submitted, or, is being concurrently submitted for a degree or diploma or other qualification at the University of Cambridge or any other University or similar institution except as declared in the Preface and specified in the text. I further state that no substantial part of my dissertation has already been submitted, or, is being concurrently submitted for any such degree, diploma or other qualification at the University of Cambridge or any other University or similar institution except as declared in the Preface and specified in the text. This dissertation does not exceed the prescribed word limit for the relevant Degree Committee.

<div align="right">

Sohaib Abdul Rehman

March 2019

</div>

Abstract

Thesis title: Super-resolution Microscopy: Novel Developments and Optimisations
Author: Sohaib Abdul Rehman

This thesis describes the design, development and optimisation of a multifunctional localisation based super-resolution microscope at Cambridge Advanced Imaging Centre. The microscope is optimised to perform single and dual-colour imaging with high localisation precision and accuracy. Moreover, three-dimensional imaging capability is included in the microscope using the double-helix point spread function and the light field imaging modality.

The thesis also describes the application of the microscope to image challenging biological samples, in collaboration with the research groups at the *Department of Physiology, Development and Neuroscience*. This includes, studying dynamics of a DNA-binding transcription factor for the Notch signalling pathway, deep within the whole salivary glands of Drosophila. Characterisation and optimisation of the microscope and the subsequent image analysis pipeline, to extract dynamics of single molecules at such depths is also discussed. Another application of the microscope, discussed in the thesis, is the study of chromatin architecture in primary spermatocytes of Drosophila. This includes optimisation of imaging conditions and data analysis software to reconstruct features with different densities of labelling dye in the imaged nuclei. Calibration and application of dual-colour localisation microscopy, to visualise the arrangement of active transcription sites in chromatin fibres is also discussed.

Finally, the thesis also presents the application of light field imaging technique to extend the depth of field of localisation microscopy to over $20\,\mu$m. Modification of the microscope for light field imaging and a method to localise point emitters with high precision in all three spatial dimensions is discussed. The effectiveness of the technique for single molecule imaging is shown by detecting emissions from single fluorophores in labelled cells.

Acknowledgements

I would like to thank my supervisor Kevin O'Holleran for his support, academic and otherwise, throughout the PhD. I have learnt a lot from him over the last four years and I hope that I was able to contribute constructively towards the super-resolution imaging at CAIC as well. I would also like to thank Martin Lenz for teaching me the alignment of optical systems and providing useful help regarding the design and development of the microscope. The data analysis presented in the thesis would not have been possible without Leila Muresan, who not only helped me to make sense of the localisation data but also always pointed me towards the right tools. The light field project would not have been possible without Ruth Sims; collectively we tried to understand the light field imaging and her insights into the reconstruction algorithms proved to be very useful throughout the project. I would also like to thank other members of the CAIC family i.e. Mewanthi Flaminia, Karin Muller and Lyn Carter.

The microscope developed as part of this PhD was used to answer challenging biological questions with the help of our collaborators at the Department of Physiology Development and Neuroscience. I would especially like to thank Maria Gomez-Lamarca, Rob White, Sarah Bray and Antonios Georgantzoglou for providing me the opportunity to work on their interesting projects and helping me understand the basics of biology.

I would also like to thank my co-supervisor Steven Lee and members of his lab, especially Alex Carr. Their experience of localisation microscopy helped me a lot to optimise imaging conditions for different samples and to understand the chemistry of fluorophores.

Outside work, I would like to thank my friends Sara, Ammar, May, Affaf, Hira, Zara, Shaista, Silvia, Aastha, Sauleha, Bart, Jon, Elise, Patrick, Amna, Parul, Muntazir, Zach, Anna, Saud, Arif Bhai, Farid Bhai, Tariq Bhai, Sharmeen, Aliya, Maria and Yani for making Cambridge a home away from home. And also Sarmad, Ahmad, Armaghan, Zahid, Usama, Haseeb and Umar for always being very welcoming during my short visits to Pakistan.

Finally, I am grateful to my brothers Khubaib, Musaab and Hussain for their support throughout the PhD and most importantly to Mama and Abbu for always being there for me.

Table of contents

List of figures

Chapter A

Introduction

Optical microscopy offers a unique benefit of the *in vivo* visualisation of biological phenomenon. Huge advancements have been made in the field, since its earliest application to biology by Hooke and Leeuwenhoek [1]. These advancements were mainly due to improved understanding of the properties of light and improved lens design [2]. Discovery and design of highly specific fluorescent probes also played a crucial role in these advancements, resulting in the creation of a subfield of optical microscopy - *fluorescence microscopy*. The probes have narrow excitation bands and are available for the entire visible spectrum of light. This combined with the ability to specifically tag them to a variety of biological molecules makes fluorescence microscopy an attractive tool to study structures and molecular dynamics in living organisms.

However, like any other optical imaging system, the resolution of optical microscopes is limited by the diffraction properties of light to 200-350 nm. At such a resolution, cells and its large organelles such as nucleus, nucleolus, mitochondria etc. are visible. But, visualisation of smaller structures and molecular interactions (between molecules and with organelles) requires much higher resolution. Studying such structures and interactions are crucial to understanding the working of cells - the building blocks of life [3].

Significant advancements to overcome the resolution limit of optical microscopes were made over the last three decades. In recognition of these efforts and their impact, the 2014 Nobel Prize in Chemistry was awarded for *"the development of super-resolved fluorescence microscopy"* [4]. One of these super-resolution techniques is localisation microscopy, which can provide up to tenfold improvement in resolution over the diffraction barrier of light in fluorescence microscopy. Localisation microscopy when combined with engineered point spread functions can provide high localisation precision over an extended depth of field (DOF) [5–7].

ABBE'S DIFFRACTION LIMIT (0.2 µm)

| ant | hair | mammalian cell | bacterium | mitochondrion | virus | protein | small molecule |

1 mm   100µm   10µm   1µm   100 nm   10 nm   1nm

Illustration: © Johan Jarnestad/The Royal Swedish Academy of Sciences
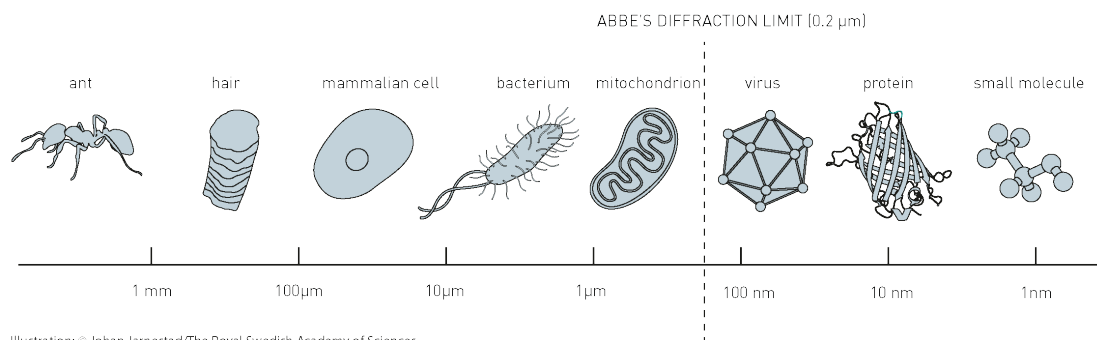
Fig. A.1 Resolution of an optical imaging system is limited by the diffraction properties of light to 200-350 nm. At such a resolution, cells and its large organelles are visible, but visualisation of smaller structures and molecular interactions requires much higher resolution.

This thesis describes the design, development and optimisation of a localisation based super-resolution microscope to answer challenging biological questions. This includes studying dynamics of a DNA binding transcription factor deep (more than $25\,\mu$m away from the coverslip) within the whole salivary glands of Drosophila, and resolving three-dimensional architecture of dense chromatin fibres in Drosophila primary spermatocytes. The thesis also proposes, for the first time to our knowledge, the use of light field imaging to extend the DOF in localisation microscopy to over $20\,\mu$m, with high localisation precision in all three spatial dimensions.

Chapter 1 of the thesis describes the origin of the diffraction limit from the diffraction properties of light. Basics of localisation microscopy and methods to extend its DOF are also discussed. Chapter 2 explains the design and development of a localisation microscope with the following functionalities:

- two-dimensional localisation microscopy with high localisation precision (better than 10 nm)

- three-dimensional localisation microscopy, using double helix point spread function, over a DOF of $3\,\mu$m

- dual-colour localisation microscopy

- light field localisation microscopy

An optimal alignment method to obtain large field of views (FOVs) in three-dimensional localisation microscopy, involving phase modifying optics, is also discussed.

Chapter 3 describes the application of the microscope to investigate the dynamics of a DNA-binding transcription factor for the Notch signalling pathway, in Drosophila salivary

glands. Moreover, application of the microscope to study the structure of chromatin in primary spermatocytes of Drosophila is discussed in Chapter 4.

Chapter 5 presents theory behind light field imaging and its application to extend the DOF in localisation microscopy. Characterisation and calibration of the microscope for light field imaging, using fluorescent beads, and its potential for single molecule imaging is also discussed. Finally, major conclusions of the thesis are summarised in Chapter 6.

Chapter 1

Theoretical Background

1.1 Introduction

Fluorescence microscopy is an essential tool to image biological samples and has provided a wealth of information about several biological phenomenon over the last few decades. This chapter explains the physical limit on the resolution of optical imaging systems and covers the basics of localisation microscopy, a technique to overcome the resolution limit in fluorescence microscopy.

1.1.1 Chapter Description

This chapter describes the origin of the resolution limit in optical microscopy from the diffraction properties of light. Basics of the localisation microscopy and required image analysis steps are also explained. Lastly, methods to extend the DOF of the technique are also presented. This includes wavefront engineering, multi-focal plane imaging and multi-view imaging. The concepts discussed in this chapter would form the basis of the analysis presented in the subsequent chapters of the thesis.

1.2 Diffraction of Light

Huygen's principle is a method to determine the diffraction of light from an aperture. Each point in the aperture is considered to be a source of spherical waves. The electric field, after the aperture, is given by the superposition of these waves as shown in Figure 1.1. Mathematically, Huygen's principle is formulated according to Eq 1.1 (the analysis in this
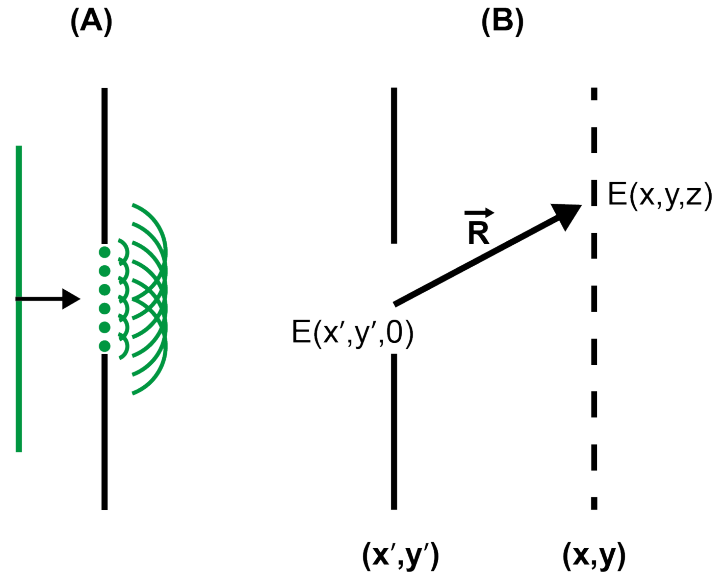
Fig. 1.1 Huygen's principle provides a method to determine the diffraction of light from an aperture. Each point in the aperture is considered to be a source of spherical waves and superposition of these waves is used to compute the electric field at a point after the aperture. The concept of this figure was taken from [8]

section is based on [8]).

$$E(x,y,z) = -\frac{i}{\lambda} \iint E(x',y',0)\frac{\exp(ikR)}{R}dx'dy' \tag{1.1}$$

where $E(x',y',0)$ and $E(x,y,z)$ are the electric fields at the aperture and at an axial distance z from the aperture respectively, and:

$$R = \sqrt{(x-x')^2+(y-y')^2+(z-z')^2}$$

Huygen's principle gives an accurate method to calculate the diffraction of light, but computing the integral in Eq1.1 is challenging even for simple aperture shapes [8]. Under the paraxial approximation, Eq1.1 can be simplified as only those rays that make small angles with the optical axis are considered. For such rays:

$$z^2 >> (x-x')^2+(y-y')^2$$

and under this approximation, the denominator in Eq1.1 can be written as $R \cong z$. This is not entirely true for the exponential term as small changes in R can introduce significant changes

in the phase. To simplify the phase term, the Taylor expansion of R is carried out as follows:

$$R = z\sqrt{1 + \frac{(x-x')^2 + (y-y')^2}{z^2}} \cong z\left(1 + \frac{(x-x')^2 + (y-y')^2}{2z^2}\right)$$

and,

$$E(x,y,z) \cong -\frac{i\exp(ikz)\exp\left(ik\frac{x^2+y^2}{2z}\right)}{\lambda z} \iint E(x,y,0)\exp\left(ik\frac{x'^2+y'^2}{2z}\right) \\ \exp\left(-ik\frac{xx'+xy'}{z}\right)dx'dy' \tag{1.2}$$

According to Eq1.2, $E(x,y,z)$ is the Fourier transform of the field, at the aperture, multiplied with a quadratic phase. This is known as the **Fresnel approximation** of the Huygen's principle. Now if it is further assumed that Eq1.2 is calculated far from the aperture, such that:

$$z \gg \frac{k}{2}(x'^2 + y'^2) \tag{1.3}$$

The quadratic phase term in Eq1.2 can be ignored, giving the **Fraunhofer approximation** of the Huygen's principle. The simplified electric field is:

$$E(x,y,z) \cong -\frac{i\exp(ikz)\exp\left(ik\frac{x^2+y^2}{2z}\right)}{\lambda z} \iint E(x,y,0)\exp\left(-ik\frac{xx'+xy'}{z}\right)dx'dy' \tag{1.4}$$

$$E(x,y,z) \cong A(x,y,z)\mathscr{F}\left(E(x,y,0)\right)$$

Hence, far from the aperture the diffraction pattern is given by the Fourier transform of the field at the aperture and it scales linearly with z.

1.2.1 Diffraction Through a Lens

The above analysis shows that the Fraunhofer diffraction pattern is observed far from an aperture i.e. as $z \to \infty$, which is not practical for the design of optical systems. However, by using a convex lens the diffraction pattern can be shifted from infinity to the focal plane of the lens. This can be understood by examining the wavefront modification as light propagates through such a lens. A thin lens of focal length f adds the following phase curvature to the incident light beam [8]:

$$\phi(x,y) = -k\frac{x^2+y^2}{2f} \tag{1.5}$$

It is this phase curvature that shifts the far-field diffraction pattern to the focal plane of the lens (for a detailed analysis see [8]). If $E(x,y)$ is the field in the front focal plane of the lens, the field in its back focal plane (BFP) is:

$$E(x,y,2f) = -i\frac{\exp(2ikf)}{\lambda f} \iint E(x',y',0)exp\left(\frac{-ik}{f}(xx'+yy')\right)dx'dy'\mathscr{O}(x,y)$$

$$\text{(1.6)}$$

$$E(x,y,2f) = -i\frac{\exp(2ikf)}{\lambda f}\mathscr{F}[E(x',y',0)]\mathscr{O}(x,y)$$

So, the field in the focal planes (front and back) of the lens are linked by the Fourier transform operation, with the scaling dependent on the focal length of the lens and the wavelength of light. The term $\mathscr{O}(x,y)$ is the field in the BFP when $E(x,y,0) = \delta(x,y)$ (a point source placed on the optical axis). Impact of $\mathscr{O}(x,y)$ on the resolution of optical imaging systems is discussed in detail in the next sections.

Two-lens Imaging System

Schematic of a two-lens imaging system is shown in Figure.1.2B. Working of this system can be explained by the duality property of the Fourier transform:

$$\mathscr{F}[\mathscr{F}[A(x,y)]] = A(-x,-y).$$

If the separation between the two lenses is equal to the sum of their focal lengths, the electric field at the object plane (front focal plane of Lens 1) is Fourier transformed twice, resulting in a flipped image of the object in the BFP of Lens 2. A two-lens system perfectly describes the imaging operation of a modern microscope (emission path, ignoring filters and other optical elements for simplicity), where the microscope objective and the tube lens perform the functions of Lens 1 and Lens 2 respectively. Our localisation microscope was also based on such an arrangement of lenses, the setup of which is discussed in Chapter 2.

1.2.2   Diffraction Limit of Light

Figure 1.2B shows imaging of a point emitter on a two-lens imaging system. Due to the finite aperture of Lens 1, rays making an angle greater than θ_o with the optical axis are not captured by the lens. Such a loss of information restricts the achievable resolution in optical imaging systems. This happens because of the Fourier transforming property of the lens, which results in linear mapping of rays making different angles with the optical axis (in the
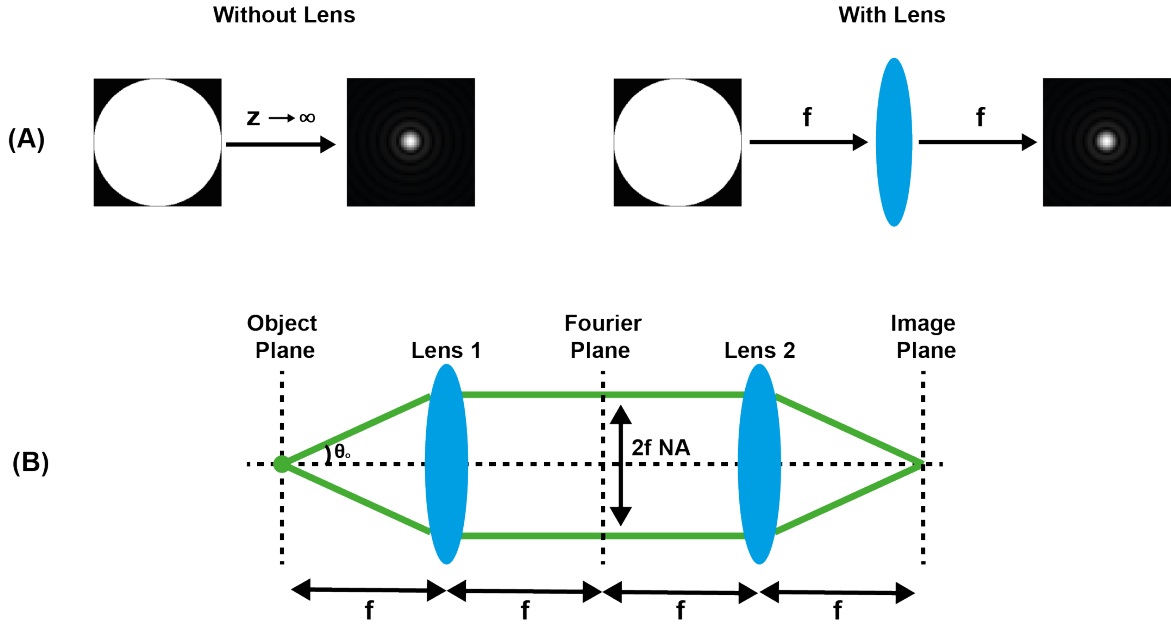
Fig. 1.2 (A) Fraunhofer diffraction is observed far from an aperture i.e. as $z \rightarrow \infty$. (B) A convex lens shifts this diffraction pattern to its focal plane. Field in the back focal plane of the lens is linked to its front focal plane by the Fourier transform. (C) A two-lens imaging system.

object plane) to different spatial frequencies in the BFP [9]. So, the cone of rays making an angle θ_o with the optical axis corresponds to the maximum spatial frequency that can be imaged on the system.

Under the paraxial approximation, for a given lens diameter d, θ_o can be calculated as:

$$\sin \theta_o \cong \frac{d}{2f} \tag{1.7}$$

here, the small angle approximation was used to get $\tan \theta_o \cong \sin \theta_o$. The term $sin\theta_o$ is called the numerical aperture (NA) of the lens (if a lens is placed in a medium of refractive index n, NA $= nsin\theta_o$). It is important to mention that modern lenses are designed to fulfil the *Abbe's sine condition*, under which Eq1.7 is true for rays collected over the entire collection angle of a lens ($2\theta_o$ in Figure.1.2B). This condition is necessary for the Fourier transforming property of a lens and aberration free imaging of off-axis objects in optical imaging systems [9]. Therefore, fulfilment of the *Abbe's* condition is necessary for an imaging system to be linear and shift invariant - an important assumption in the analysis of localisation microscopy images.

Due to the finite aperture of Lens 1, a circle of uniform amplitude is obtained in the BFP, for a point emitter in its front focal plane. Diameter of this circle is $d = 2f \sin \theta$, as shown in

Figure 1.2, which is the physical size of the BFP. It can be converted to spatial frequencies by taking the scaling of Eq 1.6 into account. So, the diameter in spatial frequency coordinates is:

$$u_{max} = 2fNA \times \left(\frac{k}{f}\right)$$

$$u_{max} = 2\pi \left(\frac{2NA}{\lambda}\right)$$

(1.8)

Here, u_{max} is the maximum frequency that can be resolved on a two-lens imaging system and its time period is known as the **Abbe's diffraction limit of light**:

$$Abbe's\ Diffraction\ Limit = \frac{\lambda}{2NA}$$ (1.9)

Resolution of the system

To determine the resolution of a two-lens imaging system, consider Figure 1.2. In the last section it was shown that for a point source in the focal plane of Lens 1, the field in the Fourier plane (BFP of Lens 1) is a circle of uniform magnitude, the diameter of which depends on the NA of Lens 1. Lens 2 then takes the Fourier transform of this circle, forming the image in its BFP. If d is the diameter of the field in the Fourier plane, Eq 1.6 can be used to calculate the intensity in the image plane, which comes out to be:

$$I(r) = I_o \left(\frac{\pi d^2}{4\lambda f}\right)^2 \left(2\frac{J_1(kd\rho/2f)}{kd\rho/2f}\right)$$ (1.10)

here $J_1(kd\rho/2f)$ is a Bessel function of the first order (see Figure 1.3B). Such a blurred image obtained by imaging a point source on an imaging system is called the point spread function (PSF) of the system. We now explore the effect of such a PSF on imaging of an arbitrary shaped fluorescent sample.

If $A(x,y)$ is the illumination pattern on a sample with the fluorescence distribution $B(x,y)$, the field in the object plane is given as $E(x,y) = A(x,y) \times B(x,y)$. For simplicity, sample is assumed to be uniformly illuminated, i.e. $A(x,y) = 1$. Writing, $E(x,y)$ as a sum of delta functions (point emitters), gives:

$$E(x,y) = \iint E(x_o,y_o)\delta(x-x_o,y-y_o)dx_o dy_o = E(x,y) * \delta(x,y)$$ (1.11)

When such an electric field is imaged by the microscope objective, the field in the BFP is given by the convolution theorem:

$$E(u,v) = (\mathscr{F}[E(x,y)] \times \mathscr{F}[\delta(x,y)])\mathscr{O}(u,v)$$
$$E(u,v) = \mathscr{F}[E(x,y)]\mathscr{O}(u,v)$$

$$(1.12)$$

$\mathscr{O}(u,v)$ is the support of the BFP and, as discussed in the last section, it is generally a circle of uniform magnitude. Now, calculating the intensity in the image plane (by taking the Fourier transform of Eq 1.12) gives:

$$I(x,y) = |E(x,y) * h(x,y)|^2 \qquad (1.13)$$

here, $h(x,y)$ is the PSF, which for a two lens system is given by Eq 1.10. Hence, the effect of the finite aperture of Lens 1 (microscope objective) is the blurring of the image by the PSF of the imaging system (microscope).

To determine the resolution of the system, two point emitters are considered in the object plane, which produce two diffraction limited spots in the image plane. As these emitters are brought closer, their images start to overlap. Resolution of a system is determined by the minimum distance between the points till their images are distinguishable [10]. According to the **Rayleigh's resolution criterion**, two points are resolvable if the minimum distance between them is such that the first zero of one image overlaps with the maximum/peak of the other. For a Bessel function of the first order, this occurs when:

$$\frac{kd\rho}{2f} = 1.22\pi$$

Solving for ρ in the above equation and using $NA = \frac{d}{2f}$, gives the minimum spacing between the two points to be:

$$\text{Rayleigh Criterion} = 0.61\frac{\lambda}{NA} \qquad (1.14)$$

The implication of the above equation is that the resolution of an optical imaging system (including microscopes) is limited to $200 - 350\,\text{nm}$ for visible light. This restricts the visualisation of structures smaller than the diffraction limit of light and interaction between biological molecules, which are vital for the proper functioning of any cell [11, 12].
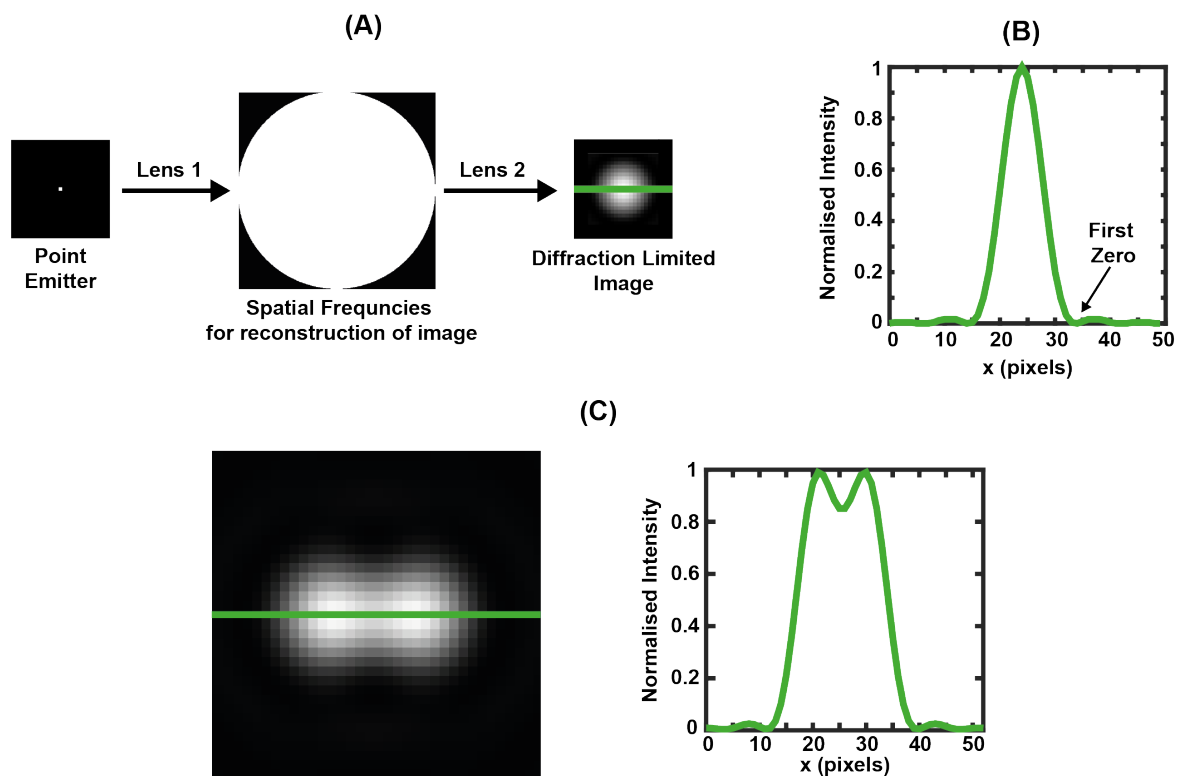
Fig. 1.3 (A) Image formation on a two lens imaging system (see Figure 1.2C). Finite aperture of Lens 1 results in the loss of high frequency information leading to a blurred PSF. (B) Intensity profile of the diffraction limited PSF. (C) Overlapping images of two point emitters, separated by the minimum resolvable distance given by the Rayleigh's criterion.

1.3   Localisation Microscopy

Localisation microscopy is a method to surpass the diffraction limit of light to obtain up to tenfold improvement in resolution, over the diffraction limit of light, in fluorescence microscopy. Sub-diffraction resolution is achieved by temporally separating emissions from fluorescent molecules within a diffraction limited region, by using photo-switchable or photoactivatable fluorescent labels [13, 14]. Depending on the use of fluorescent dyes or proteins, localisation microscopy is called Stochastic Optical Reconstruction Microscopy (STORM) or Photoactivatable Localisation Microscopy (PALM) respectively. Other than the type of fluorescent labels used for imaging, both the techniques have very similar mode of operation, which is explained in Figure 1.4. Different steps in the figure are explained below:

1. In the absence of the activation laser, all the molecules in the FOV are in the dark state. Activation laser (usually ultra-violet light) is then shown on the sample (at an optimal intensity) to activate a spatially sparse set of molecules.

2. Fluorescence from the activated molecules is collected by exposing the sample to an excitation laser

3. Centres of the imaged fluorescent molecules are localised

4. Active molecules are photo-bleached (or they return to dark state) before the next burst of the activation laser.

5. The process is repeated until all the dye molecules in the FOV are exhausted (or enough localisations are collected).
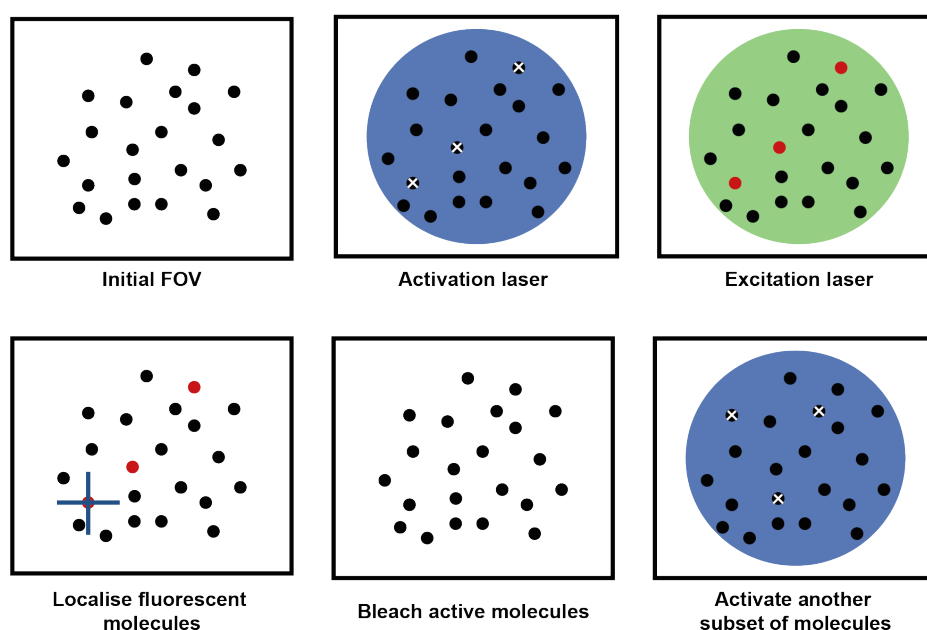
Fig. 1.4 Principle of localisation microscopy. (A) Inactive molecules in the FOV, (B) Stochastic activation of a sparse subset of molecules, (C) Imaging, (D) Localisation of imaged molecules, (E) Bleaching of active molecules before the next iteration in (F). Red and black colours indicate active and inactive molecules respectively.

It is important to note that the frames acquired on a localisation microscope contain diffraction limited spots. So, the highest spatial frequency in these frames corresponds to the Abbe's diffraction limit. It is by combining localisations from multiple frames that the underlying structure is resolved beyond the diffraction limited resolution of the microscope. Tens of thousands of localisations are usually required to construct a super-resolution image, resulting in long imaging times (from minutes to hours) [13]. Hence, high spatial resolution is achieved at the cost of low temporal resolution.

In this section, the concept of localisation microscopy was explained using separate activation and excitation lasers. This is common for labels used in localisation microscopy.

For example mEOS can be photoconverted using 405 nm laser to emit at 561 nm [15]. Similarly Cy5 can be excited by a 638 nm laser, which also sends it to the dark state. 532 nm laser then acts as an activation laser for the dye in the presence of Cy3 (Cy3-Cy5 is know as activator-reporter pair) [16]. However, use of two lasers is not always necessary. Alexa 647 can be activated and excited by using 647 nm laser line [17] and Atto 655 changes between dark and bright state in the presence of a reducing agent such as ascorbic acid [18]. Two important properties of fluorescent probes used in localisation microscopy are (i) the number of photons emitted in the active state, and (ii) the time spent in this state [17]. While the number of photons determine the localisation precision (see Eq 1.17), the on-time dictates the number of molecules that can be localised within a diffraction limited region in a given time (an on-time of Δt can only result in, on average, $t/\Delta t$ non-overlapping events in a diffraction limited region in time t). For a detailed discussion on fluorescent dyes and proteins used in localisation microscopy, see [17, 19].

1.4 Data Analysis in Localisation Microscopy

A sparse subset of fluorescent molecules emit at any given time in localisation microscopy. Emissions from these active fluorophores are captured by the objective lens and focused to the image plane by a tube lens. Hence, the emission path of the microscope is equivalent to a 4f imaging system shown in Figure 1.2 (in the absence of any phase modifying optics). In such a configuration, the electric field from the object plane (focal plane of the objective) is relayed to the image plane by the objective and the tube lens (with blurring caused by the finite aperture of the objective). For emitters in the focal plane of the objective, diffraction limited spots are obtained in the image plane. However, for an emitter outside the object plane, a spherical wave is obtained in the object plane, the amplitude of which drops as a function of the distance from the emitter (Huygen's Principle). This results in a blurred spot in the image plane. For the number of photons typically involved in localisation microscopy, such a spot is either lost in the background or localised (if possible) with deteriorated precision. Hence, in the absence of any PSF modifications, localisation microscopy is limited to a thin volume around the focal plane of the objective. This section focuses on the detection and localisation of diffraction limited spots obtained from this volume. Methods to extend the localisation microscopy to the three dimensions is discussed in Section 1.5.

1.4.1 Spot Localisation in Two-dimensional Localisation Microscopy

Raw images contain a set of fluorescent spots. By taking advantage of the spatial invariance of the PSF, fluorescent spots in an image can be modelled as:

$$h'(x,y) = Ih(x - x_o, y - y_o) + b; \qquad (1.15)$$

here, (x_o, y_o) is the position of a fluorescent spot in the image, $h(x,y)$ is the PSF of the microscope with amplitude I, which is proportional to the number of photons captured from an emitter and b is the background signal. If the microscope objective and the tube lens are modelled as thin lenses, $h(x,y)$ is given by Eq 1.10. More accurate models of the PSF can be computed by considering the vector nature of light and different interfaces between the sample and the objective [20–22]. However, such PSFs are complicated and computationally expensive to compute, especially in localisation microscopy which requires hundreds of thousands of spots to be localised. So, for all practical purposes airy function approximation of the PSF can be used [20]. In commonly used fitting algorithms, the PSF is further approximated as a two-dimensional Gaussian function, which greatly simplifies the fitting process.

$$h(x,y) = exp \left[-\frac{(x - x_o)^2 + (y - y_o)^2}{2\sigma^2} \right] \qquad (1.16)$$

[23] generated the PSF of the microscope by taking into account the vector nature of light and localised it by fitting a two-dimensional Gaussian function. The analysis showed that the Gaussian approximation of the PSF does not affect the localisation accuracy (unless the PSF is not circularly symmetric). Similar analysis carried out in [24–26] used the Gaussian approximation of the PSF to localise emitters without any loss of accuracy in localisation microscopy. Localisation software based on Gaussian approximation of the PSF have been ranked significantly high in terms of both localisation accuracy and precision in a recent assessment of localisation microscopy software [27]. However, it is important to note that in the presence of aberrations (such as coma) and fixed dipoles, symmetry of the PSF can be lost. In such cases, algorithms based on experimentally determined PSF should be used for non-erroneous results [23, 27, 28].

Precision of Localisation

In the absence of aberrations, emissions in the image plane are centred about the actual position of emitters. The light is then captured by a high quantum efficiency camera, pixels of which sample the PSF. A PSF gives the probability distribution of photons in the image plane but due to their quantised nature, the photons are randomly distributed on the camera

pixels, at any given time. This gives rise to the shot noise with a Poisson statistics [29], which deteriorates the localisation precision especially for low number of photons. Other sources of noise such as read noise, thermal noise and dark noise also affect the localisation precision as discussed in Section 2.2. In the presence of these noise sources, theoretical precision of localising an emitter, x_{th}, is given by the Thompson's Equation [29]:

$$\Delta x_{th}^2 = \frac{s^2 + a^/12}{N} + \frac{8\pi s^4 b^2}{a^2 N^2} \tag{1.17}$$

here, s is the standard deviation of the PSF, a is the pixel size, b^2 is the noise variance and N is the number of photons. The equation reduces to the formula for the *standard error of the mean* (error in estimating the mean of a probability distribution from N samples) in the absence of noise and pixel effects i.e. s^2/N. A similar expression has been obtained by using the Fisher Information analysis in [24].

According to the equation, pixel size plays an important role in determining the localisation precision. Very large pixels result in under-sampling of the PSF, affecting the fitting procedure and resulting in the loss of localisation accuracy and precision. On the other hand, very small pixels have a few photons per pixel, resulting in enhanced shot noise and hence worse precision. According to [29], and Eq 1.17, the best localisation precision is obtained when pixel size matches the standard deviation of the PSF (similar to the Nyquist sampling criterion). This was considered in the design of our microscope, as discussed in Chapter 2.

Another factor affecting the localisation precision is the size of the PSF. In the presence of shot noise, Eq 1.17 can be written as $\frac{\sigma}{\sqrt{N}}$. For a conventional PSF, σ increases away from the focal plane resulting in the loss of localisation precision. Lastly, the precision improves with an increase in the number of photons collected per emitter, a detailed analysis on which is presented in Section 2.2.

1.4.2 Detection of Spots

Irrespective of the way the PSF is modelled, detection of fluorescent spots is required before the fitting process. Image analysis carried out in this thesis was based on the following two detection techniques:

- detection in raw images

- detection by transforming raw images to the wavelet space

These methods are discussed in detail below.
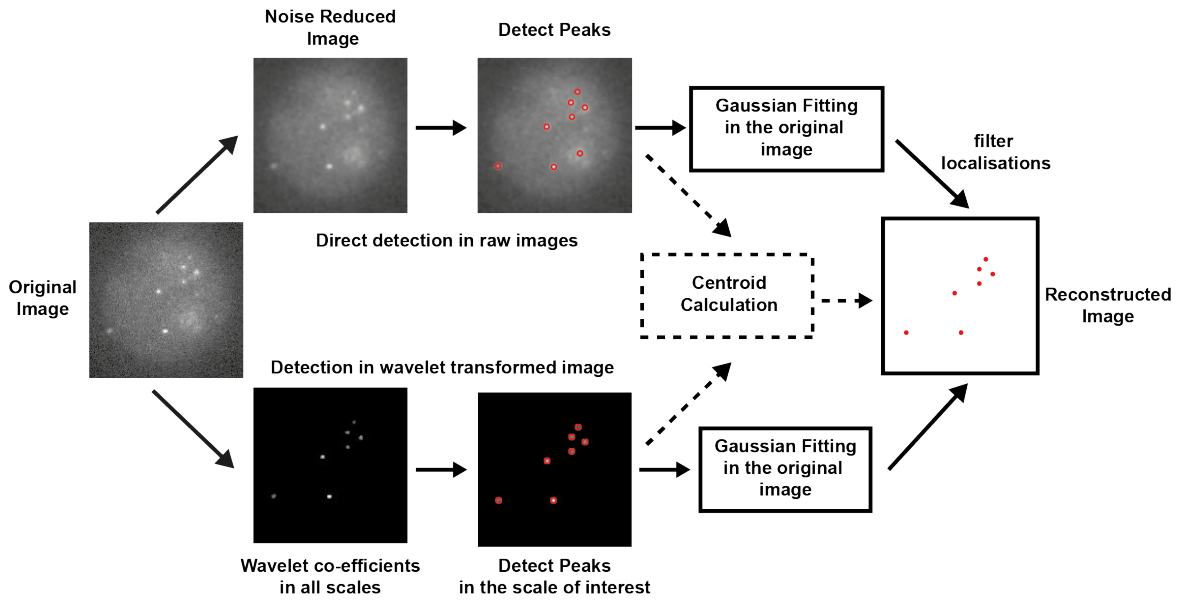
Fig. 1.5 Detection and localisation of fluorescent spots in localisation microscopy. Spot detection was carried out either in raw images or by transforming them to the wavelet space. Spot localisation was performed by fitting a two-dimensional Gaussian function to the detected spots or by calculating their centroid.

Direct Detection in Raw Images

Spot detection can be carried out by finding local maxima in raw images. *PeakFit*, a spot localisation software used in the thesis, performs spot detection using this method. The software detects fluorescent spots by finding local maxima in noise reduced images, followed by Gaussian fitting around the detected peaks. Noise reduction is carried out by applying mean, median or Gaussian filters to the raw images. Spot candidates, from filtered images, are selected by non-maximal suppression (method to find local maxima by selecting peaks with sharpest change of intensity) in a user defined rectangular region. After the detection stage, localisation of fluorophores is carried out by fitting a two-dimensional Gaussian function to the candidates in the original images. Fittings that do not meet *user defined criterion* related to signal to noise ratio, width, precision, number of photons and other fitting parameters are rejected. For a detailed discussion on the software, see [30].

Peakfit is available as an *ImgeJ* plugin [31]. Similar implementations of the above mentioned method are also used in [32, 33].
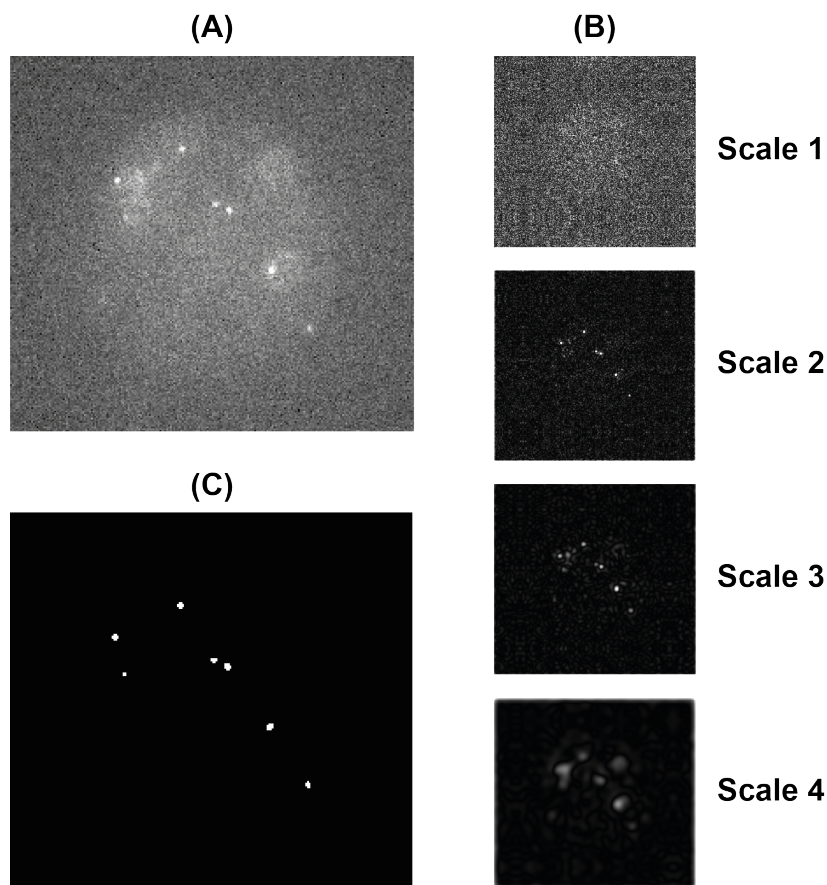
Fig. 1.6 Wavelet decomposition of a localisation microscopy image. (A) Original image, (B) its decomposition into different scales of the wavelet transform and (C) detected peaks from the scales of interest i.e 2 and 3.

Detection in the Wavelet Domain

The requirement to adjust various parameters in *PeakFit* greatly affects its output under different signal to noise ratios (SNRs) i.e. multiple parameters have to be changed, depending on the imaging conditions, to achieve its optimal performance. Moreover, finding local maxima in raw images leads to false positives, especially in experiments involving low signals, similar to the ones discussed in Chapter 3. Under such conditions we found the spot detection in the wavelet domain to be more accurate and robust. The wavelet detection software, *WaveSM*, used in the thesis was implemented in *MATLAB* and was based on [34].

Localised nature of wavelets in spatial and frequency domains makes them an attractive candidate to detect features of different sizes in an image The transform gives a multi-resolution decomposition of the image, where information about features of different sizes is contained in different scales [35]. As discussed in Section 1.4.1, for optimal precision, the pixel size should be matched to the standard deviation of the PSF. So, if an image is

decomposed into wavelet coefficients, objects matching the size of the PSF are contained in specific resolution scales. *WaveSM* uses B3-spline scaling functions for the wavelet decomposition of an image. Figure 1.6 shows that the first scale of such a decomposition contains noise, as it is composed of objects which are a single pixel in size. Scales 2 and 3 contain spots of up to 2 - 5 pixels and are of interest in localisation microscopy, as also discussed in [36].

In *WaveSM*, after the wavelet segmentation of raw images, coefficients from the scales of interest are thresholded to control the false detection rate, on the basis of a user defined parameter. The binary image, calculated from the thresholded coefficients, gives the *'support'* of fluorescent spots in the original image. A two dimensional Gaussian function is then fitted to the support of each spot in the *raw image*, for its precise localisation.

The software requires only one user defined parameter i.e. false detection rate, making it robust under different SNRs, concentration of molecules and imaging conditions. For more details about the algorithm and its implementation, see [34]. Similar implementations of the method are also used in [35, 36].

Localisation without Fitting

So far in this chapter, localisation of point emitters is discussed with reference to fitting the PSF of the microscope (or its approximation) to the fluorescent spots in an image. This requirement of the PSF model can be overcome by exploiting its isotropic nature and localising emitters by determining the centroids of their diffraction limited images. This fast method is used in QuickPALM [37], a commonly used software for image reconstruction from localisation microscopy data. [36] shows localisation accuracy obtained from the wavelet segmentation of an image followed by centroid determination (of individual spots) to be comparable to the Gaussian fitting of the PSF.

A drawback of localisation through centroid estimation is that the presence of background biases results towards the centre of the window (image segment over which the centroid is calculated), especially if the window is not chosen correctly. For optimal results under uniform background, the spot (to be localised) needs to be at the centre of the chosen window. [38] shows the performance obtained by centroid estimation to match the Gaussian fitting of the PSF, by iterative optimisation of the window size.

Image reconstruction through centre of mass calculations can be used as a fast and computationally less expensive way to optimise experiments without applying the complete localisation process. We frequently used this method to test different parameters (buffer composition, exposure time, excitation and activation laser powers) in our experiments, without undergoing the localisation process involving PSF fitting.

1.5 Three-dimensional Localisation Microscopy

Discussion in this chapter has been focused on emitters in the focal plane of the objective (object plane). This is generally not the case as the samples of interest are mostly three-dimensional in nature. In this section, the elongated axial PSF and its effect on the axial resolution of the microscope is discussed. We also discuss the loss of precision for emitters outside the focal plane of the objective due to their blurred images on the camera. Lastly, methods to increase the DOF in localisation microscopy are also discussed.

Image of an emitter outside the object plane is axially displaced from the image plane. Even a displacement of a few hundred nanometres from the object plane results in considerable blurring of the image, as high NA objectives are used in localisation microscopy. The distance over which an emitter remains *'in-focus'* is called the *depth of field* (DOF) of an imaging system. In localisation microscopy DOF can be given as the Rayleigh range (the axial distance from the Gaussian waist at which the intensity of the beam drops by a factor of 2), which is defined in Eq 1.18. The analysis in this section is carried out for the Gaussian approximation of the PSF. For a more detailed analysis on the DOF of microscopes, see [39, 40].

$$z_r = \frac{2\pi}{\lambda} w_o^2 \tag{1.18}$$

w_o is the waist of the beam corresponding to the diffraction limited spot. The waist that gives the optimal approximation of the airy functions is given as [26]:

$$w_o = 0.42 \frac{\lambda}{NA} \tag{1.19}$$

here, it is assumed that the airy function and its Gaussian approximation have the same amplitude. Substituting Eq 1.19 into Eq 1.18 gives:

$$z_r \cong \frac{\lambda}{NA^2} \tag{1.20}$$

and the DOF is twice the Rayleigh range (considering both sides of the focal plane):

$$DOF = 2 \frac{\lambda}{NA^2} \tag{1.21}$$

For excitation wavelength of 560 nm and $NA = 1.3$, DOF comes out to be 728nm (384 nm on both sides of the focal plane). Hence, the PSF is considerably elongated along the axial dimension, compared to its lateral extent (for an emitter in the object plane).

(A)   **(B)**
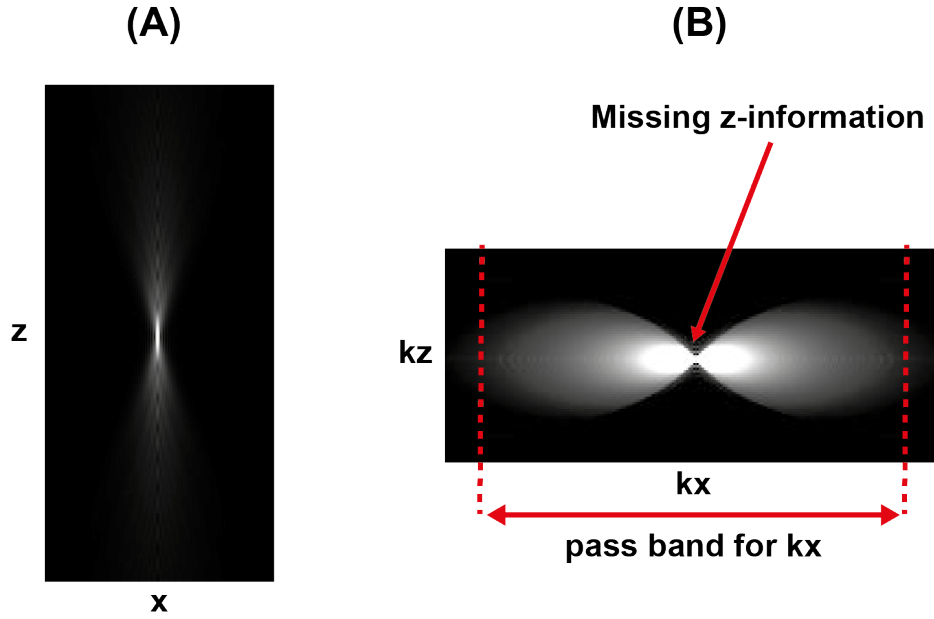
Fig. 1.7 (A) x-z cross section of the PSF. The PSF spreads laterally as the emitter moves away from the object plane. (B) k_x-k_z cross section of the OTF, obtained by the Fourier transform of the intensity pattern (A)

Eq 1.6 shows that the field in the BFP of the objective is related to the field in the object plane by the Fourier transform operation. If the equation is calculated for an emitter axially displaced from the object plane, a circle of uniform magnitude with a quadratic phase curvature is obtained. As a result of this phase, the diffraction limited image after L2, is displaced from the image plane. Hence, in the image plane the beam is spread out as seen from the xz cross section of its intensity in Figure 1.7A. If the Fourier analysis of such a cross section is performed Figure 1.7B is obtained, which is called the optical transfer function (OTF) of the microscope. Like PSF, OTF is also three dimensional in nature and the figure shows its k_z-k_x cross section. As the PSF is axially elongated, not much information is present along the k_z direction. However, in the horizontal direction the extent of the OTF is limited by the diffraction limit of light, with the highest frequency of the pass band corresponding to $\frac{\lambda}{2NA}$ (*Abbe's diffraction limit*).

The above analysis shows that the localisation microscopy can provide a sub-diffraction limit lateral resolution but its axial resolution is of the order of hundreds of nanometres. Moreover, for an emitter outside the object plane, the image is significantly blurred, which affects the localisation precision. In the next section, methods to improve the axial resolution and precision in localisation microscopy are discussed.

1.5.1 Phase Modification Techniques

Although the DOF of a microscope is around a few hundred nanometres, the symmetry of the PSF around the focal plane limits the achievable axial information (even within this range). The symmetry breaks in the presence of aberrations, a concept used by [41] to extract axial position of emitters over 800 nm in the presence of systematic aberrations of the microscope. The concept can be exploited by adding a desired phase to the emitted beam (instead of relying on the aberrations in the system) to increase the DOF in localisation microscopy. In this section, wavefront shaping techniques for extended DOF with high axial resolution and precision are discussed.
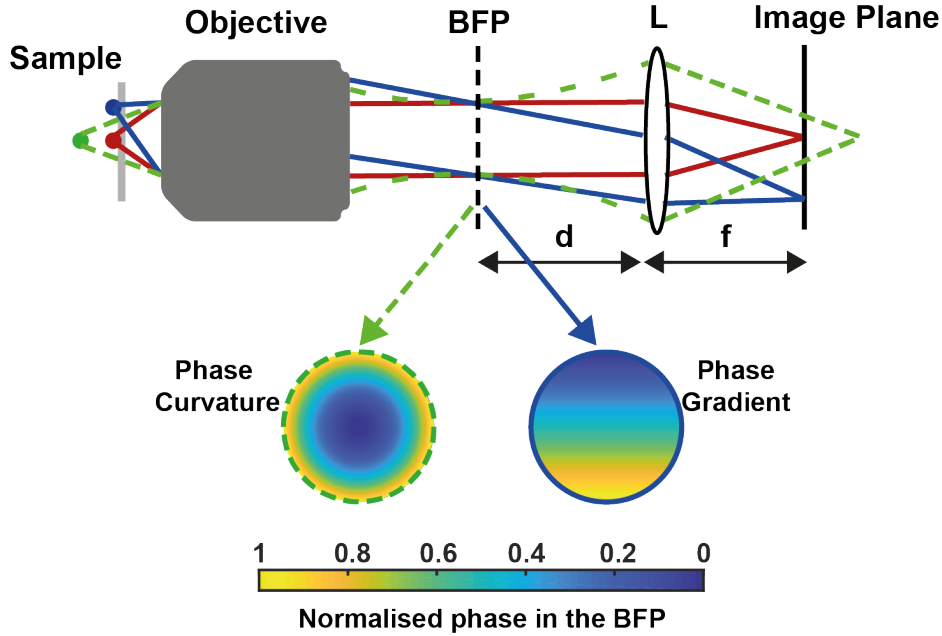
Fig. 1.8 Emission path of our localisation based super-resolution microscope. Light from emitters, in the imaged volume, overlap in the BFP with a phase dependent on the three-dimensional position of the emitters

In localisation microscopy a sparse set of fluorophores, randomly distributed over the entire FOV, emits at a given time. It can be calculated from Eq 1.6 (by using the shift property of the Fourier transform) that for an off-axis emitter, the electric field in the BFP of the objective (in the rest of the thesis it is referred to as the BFP) is a circle with a linear phase, the gradient of which depends on the lateral position of the emitter. Moreover, light from an emitter outside the object plane have a phase curvature which axially displaces the image of the emitter from the image plane, as shown in Figure 1.8. Hence, emissions from all the emitters in the imaged volume overlap in the BFP with a phase dependent on their three-dimensional position. This property of infinity corrected optical systems can

be exploited to break the axial symmetry of the conventional PSF around the focal plane. This is achieved by placing a phase modifying element in the BFP that interacts with the phase curvature of the beam to give an axially varying PSF. Some of these wavefront shaping techniques are discussed below.

Astigmatism

In this technique, the wavefront of the emitted beam is modified to break the axial symmetry of the conventional PSF by separating the focal planes of the two lateral axes [5]. The required phase in the BFP can be given by Eq 1.22, which is the Zernike representation of the phase. Zernike polynomials are commonly used to represent the phase of a beam in the BFP as they form a complete orthogonal basis set over a unit circle. Moreover, commonly occurring aberrations such as coma, astigmatism and spherical aberrations can be represented as different modes of these polynomials [42]. See Appendix B for a description of the Zernike polynomials.

$$\phi(r, \theta) = \sqrt{6}r^2 cos(2\theta) \tag{1.22}$$

Figure 1.9A shows that the phase profile required to generate the astigmatic PSF is similar to that of a cylindrical lens. So, the technique can be implemented by placing a cylindrical lens in the BFP [5] (for practical purposes the lens is usually placed just before the camera to obtain the required shift in the focal planes of the two lateral axes). Astigmatic PSF is elongated along a different lateral axis for emitters on different sides of the focal plane. Figures 1.9D&F show that the PSF is elongated along horizontal and vertical axes for emitters below ($-Z1$) and above ($Z1$) the object plane respectively. For an emitter in the object plane ($Z0$), the image is isotropic due to it being equidistant from the two focal planes. So, by determining widths of the PSF along the lateral axes, axial position of an emitter can be calculated. Similar to the conventional PSF, lateral position of the emitter is determined from the centre of the anisotropic PSF. [5] reported an axial precision of around 20 nm using astigmatic PSF.

From the above discussion, it can be concluded that for emitters outside the object plane, the astigmatic PSF is extended along one of the lateral axes. According 1.17, this results in the loss of localisation precision along that axis. Therefore, the astigmatic PSF gives a non-isotropic localisation precision outside the object plane. Moreover, though the PSF is isotropic in the object plane, it is wider compared to the diffraction limited PSF. Therefore, the axial information is obtained at the cost of lateral precision. DOF of astigmatic PSF is not very different from that of a conventional PSF as the technique just shifts the focal planes

of the two lateral axes. Hence, the power densities used in the technique (and the resulting optical damage) are very similar to the two-dimensional localisation microscopy.

Wavefront shaping techniques to extend the DOF of the microscope are discussed next.
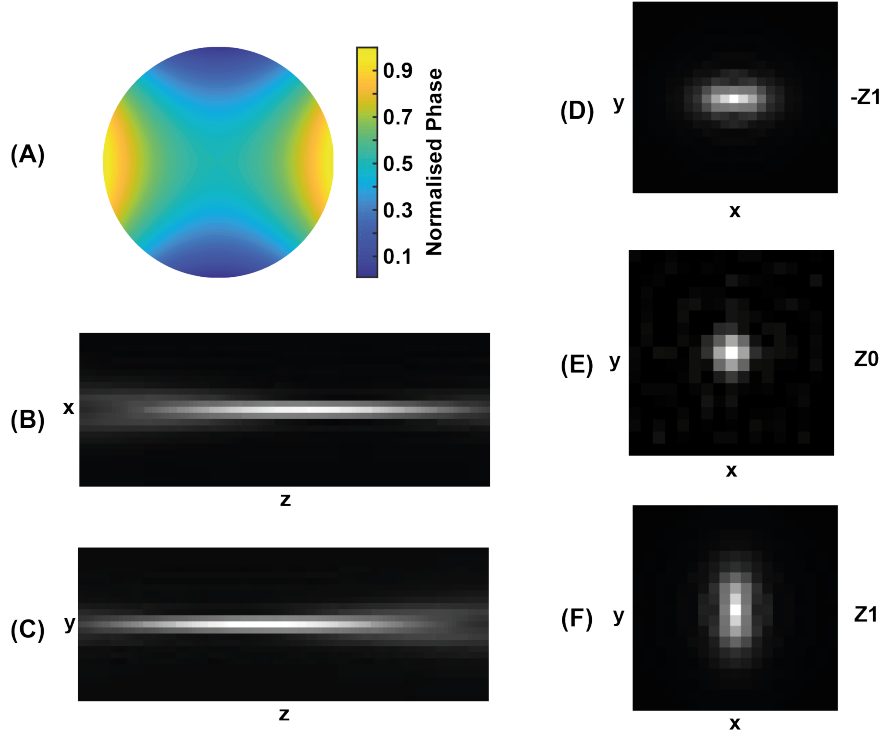
Fig. 1.9 (A) Phase required to generate the astigmatic PSF, (B) x-z cross section of the PSF, (B) y-z cross section of the PSF. (D)-(F) PSF for different axial positions of an emitter. Astigmatic PSF is elongated along a different lateral axis for emitters on different sides of the object plane. For emitters in the object plane, the PSF is isotropic.

Double Helix Point Spread (DHPSF)

In this technique, wavefront of the emitted beam is modified in such a way that instead of a single spot in the image plane, two spots are obtained per emitter. Axial and lateral positions of an emitter are then calculated from the angle between the spots and their centre respectively. So, for a given lateral position of an emitter, DHPSF rotates about the centre as a function of its axial position. Phase required to generate the DHPSF is shown in Figure 1.10A.

DHPSF is based on beams with rotating intensity i.e. beams that rotate as a function of their propagation. Mathematically, these beams can be represented as a linear superposition of Laguerre Gaussian (LG) modes. Detailed discussion on such beams is presented in Appendix C. Briefly, if a beam is formed from the super-position of LG modes along a straight line, it rotates as a function of its propagation [43, 44]. Moreover, the beam has n

rotating lobes, if its constituent azimuthal components are a multiple of n. For example, a beam with the superposition of $(1,1)$, $(3,5)$, $(5,9)$ and $(7,13)$ modes has two rotating lobes (as its azimuthal modes are a multiple of 2), similar to the DHPSF [45] .

Generation of LG beams require both phase and amplitude modulation of a beam, resulting in absorptive masks. Moreover, presence of side lobes further reduce the efficiency of such a PSF . This problem can be overcome by applying an optimised phase only modulation in the BFP which maximises the energy in the two spots of the DHPSF, as proposed by [45]. They start with a correct combination (one that generates two rotating spots) of LG modes and perform optimisations to generate phase only mask with the maximum energy in the two lobes. This was achieved by multiplying the two main lobes of the PSF with a weighting function - two spatially separated Gaussians. Since, the position and the width of the lobes change as a function of defocus (due to its continuous rotation), the weighting function was generated for multiple axial positions. The optimisation resulted in 57% of the energy in the two main lobes, which was 33 times more than the initial mask. Phase masks used in our lab were based on this principle and bought from *Double Helix Optics, USA*. These masks gave a DOF of up to $4\,\mu$m with high localisation precision in all three spatial dimensions. Such masks have also been used by [46, 47] to achieve an axial precision of $< 25\,$nm over an axial range of $3\,\mu$m.

The localisation of the DHPSF, in this thesis, was carried out using the *Easy-DHPSF* software [48]. Since the optimisation process, used to generate the DHPSF, involve Gaussian weighting functions, the software fits two 2D-Gaussian functions to the DHPSF. The axial and the lateral positions of an emitter are calculated from the angle between the fitted Gaussians and their centre respectively. Further improvement in the localisation accuracy and precision have been reported by applying algorithms that use the experimentally measured PSF in the fitting process, such as those involving spline interpolation [27].

Loss of signal in higher order lobes and high background in DHPSF result in worse localisation precision compared to the conventional PSF of the microscope . Higher background is a consequence of the focusing of light from the entire DOF ($\sim 4\,\mu$ m) to the image plane. Moreover, the main lobes of the DHPSF are bigger than the conventional PSF, further deteriorating the localisation precision. Another disadvantage of the DHPSF is its large size, which limits the number of localisable (non-overlapping) molecules in any given frame, as discussed in Section 1.6. Hence, in DHPSF axial information about an emitter is obtained at the cost of lateral and temporal resolutions. Moreover, high power densities are usually involved in the DHPSF. This is because of the low efficiency of phase masks and splitting of photons into two spots with increased background signal.
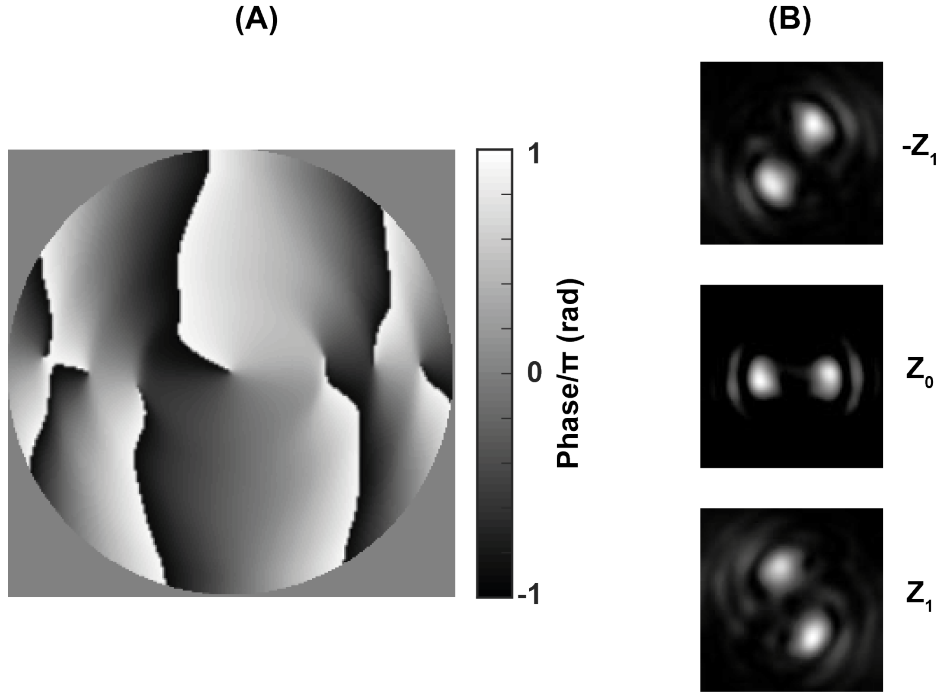
Fig. 1.10 (A) Phase required to generate the DHPSF. (B) DHPSF for different axial positions of an emitter. Axial and lateral positions of the emitter are calculated from the angle between the two lobes of the DHPSF and their centre respectively.

Depth Specific Mask Design

In this section, we discuss PSFs that work optimally over the desired DOF. These PSFs are based on the concept of Fisher information, which is a statistical measure of the sensitivity of the PSF to the change in the emitter position. Fisher information can then be used to compute Cramer-Rao lower bound (CRLB), which is the best theoretical variance achievable for a given PSF [49].

In the presence of Poisson noise and constant background, b, Fisher information is given as [50]:

$$\text{Fisher Information } (x_i) = \sum_{k=1}^{N} \frac{1}{I(k)+b} \left(\frac{\partial I(k)}{\partial x_i} \right)^2 \tag{1.23}$$

here, $I(k)$ is the intensity of the PSF at the kth pixel of an image, N is the total number of pixels in the image and $[x_1, x_2, x_3] = [x, y, z]$ (the three spatial dimensions). The equation shows that the Fisher information is a measure of the change in the PSF, as the position of the emitter changes along a given axis. CRLB can then be computed from the Fisher Information as follows:

$$\text{CRLB } (x_i) = \frac{1}{\text{Fisher Information } (x_i)} \tag{1.24}$$

Optimal PSF is found by minimising the CRLB for a given DOF. This method to generate PSFs was first proposed by [49]. As these PSFs are designed for a specific axial depth, they give near uniform precision over the entire DOF. As a consequence, shape of the PSF varies depending on the DOF they are optimised for. For example, [49] shows the optimal PSF for the DOF of $3\,\mu$m to be very different from the one optimised for $6\,\mu$m DOF. But in both the cases a precision of < 20nm was reported in all three spatial dimensions. [51] then extended the technique to $20\,\mu$m axial range with an axial precision of 60nm.

Hence, by applying this technique any DOF can be achieved. However, the localisation precision deteriorates for large DOFs due to spread of signal over large number of pixels and presence of multiple lobes in the PSF. To overcome the resultant shot noise, the required power densities increase as a function of the DOF for which the PSFs are optimised. Moreover, the size of a PSF also increases as a function of the DOF, leading to the loss of temporal resolution. Therefore, for optimal results it is important to choose the PSF that is designed for the desired DOF.

1.5.2   Non-phase Modification Techniques

So far in this chapter, techniques that extend the DOF of the localisation microscopy by wavefront modification are discussed. Multi-focal plane and multi-view imaging techniques can also be used to extract the three-dimensional position of an emitter, which will be the focus of this section.

Multi-focal Imaging

Axial information about an emitter can be obtained by imaging multiple planes, on different sides of the focal plane, and combining information from them. In the simplest case, this can be done by imaging two equidistant planes from the focal plane of the objective, as shown in Figure 1.11. In such a situation (in the absence of aberrations), if an emitter is in the object plane, its image is of the same size on the two cameras. However, for an emitter outside the object plane, spot sizes on the two cameras are dependent on the axial position of the emitter, which can be used to determine the three-dimensional position of the emitter. [52] applied this technique to track fluorescent beads in 3D with an accuracy of a few nanometres. Similarly, by using this technique [53] obtained a lateral and axial precision of 30nm and 75nm respectively over a micron DOF, with four times better accuracy than the astigmatic PSF. DOF can be further increased by imaging more axial planes as discussed in [54].

Microscope objectives (along with the tube lens) are designed to fulfil the Abbe's sine condition for the image plane only. Displacing the detector from this plane can introduce

significant spherical aberrations [55, 56], leading to the loss of localisation precision. In an interesting approach, [55] used spherical aberrations introduced in such a way to compensate for sample induced aberrations. Multi-focus methods discussed above are affected by such spherical aberrations, as they involve displacement of one or more detectors from the image plane. The problem can be overcome by introducing diffractive optical elements in the emission path of the microscope to achieve refocusing without displacing the detectors from the image plane. [57] uses a distorted diffraction grating to image three different axial planes into different diffraction orders of the grating. [58] uses a phase mask, placed in the BFP, to simultaneously image 9 different axial planes on the camera. The phase mask was designed to split fluorescent emission into nine paths, each having a different phase curvature to image a different axial plane. To further increase the DOF, [59] combined multi-plane imaging technique with the astigmatic PSF to image over an axial range of $8\,\mu$m.

In multi-focal plane imaging, splitting of light from single fluorophores onto multiple cameras leads to the loss of localisation precision in the presence of background signal. For comparable precision (to 2D localisation microscopy) higher power densities are required. Moreover, increase in the size of the PSF as a function of the axial position of an emitter, relative to the object plane, results in further loss of localisation precision. Hence, like other 3D imaging techniques, axial information is obtained at the cost of lateral precision.
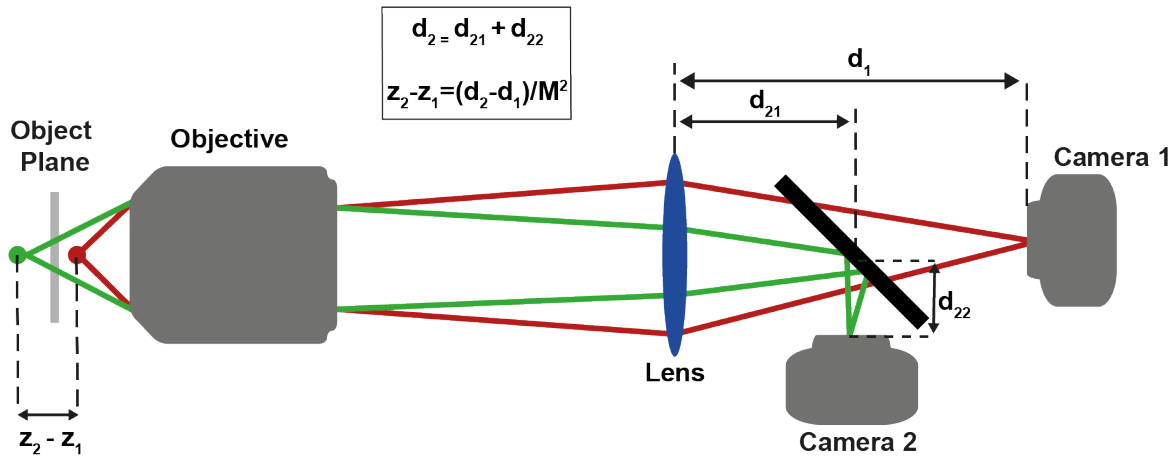
Fig. 1.11 Principle of multi-focal plane imaging. Axial information about an emitter is obtained by imaging multiple planes on different sides of the object plane.

Multi-view Imaging

Similar to multi-focal imaging, three dimensional position of an emitter can also be obtained by imaging a sample from multiple views. This approach is similar to stereo vision, a

commonly used method to extract depth information in computer vision. The technique is based on the concept of parallax, in which a detector *'sees'* displaced image of an emitter, when placed at different positions around it [60]. The displacement is dependent on the axial position of the emitter. So, the three-dimensional position can be determined by calculating disparity between images of the emitter from different views. *'Looking'* at the sample from a certain angle is similar to generating its image from a specific subset of spatial frequencies, a concept discussed in detail in Chapter 5. [61, 62] generated two images of the sample by splitting beam in the BFP, using mirrors, to get a DOF of over $2\,\mu$m. A similar method was implemented by using a wedge prism by [63].

Light field Imaging: In Chapter 5, a method to obtain multiple angular views of an emitter by placing a lenslet array in the image plane of the microscope is discussed. In such a configuration, the camera captures the focal plane of the array. By calculating disparity between multiple *views* of the emitter, we achieved a DOF of over $30\,\mu$m with high localisation precision in all three spatial dimensions. As light from single emitters is split into multiple views (17^2 in our system), significantly more photons are required to localise emitters with sub-diffraction precision compared to the conventional PSF of the microscope and phase modification techniques discussed earlier in the chapter. Future implementations of the light field microscope with fewer views and consequently less stringent requirements on the number of photons are discussed in Chapter 5.

1.6   Sampling Requirements in Localisation Microscopy

Localisation microscopy overcomes the diffraction limit of light by temporally separating emissions from a diffraction limited region. Any given frame of the technique contains signal from few active emitters, providing partial information about the labelled structure of interest. Entire structure is then resolved by combining localisations from all the captured frames. In this section, we discuss the number of samples/localisations required to accurately reconstruct structures in localisation microscopy.

In signal processing, a continuous signal should (at minimum) be sampled at the Nyquist rate for its non-erroneous reconstruction. If f_c is the maximum spatial frequency in the structure of interest, Nyquist sampling rate comes out to be:

$$N_{Nyquist} = \frac{1}{2f_c} \tag{1.25}$$

The equation assumes a periodic sampling of continuous signals, for which at least $N_{Nyquist}$ sampling rate is needed for the non-erroneous reconstruction. However, in localisation
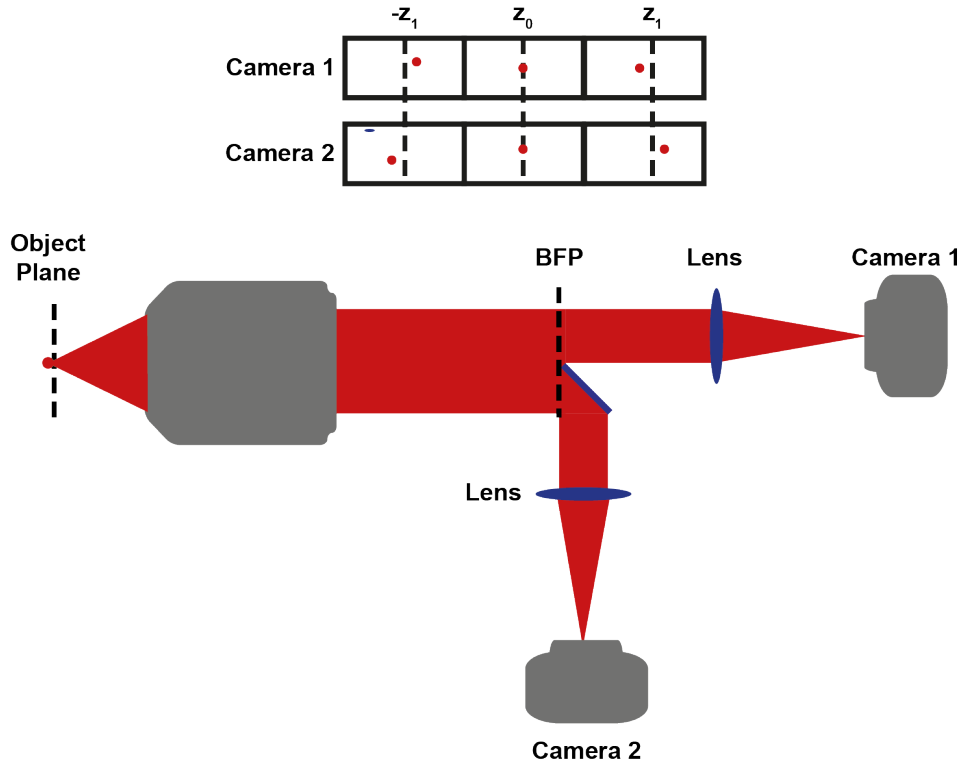
Fig. 1.12 Principle of multi-view imaging. Images on Camera 1 and Camera 2 are formed by different spatial frequencies. This is equivalent to *looking* at an emitter from two different views. Disparity between images on Camera 1 and Camera 2 can be used to determine the three-dimensional position of the emitter.

microscopy each event does not provide information about the underlying labelling density, rather the number of events in a region is proportional to the labelling density [64]. So, the sampling rate should be greater than $N_{Nyquist}$ to reconstruct the structures of interest (as more localisations come from densely labelled regions). [64] shows that even in the absence of background, sampling rate should at least be three times higher than the Nyquist rate to correctly sample a sinusoidal probability distribution.

Such a requirement results in a further loss of temporal resolution, especially in PSFs engineered for large DOFs as they are bigger than the conventional PSF of the microscope. For example, DHPSF (DOF = $3\,\mu$m) and tetrapod (DOF = $20\,\mu$m) are $3\,\mu$m and $15\,\mu$m in size respectively [45, 51]. Similarly in light field imaging, the size of the PSF changes from $1\,\mu$m at a depth of $3\,\mu$m, to $20\,\mu$m at a depth of $10\,\mu$m (See Chapter 5 for more details). So in any given frame, only 1-2 non-overlapping (and hence localisable) spots can exist, which greatly increases the number of frames required to correctly sample the underlying structure. This was the major limitation of the DHPSF based three-dimensional imaging to study the

structure of dense chromatin fibres in primary spermatocytes of *Drosophila*, as discussed in Chapter 4

1.7   Summary

The chapter covered the diffraction properties of light and use of a convex lens to shift the far-field diffraction pattern from $z \to \infty$ to its focal plane. Origin of the resolution limit in optical imaging systems was also explored from the diffraction properties of light. We then explained the application of the localisation microscopy to overcome the resolution limit by temporally separating emissions from a diffraction limited region. Methods to extend the technique to three-dimensions were also presented. This included wavefront engineering, multi-focal imaging and multi-view imaging. The chapter concluded with a discussion on the number of localisations required for the non-erroneous reconstruction of structures in localisation microscopy.

Chapter 2

Development and Optimisation of a Localisation Based Super-resolution Microscope

2.1 Introduction

Localisation microscopy overcomes the diffraction limit of light by temporally separating emissions from single molecules within a diffraction limited region. The technique, when combined with engineered point spread functions, can give high localisation accuracy and precision in all three spatial dimensions. This chapter describes the work conducted to design, develop and characterise a localisation based super-resolution microscope at Cambridge Advanced Imaging Centre (CAIC).

2.1.1 Chapter Description

The chapter begins with the description of the experimental setup for a multifunctional localisation based super-resolution microscope. Afterwards, steps taken to calibrate and characterise the setup are discussed, which include characterising gain and read-noise of sCMOS cameras and determining the achievable localisation precision for different number of photons captured (per emitter) at the camera. Origin of spherical aberrations when imaging beyond the coverslip is also discussed along with their effect on the PSF of the microscope. The chapter ends with the description of an optimal alignment procedure to obtain high localisation accuracy over large FOVs in three-dimensional localisation microscopy.

2.1.2   Published Work

The optimal alignment procedure presented in Section 2.7 was published in [65].

2.2   Experimental Setup

This section describes the design and development of a localisation based super-resolution microscope with the following functionalities:

- two-dimensional localisation microscopy

- dual-colour localisation microscopy

- three-dimensional localisation microscopy using DHPSF

- light field localisation microscopy

An inverted microscope frame, Leica DM IRE2, was modified to implement the microscope. Experimental setup of the microscope and its different components are discussed below.

2.2.1   Excitation Path

Excitation lasers were provided by Omicron LightHUB, which combined four wavelengths (405 nm, 488 nm, 561 nm and 638 nm) for compactness, ease of use and high stability. These laser lines allowed excitation of a wide variety of fluorophores throughout the visible spectrum of light. Output beam of the laser combiner was through a single mode optical fibre and it was collimated to 8 mm diameter using an off-axis parabolic mirror (Thorlabs, RC12SMA-P01). Linear polarisation of the beam was converted to circular polarisation using a quarter wave plate, which allowed us to excite fluorophores with different dipole orientations.

Two mirrors, $M1$ and $M2$, were adjusted to dictate the necessary beam deflection for widefield or HiLo illumination modes. A 250 mm focal length lens, $L1$, then focused light to the BFP of a silicone oil $60x$, 1.3 NA Olympus objective. This resulted in a collimated beam of 96 μm diameter at the sample. A quad-band filter (Chroma ZT405/488/561/640rpc) was placed between $L1$ and the objective to separate the excitation and the activation lasers from the fluorescent emissions. The sample was placed on a system of piezo-driven stages that could move in three dimensions with a resolution of 10 nm (Nanos, LPS 30-60-1-VX-S-N-XY and LPS 30-30-1-VX-S-N-XYZ). See Figure 2.1 for a schematic of the experimental setup.
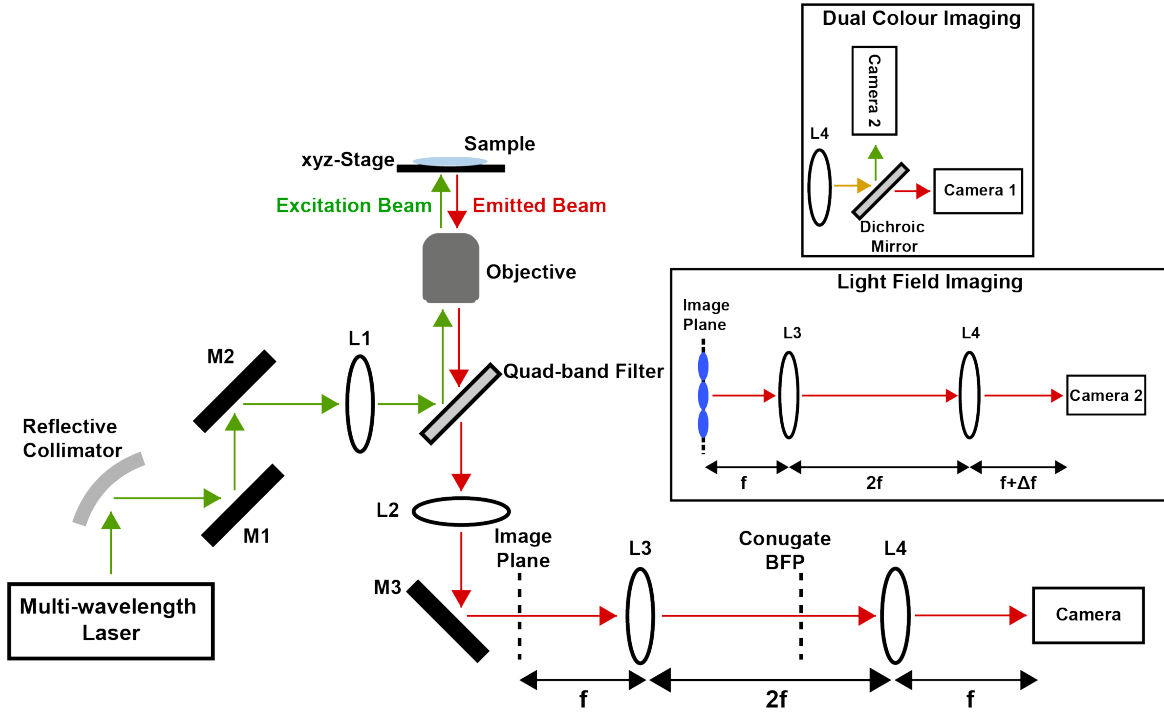
Fig. 2.1 Experimental setup for the multifunctional localisation based super-resolution microscope developed at CAIC.

2.2.2 Emission Path

Emitted light from the fluorophores in the FOV was collected by the same objective and focused to the image plane by a 200 mm focal length tube lens, *L*2. Different functionalities were implemented by modifying the subsequent emission path of the microscope as follows.

Single Colour Localisation Microscopy

In this case, lenses *L*3 and *L*4 (125 mm focal length) relayed the image plane to a camera placed in the focal plane of L4. Following cameras were used in the experiments:

- Camera 1: Photometrics Prime 95B, pixel size = 11 μm, peak QE = 95%

- Camera 2: Hamamatsu Flash 4.0, pixel size = 6.5 μm, peak QE = 82%

Due to its higher quantum efficiency (QE), Camera 1 was better suited for localisation microscopy, and is currently being used in the system. However, as this camera was added to the microscope in the later part of the PhD, earlier experiments (those discussed in Chapter 3) were performed using Camera 2. For each experiment, details of the camera are explicitly mentioned when it is discussed in the thesis.

Further band-pass filters were placed before the camera to ensure high attenuation of any remaining (unwanted) laser light. Choice of these filters depended on the excitation laser and we used the following for our laser lines:

- 488 nm laser: Semrock, FF03-525/50-25

- 561 nm laser: Semrock, FF01-600/52-25

- 638 nm laser: Semrock, BLP01-647R-25

Dual Colour Localisation Microscopy

Dual colour imaging was performed by simultaneously illuminating a sample (labelled for dual colour imaging) with two excitation lasers. Emissions corresponding to different excitation wavelengths were separated by using a dichroic filter (installed on the Cairn *TwinCam* system). The separated emissions were then imaged onto two cameras i.e. Camera 1 and Camera 2. The following dichroic filters, along with the band-pass filters mentioned above, allowed us to use the available excitation lasers in different combinations:

- Chroma T565lpxr-UF2 (transmits wavelengths above 565 nm)

- Chroma T647lpxr-UF2 (transmits wavelengths above 647 nm)

Image registration was required to correctly superimpose the data collected on different cameras. This was achieved by imaging fluorescent beads and finding the optimal affine transform between their images captured on the two cameras. Alignment and characterisation of the system for dual-colour imaging is discussed in Chapter 4.

Three-dimensional Localisation Microscopy

$L3$ was used to access the conjugate BFP of the microscope, where the phase mask (from Double Helix Optics, USA) to generate the DHPSF was placed. Focal length of the tube lens was chosen to be 125 mm to obtain a beam size of 4.8 mm in the conjugate BFP, which matched closely to the size of the phase mask. The phase mask was introduced in the setup by using a magnetic mount with a quick release plate (Thorlabs, CXY1Q). This allowed us to easily change between the two-dimensional and the three-dimensional localisation microscopy. The exact position of the conjugate BFP depended on the distance between the objective and $L2$. We found some interesting consequence of the non-optimal positioning of the phase mask on three-dimensional localisation microscopy which are discussed in Section 2.7 of the chapter.

Light field Localisation Microscopy

Light field imaging was carried out by placing a lenslet array (RPC Photonics MLA S100-f21, pitch = $100\,\mu$m, $f = 2.1$mm) in the image plane of the microscope and Camera 2 was placed in the focal plane of the array as shown in the inset of Figure 2.1. Camera 2 was chosen for light field imaging (over Camera 1) because of its smaller pixel size, which gave finer sampling of the light field PSF and hence better localisation precision. Alignment and characterisation of the microscope for light field microscopy is discussed in Chapter 5.

A Note on Magnification of the Objective

The magnification mentioned on Olympus objectives is applicable for their usage with a tube lens of 180 mm focal length [66]. So, the effective focal length of our objective can be calculated as follows (using magnification equation of a two-lens system [8]):

$$f_{obj} = \frac{f_{TL,olymp}}{M_{TL,olymp}} = \frac{180}{60} = 3\,\text{mm} \tag{2.1}$$

here, f_{obj} and $f_{TL,olymp}$ are the focal lengths of the objective and the Olympus tube lens respectively. $M_{TL,olymp}$ is the magnification obtained when the objective is used with the tube lens of $f_{TL,olymp}$ focal length. However, in our system the objective was used with a Leica tube lens (installed in the microscope frame) with a focal length of 200 mm. This resulted in an effective magnification 66.67 between the object plane and the image plane.

$$M_{system} = \frac{200}{3} = 66.67$$

Using this magnification, the pixel size (in the object plane) of Camera 1 and Camera 2 came out to be 165 nm and 97.5 nm respectively.

2.3 Control of the Microscope

Control software for the microscope was written in *LabVIEW*, the layout of which is shown in Appendix D. The software included the following functionalities:

- Control of stages for three-dimensional scanning of a sample, with the required dwell time. Step size could be selected for each dimension separately.

- Simultaneous image acquisition on two cameras (*Flash 4.0* and *Prime 95B*). The software allowed use of one camera at a time as well.
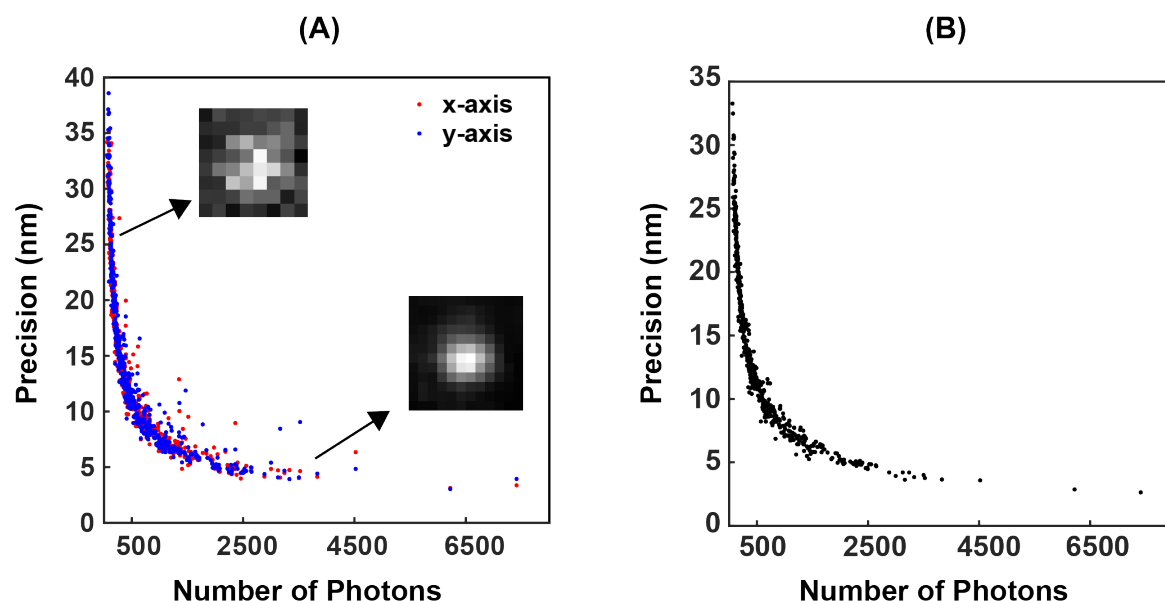
Fig. 2.2 Localisation precision as a function of the number of photons captured at the camera. (A) Precision estimated from the variation in the position of fluorescent beads over 1500 frames, captured at 10 msec exposure time, under different excitation laser powers. (B) Theoretical precision of localising the same beads (obtained from the *Peakfit* software).

- Control of lasers in pulsed or continuous mode

The control of cameras, stages and lasers from LabVIEW allowed us to automate time-lapse imaging. This was especially useful for the characterisation of the microscope for light field and DHPSF based three-dimensional imaging. The software was also used to provide regular burst of the activation laser in some experiments discussed in Chapter 3. However, experiments that did not require automated control were carried out using separate controls for lasers (from *Omicron* software) and cameras (*HCImage* for *Flash 4.0* and *Micro Manager* for *Prime 95B*). Moreover, in these experiments, the stages were manually controlled to image the required region of interest.

2.4   Precision and Number of Photons

We started our localisation microscopy experiments by determining the achievable localisation precision as a function of the number of photons captured at the camera. For these experiments, fluorescent beads (*Invitrogen*, 100 nm) were adhered to a coverslip surface using Poly-L-lysine (PLL). Imaging was performed with different excitation laser powers at an exposure time of 10 msec (as used in the imaging of biological samples). 1500 frames were captured at each laser power and beads were localised using the *Peakfit* software [31].

Localisation precision was calculated from the variation in the position of a bead over multiple frames, captured for a given laser power. A typical FOV contained around 20 beads and the precision was calculated for each bead separately. For a certain axis, x, the precision was calculated as follows:

$$\Delta x = \sqrt{\frac{\sum_1^{N_t}(x - \bar{x})^2}{N_t - 1}} \tag{2.2}$$

here, $\bar{x}$ is the mean position of the bead over N_t frames.

Figure 2.2A shows precision as a function of the number of photons captured at the camera. The figure was obtained by calculating Δx for all the beads in the FOV under different excitation laser powers. The number of photons, emitted by an emitter, were obtained from the area of the Gaussian PSF, the amplitude and width of which can be obtained using Eq 1.15. If A is the area of the Gaussian function in counts, it can be converted to the number of photons as follows:

$$\text{Number of photons} = \frac{A}{g}$$

where, g is the gain of the camera (i.e. g counts are produced for each photon at a camera pixel, see the next section for its calculations). In this section, the number of photons were directly obtained from the *PeakFit* software, which fits Eq 1.15 to the fluorescent spots in the acquired images.

As expected, the localisation precision improved with an increase in the number of photons, asymptotically reaching $\sim 4\,\text{nm}$ for large number of photons, which corresponded to the best precision achievable on the microscope. Figure 2.2 B shows the theoretical precision of localising the same beads (obtained from *PeakFit* software). The theoretical precision can be obtained by applying the Thompson's Equation, as discussed in Section 1.4.1. See [31] for details about the theoretical precision obtained for different fitting algorithms.

Theoretical precision closely matched the results presented in Figure 2.2A, which was a consequence of obtaining the latter over a short time of 15 sec. Any drift in the microscope was negligible over such a duration. Hence, the above analysis gives an estimate of:

- the localisation precision as a function of the number of photons

- the mechanical stability of the system over short time scales i.e. the effect of high frequency disturbances (if any) on the localisation precision

In single molecule tracking of Notch pathway transcription factor (Chapter 3), the average track length was around 50-60 msec. For these experiments, results presented in Figure 2.2 A explained the localisation precision and hence the smallest diffusion coefficient measurable

on the microscope. However, this was not the case when imaging was performed over long time scales e.g. in the experiments carried out to study the structure of chromatin fibres (Chapter 4). These experiments required more than 10 min of imaging, during which the mechanical drift of the microscope stage was significant. An example graph, in Figure 2.3, shows a drift of 60 nm over 10 min in both the lateral axes of the microscope. So, in experiments performed over long time scales, drift needed consideration to avoid errors in the interpretation of localisation microscopy results. This problem is explored in detail, along with the possible solutions, in Chapter 4 of the thesis.
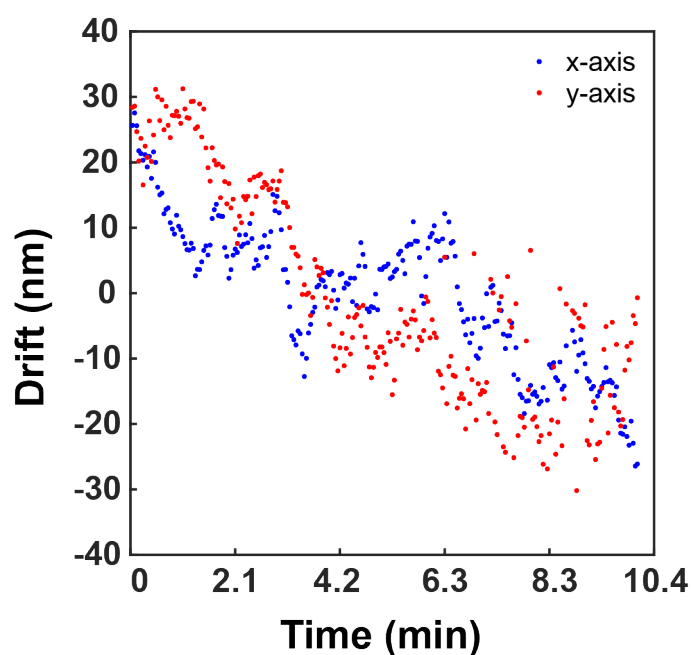
Fig. 2.3 Lateral drift in the microscope stage over 10 min. Experiments performed over long time scales required consideration of such drifts to avoid errors in the interpretation of the localisation microscopy results.

Localisation precision in DHPSF

DHPSF involves splitting of emissions from single emitters into two spots, which are localised by fitting two two-dimensional Gaussian functions. For each Gaussian fitting, the localisation precision can be given by the results presented in Figure 2.2. However, due to 57% efficiency of the DHPSF (see Section 1.5.1), only 28.5% of the light makes it to the two main lobes of the PSF.

Lateral position of an emitter is calculated from the centre of the two Gaussian functions. If shot noise is the only limiting factor, the centre of the Gaussians can be localised without

any loss of precision, as discussed in Appendix A. Therefore, the lateral precision in DHPSF is mainly affected by the loss of 42% of the photons in the higher order lobes. Other factors such as the background signal and larger size of the DHPSF lobes can further deteriorate the precision. As far as the axial precision is concerned, the angle between the spots is highly sensitive to the localisation precision obtained for individual spots. The axial precision has been reported to be nearly twice of the lateral precision [46]. For example, we expect lateral and axial precisions of 20 nm and 40 nm respectively for 500 photons, which is in line with the results presented in [46].

2.5   Characterisation of Cameras

An important step in the characterisation of the microscope was to quantify the gain and the read-noise of our cameras. We used sCMOS cameras for localisation microscopy because of their high frame rates and large FOVs compared to the EMCCD cameras [5, 67]. This section presents the quantification of the gain of these cameras, which was essential to convert between counts in an image and the corresponding number of photons captured at the camera chip. The section also highlights the pixel dependent variations in the gain and the read-noise of sCMOS cameras and their effect on localisation microscopy. These pixel dependent effects are a consequence of the pixel specific electronics, in sCMOS cameras, to convert photo-electrons to voltage and its subsequent amplification. On the other hand, in EMCCD cameras, photo-electrons from each pixel are transferred to the readout register for conversion to current, which is later multiplied and digitalised by chip-wide electronics [67]. So, the pixel dependent effects do not exist in EMCCD cameras, but they suffer from multiplication noise (introduced at the current amplification stage) which reduces the signal to noise ratio (SNR) of captured images by a factor of $\sqrt{2}$ [68]. The nature of signal acquisition and its processing in EMCCD cameras makes them slower than the sCMOS cameras, an important reason for us to choose the latter for our system. Moreover, sCMOS cameras can now provide a QE of 95 %, which is close to that of the EMCCD cameras (a major limitation of the earlier sCMOS cameras was their low QE).

2.5.1   Gain and Read Noise Calculations

When a photon reaches the sCMOS camera chip, it produces an electron with a probability equal to the QE of that camera. The electron is then converted to counts by the camera electronics with a pixel specific amplification, namely the gain of that pixel. We calculated this pixel-gain by measuring signal variations in a pixel for different intensities of the incident

light, as discussed in [69]. Briefly, if N_e is the total noise at a pixel in electrons, it can be written as a sum of different noise sources:

$$N_e^2 = R_e^2 + \sigma_{e,shot}^2 + \sigma_{e,other}^2 \tag{2.3}$$

here, R_e^2, $\sigma_{e,shot}$ and $\sigma_{e,other}$ are read noise, shot noise and fixed pattern noise, at the pixel in electrons, respectively. If S_e and S_c represent the total signal at the pixel in electrons and counts respectively, by using the Poisson statistics of the shot noise we get:

$$\sigma_{e,shot}^2 = S_e = gS_c \tag{2.4}$$

where, g is the pixel-gain. Using Eq. 2.4 in Eq 2.3 and conversion from electrons to counts, give:

$$g^2 N_c^2 = g^2 R_c^2 + gS_c + g^2 \sigma_{c,other}^2$$
$$N_c^2 = \frac{1}{g} S_c + \left(R_c^2 + \sigma_{c,other}^2 \right) \tag{2.5}$$

here, N_c, R_c and $\sigma_{c,other}$ are the total noise, read-noise and fixed pattern noise in counts respectively. Hence, the slope of the variance vs signal graph, obtained by measuring signal variations in a pixel for different intensities of incident light, can be used to estimate the gain of that pixel (see the *Methods* section at the end of the chapter). It is to be mentioned that this process is carried out over an entire image (instead of individual pixels) for EMCCD cameras but due to pixel dependent gain and read-noise in sCMOS cameras, these calculations were performed for each pixel separately. More information on the process can be found in [68–70].

Figure 2.4A&B show histograms of pixel-gains for Flash 4.0 and Prime 95B cameras respectively. As expected, a spread in pixel-gains was observed for both the cameras. Moreover, the average pixel-gain was $2.2 \, \text{counts/e}^-$ and $1.1 \, \text{counts/e}^-$ for Flash 4.0 and Prime 95B cameras respectively (close to the values provided by the manufacturers).

Next, we investigated the read-noise of these cameras, which is produced at the charge-to-voltage conversion stage in a sensor and is pixel dependent for sCMOS cameras [71]. To do so, the signal variations in a pixel were calculated in the absence of light. In such a situation, the shot noise and the fixed pattern noise do not exist, as they originate due to the discrete nature of photons and their processing on a camera chip respectively. Hence, in the absence of light, Eq 2.5 becomes:

$$N_c^2 = R_c^2 \tag{2.6}$$
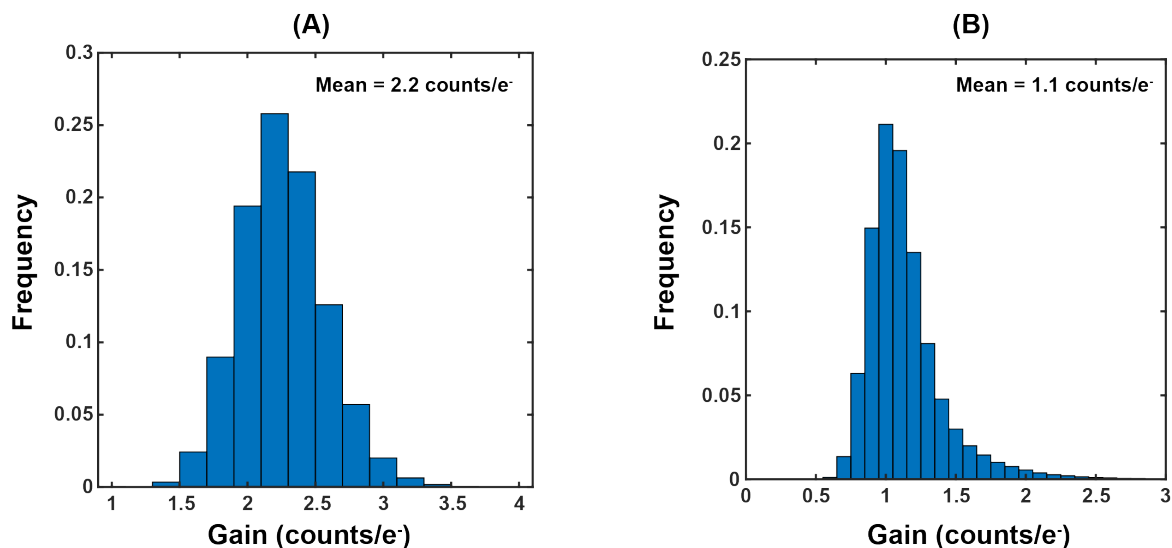
Fig. 2.4 Histogram of pixel-gains for (A) Hamamatsu Flash 4.0 and (B) Photometrics Prime 95B cameras. Spread in the histograms show the pixel dependent nature of the gain for sCMOS cameras.

Figure 2.5A&B show histograms of read-noise for Flash 4.0 and Prime 95B cameras respectively. We obtained the average read-noise of $2.87\,\mathrm{counts}$ ($1.30\,\mathrm{e}^-$) and $2.30\,\mathrm{counts}$ ($2.09\,\mathrm{e}^-$) for Flash 4.0 and Prime 95B respectively. Higher read-noise in the latter was a consequence of its larger pixels. We used this read-noise analysis to generate synthetic images, with realistic noise, to test the performance of various data analysis software used in the thesis.

Effect on localisation microscopy: Results presented in this section highlighted the pixel dependent nature of gain and read-noise in sCMOS cameras. Improvement in the localisation precision has been reported when these effects are included in the localisation process [68]. To harness the complete potential of localisation microscopy and sCMOS technology, the pixel dependent gain and noise should be considered in the localisation algorithms. Corrections can be made by weighing pixels on the basis of their read-noise and compensating for the bias introduced by *hot* (high gain) and *cold* (low gain) pixels. Such corrections can remove any pixel dependent biases (due to aberrated pixels) in our tracking (Chapter 3) and clustering analyses (Chapter 4) and is a current topic of research at CAIC.

2.6 Spherical Aberrations - Imaging Beyond the Coverslip

The most commonly encountered aberration in fluorescence microscopy is the spherical aberration (SA), which will be the focus of this section. SA mainly originates due to the
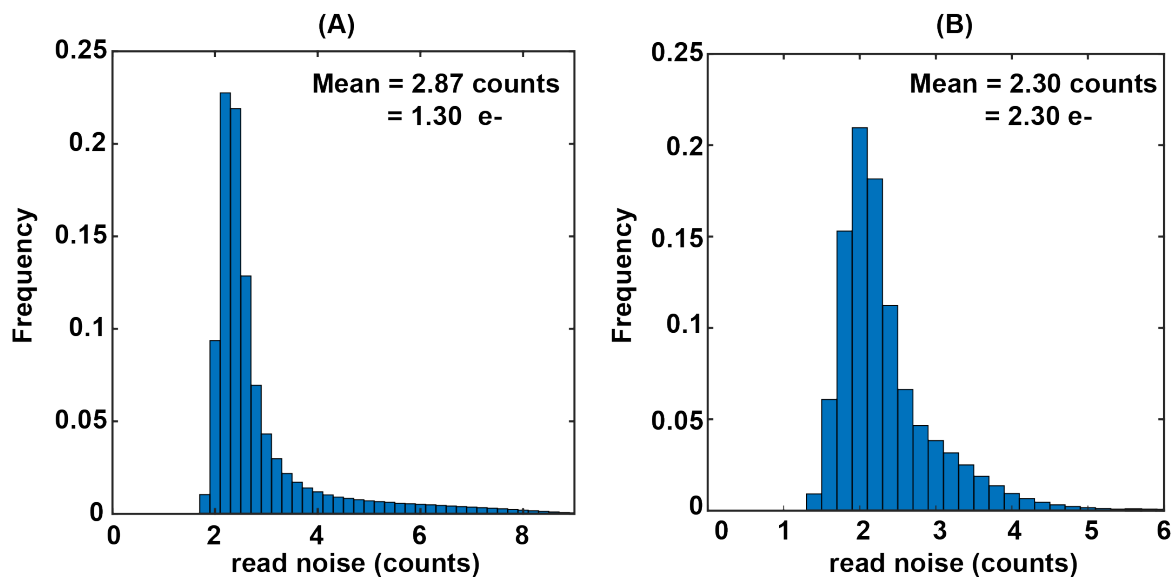
Fig. 2.5 Histogram of pixel dependent read-noise for (A) Hamamatsu Flash 4.0 and (B) Photometrics Prime 95B cameras. Spread in the histograms show the pixel dependent nature of the read-noise for sCMOS cameras.

propagation of light through an interface of mediums with different refractive indices as shown in Figure 2.6 (we will consider the emission path of our microscope as aberrations in this path are of interest in localisation microscopy). On an inverted microscope system, emitted light propagates through a glass coverslip before reaching the objective. High numerical aperture objectives, used in localisation microscopy, are usually designed to work with water, oil or silicone oil as the immersion media. So, the refractive index (*n*) of such objectives is very different from that of the glass coverslips. Modern objectives come with a correction collar to compensate for SA induced due to this difference of refractive indices between the objective and the sample. Adjustment of the correction collar changes the distance between lens groups within the objective. This produces the required change of angles between the peripheral and the axial rays [72]. So, by adjusting the correction collar of the objective, *negative* SA are added to the wavefront to compensate for the SA introduced at the interface of the coverslip and the immersion media.

For optimal imaging, correction collar should be perfectly matched to the thickness of the glass coverslips. Failure to do so adds counter SA resulting in the deterioration of the PSF. SA can also originate when imaging is performed deep within a sample, the refractive index of which is different from that of the immersion medium of the objective. For example, [73] measured different amounts of spherical aberrations in different sections of the mouse brain, where the refractive index varied from 1.35 to 4. Figure 2.6B shows the effect of such a refractive index mismatch on the focusing of light rays by a microscope objective. The figure
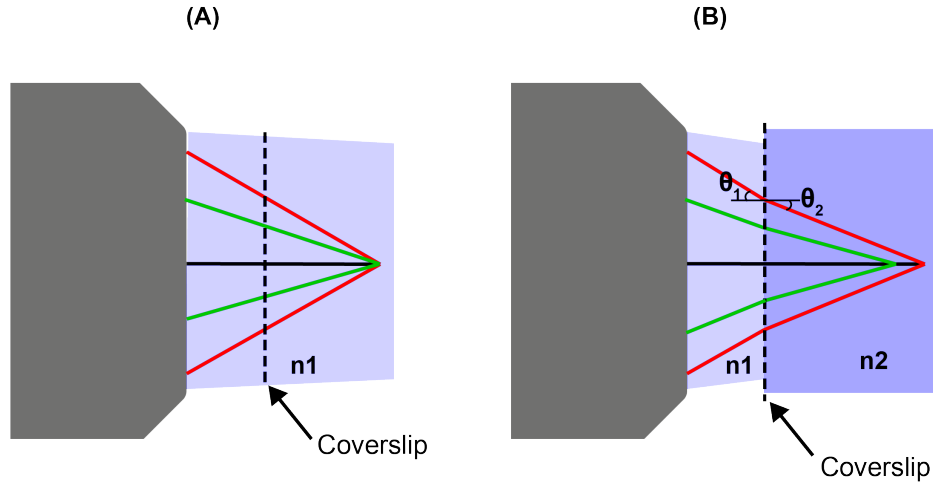
Fig. 2.6 Origin of the spherical aberrations due to propagation of light through an interface of mediums with different refractive indices.

shows that the rays which were focused to a point in a homogeneous medium, intersected the optical axis at various points when n of the sample did not match the n of the immersion media. This can be understood by the Snell's law of refraction.

$$n_1 sin(\theta_1) = n_2 sin(\theta_2)$$
$$\theta_2 = Sin^{-1}\left(\frac{n_1}{n_2}sin(\theta_1)\right) \tag{2.7}$$

here, θ_1 and θ_2 are the angles of incidence and refraction when light rays travel from a medium of refractive index n_1 to n_2. The equation shows that, for $n_2 > n_1$, larger the angle of incidence of a ray, smaller is its angle of refraction. So, off-axis rays are focused away from the focal point, obtained in the absence of aberrations as shown Figure2.6B. Such a splitting of light rays results in a blurred PSF (this blurring is in addition to the spread of the PSF due to the finite numerical aperture of the objective).

The simple analysis discussed above, explains the blurring of the PSF as light propagates through mediums with different refractive indices, but rigorous mathematical modelling is required to show that the blurring corresponds to spherical aberrations. Such a discussion is carried out in [74] and [75] for mediums with single interface and multiple interfaces respectively.

2.6.1   Effects on Two-dimensional Localisation Microscopy

From the above discussion it can be concluded that when a point emitter is imaged in the presence of SA, light (from the emitter) is not focused to a diffraction limited spot in the

image plane. In fact, light rays intersect the optical axis at a range of axial positions. The smallest spot obtained under such a situation is called the *circle of confusion* (CoC), which also corresponds to the *image* of an emitter in the presence of SA (see Figure 2.7A). Moreover, the plane containing the CoC is axially shifted from the image plane i.e. the plane in which the image is formed in the absence of aberrations.

(A)   **(B)**
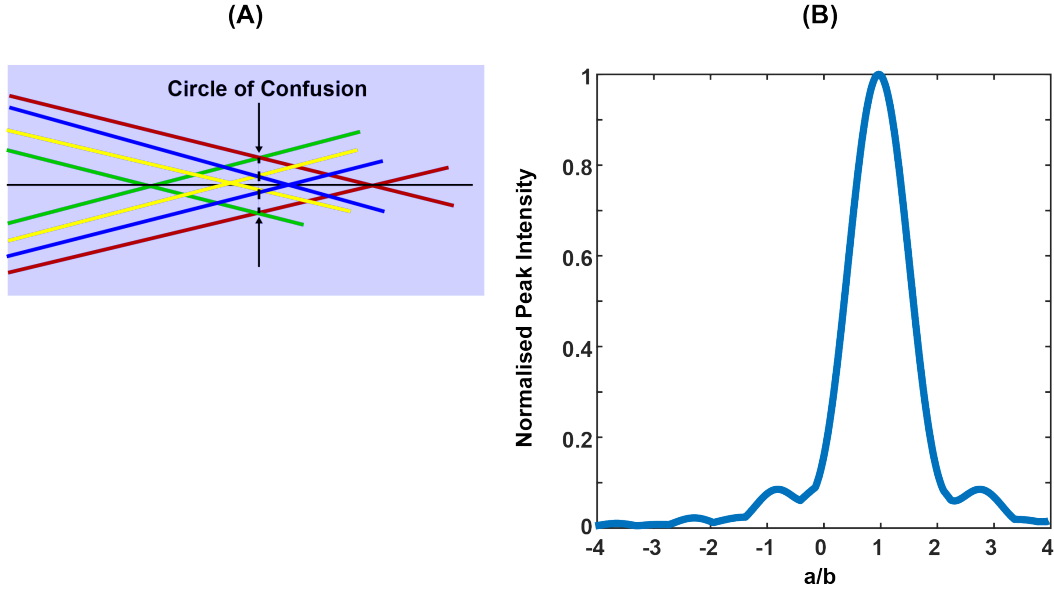
Fig. 2.7 (A) Imaging of an emitter in the presence of SA. CoC corresponds to the smallest spot obtained under such a situation. (B) In the presence of SA, image of an emitter in the object plane is axially shifted from the image plane. *a* and *b* are the coefficients of the SA and the defocus respectively in Eq 2.9

Simulations

To study the interaction between the defocus and the SA, the PSF of our microscope was simulated under these aberrations. Aberrations were added in the BFP of the objective and the corresponding PSF was calculated by taking the Fourier transform of the field in the BFP.

$$I(x,y) \propto \left| \mathscr{F}\left[A(u,v)e^{\iota\phi(u,v)} \right] \right|^2 \tag{2.8}$$

here, $A(u,v)$ and $\phi(u,v)$ is the amplitude and the phase of the beam in the BFP respectively. For simulations, we assumed the BFP to be a circle of uniform magnitude i.e.

$$A(u,v) = \begin{cases} 1 & \text{if } \rho \leq 1 \\ 0 & \text{if } \rho > 1 \end{cases}$$

Other than depending on the three-dimensional position of an emitter (as discussed in Section 1.5.1), $\phi(u,v)$ also depends on the aberrations in the system [76]. SA and defocus were added to $\phi(u,v)$ in the following form:

$$SA = a\rho^4$$
$$Defocus = b\rho^2$$

(2.9)

here, a & b are the coefficients of the spherical and the defocus aberrations respectively and $\rho = \sqrt{u^2 + v^2}$ [77]. It is important to note that the Zernike representation of SA was not used in the simulations. This is because Zernike polynomials represent balanced aberrations i.e. mathematical formulation of the SA already contains the defocus term required to obtain the maximum intensity in the image plane. As the goal of this simulation was to explore the interaction between the defocus and the SA, they were added in their *'pure'* form to the simulated beam [78].

Figure 2.7B shows the amplitude of the PSF in the image plane in the presence of SA and defocus. The highest amplitude of the PSF was achieved for $|a| = |b|$. The figure was obtained by simulating the PSF for $a = \frac{\pi}{4}$ and different amounts of b. These results show that in the presence of SA, image of an emitter is axially shifted from the image plane. Moreover, the axial symmetry of the PSF around the focal plane is also lost, as seen from Figure 2.8. The figure shows a simulated PSF for $a = 0$ and $a = \frac{\pi}{4}$ respectively. We exploited this asymmetry of the PSF to adjust the correction collar of the objective to compensate for any systematic SA in the microscope (see Section 3.3). This allowed us to efficiently collect photons, and hence improve localisation precision, especially in experiments involving low number of photons.

Experiments

SAs not only result in the axial spreading of the PSF but also enhance its side lobes [79, 80]. This effectively reduces the number of photons available for the localisation of an emitter. Figure 2.9 shows the number of photons collected at the camera as a function of SA. The figure was obtained by imaging 100 nm beads on a No. 1.5 coverslip (average thickness = 170mm). SA was introduced by changing the correction collar of the objective, which was equivalent to image at different depths inside a medium with the refractive index of glass, using a silicone oil objective. We found the variation of the correction collar to be the easiest way of introducing a controlled amount of SA. Results of the analysis are shown in Figure 2.9. The figure shows that the number of photons decreased with an increase in the amount of SA, resulting in a loss of $\sim 30\%$ photons at a depth of $15\,\mu$m. Hence for optimal
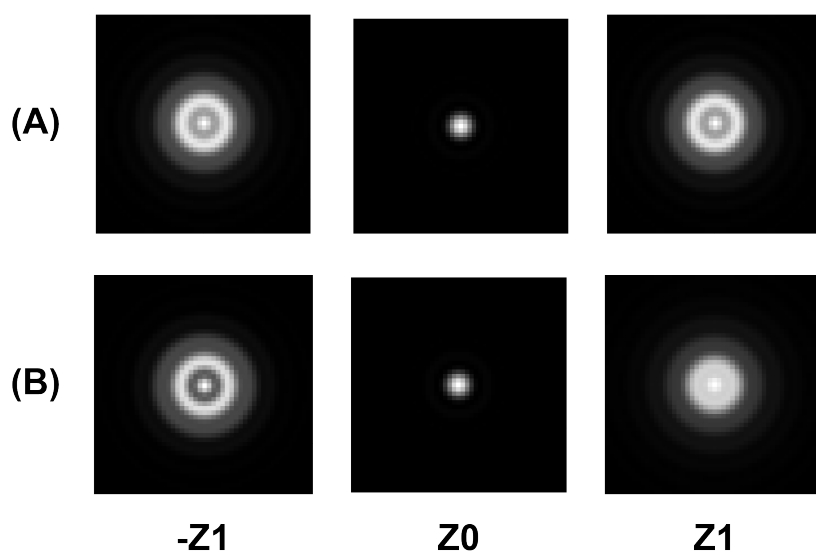
Fig. 2.8 Point spread function at different axial positions in the (A) absence and (B) presence of SA. SA result in an axially asymmetric PSF
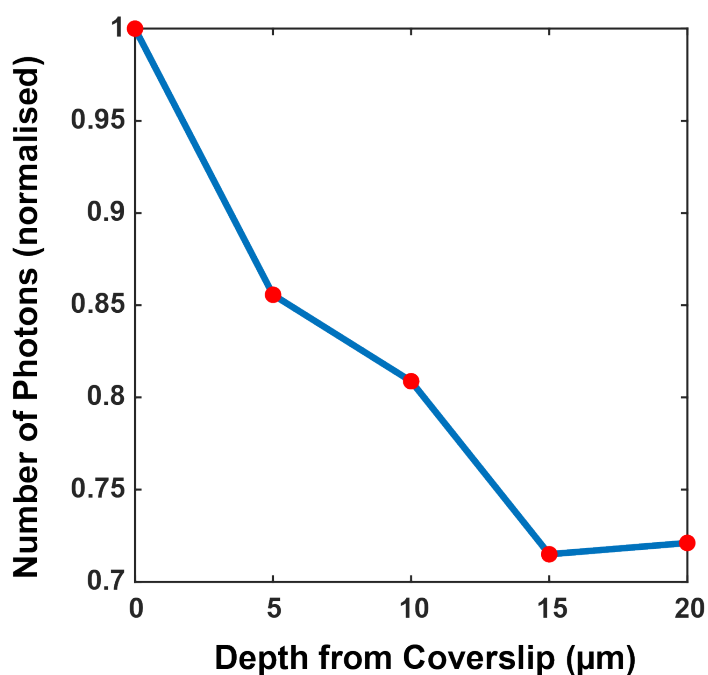
Fig. 2.9 Effect of SA on the number of photons collected at the camera. SA were introduced by changing the correction collar of the objective, which was equivalent to image at different depths inside a medium with the refractive index of glass.

imaging, the correction collar had to be perfectly matched to the thickness of coverslips. This is especially important for experiments involving low number of photons, similar to the ones carried out to study the dynamics of a DNA binding protein in Chapter 3.

2.7 Optimal Alignment for Three-dimensional Localisation Microscopy

Experimental setup for three-dimensional localisation microscopy, using DHPSF, is discussed in Section 2.2. The phase mask, required to generate the DHPSF, works optimally if placed in the conjugate BFP of the microscope. This plane contains the overlap of emissions from all the emitters in the imaged volume. We found the position of this plane to be dependent on the distance between the objective and the tube lens. Correct positioning of the phase mask is important to ensure high localisation accuracy and precision in three-dimensional localisation microscopy.

In this section, we present an optimal alignment procedure for the DHPSF to achieve high localisation accuracy and precision in all three spatial dimension. Moreover, a spatially varying aberration arising from the misplacement of the phase mask in infinity corrected optics is also investigated. It is worth mentioning that though discussed with reference to the DHPSF, the presented optimisation technique is equally applicable to the other engineered PSFs.

2.7.1 Infinity Corrected Optics and the DHPSF

We installed a phase mask to generate the DHPSF in our localisation microscopy setup, the schematic of which is shown in Figure 2.1. To obtain a spatially invariant PSF, the phase-mask was placed in the conjugate BFP of the microscope and f (focal length of L3) was chosen to match the beam diameter to the size of the phase-mask. Surprisingly, the position of the conjugate BFP did not match the focal plane of $L3$. We found this to be a consequence of the infinity corrected design of our microscope.

For a point-source in the focal plane of an infinity corrected objective, the light rays are collimated after the objective. These rays are then focused to the image plane by a tube lens. Due to highly corrected collimation of rays, after the objective, the exact distance between the objective and the tube lens is not crucial for the techniques like point-scanning or two-dimensional localisation microscopy. However, for imaging techniques involving phase-modifying optics, such as DHPSF, this distance becomes important. The distance determines the position of the conjugate BFP - the optimal plane to position the phase-mask.

In an idealised microscope shown in Figure 2.10A, the objective acts as a lens functioning in 4f setup. However, this is not the case for an infinity corrected microscope, in which the tube lens is placed closer to the objective to avoid vignetting. In such a configuration, the BFP no longer lies in the focal plane of the tube lens. As a result, the position of the
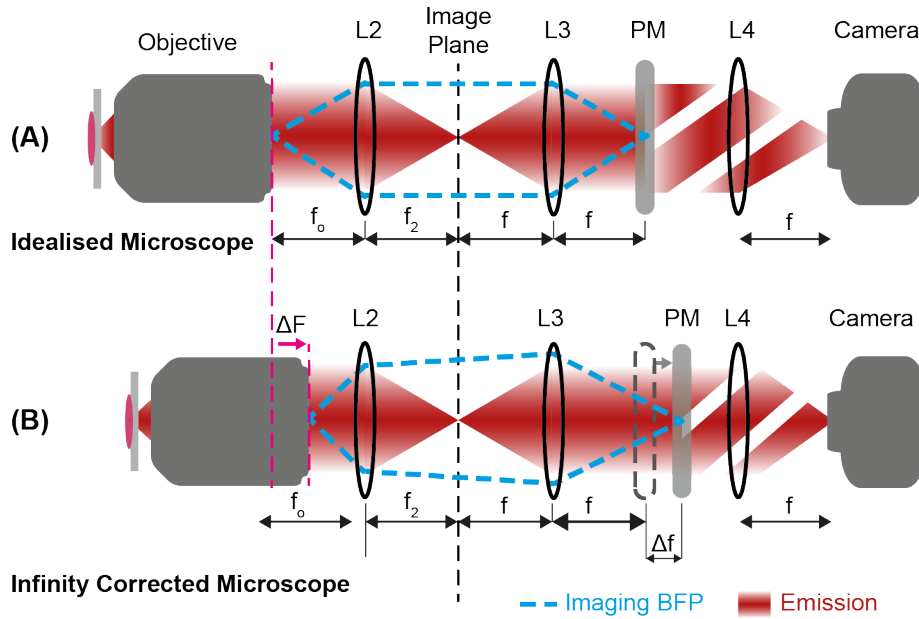
Fig. 2.10 Schematic of the emission paths for (A) idealised and (B) infinity corrected microscopes. In an infinity corrected microscope, the position of the conjugate BFP does not match the focal plane of *L*3.

conjugate BFP does not match the focal plane of *L*3, as shown in Figure 2.10B. However, in literature phase-modifying optics is routinely shown to be wrongly placed in between the relay lenses [6, 46, 81–84]. A consequence of which was the sub-optimal performance of the presented techniques.

2.7.2   Alignment of the Phase Mask

As discussed in Chapter 1, the DHPSF encodes the lateral and the axial positions of an emitter in the centre of its two lobes and the angle between them respectively. Hence, if the axial position of the emitter is changed, the DHPSF rotates about its centre. However, lateral shifts in the position of the DHPSF have been reported for such an emitter [46, 83]. These shifts, if not corrected, can significantly affect the accuracy of localisations. We found that the major source of these shifts was the infinity corrected optics of the microscope, shown in Figure 2.10B. For such a system, the exact distance between the tube lens and the objective should be considered when positioning the phase mask. If the phase mask is not placed precisely in the conjugate BFP, light from a point source *'experiences'* a phase which is dependent on its position in the FOV, as shown in Figure 2.11.

For a given microscope, the correct position of the conjugate BFP can be found by iterative displacement of the phase mask along the optical axis to minimise lateral movement
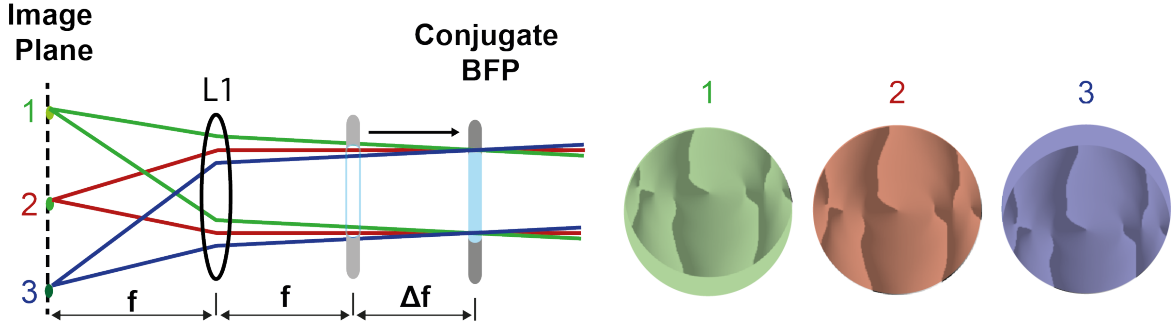
Fig. 2.11 Overlap of light beams from different points in the FOV with the phase mask, when it is displaced from the conjugate BFP. Light from a point source *experiences* a phase which is dependent on its position in the FOV.

of the DHPSF as a function of its rotation i.e. the DHPSF shouldn't move laterally if only the axial position of the emitter changes. Alternatively, it can be found by sending in a collimated light through the microscope objective, which results in a diffraction limited spot in the conjugate BFP. It is important to note that a change in the excitation wavelength results in a shift in the position of the conjugate BFP. Moreover, phase masks are designed to work optimally for a specific wavelength. Hence, different excitation wavelengths require different phase masks and consideration of chromatic aberrations.

2.7.3 Mathematical Modelling

So far we have discussed that the infinity corrected systems have an axial mismatch between the positions of the conjugate BFP and the focal plane of $L3$. Moreover, placing the phase mask in a wrong plane (e.g. in the focal plane of $L3$) results in a spatially varying PSF. In this section, we mathematically model the effect of this sub-optimal positioning of the phase mask on the DHPSF.

We start off by expressing the electric field in the BFP, $E(\mathbf{k}, f_o)$, as a function of the field in the focal plane of the objective, $E(\mathbf{r}, z)$. For N point sources in the imaged volume, $E(\mathbf{k}, f_o)$ can be give as:

$$E(\mathbf{k}, f_o) \propto \sum_{n=1}^{N} \mathscr{F}\left[E(\mathbf{r}, z)\right] \mathscr{O}(\mathbf{k}) \tag{2.10}$$

here, $\mathbf{k} = (k_x, k_y)$ are the normalised BFP coordinates, $E(\mathbf{r}, z)$ and $E(\mathbf{k}, f_o)$ are fields in the focal plane and BFP of the objective respectively and $\mathscr{O}(k)$ is the support of the Optical Transfer Function of the microscope (in most cases a unit circle).

Light field from different point sources overlap in the BFP with linear (tilt) and parabolic (defocus) phases depending on their lateral and axial positions respectively. In an idealised

microscope (see Figure 2.10A), the field in the BFP is relayed via *L2* and *L3* to the conjugate BFP. If **r** represents the lateral position of a point source in the imaged volume, the phase tilt after *L3*, by using the shift property of the Fourier Transform, is given as:

$$\phi(\mathbf{k}) = \exp\left(iM\frac{\mathbf{k}\cdot\mathbf{r}}{f}\right) \tag{2.11}$$

here, M is the magnification of the microscope. Due to this linear phase for off-axis point sources, the propagation of light beam after *L3* is no longer along the optical axis of the microscope. Hence, any axial displacement, Δf, of the phase mask from the conjugate BFP will result in a mismatch between the centres of the phase mask and the beam. This lateral shift between the centres can be given as:

$$\Delta\mathbf{k} = M\frac{\mathbf{r}}{f}\Delta f. \tag{2.12}$$

here, $\Delta\mathbf{k}$ is the shift between the centre of the phase mask and the light beam for a point source located at $(\mathbf{r},\mathbf{z})$.

The effect of the axial displacement of the phase mask from the conjugate BFP can also be understood by back-projecting the light rays to the conjugate BFP for each **r**. This virtual BFP now has perfect overlap of all ray bundles but each point source with $|\mathbf{r}| > 0$ *sees* a shifted phase mask. The phase, $\phi_{\mathbf{r}}(\mathbf{k},z)$, of a point source at $(\mathbf{r},z)$ is modified in this *virtual* BFP as follows:

$$\phi_{\mathbf{r}}(\mathbf{k},z) = \alpha(z)(2k^2 - 1) + \phi_{DH}(\mathbf{k} - \Delta\mathbf{k})) \tag{2.13}$$

here, $\alpha(z)$ represents the defocus in the conjugate BFP, the magnitude of which depends on the axial position of an emitter. $k = |\mathbf{k}|$ and ϕ_{DH} is the phase of the phase mask.

2.7.4 Simulations

After discussing the mathematical model for the sub-optimal positioning of the phase mask, we simulated the resultant DHPSF for such a situation. We considered point sources at different positions ($|\mathbf{r}| = 6.5\,\mu$m, 13 μm and 20 μm) in the FOV. MATLAB was used to generate images using, Eq. (2.13), across a DOF of 3 μm in 300 nm steps. These parameters were selected to match the simulations to our experimental setup. Localisation of the DHPSF in simulated images was carried out by using the *Easy-DHPSF* software [48]. Figure 2.12 shows results of such a simulation with $\Delta f = 35$ mm (the distance between the conjugate BFP and the focal plane of *L3* in our microscope).
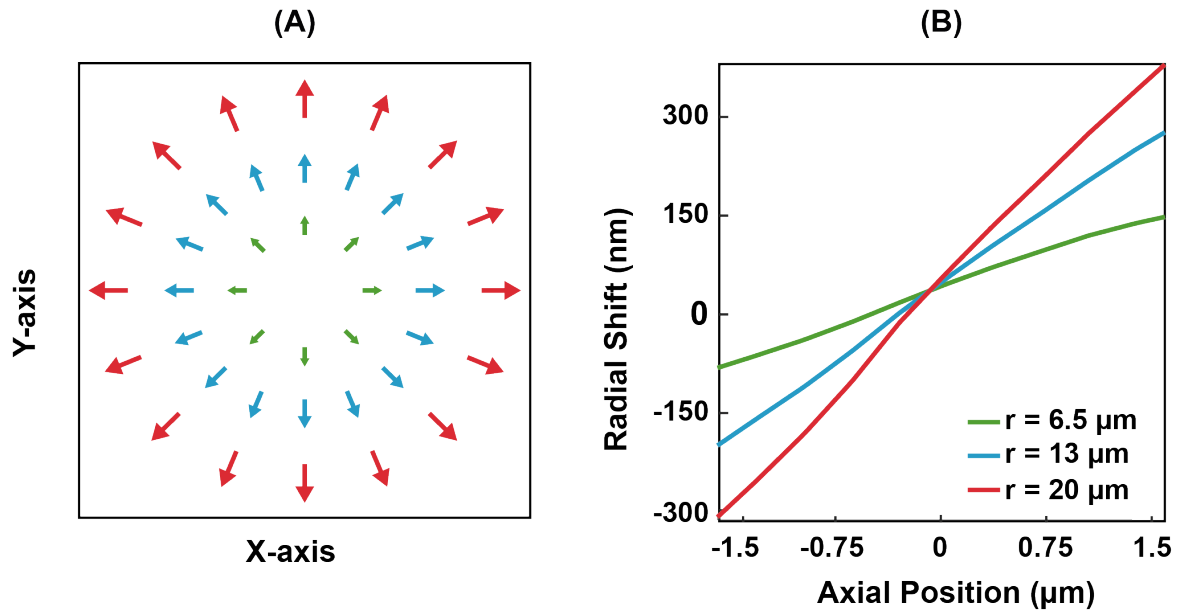
Fig. 2.12 Simulation results for 35 mm displacement between the phase mask and the conjugate BFP. (A) shows radial nature of the spatially varying DHPSF and (B) shows lateral shifts of the DHPSF for three distances from the centre of the FOV.

The figure clearly shows that a non-zero Δf results in a radial displacement of the DHPSF that grows larger with **r**. The magnitude and the direction (along **r**) of this radial shift is plotted for three different radii in Figure 2.12 B. We found the displacement to be almost linear, the gradient of which grew quickly with $|\mathbf{r}|$. So, the displacement of the phase mask from the conjugate BFP results in a loss of accuracy of up to several hundred nanometres.

2.7.5 Experimental Results

To verify our mathematical modelling and simulation analysis, we experimentally tested the effect of the axial displacement of the phase mask from the conjugate BFP, in our microscope. For this, fluorescent beads (Invitrogen, 100 nm) were adhered to a coverslip surface using poly-l-lysine (PLL). Experiments were performed by placing the phase mask at different distances (35 mm, 17 mm and 0 mm) from the conjugate BFP and a 50×50 μm area was imaged. The sample was axially scanned over a 3μm range in 100 nm steps. A typical FOV contained around 30 beads, whose positions were localised using Easy-DHPSF. These localisations were then used to interpolate across the full FOV. Results of this analysis are shown in Figures 2.13 (D)-(F).

Results, in accordance with our mathematical analysis and simulations, showed that the radial shifts were larger for beads away from the centre of the FOV and increased as
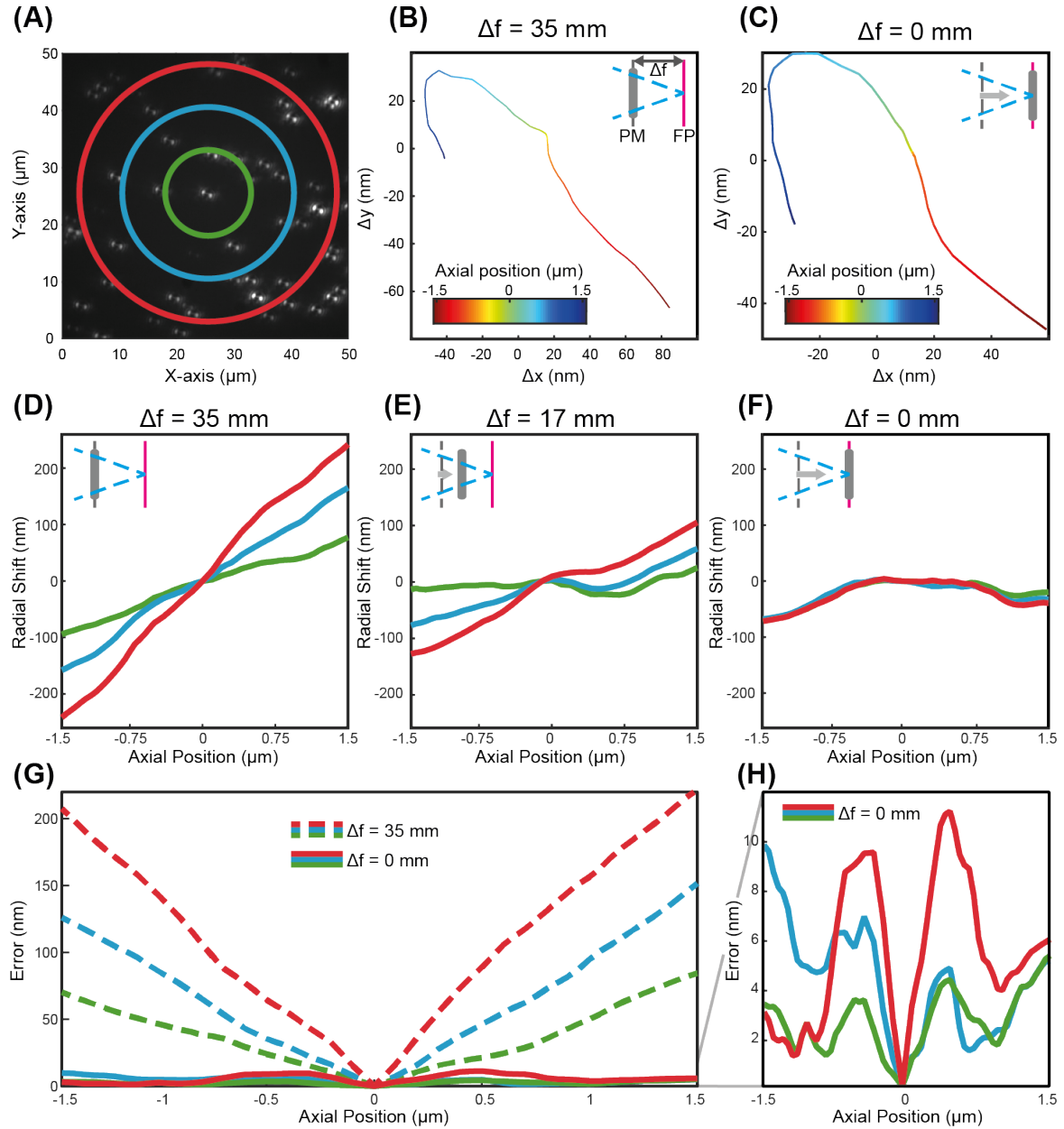
Fig. 2.13 Experimental results for the positioning of the phase mask at different distances from the conjugate BFP. (A) A representative image showing a distribution of fluorescent beads with three different radii marked at 7 μm, 14 μm and 21 μm. (B) and (C) show the global correction calculated from the average of bead positions for the phase mask displacements of 35 mm and 0 mm from the conjugate BFP respectively. (D), (E) and (F) show the radial shift in bead positions when interpolated across the FOV for the three different phase mask displacements of 35 mm, 17 mm and 0 mm from the conjugate BFP. Curves with different colours show shifts at radial distances marked in (A). (G) and (H) show resulting mean squared error if the global corrections shown in (B) and (C) are simply applied to a shifted phase mask (35 mm) and the correctly positioned phase mask respectively.

beads moved away from the focal plane of the objective. When the phase mask was moved closer to the conjugate BFP, the radial displacement reduced. This verified our hypothesis that spatially varying PSF was a consequence of the phase mask being displaced from the conjugate BFP of the objective.

The conjugate BFP contains perfect overlap of emitted light from all beads in the FOV, so PSFs no longer varied spatially. However a global correction was required to overcome the effect of uncontrollable system aberrations. The displacement of the DHPSF *due to displaced phase mask* averages to zero over the FOV because of its radial nature. So, we computed the global correction from the average lateral shifts of beads in the FOV and it is shown in Figure 2.13(C). Due to the spatial invariance of the PSF, this correction could also be computed from the lateral shifts of any single bead in the FOV. This allowed us to use common algorithms for DHPSF localisations, which assumed a shift invariant PSF [48]. After applying the global correction, we achieved an accuracy of less than 20 nm over the entire FOV, as shown in Figure 2.13(H).

To demonstrate how erroneous a global correction can be for a misplaced phase mask, we computed the global correction for $\Delta f = 35$ mm and it is shown in Figure 2.13B. Although this appears similar to the correction in Figure 2.13C, an order of magnitude higher errors were obtained in such a situation as shown in Figure 2.13G. Moreover, the common practice of using a single bead for calibration (rather than averaging as performed in Figure 2.13B) can result in further loss of accuracy to more distant locations in the FOV.

2.7.6 Multicolour Three-dimensional Localisation Microscopy

The above discussion shows that, for high accuracy, the phase mask should be placed in the conjugate BFP of the objective. However, wavefront shaping elements are usually designed to work optimally for a single wavelength. Therefore, for dual colour imaging, two phase masks should be placed in this plane. This can be achieved by dividing the emitted light (corresponding to different excitation wavelengths) before the conjugate BFP as shown in Figure 2.14. The phase masks are then placed in two equidistant planes from $L3$. This concept has been used to study chromatin dynamics in yeast cells [85], using phase masks for Tetrapod PSF. Different phase mask were used for different emission bands ('green' and 'red'), each optimised for a DOF of 6 μm.

Multicolour three-dimensional imaging can also be implemented by exploiting the dependency of phase modifying elements on the wavelength of light. In such a method, a single phase mask is designed to produce different PSFs depending on the wavelength of the incident light (i.e. the mask is simultaneously optimised to produce different PSFs for
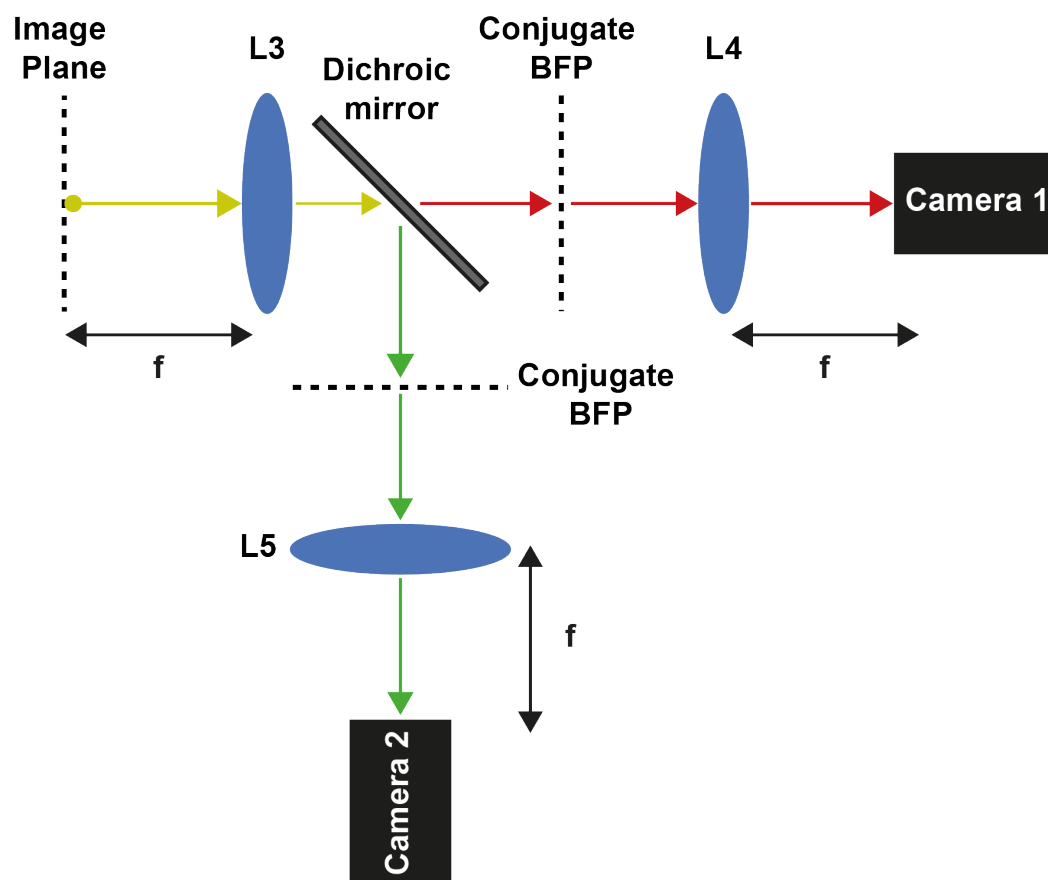
Fig. 2.14 A schematic for dual-colour three-dimensional localisation microscopy.

different wavelengths). The mask is then placed in the conjugate BFP of the objective, which allows simultaneous three-dimensional imaging by using a single optical path [86].

2.8   Summary

This chapter discussed the design, development and optimisation of a localisation based super-resolution microscope. Calibration and characterisation of the microscope was also explained. This involved estimating the pixel dependent gain and read-noise of our sCMOS cameras. Origin of SA when imaging beyond the coverslip was explored along with its effect on the localisation microscopy. A method to optimally adjust the correction collar of the objective to overcome the systematic SA in the microscope was also proposed. The chapter ended with a discussion on an optimal alignment procedure to obtain high accuracy and precision over large FOVs in three-dimensional localisation microscopy.

2.9   Contributions

The microscope, along with its multiple functionalities, was designed and developed by me with the inputs from Kevin O'Holleran and Martin Lenz. I also wrote the LabVIEW software for the control of the microscope. The optimisations discussed in the chapter were also implemented by me (both simulations and experiments).

2.10   Methods

Gain Calculations

We used the method discussed in [69] to calculate the pixel dependent gain of the camera. Required data analysis was carried out in *MATLAB*. The analysis involved the following steps:

1. Light from the halogen lamp, attached to the microscope, was sent through the microscope objective, which resulted in the illumination of the entire camera chip.

2. Light intensity (from the lamp) was varied and 100 frames were captured at each intensity level. In our analysis we considered seven of these levels.

3. Mean intensity (S_c), was calculated by determining the mean signal over 100 frames, captured for a certain intensity of light (this was done after subtracting any pixel bias present on the camera).

4. Total noise (N_c), was calculated by determining variance of the signal over 100 frames, captured for a certain intensity of light.

5. Pixel-gain was then calculated from the slope of N_c vs S_c graph (for each pixel), using the method discussed in Section 2.5.

So, by applying these steps we obtained the gain for each pixel of the camera. For quantitative analysis of our localisation microscopy data, the *average gain* of these pixels was used.

Chapter 3

Deep Localisation Microscopy for Single Molecule Dynamics

3.1 Introduction

Localisation based super-resolution microscopy overcomes the diffraction limit of light by the stochastic activation of fluorophores in the field of view. This allows localisation and tracking of individual fluorophores, making the technique an attractive tool to study dynamics of single protein molecules. This chapter discusses the application of our localisation microscope to understand the dynamics of a DNA binding protein. To study the dynamics in the natural physiological state of a cell, imaging had to be carried out in the whole salivary glands of Drosophila, at a depth of more than $25\,\mu$m from the coverslip. This required careful optimisation of the microscope to maximise the (usable) number of photons collected from single fluorophores.

Aberrations due to imaging in thick tissues, combined with the requirement of high frame rates to track freely diffusing molecules, resulted in few photons (less than 100 on average) per localisation. Data analysis software, discussed in the chapter, were characterised and optimised to work under such conditions. We extended the use of motion blurring analysis to detect the presence of freely diffusing and bound molecules in the localisation data, and to quantify their relative proportions. We also applied single molecule tracking and subsequent trajectory analysis to precisely estimate the exact number of diffusion states and their properties (occupational probabilities, transition probabilities and dwell times) from the localisation data. The complete image analysis pipeline was tested on synthetic data to optimise important parameters of multiple software (used in the analysis) for our experimental data. This chapter discusses the hardware and software optimisations carried

out to perform localisation microscopy in living cells, deep within thick salivary glands of Drosophila.

3.1.1 Chapter Description

The chapter describes the work conducted to understand the dynamics of a DNA binding protein for the Notch signalling pathway. First, the experimental setup for localisation microscopy and tools for subsequent data analysis are discussed. Afterwards, two methods to study the dynamics of the protein are explained. The first one, *motion blurring experiments*, is based on counting the number of protein molecules localised at different exposure times, as fast moving molecules are not detectable over a long exposure time. This method can be used to verify the presence of multiple diffusion behaviours in the localisation data. The second method is *single molecule tracking* (SMT), which can extract the exact number and values of all the diffusion coefficients from the data. We also used SMT to calculate the occupational probabilities and the transition probabilities of these diffusion states. The chapter finishes with a discussion on the application of localisation microscopy to understand the dynamics of the histone-DNA interaction.

3.1.2 Published Work

Results presented in this chapter were published in [87]. The paper covered the application of the motion blurring and the SMT analyses to study the dynamics of CSL molecules, as well as benchmarking of the image analysis pipeline.

3.2 Biological Significance

Notch pathway is a highly conserved signalling pathway, essential during development and adult life of an organism. Malfunctioning of the pathway can result in many diseases including cancer [88, 89]. So, study of the pathway is crucial to not only understand development but also for the treatment of human diseases.

The pathway is activated when the ligand in the surface of the signalling cell binds to the receptor, Notch, in the receiving cell, triggering a series of proteolytic cleavages of the Notch receptor. These events result in the release of the Notch intracellular domain (NICD) that enters the nucleus and interacts with a DNA-binding protein, Suppressor of Hairless (Su(H), also known as CSL) and other proteins known as co-activators, leading to the transcription of genes as shown in Figure 3.1A. We will refer to the genes transcribed as a result of the

Notch signal, as the *target genes*. The activation of the pathway and steps leading to the transcription of the target genes are discussed in detail in [90–92].

When the pathway is inactive i.e. in the absence of Notch signal, CSL interacts with a different set of proteins, known as co-repressors, and together they act as repressors of target genes [93, 94], as shown in Figure 3.1B. In the existing model of gene regulation, NICD replaces co-repressor in the presence of Notch signal, while CSL remains bound to the DNA [95]. However, recent reports have shown similar affinity of NICD and co-repressors for the CSL, raising questions over the replacement model [96–98]. Moreover, techniques such as chromatin immunoprecipitation (ChIP) assays in fixed samples show a significant increase in the occupational level of CSL in the active state of the pathway, compared to the inactive one, implying that there is an active recruitment of CSL after Notch activation [99–101]. These results highlight the shortcomings of the existing model and a need to better explain the dynamics of CSL in the Notch pathway under different conditions i.e. when the pathway is active and inactive.
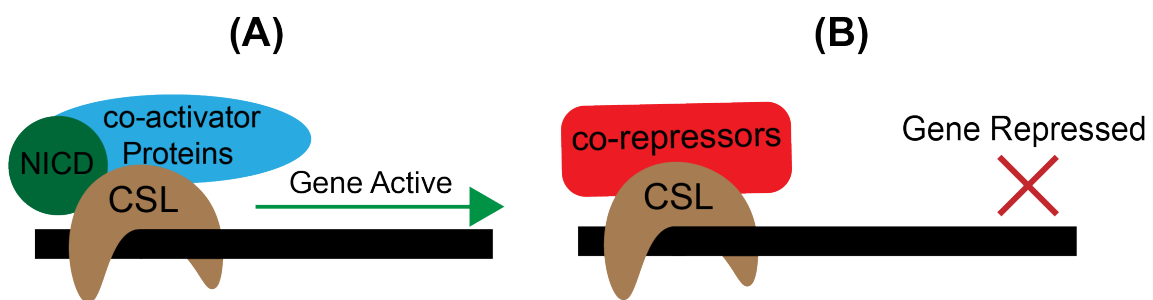
Fig. 3.1 Principle of the Notch pathway regulation. Binding of NICD protein to CSL, in the presence of other activation proteins, leads to the transcription of target genes. In the absence of NICD, CSL acts as the repressor of these genes, with the help of co-repressor proteins.

Bray lab, at the *Department of Physiology Development and Neuroscience* is interested in understanding the regulatory mechanism of the Notch pathway. They use *Drosophila* as the model organism to study the pathway and have identified a range of target genes involved in the process. They have also developed tools to study the behaviour of CSL at these localised target sites and elsewhere in the nucleus. This project was carried out in collaboration with the *Bray lab*, with the goal to study the dynamics of CSL in various parts of the nucleus and to understand its interaction with the DNA under different conditions. We used localisation microscopy for this project as it allowed us to analyse the behaviour of CSL molecules at the single molecule resolution.

3.3   Experimental Setup

Detailed experimental setup of our localisation microscope is discussed in Chapter 2. This section covers the experimental details, imaging conditions and optimisations specific to the experiments discussed in this chapter. Imaging was carried out by labelling CSL molecules with mEOS3.2 fluorescent protein, which in its native state has the excitation maximum at 507 nm. In the presence of UV light, a cleavage happens in the poly-peptide backbone, shifting the excitation maximum to 572 nm [102–104]. In our experiments, cells were exposed to a low intensity of 405 nm laser to photoconvert a sparse set of molecules, which were then imaged with 561 nm laser. Cell preparation and labelling for the experiments discussed in this chapter was done by the *Bray Lab*, the protocols for which are discussed in *Materials and Methods* section at the end of this chapter.

We used an inverted microscope frame, Leica DM IRE2, customised for localisation microscopy. Excitation (561 nm) and activation lasers (405 nm) were provided by a laser combiner (Omicron LightHUB). Output of the laser combiner was through a single mode optical fibre, which was collimated to a 8 mm diameter beam using a reflective collimator and then circularly polarised using an achromatic quarter wave plate. The beam was then demagnified on the sample through a 250 mm tube lens and 60x silicone oil objective (Olympus UPLSAPO60XS2, 1.3 NA). This resulted in a collimated beam of 96 μm diameter at the sample. Fluorescence was collected through the same objective lens, filtered (Chroma-ZT405/488/561/640rpc) to remove scattered and reflected excitation (or activation) light, before its focusing to the image plane through a 200 mm focal length tube lens. Lenses of 125 mm focal length then relayed the image plane to a *Hamamatsu, Flash 4.0* camera. A final band-pass filter (Semrock-FF01 600/52-25) was placed before the camera to ensure high attenuation of any remaining laser light. For each experiment, a $50 \times 50 \mu$m region was imaged, which was sufficient to observe a nucleus. Imaging was carried out with a continuous excitation beam (80-150 W/cm2) along with regular bursts of the activation beam every 20 sec (at 0.3-0.8 W/cm2). Intensity of the activation laser was carefully adjusted to obtain a set of non-overlapping active molecules in the FOV.

Overcoming Systematic Spherical Aberrations

As we were interested in the *in vivo* behaviour of the Notch pathway, imaging had to be performed at a depth of 20-40 μm from the coverslip, in thick salivary gland tissues. Propagation of light, through such a sample, led to spherically aberrated PSF due to refractive index inhomogeneities in the path as explained in Section 2.6. A consequence of this was the loss of signal in higher order lobes of the PSF, *effectively* reducing the number of photons

available for its localisation. Moreover, SMT experiments were carried out at high frame rates (exposure time of 10 msec) to capture the dynamics of freely diffusing molecules. This further limited the number of photons (collected per emitter) in any given frame. So, careful optimisation of the microscope was required to efficiently collect emissions from single fluorophores.

One of these optimisations was to adjust the correction collar of the objective, depending on the thickness of glass coverslips. We used No. 1.5 and No. 1 coverslips, which have an average thicknesses of 170 μm and 150 μm respectively. However, there can be a variation of up to 20 μm from these average values [105]. If the correction collar is not corrected for this inter coverslip variation, it can lead to spherical aberrations in the light path. This happens because such a situation is equivalent to imaging in glass with a silicone oil objective. Even a mismatch of a few microns leads to a significant loss of photons (see Figure 2.9 and [105]), which greatly affects the localisation precision especially in experiments involving low number of photons.

So, for the optimal performance, the correction collar had to be adjusted for each coverslip separately. This was achieved by exploiting the *asymmetry* of the PSF around the focal plane in the presence of spherical aberrations (see Section 2.6). For a given coverslip, the PSF was measured by adhering 100 nm fluorescent beads to its surface, next to the sample. The correction collar was optimised by iteratively adjusting its value and observing the axial symmetry of the PSF around the focal plane. The value for which the maximum symmetry was observed was chosen for the coverslip under consideration.

3.4   Analysis of Localisation Microscopy Data

Raw images acquired in localisation microscopy contain a sparse set of diffraction limited spots, corresponding to single fluorescent molecules. These images were analysed to quantify the dynamics of CSL molecules. This involved detection and localisation of spots, which was the main step in the analysis of motion blurring experiments and the initial one in the SMT analysis. For the latter, localisations were subsequently linked over multiple frames to track the movement of individual protein molecules. Trajectory analysis was then performed to extract multiple diffusion populations from the obtained tracks. In this section, our data analysis methods for localisation, tracking and trajectory analysis of single CSL molecules are discussed.

3.4.1   Detection and Localisation

Spot localisation was carried out by fitting a two-dimensional Gaussian function to the fluorescent spots in raw localisation microscopy images. We used *PeakFit* and *WaveSM* software for the analysis of motion blurring and SMT experiments respectively (motion blurring analysis was performed in the initial stages of the PhD, when *WaveSM* was being optimised and tested). While both assume a Gaussian PSF, *PeakFit* performs spot detection by finding intensity peaks in noise reduced raw image. Whereas, in the *WaveSM* software, this is done by transforming the images to the wavelet space and finding peaks in the scales of interest. Both the software are discussed in detail in Chapter 1.

3.4.2   Tracking from Localisations

The next step in the SMT analysis was to link the localised molecules over consecutive frames, for which we used multiple hypothesis tracking (MHT) algorithm. MHT algorithm links localisations in time by building trees of potential tracks. For each frame existing trees are updated with localisations from within a certain area. New trees are also formed for each localisation, to consider the possibility of new tracks. These tracks are then scored and set of best, non-conflicting trees are selected as tracks [106]. We used an MHT based software, implemented in *icy*, for the tracking of localised molecules. *icy* also has a spot detection plugin [35], the data from which can be directly imported to the tracking plugin. Since, this detection plugin is based on less precise centroid based fitting, localisation of fluorescent spots was carried out using the *WaveSM* software. Output of the *WaveSM* was imported to *icy* (in the correct format) using the *'Spot Detection Import and Export'* plugin [107].

   In the tracking software, molecules were assumed to undergo Brownian motion and the software pre-estimated different tracking parameters such as expected movement of molecules between frames, expected track length and probability of false detection from the localisation data. We found the pre-estimation step to work reasonably well under our experimental conditions. We also benchmarked the software against the simulated data generated for different diffusion coefficients, as discussed in Section 3.6.1. For a detailed description of the software and its performance, see [108].

3.4.3   Trajectory Analysis

Tracks obtained from *icy* were analysed to extract multiple diffusion populations and their characteristics. This section covers trajectory analysis methods used in this chapter, which included:

- Mean Squared Displacement (MSD) analysis

- Jump Distance analysis (JD)

- Variational Bayes single particle tracking (vbSPT)

MSD and JD Analyses

For an instantaneous point source of freely diffusing molecules located at the origin at $t = 0$, the probability density of finding a molecule at a distance r from the origin, after time t, can be obtained by solving the diffusion equation [109]:

$$P(r,t) = \frac{2r}{\langle r^2(t) \rangle} \exp \left(-\frac{r^2}{\langle r^2(t) \rangle} \right) dr \tag{3.1}$$

$$\langle r^2(t) \rangle = 4Dt \tag{3.2}$$

here, $\langle r^2(t) \rangle$ is the mean squared displacement (MSD) of a molecule diffusing with the diffusion coefficient, D. The probability that the molecule has diffused a distance r_o, in time t, is then given as:

$$P(r \leq r_o, t) = 1 - \exp \left(-\frac{r_o^2}{4Dt} \right) \tag{3.3}$$

For multiple diffusing populations, the equation can be modified as follows [110]:

$$P(r \leq r_o, t) = 1 - \sum_{i=1}^{N} f_i \exp \left(-\frac{r_o^2}{4D_i t} \right) \tag{3.4}$$

Equation 3.2 shows that the MSD of a freely diffusing molecule varies linearly as a function of time, with the slope proportional to the diffusion coefficient of the molecule. So, MSD calculations over a track can be used to estimate its diffusion coefficient. Such an analysis preserves information about individual tracks, allowing the spatially mapping of different diffusion populations within a cell. However, calculating the MSD over an entire track results in the loss of information about multiple dynamics within the track [111]. Moreover, the analysis gives erroneous results for short tracks [110] e.g. [112] shows that at least 32 time points were required to accurately calculate the diffusion coefficient of a track using the MSD analysis. Therefore, because of small tracks obtained in our experiments (average length of less than 6 frames), the MSD analysis could not be used to calculate the diffusion coefficients of individual tracks.

The limitations of the MSD analysis can be overcome by applying the JD analysis. The algorithm fits a theoretical probability distribution, given by Eq 3.4, to the distance covered

by an ensemble of molecules in a given time. The JD analysis can find sub-populations (with different diffusion behaviours) from tracks and works well for short trajectories. However, individual trajectory information is lost in such an analysis [110] . This information was required to study the dynamics of CSL molecules in different parts of the nucleus, which restricted the use of the JD analysis for our experiments. For a description of the MSD and the JD analyses and their comparison see [110].

vbSPT Software

Shortcomings of the MSD and the JD analyses can be overcome by taking a variational Bayesian approach to the trajectory analysis problem, as proposed in [113]. The paper also provides a MATLAB implementation of the method, named *vbSPT*. In *vbSPT*, diffusion coefficients are modelled as different states of a Hidden Markov Model. So, multiple diffusion coefficients and parameters like dwell times, transition probabilities and occupational probabilities can be obtained from the software.

vbSPT assumes the molecules to undergo free diffusion and the position, **x**, of a particle at time, t, is calculated as:

$$\mathbf{x}(t) = \mathbf{x}(t-1) + \Delta\mathbf{x}(D_{s_t}) \tag{3.5}$$

here, $\Delta\mathbf{x}(D_{s_t})$ is the distance covered by the particle, diffusing with the diffusion coefficient D, in a unit time. Different diffusion behaviours within a track, e.g. binding and unbinding events, are modelled as a variation in the diffusion coefficient. Hence, the software can extract multiple diffusion coefficients from short tracks while maintaining the track information. For a detailed discussion on the implementation of the software and its working, see [113]. The software was tested on simulated data, as discussed in Section 3.6.1, before its application to the experimental data.

After discussing the data analysis methods, we apply them to study the dynamics of the CSL protein. This will be the focus of the rest of this chapter.

3.5   Motion Blurring Experiments

One of the main goals of the project was to confirm the presence of multiple diffusion populations (i.e. freely diffusing and DNA-bound) in the imaged nuclei. To approach this question, we imaged cells under different exposure times. The idea was that if the CSL molecules undergo multiple diffusion behaviours, the number of localisations in living cells, N_{living}, should vary as a function of the exposure time at the camera. However, the number of localisations in fixed cells, N_{fixed}, should remain (nearly) constant over these exposure

times. This is because the freely diffusing molecules are not detectable over long exposure times, due to the spread of their signal over multiple pixels (as they move over multiple pixels over the exposure time). This weak signal is lost in the background fluorescence and noise, which are captured by the camera pixels over the entire exposure time. On the other hand, localised emissions from bound molecules are captured by the same set of pixels over the entire exposure time (assuming that the molecules do not photobleach during this time). This method was first applied by [114] to selectively image different protein populations. We performed simulations for a diffusion coefficient of $1.5\,\mu\mathrm{m}^2/\mathrm{sec}$ (it was the highest diffusion coefficient obtained from the SMT analysis as discussed in the next section), results of which are shown in Figure 3.2. Approximately $23,000$ spots were detected at an exposure time of $10\,\mathrm{msec}$. The number decreased as the exposure time increased, reaching ~ 115 (0.5%) at $500\,\mathrm{msec}$. A detailed analysis of the motion blurring technique (through both simulations and experiments) is carried out in [114].

In this project, we extended the motion blurring to quantify the molecular dynamics of CSL, which included the detection of multiple diffusion populations in a region of interest and determining their relative proportions. A difference in N_{fixed} and N_{living}, over different exposure times, was observed because CSL molecules had multiple diffusion behaviours in living cells. Whereas, only static molecules were present in fixed cells. So, by comparing N_{living} and N_{fixed} over different exposure times, existence of multiple diffusion populations in the imaged nuclei was predicted.

Experimental Results

5-7 nuclei (both fixed and living) were imaged at exposure times of $10\,\mathrm{msec}$, $50\,\mathrm{msec}$, $100\,\mathrm{msec}$, $200\,\mathrm{msec}$ and $500\,\mathrm{msec}$. Results of the analysis are shown in Figure 3.3D. While N_{fixed} was nearly constant over different exposure times, N_{living} decreased as the exposure time increased. The proportion of bound molecules was estimated by measuring the change in N_{living} over long exposure times, relative to N_{living} at $10\,\mathrm{msec}$. At $100\,\mathrm{msec}$, only $\sim 26\%$ of the localisations remained and they reduced to $\sim 10\%$ at $200\,\mathrm{msec}$. Hence, we expected the population of bound molecules to be in this range, which was close to the number obtained from the SMT analysis discussed later in the chapter. These results signify the effectiveness of the motion blurring technique to extract molecular dynamics from single molecule localisation microscopy data.

It is important to note that although N_{fixed} was constant over different exposure times, it was significantly lesser than N_{living} at short exposure times. This was contradictory to our expectations, as fixed samples should contain all the populations of the CSL molecules. The contradiction can be explained by the quenching of fluorescent molecules in the fixation
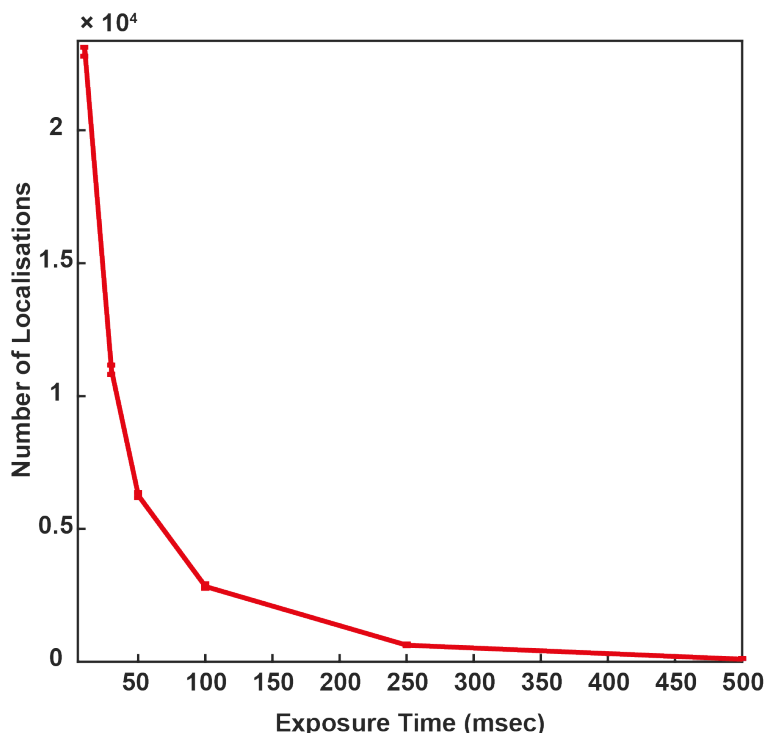
Fig. 3.2 Number of localisations as a function of exposure time for simulated molecules with $D = 1.5\,\mu\mathrm{m}^2/\mathrm{sec}$.

process. Hence, although the motion blurring analysis provided valuable information, its predictions had to be verified through the SMT analysis. SMT was also required to quantify the dynamics of molecules with intermediary diffusion characteristics. This included extracting and quantifying diffusion coefficients of all the CSL populations in a nucleus; and calculating their dwell times, relative proportions and transition probabilities. The remainder of this chapter will focus on the SMT analysis to completely understand the dynamics of CSL molecules.

3.6   Single Molecule Tracking

Motion blurring experiments predicted that the CSL molecules exhibit multiple diffusion behaviours in the nuclei of living cells. We further investigated the dynamics of the protein at the single molecule resolution by carrying out the SMT experiments. A schematic of our SMT data analysis method, involving localisation and tracking of molecules followed by trajectory analysis is shown in Figure 3.4.
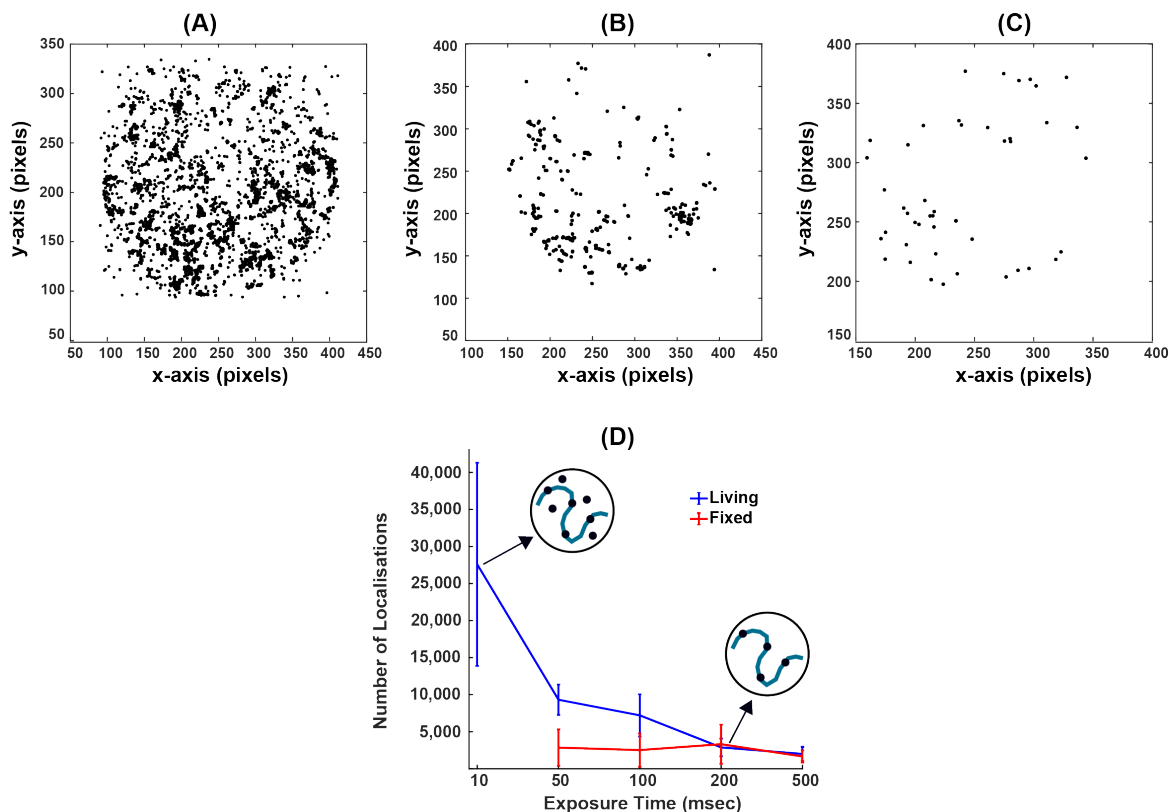
Fig. 3.3 Results for motion blurring experiments. (A), (B) and (C) show localisations in an example nucleus over exposure times of 10 msec, 50 msec and 500 msec respectively, in living cells. (D) A graph showing the number of localisation in living and fixed cells over multiple exposure times. In living cells, the number of localisations decreased as the exposure time increased, due to the spread of photons over multiple pixels for fast diffusing molecules. On the other hand fixed cells contained only static molecules, resulting in the same number of localisations at different exposure times. This analysis shows the presence of multiple diffusion behaviours of CSL molecules in living cells.

We first tested the performance of various software involved in the image analysis pipeline on the synthetic data and later applied them to the experimental data. In this section, results of both the analyses are presented.

3.6.1 Simulations

To analyse the performance of our SMT data analysis pipeline (Figure 3.4), we tested it on the synthetic data sets. Trajectories were generated in a discretised cell geometry of $20\,\mu$m diameter by using the synthetic data generation capability of the *vbSPT* software. The software could generate trajectories of the desired (average) length, with multiple diffusion coefficients and required transition probabilities [113].
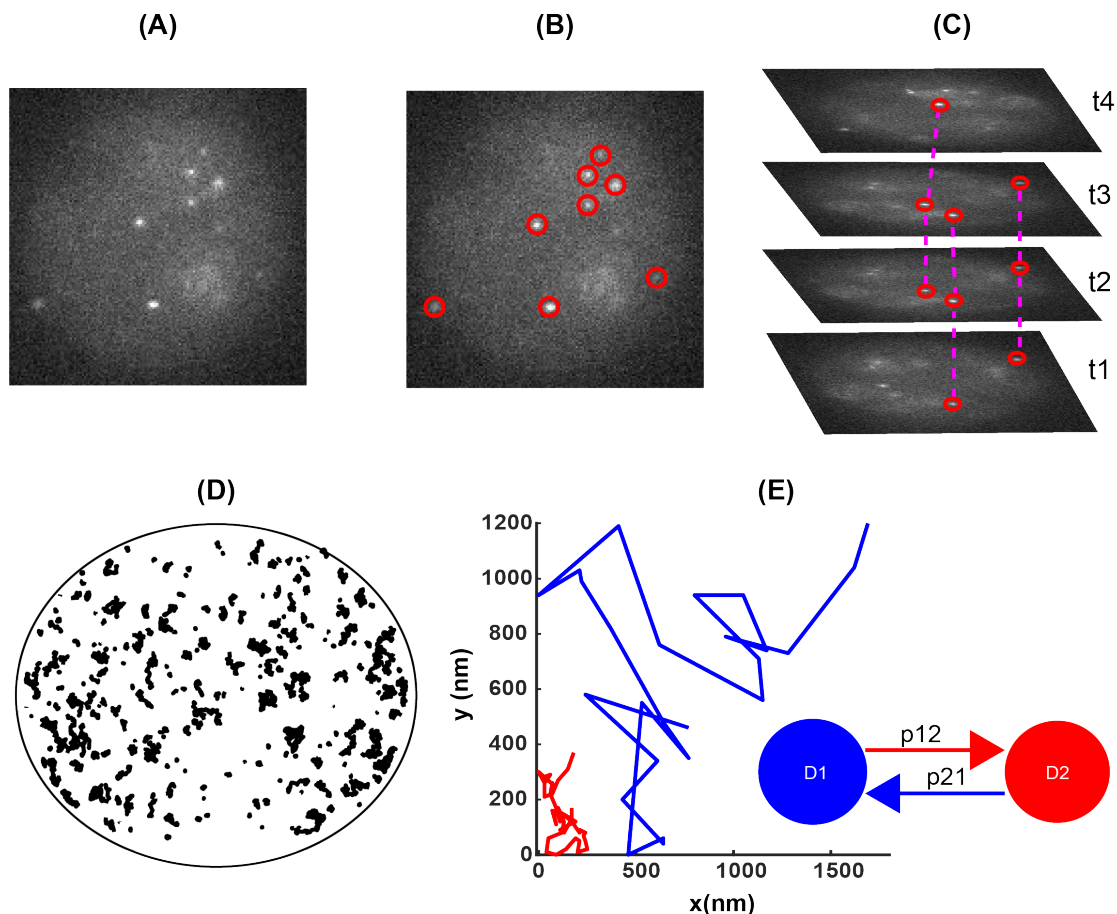
Fig. 3.4 Complete schematic of our data analysis process. (A) shows a representative image of our localisation microscopy, from which fluorescent spots were localised, using the *WaveSM* or the *PeakFit* software, as shown in (B). (C) shows the linking of these localisations over consecutive frames by carrying out the SMT analysis in *icy*. (D) shows cartoon of a cell containing multiple short tracks, from which the dynamics of diffusing molecules were extracted using the *vbSPT* software. (E) An example output of the trajectory analysis software.

A MATLAB script was written to generate images from these trajectories. The width of the PSF and the pixel size was matched to the experimental setup. Shot noise and read-noise, similar to that of the camera, were also added to these images (see Section 2.5 for the read-noise calculations for our cameras). Images were generated for different number of photons to test the performance of our analysis pipeline under different conditions. The trajectory analysis software has been tested for a range of conditions in [113]. Here we show the results of testing the performance of our *complete image analysis pipeline*, applied to study the dynamics of CSL molecules. So, our simulations had the following steps:

1. Generate synthetic trajectories using the vbSPT software

2. Generate images from these trajectories with parameters matching the imaging conditions

3. Perform spot localisation

4. Carry out tracking of localised spots

5. Perform trajectory analysis

We started off by simulating images of single molecules, diffusing with D=1 μm^2/sec. Ten synthetic data sets were generated, with an average track length of 5.5 frames at an exposure time of 10 msec, which matched the experimental conditions. These images were then analysed for localisation, tracking and trajectory analysis of simulated spots.
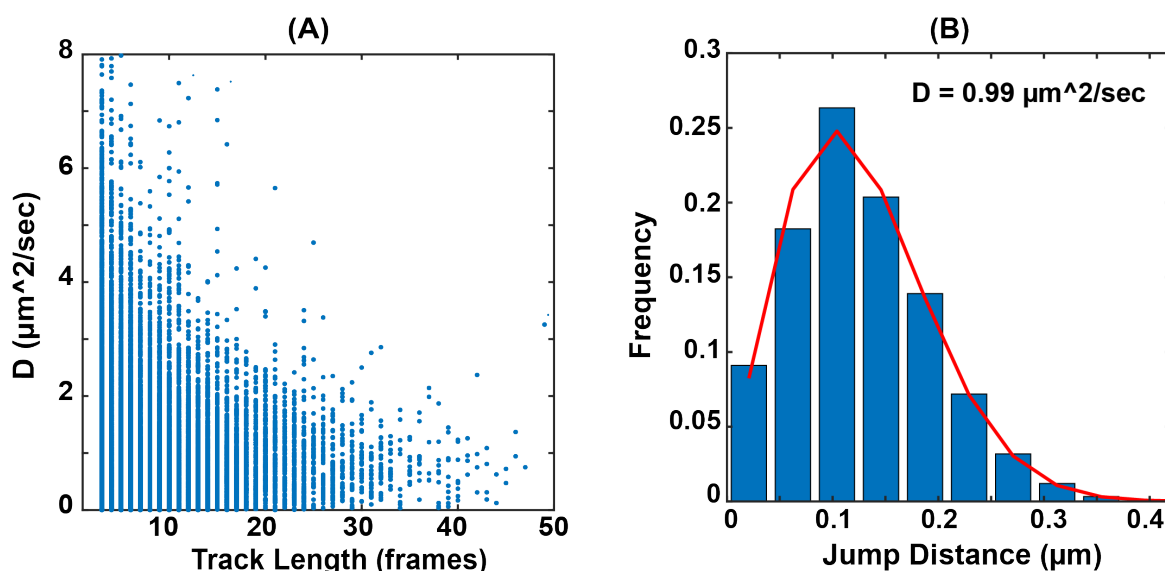
Fig. 3.5 MSD and JD analysis on synthetic data generated for $D = 1\,\mu$m^2/s. (A) shows that the MSD analysis gave a range of diffusion coefficients for short trajectories. However, for long trajectories it converged to the single and correct diffusion coefficient. (B) shows that the JD analysis returned the correct diffusion coefficient by fitting a probability distribution to the jumps from multiple short trajectories.

MSD and JD analysis

The tracks were first analysed by using the MSD and the JD algorithms. By doing so, the accuracy of the synthetic data generation software was tested i.e. we confirmed that the software was generating trajectories with the required diffusion coefficients. As expected the MSD analysis gave a range of diffusion coefficients for short trajectories, however for long

trajectories it converged to a single and correct diffusion coefficient, as shown in Figure 3.5A. Average track length in our experiments was between 5-6 frames, so the MSD analysis was not suitable for calculating the diffusion coefficients of individual tracks in these conditions. As far as the JD analysis is concerned, it combined jumps from multiple short tracks to correctly extract the correct diffusion coefficient, as shown in Figure 3.5B. But in doing so information about individual tracks and their possible spatial mapping was lost. So, the above analysis:

- verified that the *vbSPT* was generating trajectories with the correct diffusion coefficients, which was important for the discussion in the rest of this section

- confirmed the limitations of the MSD and the JD analyses for our experiments, as also highlighted in Section 3.4.3
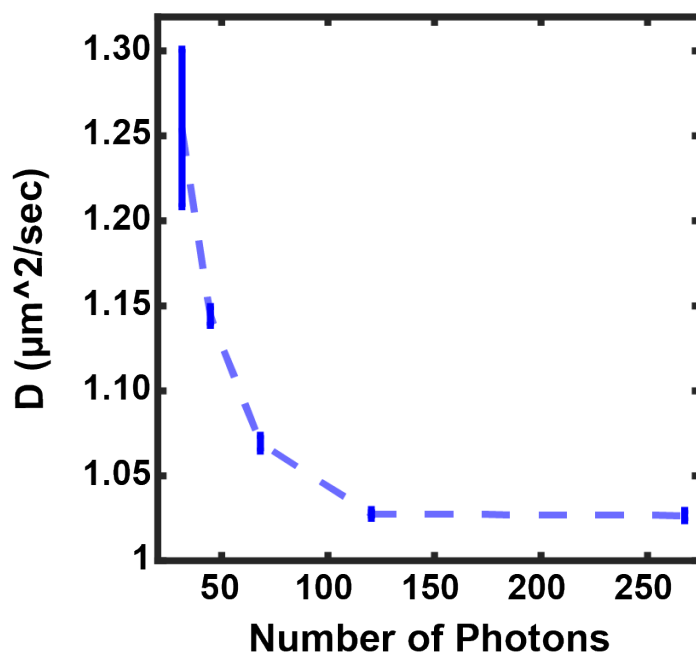
Fig. 3.6 Output of the *vbSPT* analysis on the synthetic data generated for $D = 1\,\mu\mathrm{m}^2/\mathrm{s}$ and for different number of photons (track length = 5.5 frames, at an exposure time of 10 msec). Large localisation errors for fewer photons resulted in an *apparently* high diffusion coefficient.

vbSPT Analysis

We then analysed tracks using the vbSPT software and results are shown in Figure 3.6. Under all the tested conditions, the software returned a single diffusion state. This verified that our

data analysis method did not produce multiple states under realistic SNRs. However, the value of the diffusion coefficient increased with a decrease in the number of photons. For example, we obtained diffusion coefficients of $1.25\,\mu\mathrm{m}^2/\mathrm{s}$ and $1.02\,\mu\mathrm{m}^2/\mathrm{s}$ for an average of 30 and 200 photons per emitter respectively. This can be explained by the deterioration of the localisation precision with a decrease in the number of photons, which resulted in an *apparent* increase in the diffusion coefficient [113].

To test the performance of our data analysis method in extracting different parameters from single molecule images, we generated trajectories with four diffusion coefficients. Parameters used to generate the synthetic data are shown in Figure 3.7, and were chosen to match the experimental conditions. Ten image sets were generated, with the average track length (5.5 frames) and number of photons (less than 100) matching the experimental conditions. Images were analysed using our data analysis pipeline and results are shown in Figure 3.7. The software correctly identified the number of diffusion states and quite accurately extracted parameters like diffusion coefficients, their populations and transition probabilities.

However, values of the diffusion coefficients were found to be higher for all the diffusion states except $D4$. This was due to large localisation errors, as the simulations were carried out for a low number of photons. The error also affected $D4$, but confinement due to finite geometry of nuclei restricted the movement of fast molecules, resulting in an overall decrease in the value of $D4$. More information on this can be found in [113].

Confinement of Molecules: The effect of confinement on the diffusion of molecules was further investigated by analysing their movement in a confined regions. Five data sets with $D = 1.5\,\mu\mathrm{m}^2/\mathrm{s}$ were generated in regions with radii of 50, 150 nm, 300 nm, 500 nm and 1500 nm. Trajectory analysis indicated that confinement hindered the free diffusion of molecules, resulting in an *'apparent'* decrease in the calculated value of diffusion coefficient as shown in Figure 3.8 C. We obtained average diffusion coefficients of $0.09\,\mu\mathrm{m}^2/\mathrm{s}$, $0.62\,\mu\mathrm{m}^2/\mathrm{s}$ and $1.1\,\mu\mathrm{m}^2/\mathrm{s}$ in regions with radii of 50 nm, 150 nm and 300 nm respectively. This can be explained by comparing the histogram of jump distances of a confined particle with the one obtained for a freely diffusing particle. For example, the maximum jump size in regions of 50 nm and 1500 nm radii was 90 nm and 800 nm respectively as shown in Figure 3.8A&B. In our experiments, such a situation arose when molecules were confined due to obstacles, such as chromosomes, in nuclei.

After testing our data analysis pipeline on simulated data, we applied it to the SMT experiments carried out to investigate the dynamics of CSL molecules.
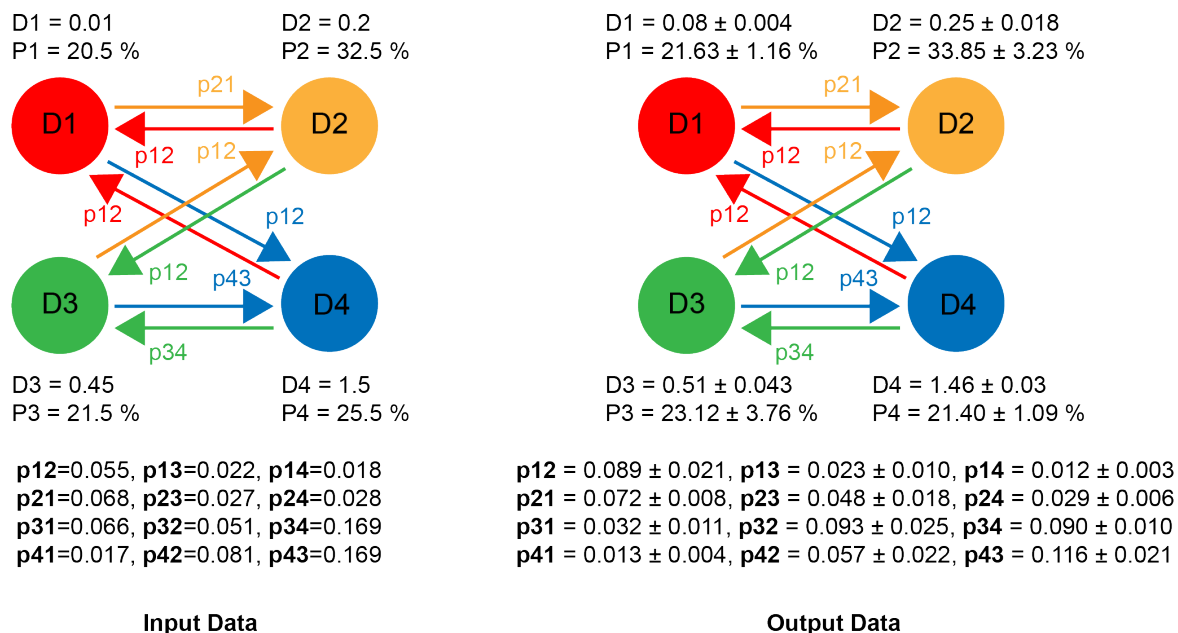
Fig. 3.7 Results of the *vbSPT* analysis on the synthetic data generated with four diffusion coefficients. The software correctly identified the number of diffusion states and quite accurately extracted parameters like diffusion coefficients, their respective populations, occupation probabilities and transition probabilities

3.6.2   Experimental Results

We performed SMT experiments on CSL molecules, labelled with mEOS, in the nuclei of Drosophila salivary glands. Low intensity of 405 nm laser was used to activate a spatially sparse set fluorophores at any given time, which was then imaged with 561 nm laser.

Imaging inside Nuclei

A cross section of salivary gland nuclei was imaged at an exposure time of 10 msec, which was suitable for the tracking of freely diffusing molecules while maintaining reasonable SNRs. An example image is shown in Figure 3.9A. Fluorescent spots, in such images, were localised and tracked using the image analysis pipeline discussed earlier. Figure 3.9B&C show representative histograms for the number of photons per emitter and track lengths respectively, obtained in our experiments. As imaging was performed inside the whole salivary glands of Drosophila, more than $20\,\mu$m away from the coverslip, an average of 63 photons were collected per localisation. Due to this low number of photons and factors like photo-bleaching and narrow DOF (molecules were not detectable outside a 200-300 nm region around the focal plane), the average track length in our experiments was ~ 5.23 frames. Although it was not possible to extract dynamics from one such track, *vbSPT* combined

(A)

(B)

(C)

Confinement Radius (nm)	50	150	300	500	1500
Diffusion Coefficient (μm^2/sec)	0.09 ±0.0002	0.62 ±0.002	1.1 ±0.0042	1.3 ±0.015	1.47 ±0.05
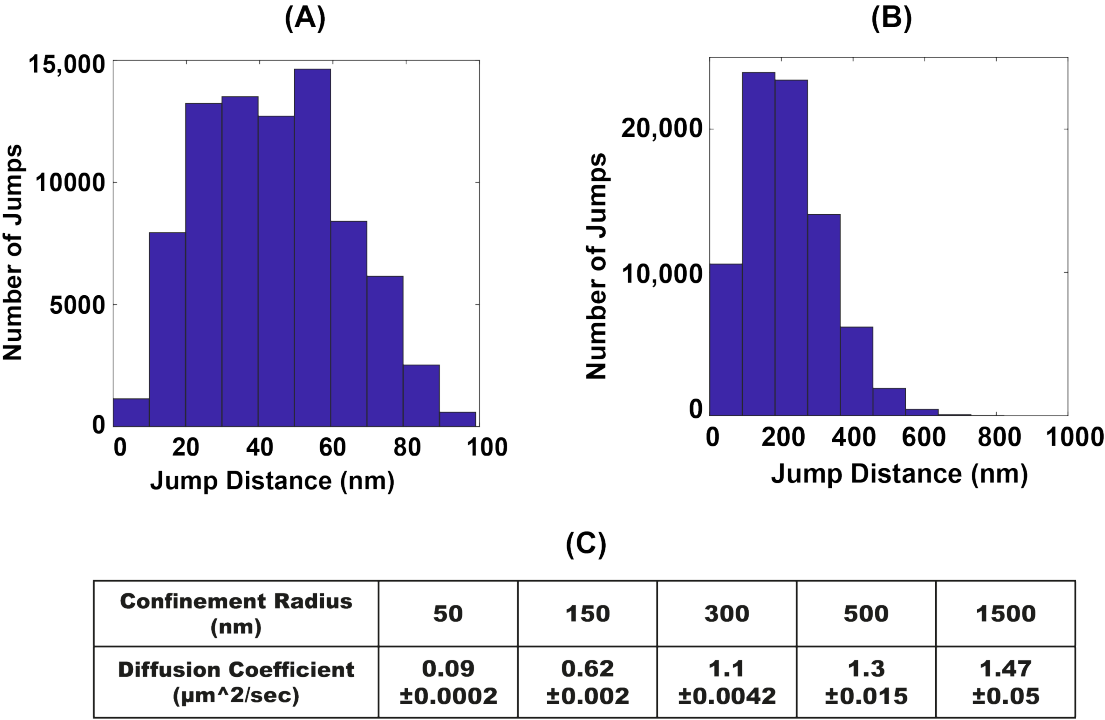
Fig. 3.8 Effect of confinement on the diffusion coefficient of a particle, otherwise diffusing with $D = 1.5\,\mu m^2/s$. (A) and (B) show histograms of jump distances for a particle diffusing in the regions of 50 nm and 1500 nm radii respectively. (C) shows *'apparent'* diffusion coefficients of a particle diffusing in regions of different radii. Confinement hindered the free diffusion of the particle, resulting in an *'apparently'* small diffusion coefficient.

(A) **(B)** **(C)**
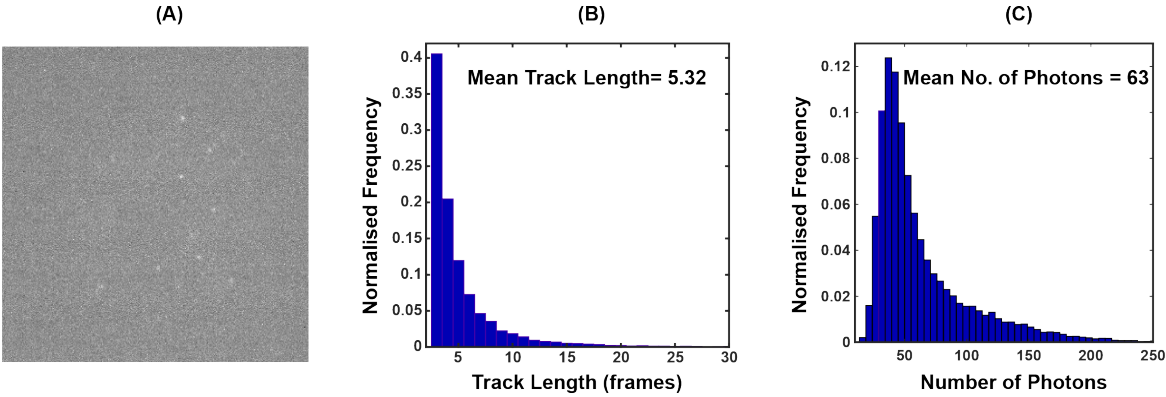
Fig. 3.9 (A) shows example image of our localisation microscopy in living Drosophila salivary glands. (B) and (C) show representative histograms of the number of photons per localisation and the track lengths respectively, obtained in our experiments.

information from multiple short tracks, more than $10,000$ in our experiments, to completely quantify the dynamics of the tracked molecules.

Imaging was first performed for the Notch OFF condition i.e. in the absence of the Notch signal. Results from the SMT analysis are shown in Figure 3.10A. The results were obtained from $30,036$ trajectories, extracted from 18 nuclei imaged in 5 different organisms. Error bars in the figure show the variation in the diffusion coefficients obtained for different organisms, or set of organisms, for which the trajectory analysis was carried out. It is important to mention that the number of diffusion states output by the *vbSPT* software depended heavily on the number of tracks. For small number of tracks, multiple diffusion states were merged, making it difficult to fully investigate the behaviour of molecules. For our experiments, at least $7,500$ trajectories were required to completely resolve the dynamics of CSL molecules. For organisms that did not produce the required number of tracks, the analysis was carried out on their collective tracks. For example, organisms 1, 2 and 3 produced 5142, 6795 and 2127 tracks respectively. So we ran *vbSPT* on their combined tracks, i.e. on $14,064$ tracks, to fully resolve the dynamics in these organisms. Once the trajectory analysis was performed, the dynamics could be studied in individual organisms as the *vbSPT* software returned the diffusion state of each jump in the analysed tracks.

Results indicated that the transcription factor had at least four different diffusion states in the imaged nuclei, which can be attributed to the following characteristics of the transcription factor:

- **State F1**, $D = 1.89\mu m^2/s$: freely diffusing molecules

- **State B1**, $D = 0.09\mu m^2/s$: immobile molecules, which were engaged in the specific DNA binding

- **State F2**, $D = 0.5\mu m^2/s$: molecules undergoing confined diffusion due to obstacles (such as chromosomes) in the nucleus

- **State B2**, $D = 0.22\mu m^2/s$): molecules involved in the non-specific interactions with the chromatin

The proposed model is shown in Figure 3.10B. It is important to mention that other than the reasons given above, tight confinement could also result in molecules to have the diffusion states B1 and B2, as discussed in Section 3.6.1. So, to fully understand the interaction of the CSL with the DNA, it was important to study its dynamics in a region containing large number of target genes. This was evident when a cross section of salivary gland nuclei was imaged in the presence of Notch signal i.e. under the Notch ON condition. No global change in the diffusion characteristic of the CSL was observed, except in a chromosomal region containing large number of Notch target genes. This analysis is covered in detail in the next section of the chapter.

(A)

(B)

	State F1	State F2	State B2	State B1
D (µm²/sec)	1.85 ± 0.045	0.49 ± 0.030	0.22 ± 0.025	0.09 ± 0.004
Population (%)	21.51 ± 5.45	32.86 ± 2.67	22.01 ± 6.96	23.62 ± 1.38
Dwell Time (ms)	37.97 ± 2.92	39.52 ± 6.37	73.94 ± 8.36	88.77 ± 14.87
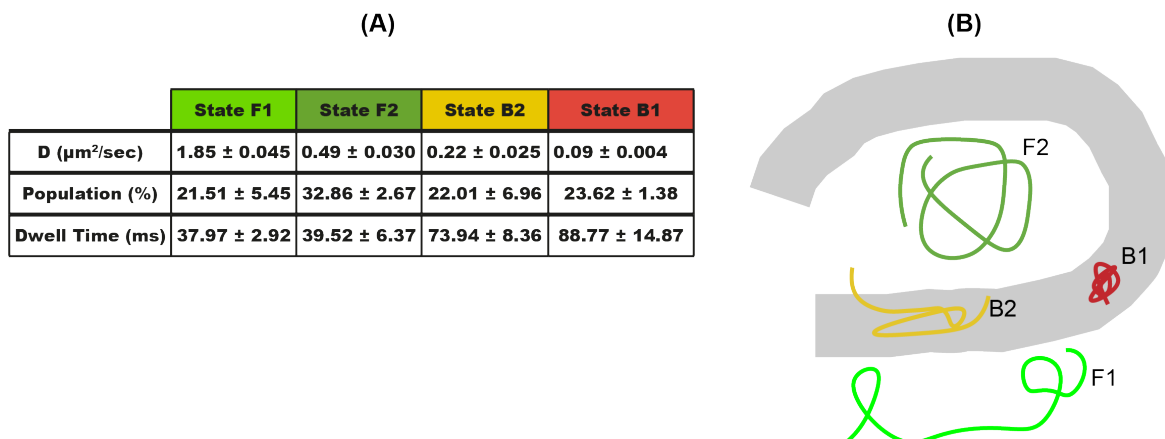
Fig. 3.10 Results of the SMT analysis in the Notch OFF condition. (A) shows the results of the trajectory analysis in the Notch OFF condition. CSL molecules showed multiple diffusion behaviours and the proposed model, about the origin of these different dynamics, is shown in (B).

Comparison with FRAP: Along with the SMT experiments, FRAP experiments were also performed on the CSL by the *Bray Lab* [87]. These experiments did not provide information about the behaviour of individual molecules, so different diffusion states could not be extracted from them. However, the ensemble FRAP measurements were in accordance with the SMT results. For example, FRAP experiments indicated that the highest diffusion coefficient for the CSL molecules was $2.2\,\mu\mathrm{m}^2/\mathrm{sec}$, which was close to the value obtained from the SMT analysis. Moreover, similar to the SMT results, around 20% of the molecules were found to be in the bound state.

The SMT results deviated from the FRAP with regards to the dwell time of the bound molecules. SMT suggested a very short dwell time of $\sim 100\,\mathrm{msec}$, which was significantly different from the FRAP estimates of 0.5-2 sec. This anomaly can be explained by the short trajectories, ~ 5 frames, obtained in the SMT experiments. It was not possible to estimate the correct dwell time from such a short trajectories.

The above discussion suggests that the SMT experiments were essential to understand the dynamics of CSL molecules. However, these experiments could not provide a correct estimate of the residency times, for which the FRAP experiments gave useful results. Hence, a combination of FRAP and SMT experiments was needed to completely understand the dynamics of the CSL molecules.

To better visualise and quantify the interaction of the CSL molecules with the DNA, SMT experiments were performed in a region containing high density of target genes. Results of those experiments are discussed next.

Imaging with the Locus Tag

The polytene chromosomes of salivary glands contain hundreds of aligned copies of DNA [115], resulting in several copies of the same gene staying spatially close in a nucleus. Hence, if a region of a chromosomes with high density of target genes is imaged, it can help in visualisation of the CSL dynamics and its interaction with the DNA. One such region is Enhancer of split-Complex (E(spl)-C), which contains multiple copies of highly responsive Notch target genes, making it an attractive candidate to study the CSL dynamics [87]. *Bray Lab* have designed a DNA-tagging technique, known as locus tagging, which allows identification of this chromosomal region in living cells. This is done by inserting a segment of DNA, *int*, in the E(spl)-C band using CRISPR/Cas9 genome editing technique. A protein named *ParB*, labelled with GFP, binds to this DNA segment, allowing the visualisation of *ParB-int* interaction and hence the E(spl)-C region. For a detailed explanation of these techniques, see [87]. The advantage of labelling *ParB* with GFP was that the band was identified using 488 nm laser and single molecule imaging was subsequently carried out using 561 nm laser, at the E(spl) locus with no cross talk.

	$d_{bound,Locus}/ d_{bound,Nucleus}$	$d_{all,Locus}/ d_{all,Nucleus}$
Notch ON	20.5 ± 10.8	17.0 ± 6.9
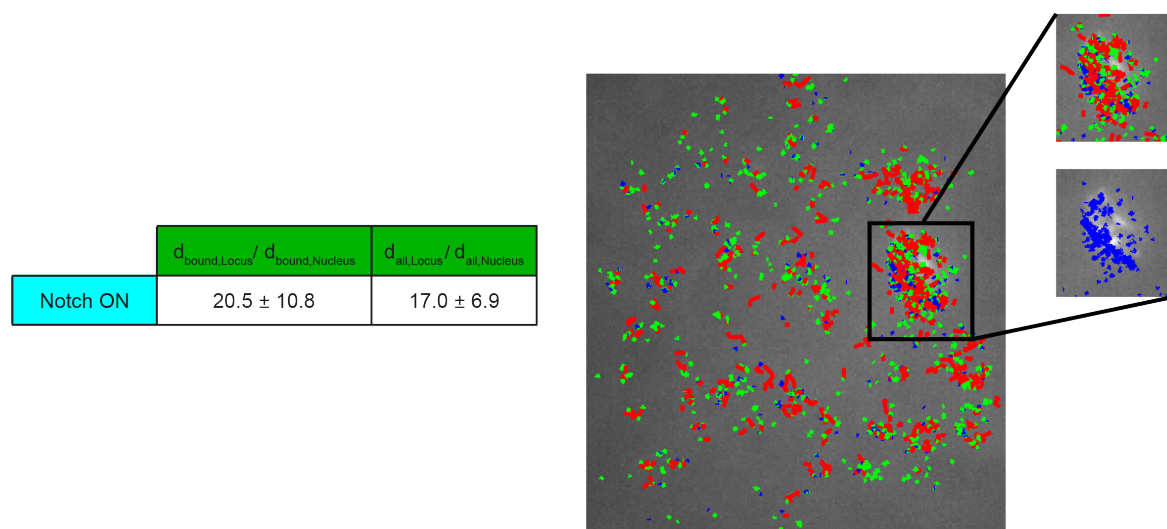
Fig. 3.11 SMT experiments with the locus tag in the FOV for the Notch ON condition. Left: table shows the density of molecules at the locus tag with respect to the density elsewhere in the nucleus. $d_{all,Nucleus}$ and $d_{all,Locus}$ are the densities of all the molecules in the nucleus and at the locus tag respectively. Similarly, $d_{bound,Nucleus}$ and $d_{bound,Locus}$ are densities of bound molecules in the nucleus and at the locus tag respectively. Right: a representative image of the cross section of a nucleus containing the locus tag, with tracks plotted on top. Blue, green and red colours represent jumps in the bound (state B1), non-specifically bound (state B2) and freely diffusing & confined (states F1 & F2) states respectively.

We started off by performing the SMT experiments on CSL molecules in the Notch ON condition, with the locus tag in the FOV. Results of the experiments are shown in Figure 3.11. We found a striking contrast in the density of bound molecules at the band and elsewhere in the nucleus. On average the density of bound molecules at the locus, $d_{bound,Locus}$, was around 20 times higher than elsewhere in the nucleus, $d_{bound,Nucleus}$. Not only this, the overall density of molecules at the locus tag, $d_{all,Locus}$, was on average 17 times higher than elsewhere in the nucleus, $d_{all,Nucleus}$. This can be seen from an example image of the FOV, containing the locus tag (obtained using 488 nm excitation), with tracks (for that nucleus) plotted on top. Blue, green and red colours represent jumps in the bound (state B1), non-specifically bound (state B2) and freely diffusing & confined (states F1 & F2) states respectively. This was done by colouring jumps on the basis of their diffusion state obtained from the *vbSPT* software. Clearly there was a very high density of tracks at the locus tag, compared to elsewhere in the nucleus. This indicates that this locus tag acts as a local attractor of molecules in the Notch ON condition. We also analysed the CSL dynamics at the locus for the Notch OFF condition and results are shown in Figure 3.12. The figure shows that the density of molecules was same everywhere in the nucleus i.e. no obvious change was observed at the locus tag. This suggests that only a small number of CSL molecules were required to suppress the transcription of target genes.

	$d_{bound,Locus}$/ $d_{bound,Nucleus}$	$d_{all,Locus}$/ $d_{all,Nucleus}$
Notch OFF	0.81 ± 0.47	0.73 ± 0.34
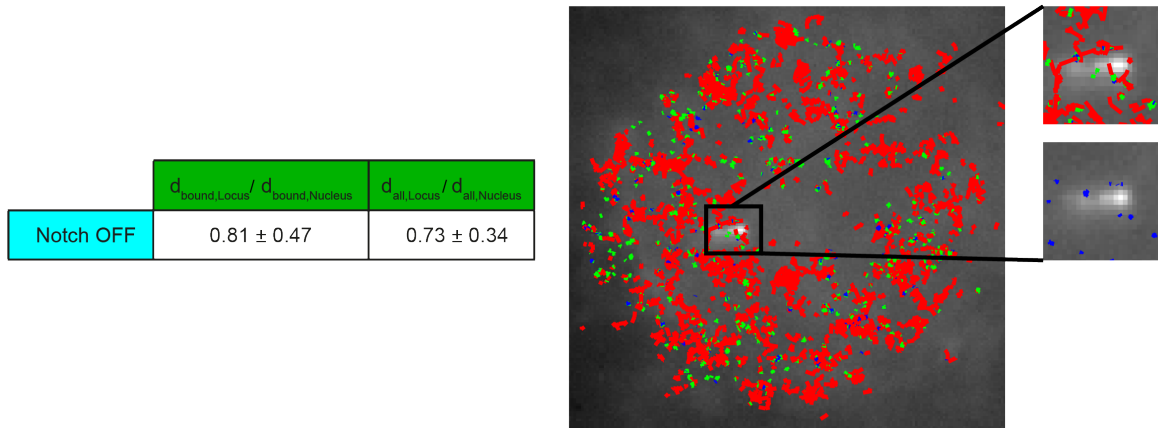
Fig. 3.12 SMT experiments with the locus tag in the FOV for the Notch OFF condition. Left: table shows density of molecules at the locus tag with respect to the density elsewhere in the nucleus. $d_{all,Nucleus}$ and $d_{all,Locus}$ are the densities of all the molecules in the nucleus and at the locus tag respectively. Similarly, $d_{bound,Nucleus}$ and $d_{bound,Locus}$ are densities of bound molecules in the nucleus and at the locus tag respectively. Right: a representative image of the cross section of a nucleus containing the locus tag, with tracks plotted on top. Blue, green and red colours represent jumps in the bound (state B1), non-specifically bound (state B2) and freely diffusing & confined (states F1 & F2) states respectively.

Residency Times: As discussed earlier, the SMT analysis did not provide correct estimates of the residency times, due to short tracks in our experiments. The *Bray Lab* performed FRAP experiments at the locus tag to calculate the residency times of the bound molecules [87]. They found a residency time of around 10-15 sec at the locus tag, in the presence of the Notch signal, compared to 0.5-2 sec in the inactive state of the pathway [87].

Hence, contrary to the existing model of the Notch pathway regulation, we found significant changes in the dynamics of the CSL in the active and inactive states of the pathway. Notch increased the recruitment of CSL molecules at the target genes and they spent greater time bound to the DNA, compared to the Notch OFF condition. The next step in this project was to further investigate how this dynamics changes are brought about. One hypothesis is that the Notch activation changes the density of histones around the target genes allowing CSL to bind those regions more efficiently. In order to test such hypothesis, we performed SMT experiments on histones.

SMT Experiments on Histones- the Future Direction

(A)

$D_{BOUND} = 0.083 \ \mu M^2/SEC$

(B)

$D_{BOUND} = 0.0941 \mu M^2/SEC$
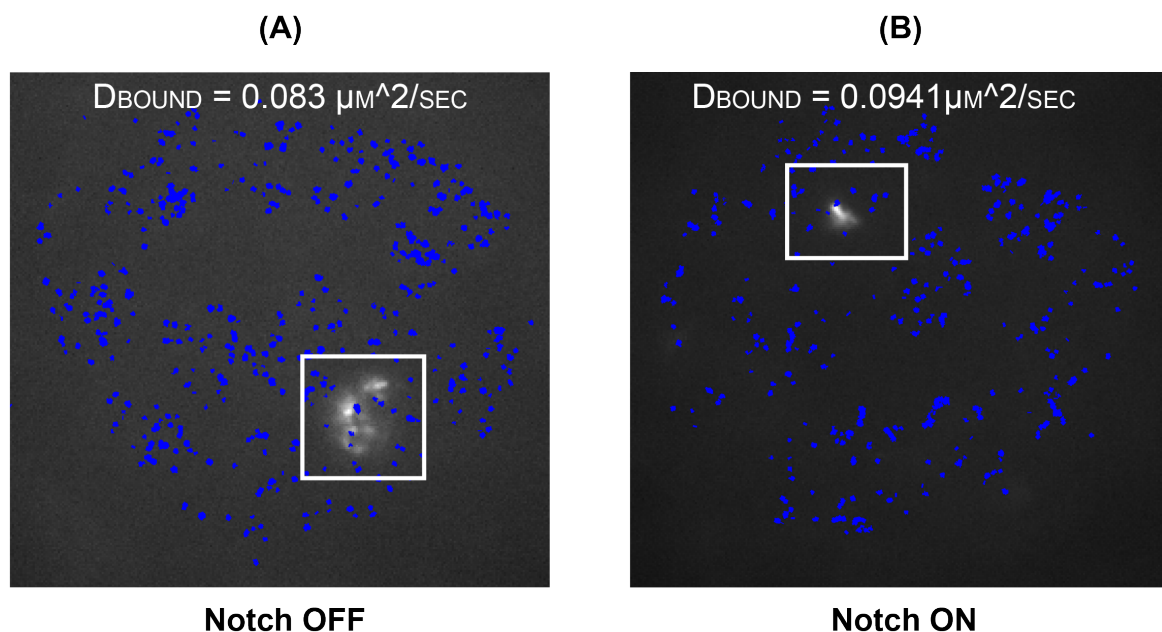
Notch OFF   **Notch ON**

Fig. 3.13 SMT experiments on histones. (A) and (B) show representative images of salivary gland nuclei with the locus tag in the FOV, for the Notch OFF and the Notch ON conditions respectively. Jumps in the bound state are plotted on top. No change in the dynamics of histone molecules was observed in the presence of the Notch signal (see text for more details)

For SMT experiments, histones were labelled with mEOS and imaging was performed at 10 msec exposure time. Results for SMT analysis are shown in Figure 3.13. As expected,

more than 90% of the molecules were found to be in the bound state with an average diffusion coefficient of $0.083\,\mu\mathrm{m}^2/\mathrm{sec}$ and $0.094\,\mu\mathrm{m}^2/\mathrm{sec}$ for the Notch OFF and the Notch ON conditions respectively. High density of histone molecules in the nucleus resulted in some false tracks due to wrongly linked molecules in consecutive frames. This gave rise to a small percentage of molecules with apparently high diffusion coefficients, which were excluded from the subsequent analysis. Example images of nuclei for the Notch OFF and the Notch ON conditions, along with the obtained tracks plotted on top, are shown in Figures 3.13A&B respectively.

In the Notch ON condition we expected a higher diffusion coefficient at the locus tag, due to relatively open chromatin fibres. As discussed in Chapter 4, such an arrangement is important for protein molecules to access the target genes for their transcription. However, such a change in the diffusion coefficient was not observed in the presence of Notch signal. A possible reason for this could be the short trajectories, around 50-60 msec, in our SMT experiments. Very small changes in the diffusion coefficient were not observable at this scale. For a change to be detectable, the displacement of histone molecules (in 50-60 msec) had to be more than the localisation precision, which corresponded to a diffusion coefficient of around $0.09\,\mu\mathrm{m}^2/sec$ (the smallest diffusion coefficient in our SMT experiments).

Hence, to study these small changes in the diffusion coefficient, SMT analysis has to be performed on long tracks. This requires use of a photostable dye, which is a current topic of research at the *Bray Lab*. They are designing Halo-tags to tag histones and CSL molecules with bright and photostable dyes, such as Janelia fluor [116].

3.7   Summary

This chapter described the application of localisation microscopy to study the dynamics of a DNA binding protein, deep within the whole salivary glands of Drosophila. Careful optimisation of the microscope was required to efficiently collect photons from single fluorophores at such depths. We proposed a method to exploit the asymmetry of the PSF in the presence of SA, to optimally adjust the correction collar of the objective. Other than the microscope, image analysis software were also optimised to achieve their best performance under our imaging conditions. We proposed the use of motion blurring analysis to detect the presence of multiple diffusion populations in the localisation data. This simple technique quite accurately predicted the relative proportions of freely diffusing and bound molecules in the imaged nuclei. To more accurately explain the diffusion behaviour of CSL, SMT experiments were carried out. Tracking and trajectory analysis software were characterised using synthetic data, to optimise their performance under our imaging conditions. These

optimisations were important to accurately estimate the dynamics of CSL molecules from very short trajectories (average length of 5-6 frames) obtained in the experiments.

Hardware and software optimisations, discussed in the chapter, allowed us to perform and analyse SMT experiments in the whole salivary glands of Drosophila i.e. close to the natural physiological state of a cell. Our results were supported by other imaging techniques, such as FRAP, and gave significant insights into the regulatory mechanism of the Notch signalling pathway. The results presented in this chapter were also published in [87].

3.8   Contributions

The microscope was designed and developed by me with inputs from Martin Lenz and Kevin O'Holleran. I also optimised the imaging conditions and carried out the single molecule experiments with the help from the *Bray Lab*. I also carried out simulations and experimental data analysis, discussed in the chapter, with inputs from Leila Muresan and Kevin O'Holleran. Samples, used in the project, were prepared and labelled by the *Bray Lab*, who also led the biological interpretation of the data.

3.9   Materials and Methods

Preparation and Labelling of Cells

The *Bray Lab* used the following procedures for the preparation and the labelling of cells.

Salivary Gland Cultures

Salivary glands of early third-instar larvae were dissected in dissecting media [Shields and Sang M3 insect medium (Sigma, S3652), supplemented with 5% FBS (Sigma, F9665) and 13 Antibiotic-Antimycotic (Gibco, 15240-062)]. Unharmed gland pairs were placed in a Poly-L-lysine treated observation chamber [117]. The chamber was made with a double layer of double side tape (Sellotape acid free perforated using a hole puncher of 9 mm diameter hole). The tape was attached to a 22×50 mm coverslip. The coverslip was then attached to a metal slide with a cut-out panel. Finally, the chamber/hole was filled with medium and the discs placed in it and then covered with the semipermeable membrane and covered with viscous media [dissecting media $+ 2.53$ wt/vol methyl-cellulose (Sigma-Aldrich)]. For PALM imaging of fixed samples, salivary glands were fixed in 4% Formaldehyde for 15min, washed 3×15 min in PBT (PSB $+ 0.3\%$ Triton X-100) then left in PBT at 4°C overnight before mounting as for live samples.

Fly Stocks

To analyse Su(H) dynamics, we used a fly stock expressing endogenous levels of Su(H) tagged with the photoconvertible tag mEOS [87]. In order to visualised the E(Spl) genomic region, we used the locus tag technique [87]. In brief, this consist of expressing the protein ParB1-mCherry, using the UAS-Gal4 system [118]. ParB1binds the genetic sequence, Int1, inserted into an intergenic region in E(spl)-C.

Chapter 4

Localisation Microscopy to Investigate the Chromatin Architecture

4.1 Introduction

Localisation microscopy provides up to tenfold improvement in resolution, over the diffraction limit of light, in fluorescence microscopy. In this chapter, the application of our localisation microscope to study the architecture of chromatin in primary spermatocytes of Drosophila is described. We discuss optimisation of imaging conditions and data analysis pipeline to super-resolve regions with different densities of chromatin fibres in a nucleus. Calibration and characterisation of the microscope for dual-colour imaging is also discussed in the chapter.

4.1.1 Chapter Description

First, the experimental setup and the imaging conditions for localisation microscopy are described along with the subsequent data analysis. This involves spot localisation and cluster analysis over the acquired images. Such an analysis in different regions of a nucleus provided useful insights into the formation and packaging of chromatin fibres. We also discuss the calibration of the experimental setup for dual-colour localisation microscopy and its application to investigate the arrangement of active transcription sites within a nucleus. The chapter ends with a discussion on the use of DHPSF to visualise the three-dimensional chromatin architecture.

4.2   Biological Significance

The human genome consists of over 3 billion base pairs, separated by a distance of 3.4 angstroms [119, 120]. If arranged linearly, it would cover a distance of around 1 m. However, the entire genome is packed inside the $10\,\mu$m nucleus of a cell, requiring highly condensed packaging of DNA fibres. At the same time, the packaging needs to be dynamic to allow various protein complexes to access different regions of DNA, to perform biologically important processes such as transcription, DNA replication and DNA repair [121].

In cells, DNA exists in the form of chromatin i.e. bound to proteins, which efficiently pack it inside the nucleus of a cell. The first level of packaging is the wrapping of DNA around eight histone proteins to form a structure called nucleosome, which results in up to seven fold compactness of DNA fibres [119]. Nucleosomes then interact with each other and segments of DNA fibres to form higher order chromatin structures. Such an organisation is important for gene regulation because DNA control units and their corresponding genes are not always next to each other along the linear sequence of DNA [119, 122]. The fundamental unit of the three-dimensional DNA packaging are the topologically associated domains (TADs) [123], which are regions of chromatin that interact more within themselves than with the neighbouring regions. These structures are highly conserved across different cell types and species [124]. Higher level organisation of TADs result in the compartmental distribution of chromatin, in which compartments with high and low levels of active genes are categorised as *A* and *B* respectively. Finally, the compartments are arranged into chromosomal territories, where the inter-chromosomal contacts are minimised [119].

Although domains are the fundamental unit of the three-dimensional chromatin architecture, their composition and mechanism of formation is not completely understood and is a matter of ongoing investigation [119]. Their sub-diffraction size and dense packaging (within the nucleus) make these questions challenging to answer. Initial super-resolution experiments on mammalian cells have confirmed the existence of chromatin domains in them [125], but most of the above information is obtained through fluorescent *in situ* hybridisation experiments and genomic proximity assays [119].

The *White Lab* at the *Department of Physiology, Development and Neuroscience*, investigates the regulatory architecture of genome. The lab uses primary spermatocytes of Drosophila as the test sample, because the formation of these cells is accompanied by around 25-fold increase in the nuclear volume [126]. As a result of this expansion, their chromatin becomes less dense. Moreover, the Y-chromosome in their nuclei, normally repressed in other cell types (and stages), is active and expands as Y-loops filling much of the central nucleoplasm [127]. These Y-loops contain open chromatin fibres and represent an enormous single transcription unit, making them a convenient model to visualise the topology of gene

transcription. These characteristics make primary spermatocytes an attractive candidate to study the chromatin architecture.

This project was carried out in collaboration with the *White lab*, with the goal to apply the localisation microscopy to study the structure of chromatin in Drosophila primary spermatocytes.

4.3   Methodology

Imaging was carried out on the custom built microscope at CAIC, the experimental setup of which is described in Chapter 2. Here the experimental details, imaging conditions and optimisations specific to the experiments discussed in this chapter are presented. Subsequent data analysis; involving spot localisation and clustering is also discussed in the section.

4.3.1   Experimental Setup

Detailed setup of our localisation microscope is discussed in Chapter 2. Briefly, an inverted microscope frame, Leica DM IRE2, was customised for localisation microscopy. Excitation (638 nm and 561 nm) and activation lasers (405 nm) were provided by a laser combiner (Omicron LightHUB). Output of the laser combiner was through a single mode optical fibre, which was collimated to a 8 mm diameter beam using a reflective collimator and later circularly polarised using an achromatic quarter wave plate. The beam was then demagnified on the sample through a 250 mm tube lens and 60x silicone oil objective (Olympus UPLSAPO60XS2, 1.3 NA). Imaging was carried out at an exposure time of 10 msec with a continuous excitation beam ($0.25 - 0.4$ KW/cm2) and bursts of the activation beam ($0.1 - 0.3$ W/cm2). Such a low intensity of the activation laser was optimal to activate and subsequently image a sparse set of molecules under our imaging conditions.

Fluorescence was collected through the same objective lens, filtered to remove scattered and reflected light and focused to the image plane using a 200 mm focal length lens, *L*2. Conjugate BFP of the microscope was accessed using lens, *L*3 (focal length = 125 mm), where the phase mask for the generation of the DHPSF was placed for three-dimensional localisation microscopy. Lens, *L*4 (focal length = 125 mm), then focused light onto a Cairn *TwinCam* system, which had a dichroic filter to separate the emissions corresponding to different excitation wavelengths. It also optimally relayed the image plane to the attached cameras, shown in the inset of Figure 4.1. Further band-pass filters were introduced in the light path (using slots available in the *TwinCam*) to ensure high attenuation of any remaining (unwanted) laser light.

Camera 1, Photometrics Prime 95-B, captured the emission signal of wavelengths greater than 647 nm. Camera 2, Hamamatsu Flash 4.0, captured the emission signal of wavelengths between 574 nm and 626 nm. It is important to mention that the dependency of the phase mask on the wavelength of light limited the three-dimensional imaging to a single excitation wavelength only.
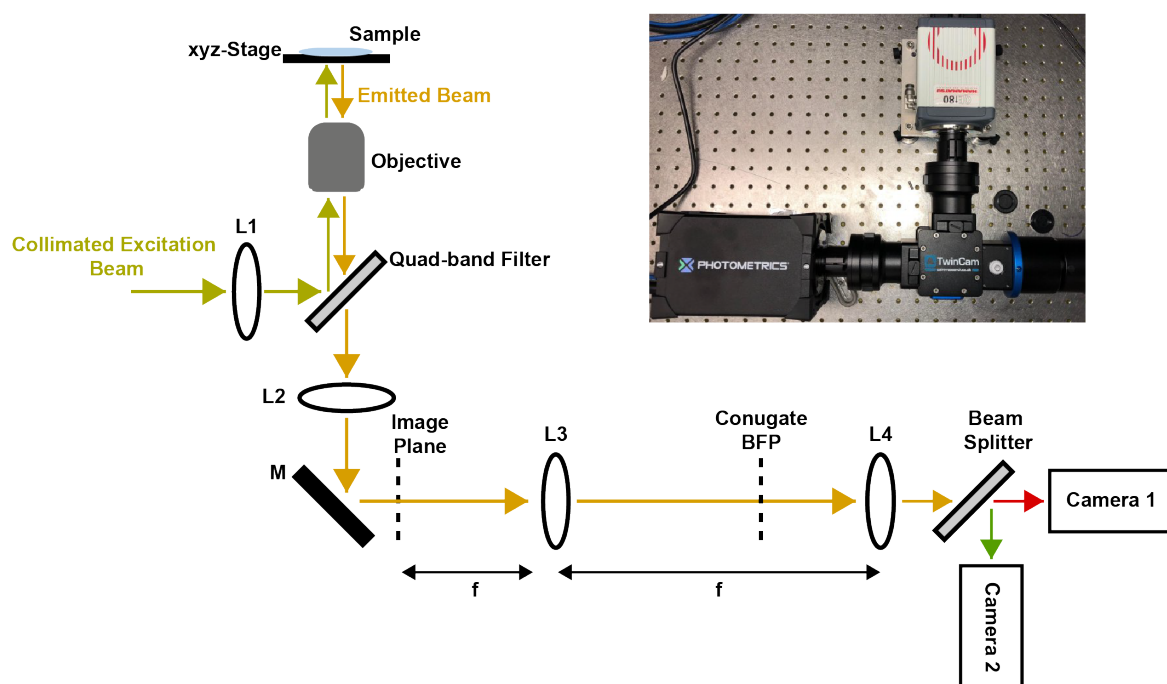
Fig. 4.1 Experimental Setup of the custom built microscope at CAIC.

4.3.2   Imaging Buffer

To study the chromatin architecture, histone molecules were labelled with alexa-647 dye. We found the following buffer composition to work optimally for our experiments. Protocols for labelling and buffer preparation are discussed in the *Materials and Methods* section, at the end of the chapter.

- Glucose 50 mg/ml

- Catalase 45 μg/ml

- Glucose Oxidase 0.8 mg/ml

- MEA (Cysteamine) 0.77 mg/ml

- TRIS-HCl, pH8, 50 mM

- NaCl 10 mM

Photostability of fluorophores depends strongly on the composition of an imaging buffer [17]. In the discussed buffer, glucose, glucose oxidase and catalase work as an oxygen scavenging system, named GLOX, as they remove oxygen from the solution. This greatly reduces photo-bleaching, leading to improved lifetime of fluorophores [17, 128]. GLOX system works as follows [129, 130]:

$$
\begin{aligned}
\text{Glucose} + H_2O + O_2 \xrightarrow{\text{Glucose Oxidase}} \text{Gluconic Acid} + H_2O_2 \\
H_2O_2 \xrightarrow{\text{catalase}} H_2O + \frac{1}{2}O_2
\end{aligned}
\tag{4.1}
$$
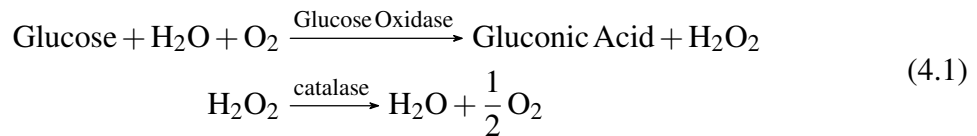
Oxygen present in the solution changes to Gluconic acid and Hydrogen peroxide in the presence of Glucose Oxidase. H_2O_2 is then converted to water and oxygen by the catalase. So, the amount oxygen halves as a result of such a reaction and over time the concentration of oxygen drops in the solution.

A by-product of the reaction is Gluconic acid which makes the solution acidic (pH<4), affecting the binding ability of antibodies (both primary and secondary). So, over time acid accumulates in the solution, eventually leading to the fall-off of antibodies from their targets. In our experiments, this resulted in freely diffusing dye in the FOV, which significantly increased the background signal.

The problem was overcome by sealing the dish, containing cells and the buffer, with an aluminium foil to minimise the contact between the solution and the external oxygen. Moreover, we used large volumes (5 mL) of the imaging buffer to slow down the pH change. These steps allowed us to image a sample for more than two hours (from initial 20 minutes of imaging) without a need of changing the imaging buffer.

4.3.3   Localisation of Single Molecules

Single molecules were localised using the *WaveSM* software, implemented in MATLAB. The software uses wavelet segmentation of raw (localisation microscopy) images to detect features matching the size of the PSF of the microscope. A two-dimensional Gaussian function is then fitted to each detected spot to localise it with high precision. The software is discussed in detail in Chapter 1.

One of the challenges in the localisation of molecules was the varying distribution of dye in the imaged nuclei. This was due to dense packing of chromatin within chromosomes and relatively open chromatin fibres at the centre of nuclei, as seen from a representative image in Figure 4.2. Consequently, higher concentration of the dye in chromosomes required

significant photo-bleaching to reach the optimal number of active molecules in any given frame. For this, high powers of the activation and the excitation lasers were used to photo-bleach the excessive dye. However, relatively low density of dye outside the chromosomes meant that most of it was exhausted by the time the optimal blinking density was achieved in chromosomes.
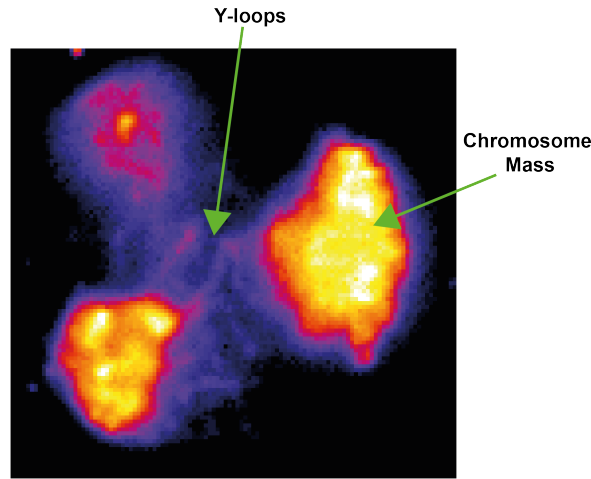
Fig. 4.2 The distribution of chromatin in an example nucleus. The chromatin is densely packed in chromosomes and is relatively *open* at the centre of the nucleus (where the Y-loops are located).

Example images of a nucleus at the beginning of a typical experiment and after photo-bleaching are shown in Figure 4.3A&B respectively. Initially, chromosomes had high concentration of dye resulting in the overlap of emissions from neighbouring molecules. However, outside the chromosomes the spots were non-overlapping and localisable. When such a sample was exposed to the activation and the excitation lasers for around 10 min, enough dye molecules were photo-bleached to get non-overlapping emissions in chromosomes as well. So, we overcame the problem of varying dye density by reconstructing the super-resolution images of Y-loops and chromosomes from frames recorded at different time points.

The required sectioning was achieved by filtering localisations on the basis of their width. For the Gaussian approximation of the PSF (airy disk), the standard deviation of the diffraction limited spot is given as [26]:

$$\sigma = 0.42 \frac{\lambda}{2NA} \tag{4.2}$$

For a wavelength of 665 nm, the peak emission wavelength for alexa-647, σ comes out to be 107.4 nm (Note: this is the standard deviation and not the half width of the Gaussian

(A)   **(B)**
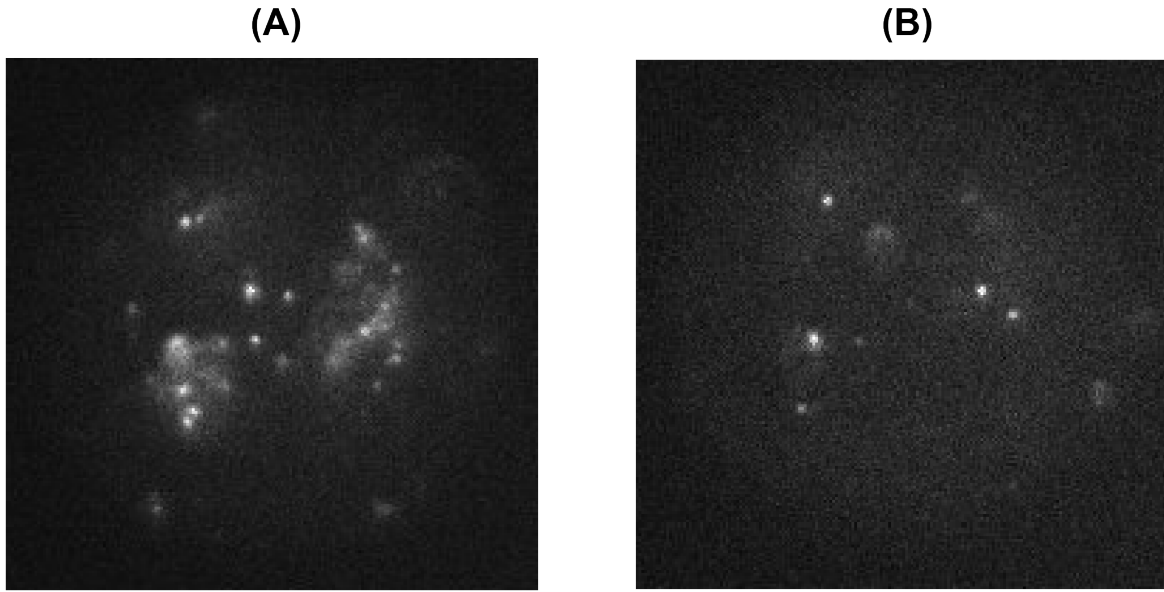
Fig. 4.3 Example images of a nucleus: (A) at the beginning of a typical experiment and (B) after photo-bleaching. Photo-bleaching was required to reach the optimal density of active molecules in chromosomes.

and it is the latter which corresponds to the Rayleigh criterion). So, localisations with σ between 100 nm and 150 nm were selected. By applying such a filtering process, we not only discarded overlapping emissions but also selected high precision localisations from a thin volume close to the focal plane of the objective.

4.3.4   Effect of Drift

As different regions of a nucleus were resolved at different time points, over 20 min of imaging was required to obtain enough localisations in all its regions. Stage drift, greater than the localisation precision, was observed over such time scales (see Figure 2.3). The problem was overcome by calculating the drift between low resolution images of the nucleus, constructed from the localisations collected over a short time. The technique was based on the method presented in [100] and we used MATLAB implementation of the technique provided with the publication.

The structure of chromatin fibres was sampled by localisations collected over the entire imaging time. So, low resolution images of the underlying structure could be obtained by combining localisations from multiple subsets of consecutive frames. The time period, from which the localisations were combined was chosen to be small enough to ignore the effect of drift within a subset. If I_n is the low resolution image obtained by binning localisations in the nth subset, the drift was calculated by determining cross-correlations between I_1 and I_n for

$n = 1, 2, 3...N$ (N=total number of subsets). The bin size was chosen to be small enough to resolve drifts of the order of tens of nanometres but at the same time large enough to contain reasonable number of localisations to robustly calculate the cross-correlations. Moreover, the number of frames in a subset was optimally chosen to obtain same structures in all the low resolution images.

Cross-correlations between low resolution images gave drifts between groups of localisations from which these images were generated. Spline interpolation was then performed to calculate the drift for each frame. For a detailed explanation of the method, see [5, 100, 131]. In our analysis we combined information from 3000-5000 frames (corresponding to 30-50 seconds) and used a bin size of 55 nm. In Section 4.4.1 characterisation and testing of the software, using simulated data, is discussed before its application to the experimental data.

4.3.5 Cluster Analysis

As discussed earlier, TADs are the fundamental unit of the three-dimensional chromatin architecture and our experiments showed their existence in the imaged nuclei. Cluster analysis was carried out to quantify the presence of chromatin domains in the localisation data and to determine their sizes. In this section, the theory behind our cluster analysis method and its implementation is discussed.
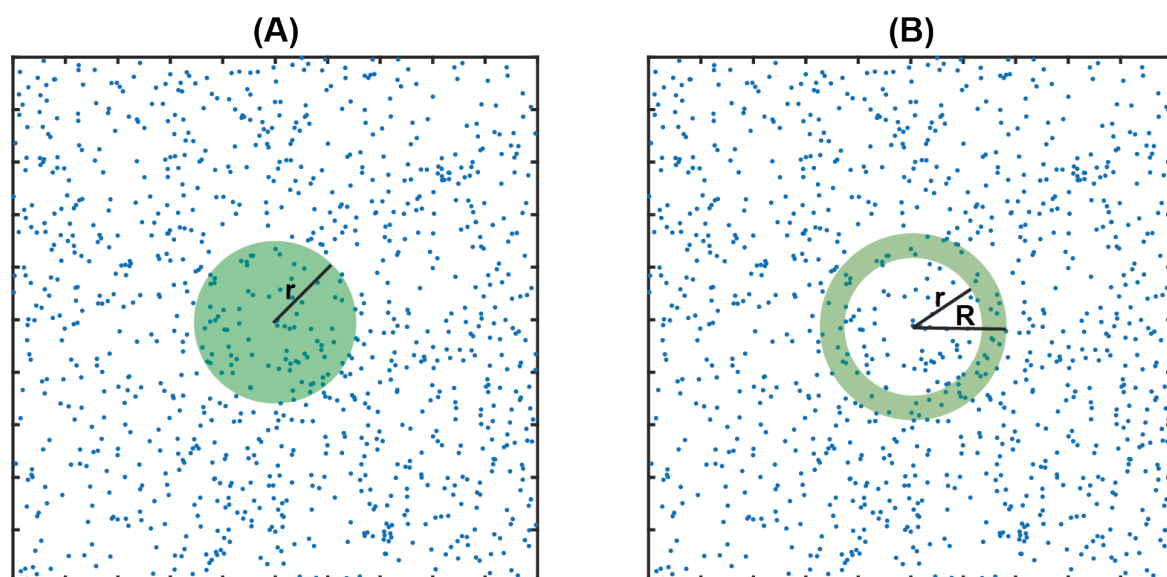
Fig. 4.4 (A) Method to calculate the K-function from the localisation data. It is a measure of the average number of points *within* a distance r from a point in the data. (B) Method to calculate the PCF from the localisation data. It gives the average number of points *at* a distance r from a point in the data

For clustering, we considered localisations as a spatial point process [132]. This allowed us to use the characteristics of the point processes to detect clusters in the data and to determine their sizes. Suppose, N points are randomly scattered over an image, with $E(N(r))$ as the average number of points within a distance r from a point, $s(x,y)$. We calculated the following function to detect clustering in the localisation data:

$$K(r) = \frac{E(N(r))}{\lambda} \tag{4.3}$$

$K(r)$ is known as the K-function and it is a measure of the average number of points *within* a certain distance from any other point in the data as shown in Figure 4.4A. λ is the density of molecules in the image (or the region of interest). If points are randomly distributed over the image, $E(N(r)) = \lambda \pi r^2$ and the K-function increases linearly as a function of r^2. However, for clustered data this is not the case because the K-function decreases with an increase in r, as seen from Figure 4.5B. Therefore, by using the following conditions, the K-function can be used as an indicator of clustering or repulsion in the localisation microscopy data [133].

$$
\begin{aligned}
K(r) &= \pi r^2 && \text{Randomly distributed data} \\
K(r) &> \pi r^2 && \text{Clustered data} \\
K(r) &< \pi r^2 && \text{Dispersed data}
\end{aligned}
\tag{4.4}
$$

If the distribution of points in clusters is known, K-function can also be used to determine the average cluster size in an image. This is done by fitting the theoretical K-function to the K-function calculated from the data. We assumed a Gaussian distribution of points in chromatin clusters, for which the K-function takes the following form [134]:

$$K(r) = \pi r^2 + \frac{1}{\alpha}\left(1 - exp\left[\frac{r^2}{4\sigma^2}\right]\right) \tag{4.5}$$

here, σ is the standard deviation of clusters and α is the mean number of clusters in the data.

The linear variation of the K-function, as a function of r^2, for randomly distributed points can be changed into a constant by determining the average number of points *at* a distance r (instead of the total number of points *within r*) from $s(x,y)$. Such a function is known as the point correlation function (PCF) and it is the derivative of the K-function with respect to r, as shown in Figure 4.4B. PCF deviates from the constant value for clustered data and, like K-function, can be used to detect the presence of clusters in the localisation data. Moreover, if points are assumed to be normally distributed in clusters, the theoretical PCF is given as
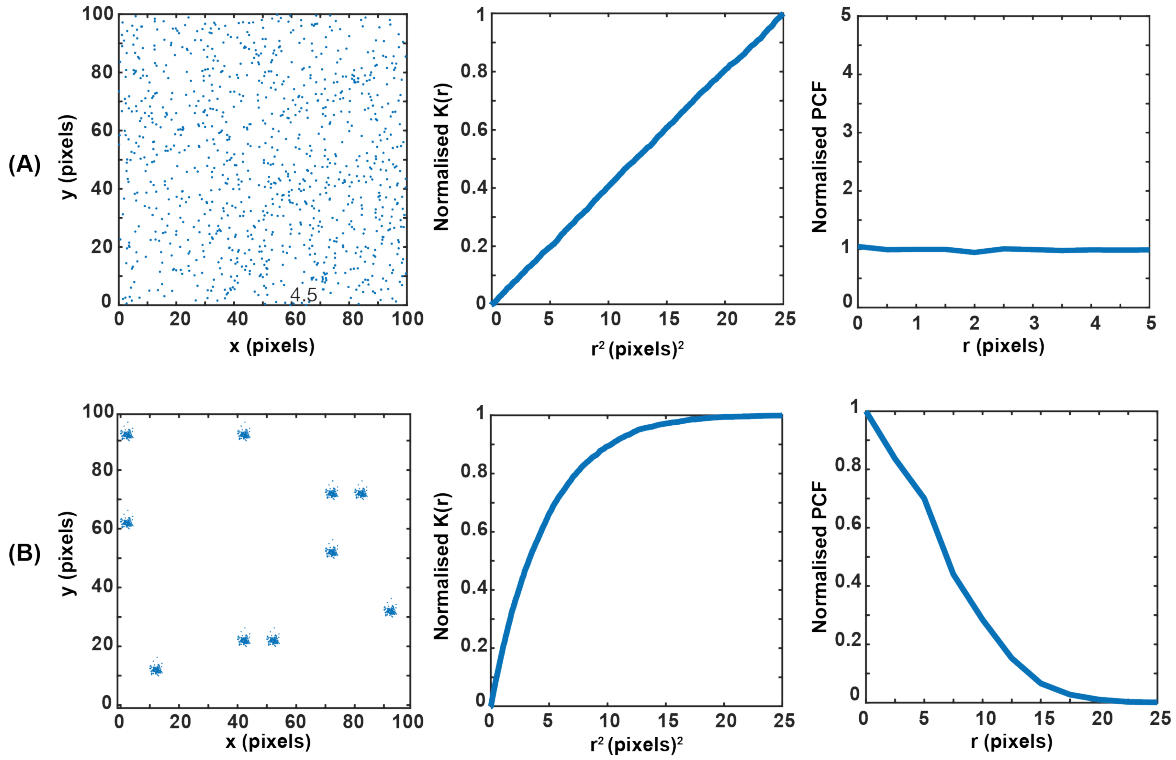
Fig. 4.5 K-function and PCF for (A) randomly distributed data and (B) clustered data. For randomly distributed data, the K-function varies linearly as a function of r^2 and PCF is constant over r. However, the shape of these functions change when evaluated for clustered data.

[135]:

$$PCF(r) = 1 + \frac{1}{4\pi\alpha\sigma^2} exp\left[-\frac{r^2}{4\sigma^2}\right] \tag{4.6}$$

So, by fitting such a function to the PCF calculated from the localisation data, cluster sizes can be determined.

The K-function and the PCF can only be used to calculate the average cluster size over the region of interest. Hence, in our analysis, nuclei were divided into chromosomes and Y-loops before carrying out the cluster analysis. On average, both the methods gave similar cluster sizes but we found the PCF to be more robust under different localisation densities. Hence, results discussed in this chapter are based on fitting Eq 4.6 to the PCF calculated from the localisation data (unless specified otherwise). The *spatstat* package in *R* was used for the implementation of the K-function and the PCF, the script for which was written at CAIC (by Leila Muresan) and is available at [136]. The software was tested on simulated data, as discussed in Section 4.4.2, before its application to the experimental data.

4.4 Software Characterisation

In this section, characterisation and testing of the drift correction and the cluster analysis software, using simulated data, is discussed. Such a testing allowed us to adjust important parameters of both software to obtain their optimal performance on our localisation microscopy data.

4.4.1 Characterisation of the Drift Correction Software
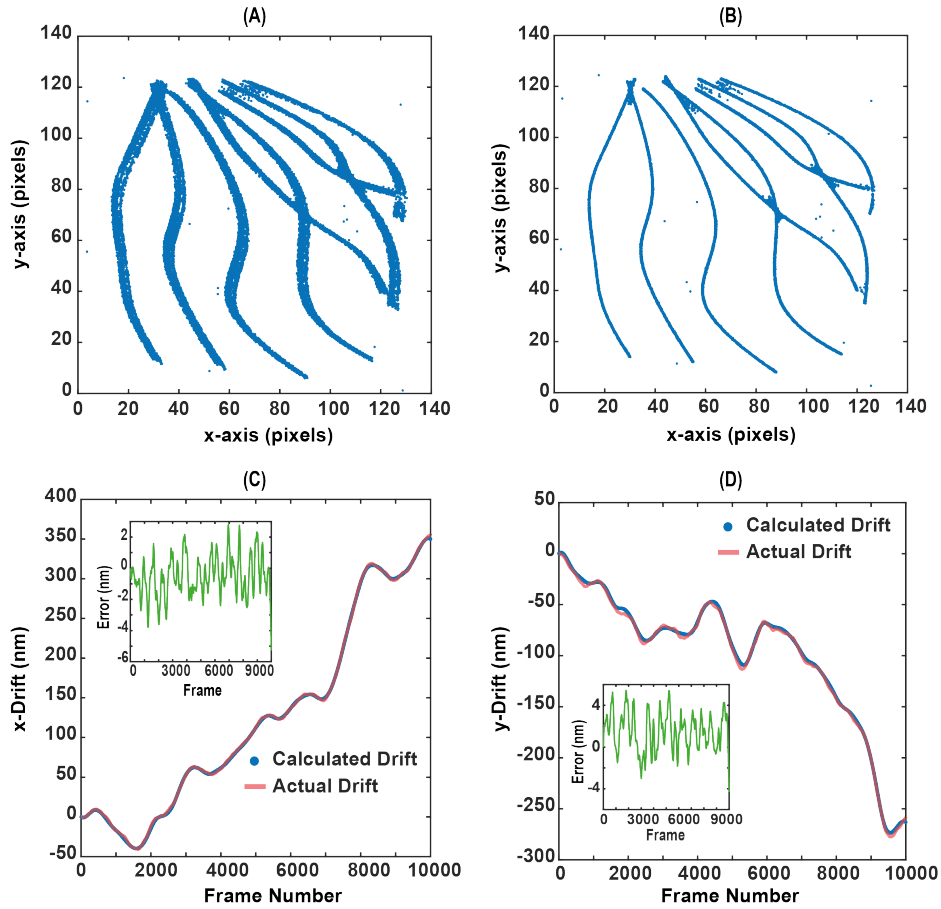
Fig. 4.6 Reconstructed images of tubulin fibres: (A) in the presence of drift and (B) after drift correction. Calculated drift, along the two lateral axes, is shown in (C) and (D).

The software was tested on simulated localisation microscopy images of tubulin fibres, obtained from [137] (a website containing simulated data to benchmark the performance of localisation algorithms). Fluorescent spots were localised in all the frames, using *WaveSM*, and a drift was added to the localised positions. Drift estimation was then carried out using the software discussed in Section 4.3.4.

The software generated low resolution images of the underlying structure, from multiple (temporal) subsets of the localisation data. The number of frames used to generate these images depended on the labelling density. In the simulations, at least 250 frames were needed to obtain a good estimate of the drift. The software used cross-correlations to calculate shifts between these low resolution images. Results of the analysis are shown in Figure 4.6. The software correctly identified the drift over all the frames with an error of less than 5 nm in both the lateral dimensions. This resulted in compact tubulin fibres compared to the ones affected by drift as shown in Figure 4.6A&B respectively.
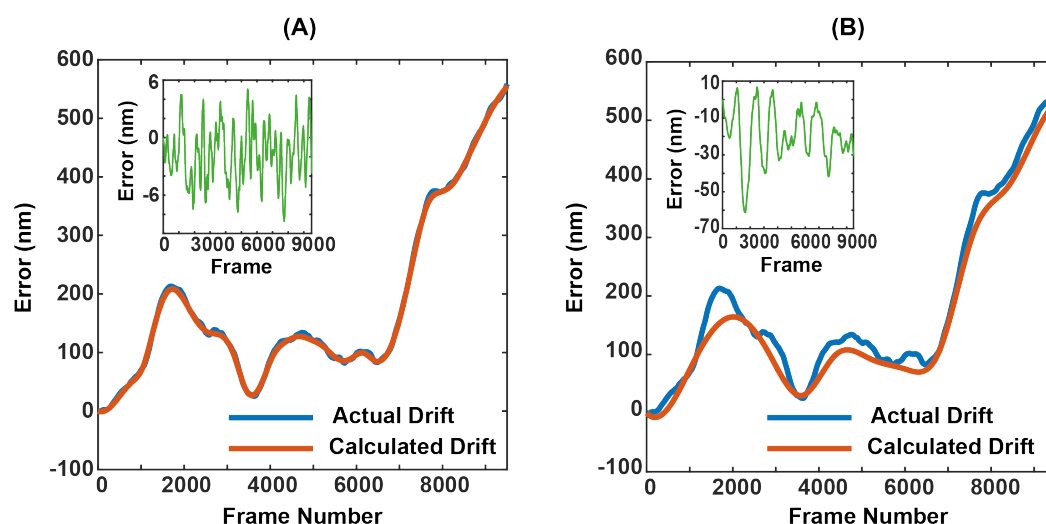
Fig. 4.7 Drift calculated by generating low resolution images from the localisations collected over (A) 250 frames and (B) 800 frames. For optimal performance of the software, drift needs to be negligible over the localisations used to generate the low resolution images. This was not true for (B), which resulted in errors of up to 70 nm.

We also tested the effect of the number of frames used to generate low resolution images on the drift estimation. As expected, with a fine temporal sampling the drift was better estimated, compared to when large number of frames were used. In the latter case, the average drift calculated over the entire subset resulted in under or over estimation of the drift for individual frames. For the best performance of the software, drift had to be negligible over the frames used to generate the low resolution images. Errors of up to 70 nm were observed when 800 frames were used, compared to less than 5 nm for 300 frames as shown in Figure 4.7. However, using too few frames could result in varying structures in low resolution images, leading to highly erroneous results as shown in Figure 4.8.

The above analysis shows that the drift correction software worked optimally when:

- all low resolution images had same structures
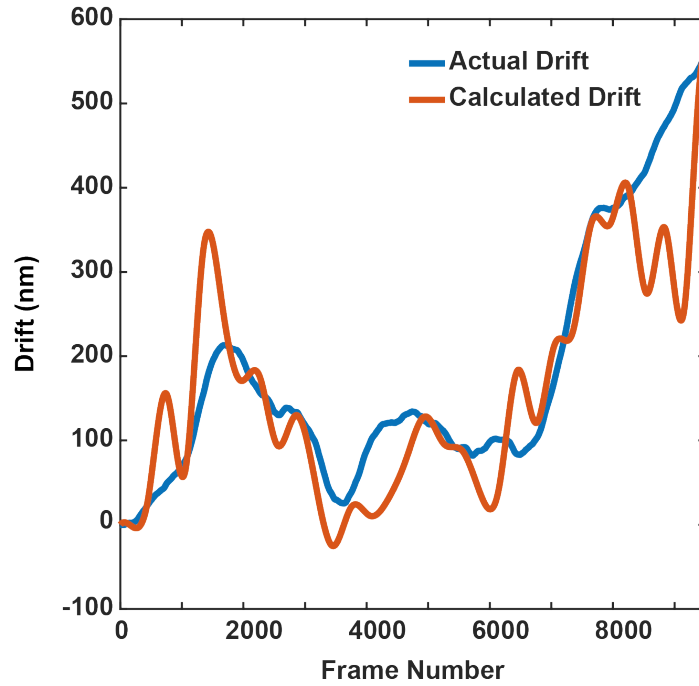
Fig. 4.8 Drift calculated from low resolution images with different structures. This happens if subsets of the localisation data, used to generate low resolution images, does not contain enough localisations to have same structures.

- drift was negligible over the frames used to generate these low resolution images

4.4.2 Characterisation of the Clustering Software

In this section, characterisation of the clustering software is discussed under different conditions. Gaussian clusters of various sizes (here, size corresponds to the standard deviation, σ, of the Gaussian) and with different number of points per cluster were generated in MATLAB. Cluster analysis was then carried out in R using the software discussed in Section 4.3.5

First, simulated clusters with large number of points ($N = 5000$) were analysed. Five data sets were generated for various cluster sizes and results of the analysis are shown in Figure 4.9. The figure was generated by calculating mean and standard deviation of cluster sizes obtained from multiple data sets having the same (theoretical) value of σ. The figure shows that the software extracted σ with reasonable accuracy. However, the error increased with an increase in σ e.g. it varied from below 5 nm to 17 nm for cluster sizes of 116 nm and 165 nm respectively. This is because analogous to the sampling requirement of continuous signals, more points are required to sample the underlying Gaussian distribution with increasing cluster size. This can also be seen from the inset of the figure, in which for a given N, larger errors are observed for $\sigma = 116$ nm compared to $\sigma = 58$ nm.

The above analysis shows that the software correctly identified the cluster sizes ranging from 40 nm to 165 nm. Moreover, the obtained precision was significantly better than the cluster sizes obtained from the experimental data.
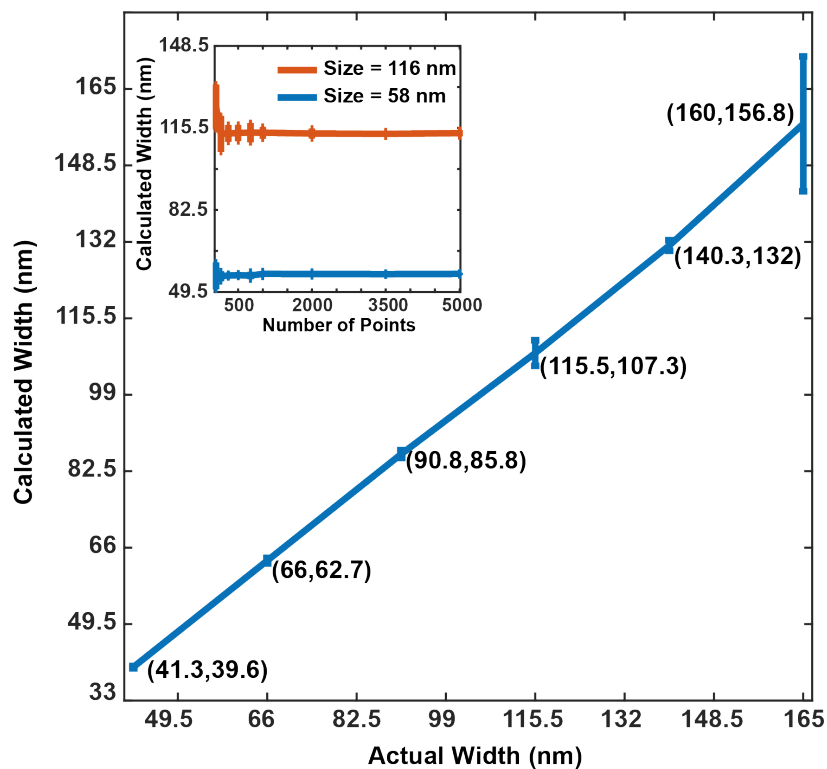
Fig. 4.9 Results for testing the clustering software on simulated data. The plot was generated from the mean and the standard deviation of the cluster sizes calculated for five data sets, simulated with the same cluster size. The inset shows results for testing the software for different number of points per cluster. For a same N, error increased with an increase in the cluster size.

4.5   Experimental Results

This section discusses the results of the localisation microscopy experiments carried out to study the structure of chromatin in primary spermatocytes of Drosophila. Reconstructed images are first analysed qualitatively. Afterwards, results from the application of the cluster analysis to the localisation data are presented.
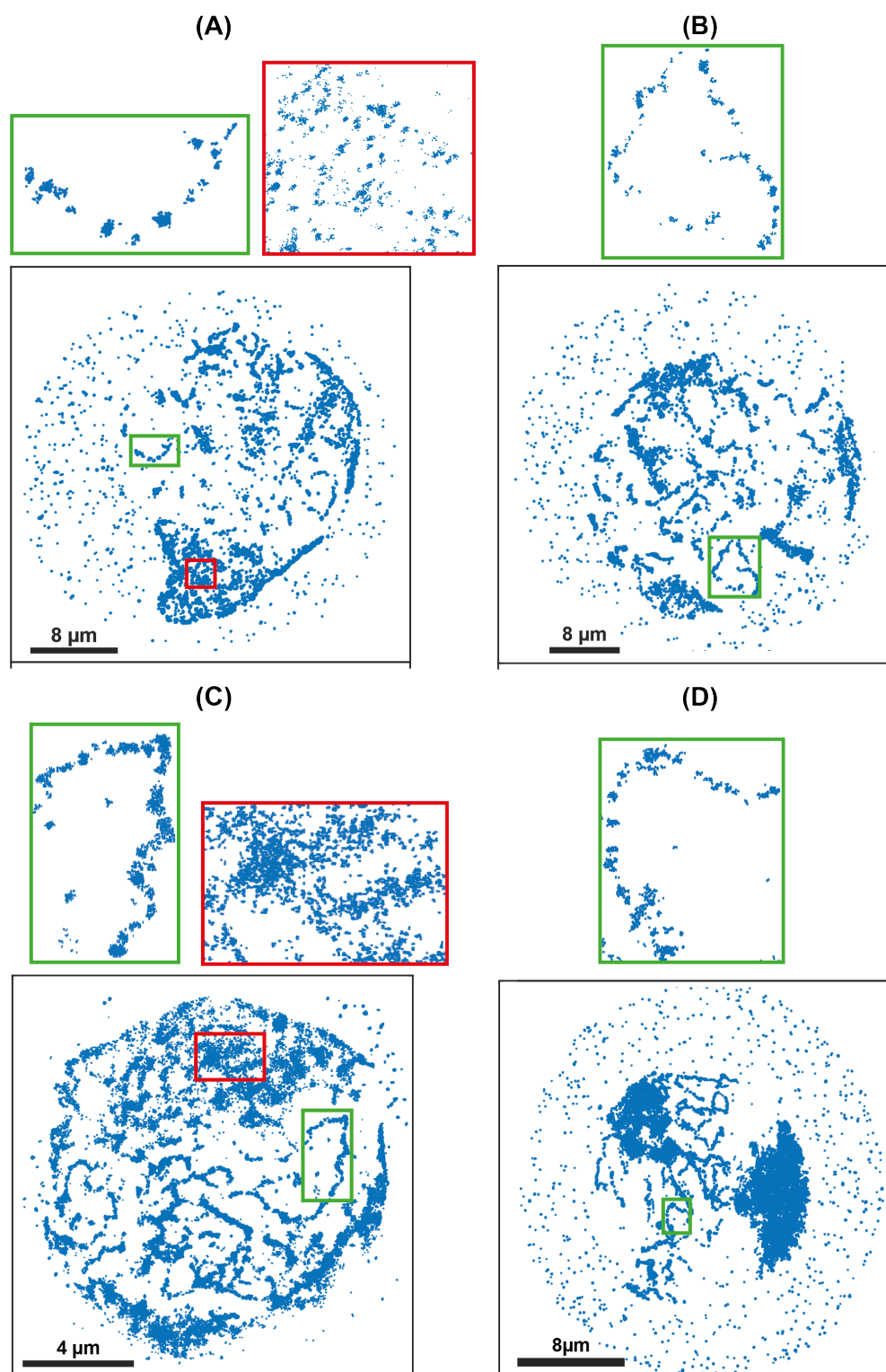
Fig. 4.10 Example reconstructed images from the localisation microscopy carried out by labelling histone molecules.
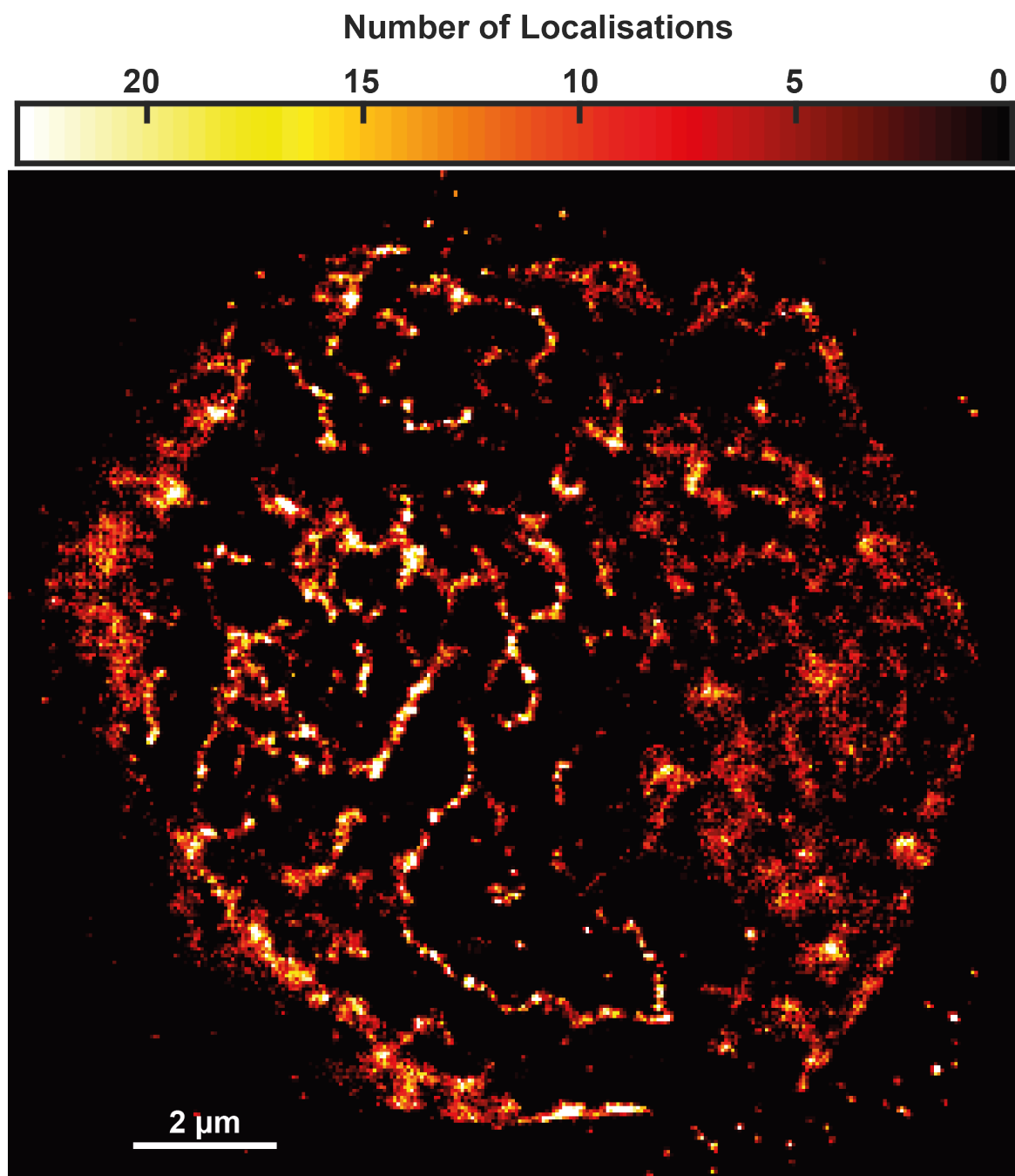
Fig. 4.11 An example density plot obtained from the localisation data. Here the bin size is 50 nm

4.5.1   Packaging of Chromatin

Raw localisation microscopy images were analysed using the *WaveSM* software for the localisation of fluorescent spots. Four representative, super-resolved images of nuclei are shown in Figure 4.10 along with an example density plot in Figure 4.11. In these images, the organisation of chromatin in the form of fibres can be seen at the centre of nuclei due to relatively *open* chromatin in their Y-loops. Moreover, these fibres did not exist in the form of *ribbons*, but were composed of regularly spaced clusters. This was interesting because Y-loops are a single transcription site within which such an organisation of dense and open chromatin fibres was not expected (regions with few localisation in between the clusters correspond to open chromatin fibres as discussed later in the chapter). The mechanism of cluster formation within a single gene is still a matter of research at the *White Lab*.

In chromosomes, due to dense packaging of chromatin, individual fibres were not identifiable. However, clusters were observed in these dense chromosomes as seen from the insets of Figure 4.10A&C. We hypothesise these clusters to be a result of the TAD organisation of the genome, as also suggested by earlier localisation microscopy experiments and genomic proximity assays [119, 125]. Since, histone molecules were labelled in the experiments, absence of localisations in between the clusters showed the existence of open chromatin fibres. Such regions could be associated with the presence of housekeeping and other active genes, a concept explored in the next section of the chapter.

Similar to the genomic techniques, cryo-electron microscopy also predicts the arrangement of chromatin into fibres [138] . However, the fibres are not always visualised in light microscopy due to densely packaged chromatin in majority of cell types. For example, [125] showed the existence of TADs in mammalian cells using single molecule imaging but their higher order arrangement into fibres was not identifiable. In an interesting approach, [139] used the information from genomic techniques (such as Hi-C) to find chromatin fibres and their three-dimensional arrangement in the dense point cloud obtained from localisation microscopy. Primary spermatocytes have relatively open chromatin, which allowed us to directly visualise the chromatin fibres and their constituent clusters. Moreover, the enormous Y-loops in these cells provided a convenient model to study the arrangement of chromatin within a gene.

The above discussion shows that the reconstructed images from our localisation microscopy experiments predicted the arrangement of chromatin into clusters, which were then organised in the form of fibres. Higher order chromatin structures were finally formed by the three-dimensional arrangement of these fibres.

4.5.2   Drift Analysis

Before performing the cluster analysis, mechanical drift of the stage, over the imaging time of a nucleus, was measured and corrected by using the method discussed in Section 4.3.5.
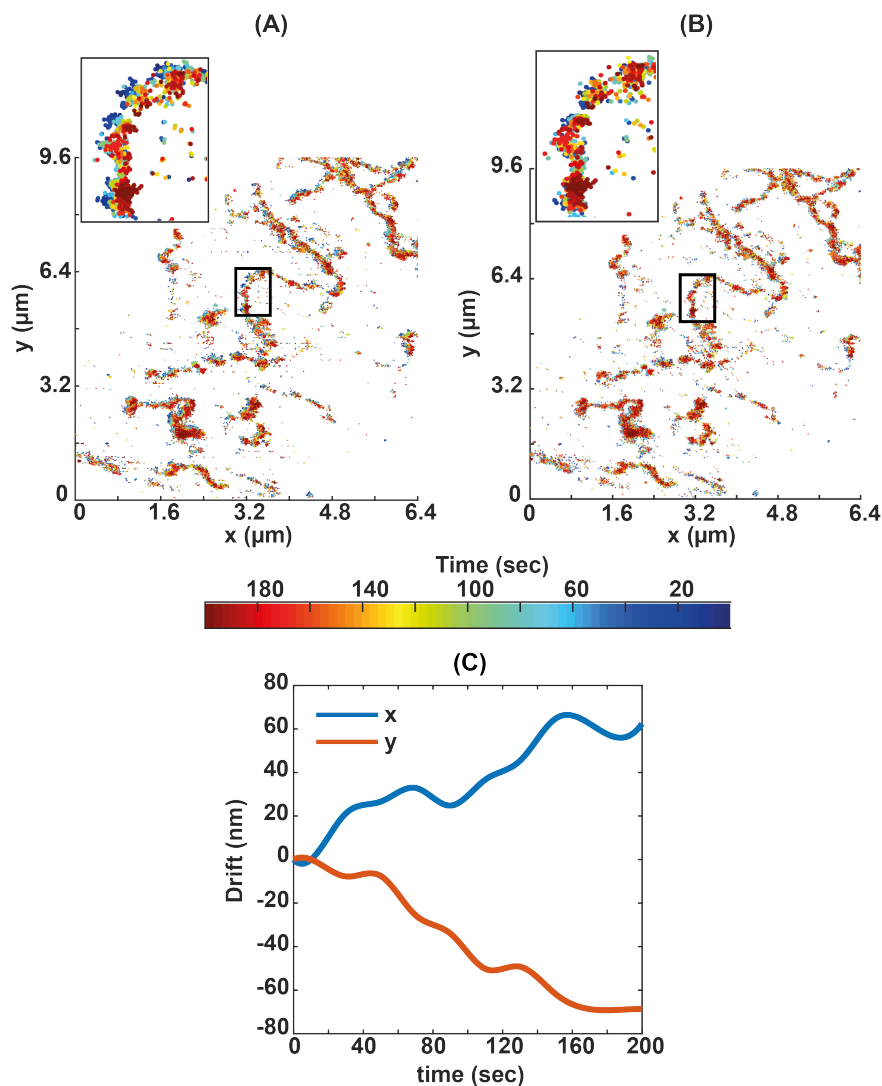
Fig. 4.12 Applying drift correction to the localisation microscopy data. (A) Localisation data before the drift correction. (B) Localisation data after the drift correction. (C) Drift in the two lateral axes, calculated using the drift correction software.

The drift was measured by cross-correlating low resolution images generated from the subsets of the localisation data collected over short time intervals. We found the algorithm to work optimally when the images had well defined structures. So, the analysis was carried out at the centre of nuclei as it contained chromatin fibres, similar to the ones shown in Figure 4.10. Due to the dense packaging of chromatin in chromosomes, such fibres or other

structures were not recognisable. Calculating shifts between images of such a dense region gave less accurate estimation of the drift compared to when Y-loops were used. For drift correction, a localisation data set was divided into intervals of 20 sec, and a bin size of 55 nm was used to generate low resolution images. These parameters were optimal for our experiments, as enough localisations were obtained per bin to accurately calculate cross-correlations. Moreover, the temporal resolution was enough to calculate drifts of up to tens of nanometres. An example drift is shown in Figure 4.12C. This drift of 80 nm over 200 sec can also be seen from the localisation data shown in Figure 4.12A, where localisations are coloured according to the time of their acquisition. Such a drift, if not corrected, could significantly affect the cluster analysis carried out to determine the size of chromatin domains. Figure 4.12B shows drift corrected data, in which localisations collected at different time points overlap.

It is important to note that the drift varied from sample to sample and over time. For example, a large movement of the stage was observed at the start of an experiment, which decreased over time. So, the localisation data acquired at a later time (after 20-30 min of not touching the stage) did not require drift correction because the drift in this case was close to the localisation precision. Consequently, it was important to calculate drift for each nucleus and its multiple temporal stacks separately (each temporal stack had $20,000$ frames, captured at an exposure time of 10 msec). The drift correction, wherever required, was applied to the localisation data before the cluster analysis.

4.5.3 Cluster Analysis

The next step in the data analysis pipeline was to determine the cluster sizes in different regions of the imaged nuclei. As per our hypothesis, clusters in the localisation data corresponded to the dense packaging of chromatin fibres. So, this analysis provided information about the low level packaging of chromatin in the primary spermatocytes of Drosophila.

Our clustering algorithm calculated the average cluster size over the region of interest and was dependent on the density of clusters (see Eq 4.6). Since, Y-loops and chromosomes had very different densities of chromatin fibres and contained intra and inter gene clusters respectively, they were analysed separately. Representative reconstructed images from these regions are shown in Figure 4.13A&B respectively along with the corresponding PCF curves in Figure 4.13C. Higher PCF values in the chromosome, compared to the Y-loops, was due to relatively higher localisation density in them. Theoretical PCF was then fitted to these curves under the assumption of Gaussian clusters in the data and results are shown in Figure 4.14. The data was collected from seven nuclei, extracted from multiple organisms.
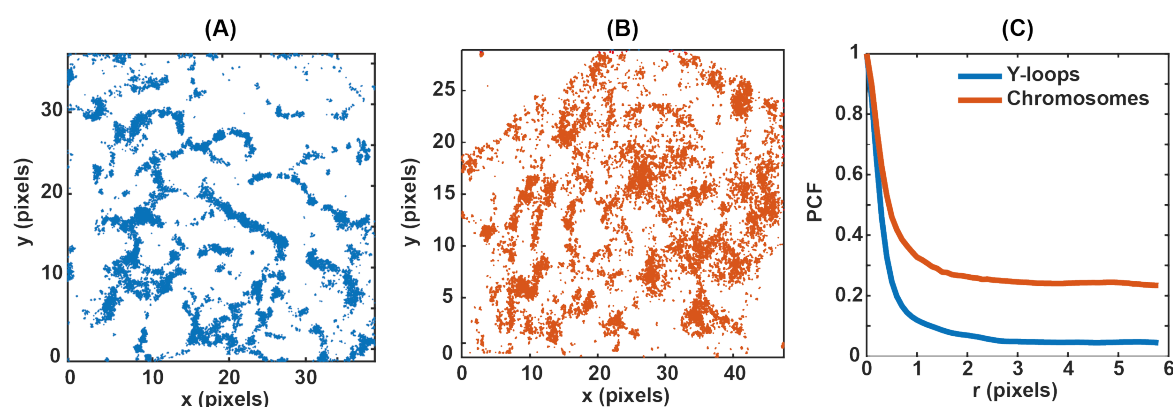
Fig. 4.13 Representative images of (A) Y-loops and (B) chromosomes. (C) PCF calculated for the data shown in (A) and (B). Here, the pixel size corresponds to 165 nm

We calculated an average cluster size of 90.8 nm and 113.9 nm in Y-loops and chromosomes respectively. These results matched closely to the TAD sizes reported in earlier localisation microscopy studies on chromatin architecture [125]. Although the average cluster size was quite similar in the two regions, clusters in chromosomes were found to be more variable in size. This was because of the variation in the density of chromatin (in chromosomes), depending on the axial position of the imaged cross-section of a nucleus. The chromatin was less dense near the edges of chromosomes, as seen from Figure 4.10A&D, where the image plane was close to the middle and edge of chromosomes respectively. The axial position of the plane affects the cluster analysis because high labelling density can lead to the overlap of neighbouring clusters, resulting in an apparent increase in the calculated cluster sizes.

4.5.4   Effect of Labelling Density on Reconstructed Images

Figures 4.15A-C show reconstructed images from different number of localisation. Similar structures were obtained from the first two stacks of 20,000 frames (each containing around 400,000 localisations), indicating the availability of enough localisations to resolve the entire labelled structure of chromatin. Significant photobleaching resulted in only 92,000 localisations in the third stack of 20,000 frames. Moreover, most of these localisations came from relatively dense regions of chromatin, indicating that if enough localisations are not acquired, results can be biased towards the dense regions of chromatin.

This bias due to labelling density can be explained by using the schematic in Figure 4.16. In the figure, two clusters, separated by a sub-diffraction distance, are linked by a thin chromatin fibre. At the start of our experiments, emissions from single fluorophores (within the clusters and the linking chromatin) will overlap. To resolve all the structures in the
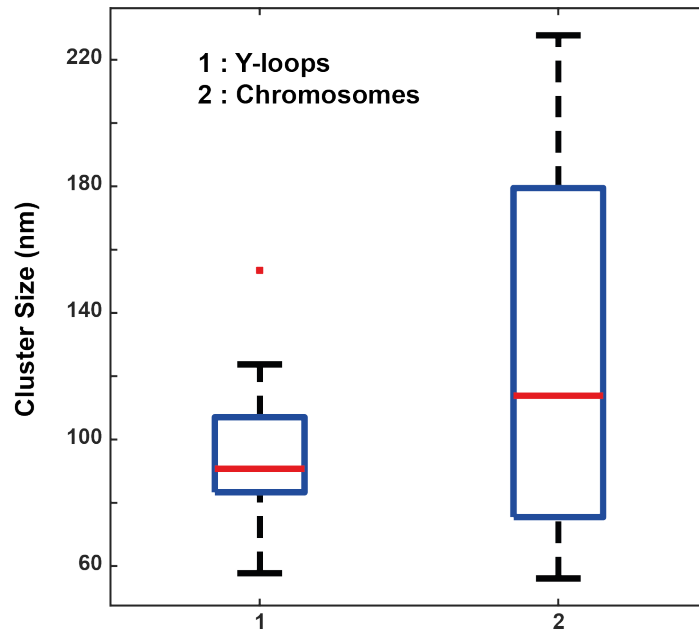
Fig. 4.14 Calculated cluster size in the chromosomes and the Y-loops using the PCF analysis. For the analysis, points were assumed to be normally distributed in the clusters.

FOV, photobleaching will have to be carried out to reach non overlapping emissions from single fluorophores. Since, clustered regions have much higher labelling density (than the linking region), most of the localisation would come from these regions. As discussed in Section 1.6, high number of localisations from densely labelled regions means that the number of localisations required to resolve all the structures in an image are much higher than the number obtained from the Nyquist sampling criterion (as more localisations come from densely labelled regions). [64] shows that even in the absence of background, sampling rate should at least be three times higher than the Nyquist rate to correctly sample a sinusoidal probability distribution. Tools similar to *Fourier Ring Correlation* can be used to calculate the resolution of a reconstructed image and its dependence on the number of localisations [140].

4.6   Dual-colour Experiments

Localisation microscopy results presented in the last section have shown that the chromatin in the primary spermatocytes of Drosophila is packaged into fibres, which then fold to form higher order structures. These fibres, instead of being continuous, are composed of chromatin domains. As our experiments were carried out by labelling histones, absence of localisations in-between the clusters shows the presence of open chromatin fibres. We hypothesise these

(A)

(B)

(C)
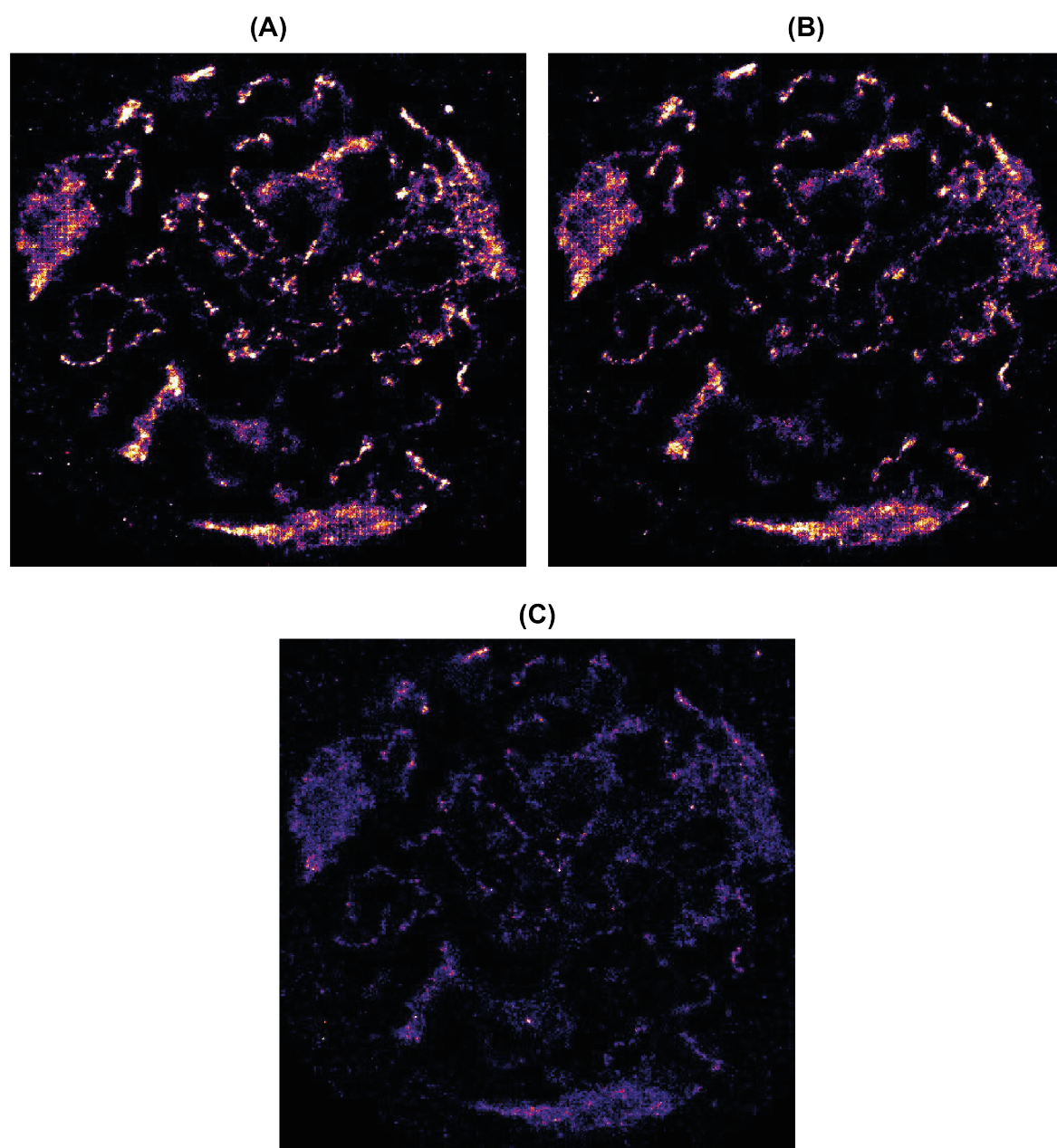
Fig. 4.15 Image reconstructed from (A) 1-20,000 frames, (B) 21,000-40,000 frames and (C)41,0000-60,0000 frames at an exposure time of 10 msec. The images were reconstructed from approximately 440,000, 390,000 and 92,000 localisations respectively (striping arte-facts in the chromosomes are due to high density of localisations in them).

regions to contain transcriptionally active regions of DNA because such an arrangement allows the protein complexes, required for transcription, to access the DNA. To study this in more detail, dual-colour localisation microscopy was carried out by labelling active RNA polymerase along with the histones. Active RNA polymerase molecules were labelled, by the

Linking Chromatin

Cluster 1   **Cluster 2**

d
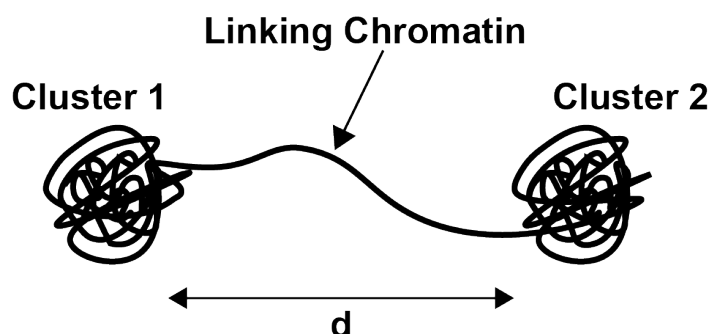
Fig. 4.16 A schematic showing the effect of labelling density on reconstructed images. Cluster 1 and Cluster 2 are separated by a sub-diffraction distance. If enough localisations are not captured (after photobleaching), the linking chromatin fibre would not be reconstructed completely.

White Lab, by using an antibody that recognised molecules with phosphorylation of Serine 2 in the C-terminal domain, which is a marker of the active RNA polymerase (in the rest of the chapter, RNA polymerase will refer to the *active RNA polymerase* molecules). Such a labelling allowed us to visualise chromatin architecture at the active transcription sites.

In this section, characterisation of our experimental setup for dual-colour imaging is discussed, followed by its application to image primary spermatocytes in Drosophila. .

4.6.1   Image Registration

Multi-colour imaging was carried out by using Hamamatsu (Flash 4.0) and Photometrics (Prime 95-B) cameras, installed on the Cairn TwinCam system (see Figure 4.1 for details of the experimental setup). Before analysing dual-colour localisation data, image registration was required to accurately superimpose images from the two cameras. This section discusses the required alignment of the microscope and the registration procedure for dual-colour imaging.

Dual-colour experiments required axial alignment of the cameras, so that the focal plane of the objective is imaged onto both. This was achieved by using 100 nm fluorescent beads as a test sample and imaging them in the presence of DHPSF. DHPSF allowed correction for small axial shifts between the cameras, which would have been difficult to detect using the conventional PSF of the microscope. Once the cameras were axially aligned, the lateral registration parameters were calculated by imaging fluorescent beads (after removing the phase mask). The beads were localised in frames captured on the two cameras, an example image of which is shown in Figure 4.17A. The figure shows that the output of the cameras
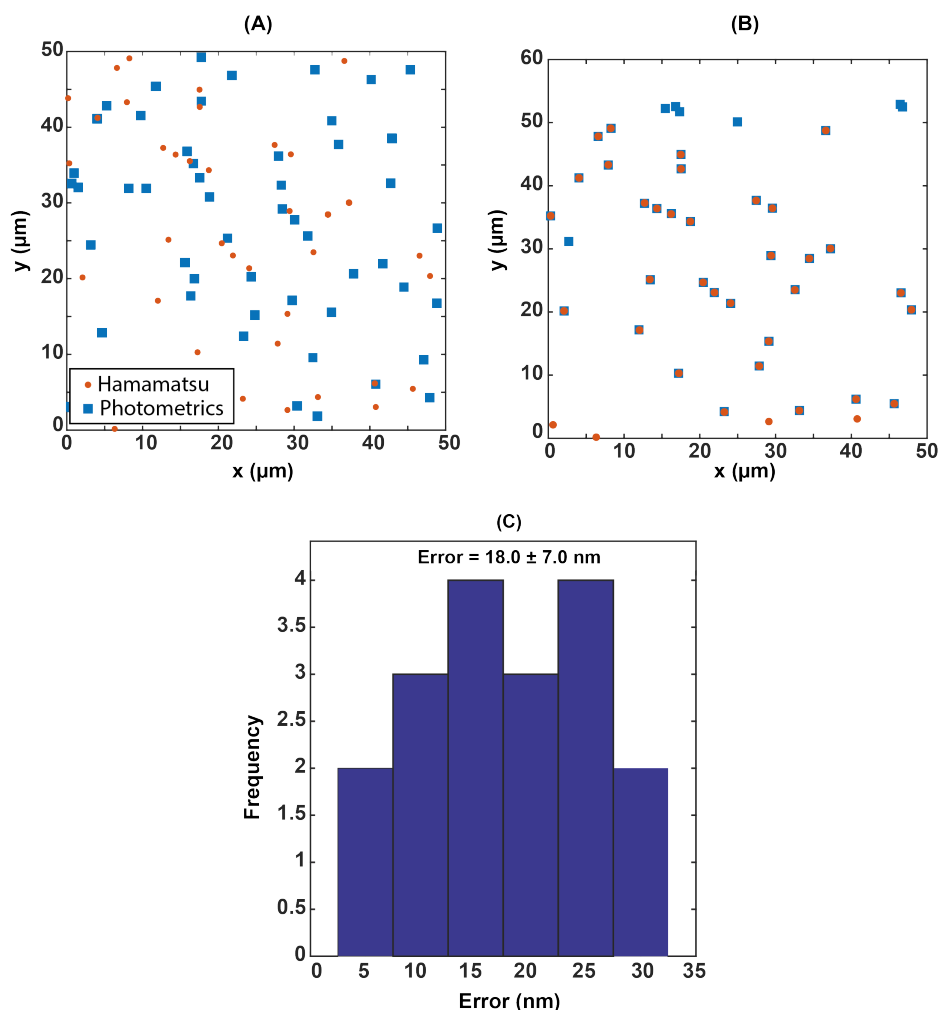
Fig. 4.17 Fluorescent beads localised in images obtained from the cameras used for dual-colour localisation microscopy: (A) without registration (B) with registration. For registration, *red* localisations were rotated (90° right) and flipped (vertically). Afterwards, an affine transform was calculated to minimise the average euclidean distance between the two data sets. (C) Residual error after applying the affine transform.

required a rotation (90° right) and flipping (vertical), before other registration parameters could be found.

After applying these steps, an affine transform was found between the two data sets. The transform not only allowed us to correct for translation, but also for shearing and scaling introduced in the alignment process. Affine transform was calculated in MATLAB, using the *lsqnonlin* optimisation function. Different parameters of the transform were optimised while minimising the mean squared distance between the positions of beads in the two data sets. The final error is shown in Figure 4.17C, along with the overlapped localisations in Figure 4.17B. We obtained a mean error of 18 nm over a 50 μm FOV. The error was calculated

from the Euclidean distance between positions of a bead in the two data sets, after applying the optimal affine transformation. The mean error was close to the theoretical localisation precision that could be achieved for the alexa dyes (568&647) and much smaller than the cluster sizes calculated in the last section.

Once the registration parameters were determined using fluorescent beads, they were were applied to the dual-colour localisation data obtained from the simultaneous imaging of histones and RNA polymerase.

4.6.2   Histone and RNA-polymerase Simultaneous Imaging
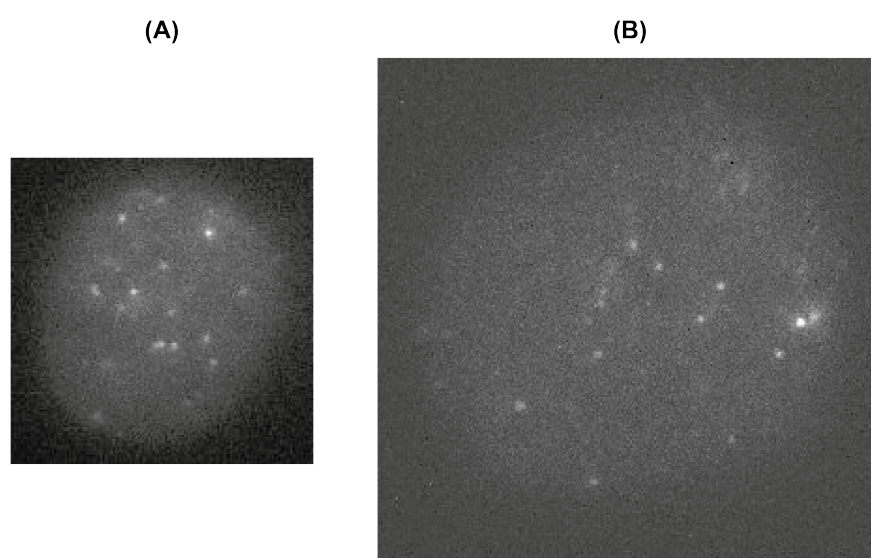
Fig. 4.18 Representative images from dual-colour localisation microscopy. Fluorescent spots correspond to (A) histones and (B) RNA polymerase. The size difference between the two images is due to the different pixel sizes of the two cameras (Hamamatsu: 97.5 nm, Photometrics: 165 nm).

For dual-colour localisation microscopy, histones and RNA polymerase were labelled with alexa-647 and alexa-568 respectively. We found the imaging buffer, discussed in Section 4.3.2, to be suitable for the simultaneous imaging of the two dyes. Example localisation microscopy images are shown in Figure 4.18 A&B (the size difference between the two images is due to different pixel sizes of the two cameras). Fluorescent spots, in such images, were localised by using the *WaveSM* software and registered by applying the method discussed in the last section. Localisations were then overlapped and results from two example nuclei are shown in Figure 4.19.

The figure shows that the RNA polymerase existed in the form of clusters in the nuclei. We estimated a cluster size of 42.9 ± 10.26 nm from five nuclei extracted from multiple
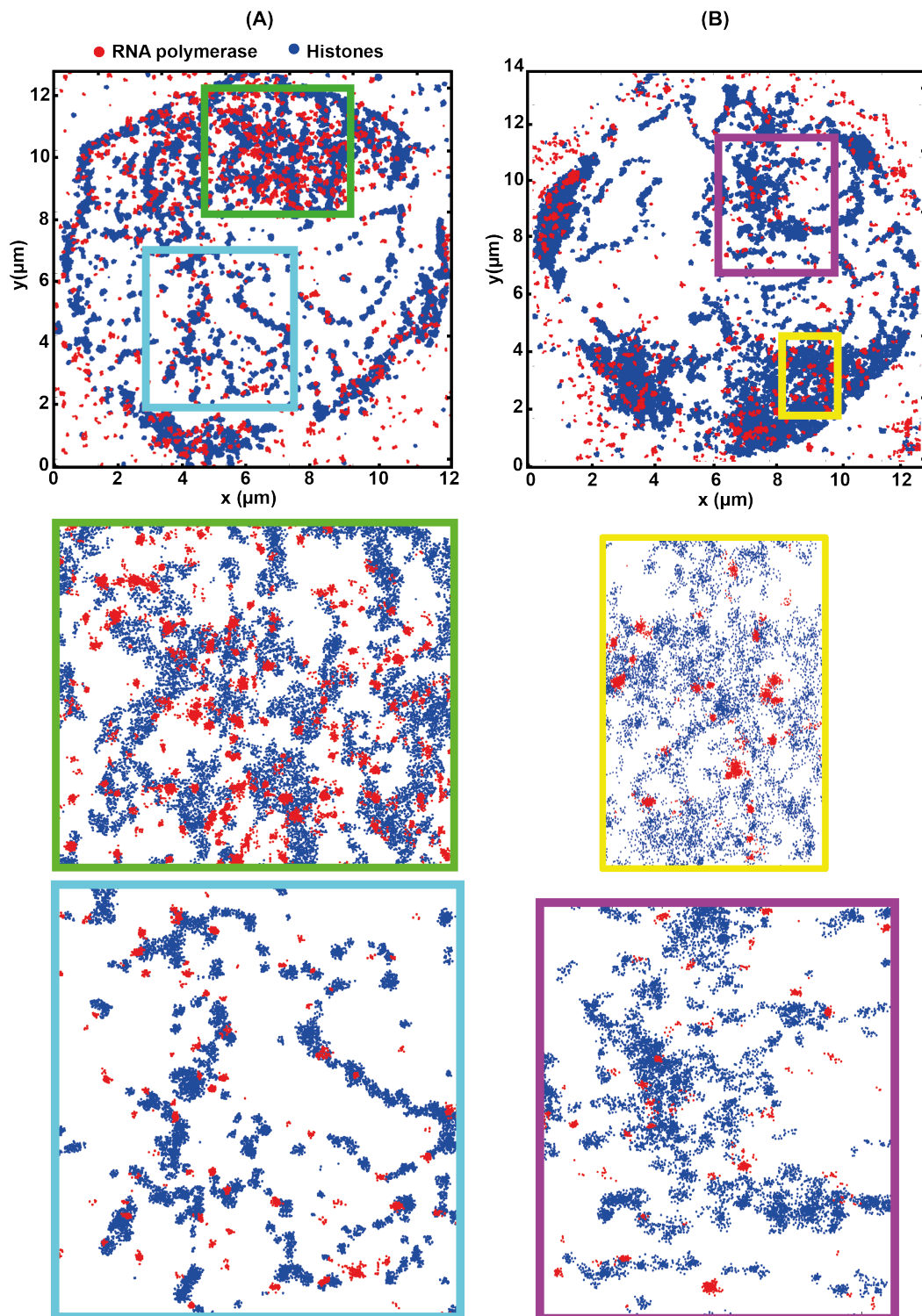
Fig. 4.19 Example reconstructed images from dual-colour localisation microscopy. Clusters of RNA polymerase occur more frequently in regions with a low density of histone molecules

organisms. The figure also shows that the clusters occurred more frequently in regions with low density of histone molecules. As these regions contain open chromatin fibres, such an arrangement of RNA polymerase supports the hypothesis that active genes are located in between the chromatin clusters.
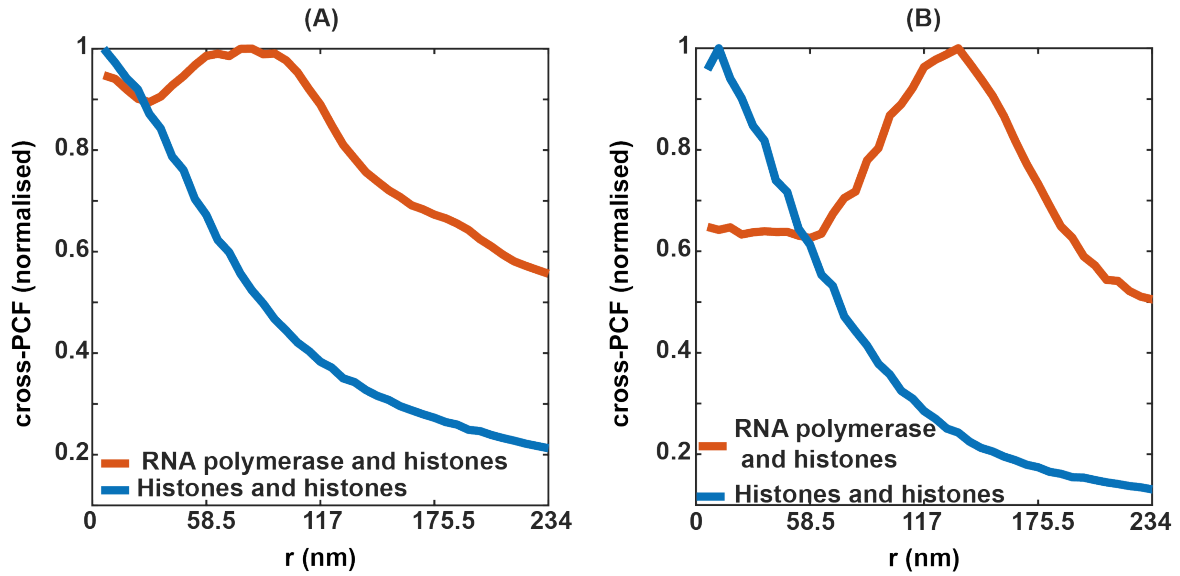
Fig. 4.20 (A)&(B) show cross-PCF analysis between the molecules of RNA polymerase and histones, carried out for data shown in Figure 4.18A&B respectively. *PCF* for histones is also included in figures. The cross-PCF peaks for $r > 0$, which shows a divergence between the two data sets.

Quantitative Analysis: To quantify the minimal distance between RNA polymerase and histone molecules, the PCF analysis was modified for dual-colour imaging. This was achieved by calculating the average number of *histone molecules* within a distance r from *molecules of RNA polymerase*. We will refer to this modified PCF as the cross point correlation function (cross-PCF).

Results of the analysis are shown in Figure 4.20A&B, which were obtained by calculating the cross-PCF over the nuclei shown in Figure 4.19A&B respectively. The figure also shows the PCF calculated for histone molecules (this is similar to the PCF used in single colour cluster analysis, see Figure 4.13C). As expected, the PCF peaked at $r \approx 0$ and decreased monotonically with increasing r. On the other hand, we found the cross-correlation functions to peak at $r > 0$, which indicates a divergence between the two data sets. The average distance between the histone and the RNA polymerase clusters was calculated by determining r, for which the cross-PCF peaks. It came out to be 76 nm and 146 nm for the data plotted in Figures 4.20A&B respectively.

The cross-PCF analysis supports the hypothesis that active transcription sites are located between the chromatin clusters. However, we found the average separation between the two data sets to be dependent on the density of chromatin in the imaged plane. In case of dense packaging, which happens when the imaged plane is located in the middle of chromosomes, the *apparent* separation between clusters of the two types was small. This can be because our analysis only considered the lateral positions of the three dimensional arrangement of clusters (the imaging depth was around 200 nm). And, for dense packaging of chromatin, the 2D projections of axially separated clusters were more likely to overlap.

4.7   Three-dimensional Imaging - Challenges

The discussion in this chapter have been based on two-dimensional localisation microscopy, in which a thin volume around the focal plane of the objective was imaged. In the discussed experiments, the volume was carefully chosen to contain both Y-loops and chromosomes (see Figure 4.10). Such an analysis gave great insights into the arrangement of chromatin in different parts of nuclei. A natural next step is to extend the super-resolution imaging to all three dimensions. Three-dimensional information is important because we found the chromatin structure to vary depending on the imaged volume e.g. the chromatin was denser in the middle of chromosome compared to its edges. Moreover, the cross-PCF analysis was sensitive to the structure of chromatin in the chosen volume. So, to super-resolve the complete regulatory architecture of chromatin, three-dimensional localisation microscopy is required.

We carried out initial experiments using DHPSF to extend the imaging depth of the microscope to over $3\,\mu$m. For such a PSF, it was challenging to achieve the optimal number of active molecules in the FOV. This was because of the size of the DHPSF, which is significantly larger (more than 6 times) than the size of the diffraction limited conventional PSF of the microscope. Moreover, it focuses light into two spots from an axial range of $3\,\mu$m to the image plane. So, to avoid overlapping emissions in the image plane, very few molecules could be active at any given time. The optimal density was achieved at the cost of significant photo-bleaching of the dye labelling histone molecules (alexa-647). An example of the reconstructed nucleus using the DHPSF is shown in Figure 4.21 along with the results from the two-dimensional microscopy of the same region. While Y-loops are clearly visible in the latter, not enough localisations were collected to correctly reconstruct the image using the DHPSF

This shows that further optimisations are required to carry out three-dimensional imaging in large and dense primary spermatocytes. A possible option could be to use a different dye,
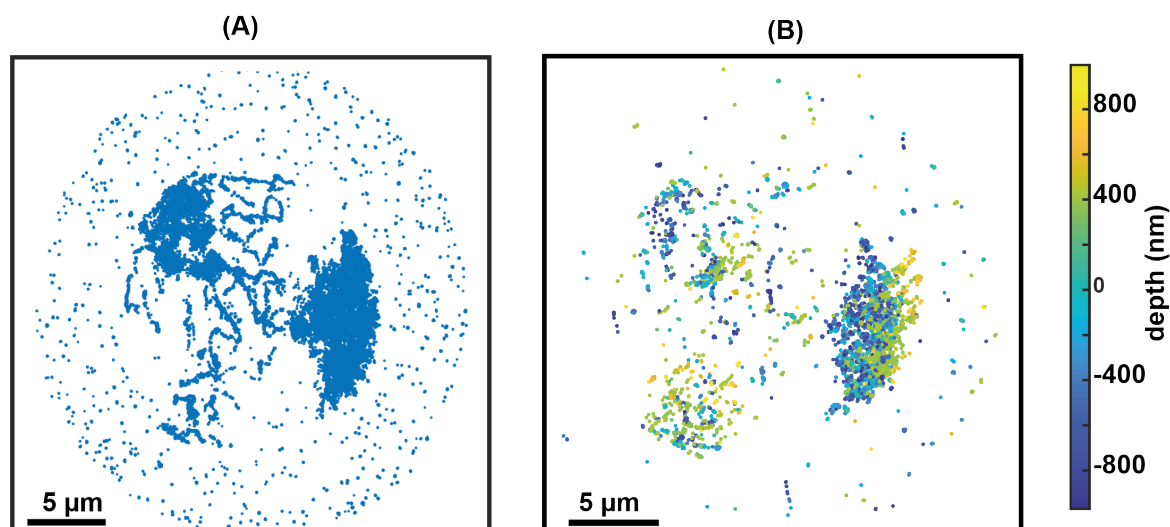
Fig. 4.21 Images reconstructed from localisation microscopy carried out using (A) conventional (2D) PSF and (B) DHPSF. Due to the large size of the DHPSF, optimal density of active molecules was achieved after significant photo-bleaching of the dye. Therefore, not enough localisations were collected for the reconstruction of the entire imaged volume. Here, the pixel size corresponds to 165 nm

such as DNA paint, which offers better control on its activation and emission [141]. Other PSF modification techniques such as light field could also be considered to further extend the DOF of the microscope. Lastly, imaging techniques that can provide three-dimensional imaging capability without some of the problems encountered in localisation microscopy, such as 3D-STED, could also be considered. All of these options are being explored by the *White Lab* in collaboration with CAIC.

4.8   Summary

In this chapter, the application our localisation microscope to study the chromatin architecture in primary spermatocytes of Drosophila was discussed. Imaging conditions and the subsequent data analysis pipeline was optimised to super-resolve features with different densities of the labelling dye. Mechanical drift in the stage was corrected by calculating shifts between low resolution images of a nucleus, reconstructed from the localisation data captured at different time points. We modelled the localisation data as a spatial point process to detect clusters in the data and to quantify their characteristics. Drift correction and clustering software were tested on synthetic data before their application to the experimental data. Our results showed the chromatin to be organised in the form of fibres, which were composed of chromatin clusters.

To study the nature of DNA between the clusters, dual-colour localisation microscopy was carried out by labelling active RNA polymerase along with the histones. This required characterisation of the experimental setup and finding optimal affine transform between images captured on different cameras. Our dual-colour analysis supported the hypothesis that the DNA, in between the chromatin clusters, contain transcriptionally active genes. This was shown both qualitatively, by overlapping localisations from histones and RNA polymerase, and quantitatively, through the cross-PCF analysis between the two data sets. Finally, three-dimensional localisation microscopy using the DHPSF was also discussed. We highlighted the potential of the technique and existing challenges in its application to study the chromatin architecture.

4.9   Contributions

The microscope used for the experiments was designed and developed by me with inputs from Martin Lenz and Kevin O'Holleran. I also optimised the imaging conditions and carried out the experiments with the help from Rob White (from the *White Lab*). I also carried out simulations and experimental data analysis, discussed in the chapter, with inputs from Leila Muresan and Kevin O'Holleran. Rob White and I optimised the composition of the imaging buffer for the experiments. Samples, used in the project, were prepared and labelled by Rob White, who also led the biological interpretation of the data.

4.10   Materials and Methods

Sample Preparation

The *White lab* used the following procedures to extract cells from Drosophila testes, and their subsequent labelling.

Cell Extraction

Drosophila testes (from 10-20 flies) were dissected in ice-cold PBS, treated with collagenase (5 mg/mL; Sigma) for 5 min and cells (primary spermatocytes) were released by gentle pipetting. For fixing, cells were treated with 4% formaldehyde (prepared in PBS) and incubated for 20 min. Cells were then washed with PBS/0.01% Triton X-100 and filtered using 50 μm filter. They were then resuspended in 10μL PBS/0.01% and adhered to a glass bottom dish by slowly releasing them at the bottom of the dish, containing PBS, using a pipette.

Labelling

: The cells were blocked for 2 hours in a solution containing PBS/0.5%, WBR/0.5% and Triton X-100 (WBR is Roche Western Blot Blocking Reagent). They were then incubated in primary antibodies i.e. MabE71 Mouse anti-Histone (1 : 1000 in PBS/0.5% WBR; Millipore) and 193468 Rabbit anti-RNAPol (1 : 200 in PBS/0.5% WBR; AbCam). The Cells were then washed with PBS/0.1% Tween-20).

Solution containing secondary antibodies i.e. anti-mouse IgG conjugated with alexa-647 (1 : 1000 in PBS/0.5% WBR; Invitrogen) and anti-Rabbit IgG conjugated with alexa-568 (1 : 1000 in PBS/0.5% WBR; Invitrogen), was added to the cells and they were incubated for 1.5 *hours*. The cells were washed with PBS/0.1% Tween-20 before fixation with 4% formaldehyde (prepared in PBS) for 20 *min*. Lastly cells were washed with PBS and stored at 4°C.

Imaging Buffer

After repetitive iterations, we found the following buffer composition to work optimally for both alexa-647 and alexa-568, and their simultaneous imaging.

- Glucose 50 mg/ml

- Catalase 45 μg/ml

- Glucose Oxidase $0.8\,\text{mg/ml}$

- MEA (Cysteamine) $0.77\,\text{mg/ml}$

- TRIS-HCl, pH8, $50\,\text{mM}$

- NaCl $10\,\text{mM}$

Preparation of the Buffer

The following stock solutions were prepared before making the final solution:

- **10X TBS**: Prepared by mixing $5\,\text{mL}$ of $1\,\text{M}$ TRIS-HCl (pH8), $1\,\text{mL}$ of $1\,\text{M}$ NaCl and $4\,\text{mL}$ of double distilled wated

- **100X MEA**: $77\,\text{mg}$ of MEA (Cysteamine, Sigma 30070-10G) in $1\,\text{mL}$ of double distilled water

- **10X Glucose Oxidase**: $8\,\text{mg}$ of Glucose Oxidase (Sigma G7141) in $1\,\text{mL}$ of TBS ($100\,\mu\text{L}$ 10X TBS $+$ $900\mu\text{L}$ double distilled water)

- **2X Glucose**: $1\,\text{g}$ of Glucose (Sigma G8270) in $10\,\text{mL}$ of double distilled water

- **10X Catalase**: $10\,\mu\text{L}$ of Catalase in $1\,m\text{L}$ of TBS ($100\,\mu\text{L}$ 10X TBS $+$ $900\mu\text{L}$ double distilled water)

  The final solution was made by mixing 10X TBS ($1\,\text{mL}$), 2X Gluxose ($5\,\text{mL}$), 10X Catalase ($1\,\text{mL}$) and 100X MEA ($100\,\mu\text{L}$) in $1.9\,\text{mL}$ of double distilled water. Finally, $1\,\text{mL}$ of 10X Glucose Oxidase was added to the prepared solution just before imaging.

Chapter 5

Light Field Imaging for Localisation Based Super-resolution Microscopy

5.1 Introduction

In the thesis so far, the sub-diffraction limit resolution achieved through localisation microscopy is used to study dynamics and structures at the nanoscopic scale. However, imaging was restricted to a thin volume around the focal plane, due to the narrow DOF of the conventional PSF of the microscope and its symmetry around the focal plane. Commonly used three-dimensional localisation microscopy techniques, such as astigmatism, DHPSF and bi-plane imaging extend the DOF to 1-4 μm, which is still significantly smaller than the diameter of nuclei discussed in the thesis. Hence, axial scanning would be required to map out the complete three-dimensional structure of such nuclei using these techniques. Phase masks based on Fisher information (as discussed in Chapter 1) can provide larger DOFs, but have complicated fitting procedures and varying shapes depending on the axial range they are optimised for. In this chapter we propose the use of light field imaging to overcome some of the shortcomings of the existing three-dimensional localisation microscopy techniques. We use the concept of parallax between perspective/angular views of an emitter to calculate its three-dimensional position. Parallax is not a new concept, and has been applied to obtain axial information in localisation microscopy by splitting light in the BFP of the objective (see Section 1.5.2). However existing implementations of the method are limited to $\sim 2\,\mu$m DOF, due to the availability of only two angular views of the sample. Here we use a lenslet array to capture significantly more angular views and extend the DOF to over $20\,\mu$m with high localisation precision in all three spatial dimensions.

To the best of our knowledge light field imaging has not been previously applied to the localisation microscopy and the existing reconstruction software are not optimised for the localisation of point emitters. This chapter explains the origin of three-dimensional information in light field imaging and proposes an image analysis pipeline to localise point emitters with high precision and accuracy over a large DOF. A prototype system, implemented with an off-the-shelf lenslet array, to test the proposed localisation procedure is also discussed. We show the capability of light field microscopy to localise fluorescent beads with sub-diffraction precision. Moreover, limitations of the prototype system and optimisations required to localise single molecules over the entire volume of a cell are also discussed.

5.1.1 Chapter Description

The chapter first discusses the origin of the three-dimensional information in light field imaging due to the mixing of spatial and frequency domains in the image plane. Afterwards, a method to exploit this information, by placing a lenslet array in the image plane, to extend the DOF in localisation microscopy is discussed. The method is based on calculating disparity between images of an emitter in multiple perspective views. The proposed image analysis pipeline is first tested on simulated data before its application to characterise and calibrate the microscope using fluorescent beads. The chapter ends with a discussion on the potential of the technique to detect single molecule emissions in labelled cells.

5.1.2 Published Work

The discussion and results presented in this chapter are also available on bioRxiv [142]. At the time of writing of this thesis, the manuscript is being modified for submission to *Optics Express* (or a similar journal).

5.2 Light Field Imaging and Three-dimensional Information

This section covers the basics of light field imaging and its application to extend the DOF in fluorescence microscopy. Presence of both angular and spatial information in raw light field images is discussed along with a method to generate multiple perspective views of an object from these images. Use of these views to calculate the three-dimensional position of the object is also discussed.

5.2.1 Capturing Angular Information

Localisation microscopy achieves a sub-diffraction resolution by the stochastic activation of a sparse subset of fluorophores in the FOV. In the absence of aberrations, emitted light rays from the fluorophores in the imaged volume overlap in the BFP. The rays are then focused to diffraction limited spots after the tube lens, which correspond to the images of single fluorophores. For an emitter in the focal plane of the objective, the image is formed in the image plane of the microscope. From the point of view of geometrical optics, this means that all the rays in the BFP (from that emitter) are focused to a point in the image plane as shown in Figure 5.2B. If, for such an emitter, the position of light rays in the image plane, (x, y), is plotted as a function of their position in the BFP, (u, v), a vertical line is obtained. This shows the focusing of all the light rays, irrespective of their position in the BFP, to a point in the image plane. However, the image of an emitter outside the focal plane of the objective is axially shifted from the image plane as shown in Figure 5.2 A&C. In such a case, the position of the lights rays in the image plane depends on their position in the BFP, resulting in the mixing of spatial and frequency domains in the image plane. So, the (x, y) vs (u, v) plot for such an emitter is a tilted line, the gradient of which depends on the axial position of the emitter in the imaged volume, relative to the object plane [143]. Light field microscopy exploits this mixing of spatial and frequency domains to capture the three-dimensional information about the object.

In light field microscopy, a lenslet array is placed in the image plane of the microscope and the camera captures the focal plane of the array [144]. When an emitter is in the object plane (focal plane of the objective), its image is formed at a μ-lens. Result is the illumination of all the pixels behind the lens as shown in Figure 5.2 B. However, for emitters outside the focal plane of the objective, the emitted light covers multiple μ-lenses. In such a situation, the position of illuminated pixels behind a μ-lens is dependent on the angle of incidence of the light rays on the lens. For example when the image of an emitter is formed in front of the MLA, (Figures 5.2A), top and bottom pixels behind lenses 1 and -1 are illuminated respectively. On the other hand when the image is formed behind the MLA (Figures 5.2C), this is reversed. So, depending on the axial position of the emitter, different pixels behind different μ-lenses are illuminated [145, 146]. This information can be used to infer the three-dimensional position of an emitter from light field images [143, 145, 147, 148] and will be the focus of the rest of this chapter.
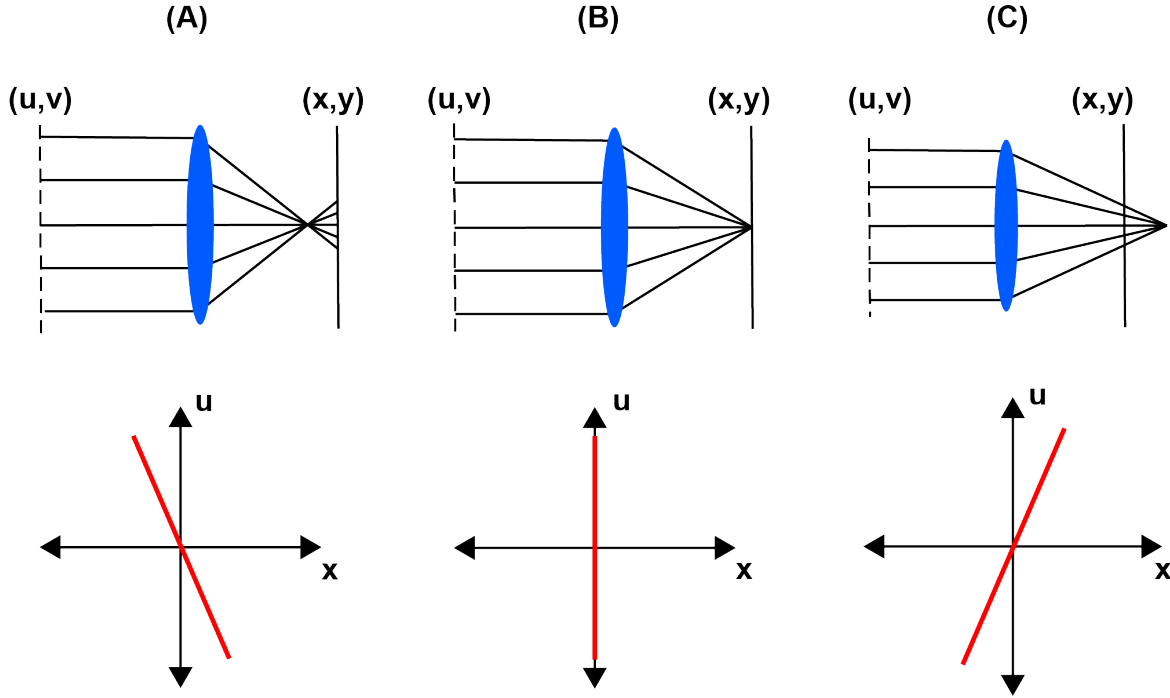
Fig. 5.1 Position of light rays in the image plane,(x,y), as a function of their position in the BFP of the objective, (u,v), when an emitter is (B) in the object plane and (A)&(C) outside the object plane. The bottom row contains x vs u plots for images in A-C. Mixing of spatial and frequency information in the image plane can be used to calculate the three-dimensional position of an object.

5.2.2   Different *'Views'* in Light Field

An example image captured on a light field microscope is shown in Figure 5.3 (taken from the Stanford light field image archive). The figure shows that the image consists of signal captured behind multiple μ-lenses. Lenses perform spatial sampling of the object and a low resolution image of it can be obtained by summing all the pixels behind a μ-lens. Such an image, with the pixel size equal to the array pitch, is simply a low resolution version of the one obtained by placing the camera in the image plane i.e. in the absence of the lenslet array. The latter, though having higher lateral resolution does not contain any depth information about the object. On the other hand, a light field image contains both spatial and angular information about the object, which can be used to determine its three-dimensional position.

In a light field imaging system, spatial (angular) frequencies are mapped to the focal plane of each μ-lens i.e. pixels behind a μ-lens contain spatial frequency content of the beam segment incident on that μ-lens. Low and high frequency information is captured close to the centre of the μ-lens and away from it respectively. This can be explained by imaging a single spatial frequency, (u_o, v_o), from the BFP of the objective to a camera placed in the
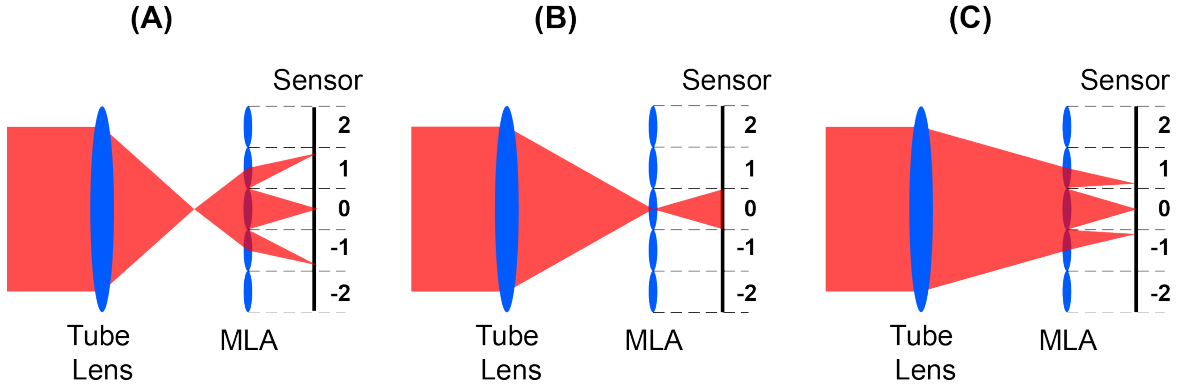
Fig. 5.2 (B) For an emitter in the object plane, all the pixels behind a single μ-lens are illuminated. (A)&(C) For emitters outside the object plane, beam is spread over multiple μ-lenses. These lenses sample the beam and focus it at different positions in their focal plane, depending on the local phase gradient of the beam.

focal plane of the lenslet array. In such a situation the electric field in the image plane of the microscope, $E(x,y)$, will be:

$$
\begin{aligned}
E(x,y) &= A\mathscr{F}\left(\delta(u-u_o, v-v_o)\right)D(x,y) \\
E(x,y) &= AD(x,y)exp(i(u_ox+v_oy))
\end{aligned}
\tag{5.1}
$$

here, $\mathscr{F}$ is the Fourier transform operation, $D(x,y)$ is the aperture of the tube lens and A is the normalisation factor. So, the electric field in the image plane is a circle of uniform magnitude with a linear phase, the gradient of which depends on the spatial frequency (u_o, v_o). Such a beam is sampled by multiple lenses in the lenslet array and since each lens *'sees'* the same phase tilt, pixels at the same position behind all the μ-lenses are illuminated as shown in Figure 5.4A-C. From this it can be concluded that each pixel behind a μ-lens corresponds to a different spatial frequency. Consequently, an image generated by extracting the same pixel from all the μ-lenses, in the lenslet array, contains information specific to a single spatial/angular frequency (in reality each pixel captures a range of spatial frequencies depending on its size).

$M \times N$ such images can be generated from a raw light field image, where M and N are the number of pixels along the horizontal and the vertical directions behind a μ-lens respectively. These images contain specific angular information about the object and are equivalent to imaging the object using $M \times N$ pinhole cameras placed at various angles around the sample (as in the object plane, spatial frequencies correspond to the angles of the emitted rays with the optical axis). So, these images are also called the *perspective views* or the *sub-aperture views* (as they sample the BFP of the objective) [143, 145, 149]. See [150] for a discussion
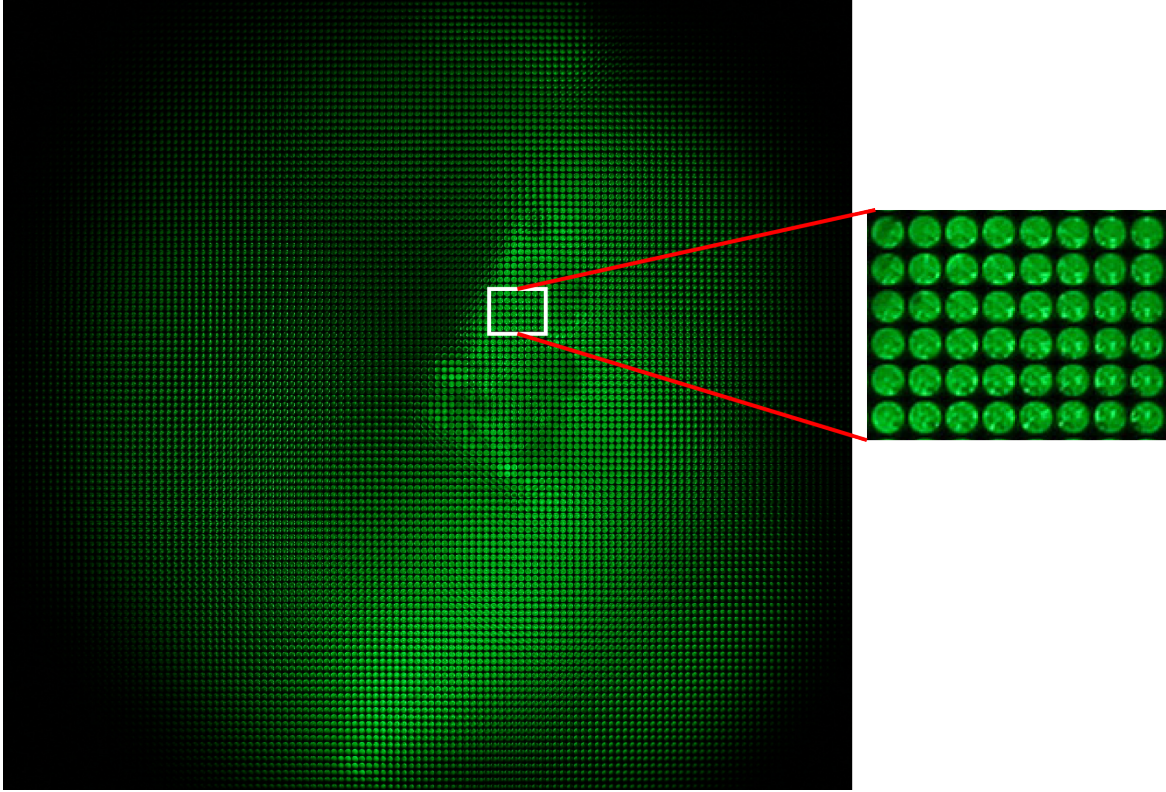
Fig. 5.3 An example light field microscopy image obtained from the Stanford light field image archive.

on the relationship between such an arrangement of pinhole cameras around the object, and the sub-aperture views generated from a light field image.

Mathematically, a sub-aperture view can be obtained from a raw light field image using the following equation:

$$s_{u_o,v_o}(p_x,p_y) = I(u_o + (p_x - 1)N, v_o + (p_y - 1)M) \tag{5.2}$$

here, $s_{u_o,v_o}(p_x,p_y)$ is a sub-aperture view formed by extracting (u_o,v_o) pixel from all the μ-lenses and (p_x,p_y) is the coordinate system of the sub-aperture view.

An important conclusion that can be drawn from the above discussion is that the light field microscopy provides axial information at the cost of lateral resolution. This is because for a given pixels size, using small μ-lenses gives higher lateral resolution but fewer angular samples resulting in the loss of axial resolution. On the other hand, using large μ-lenses gives more angular samples but lateral resolution deteriorates in this case.
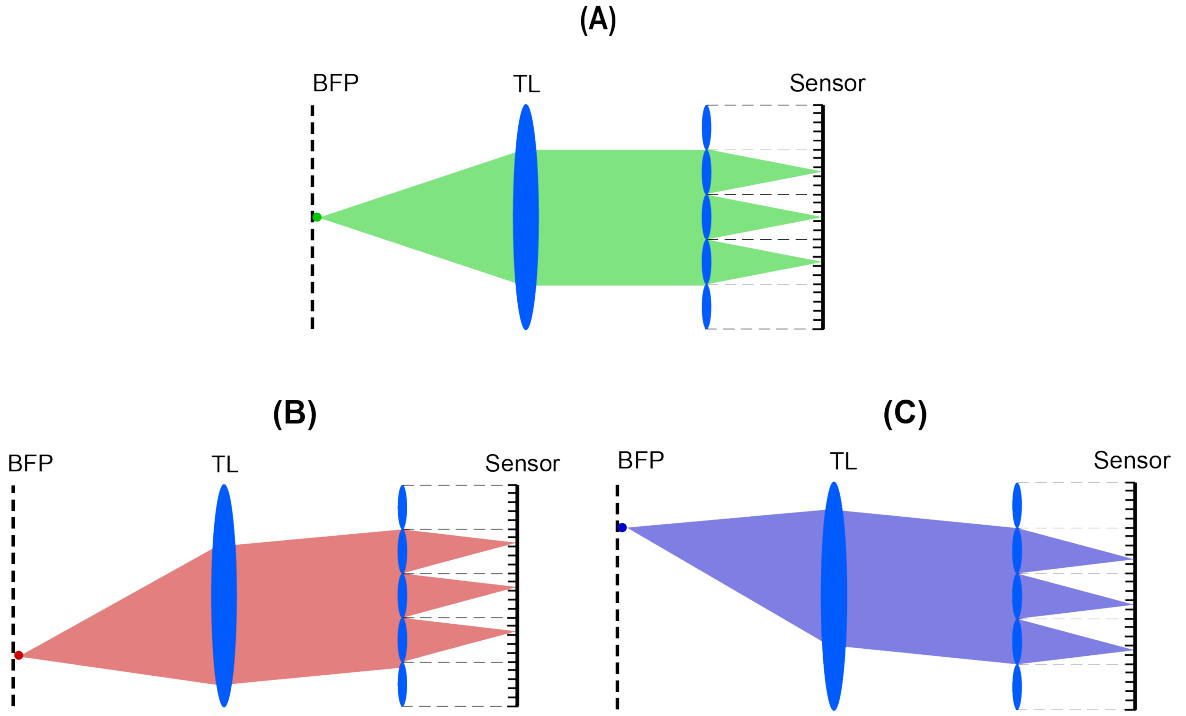
Fig. 5.4 In our experimental configuration of the light field microscope, spatial frequencies were mapped to the focal plane of each μ-lens. Low and high frequency information was captured by the pixels near the centre of the μ-lens and away from it respectively

5.3 Light Field Super-resolution Microscopy

In the last section, it was shown that the light field imaging combines spatial and angular information by using a lenslet array, to capture the three-dimensional information about an object. The technique can be applied to increase the DOF of localisation based super-resolution microscopy, the mechanism of which is discussed in this section.

If $E(x,y)$ is the electric field in the image plane, the field in the focal plane of a μ-lens, $E(u',v')$, is given as [151]:

$$E(u',v') = \frac{exp\left(\frac{ik}{2f}(u'^2 + v'^2)\right)}{i\lambda f_\mu}\mathscr{F}(E(x,y)d(x,y)) \qquad (5.3)$$

here, λ is wavelength of light, $k = 2\pi/\lambda$ and f_μ and $d(x,y)$ are the focal length and the aperture of the μ-lens. In light field imaging, the camera captures the focal plane of the lenslet array, so the phase term in Eq. 5.3 can be ignored.

For an emitter in the object plane, the image (diffraction limited spot) is formed at a μ-lens of the lenslet array. According to Eq 5.3 this results in the illumination of all the

(A)   **(B)**   **(C)**

(D)

Pixels behind μ-lenses   Reconstructed Views
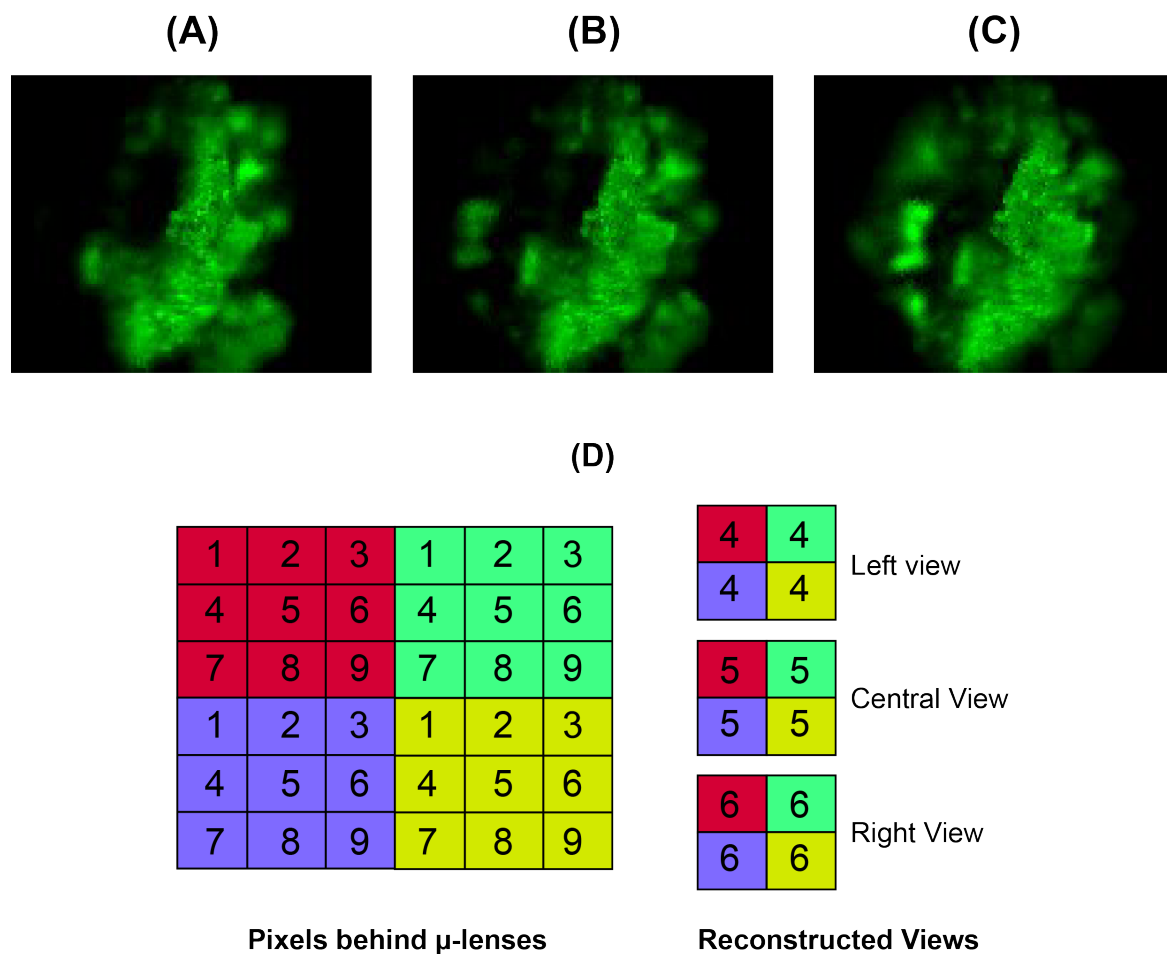
Fig. 5.5 (A)-(C) left, central and right sub-aperture views of the light field image shown in Figure 5.3. (D) Generation of sub-aperture views by extracting the same pixel from all the μ-lenses in the lenslet array.

pixels behind that lens. In sub-aperture view configuration, where each *view* is generated by taking the same pixel from different μ-lenses, signal is present at the same position in all the views as seen from Figure 5.6, for $z = Z0$. However, when the emitter is not in the focal plane of the objective, emitted beam is spread over many μ-lenses. Such a defocused beam has a quadratic phase curvature which is symmetrical around the lateral position of the emitter. The beam is sampled by μ-lenses and focused to their focal plane, at a position dependent on the local phase curvature of the beam. As a result, images of the emitter are laterally shifted in different sub-aperture views as seen in Figure 5.6 for $z = Z1$ and $z = -Z1$.

These displaced images of the emitter in different sub-aperture views can be used to determine its three-dimensional position, which was the basis of our light field data analysis method.

Raw Light field Images
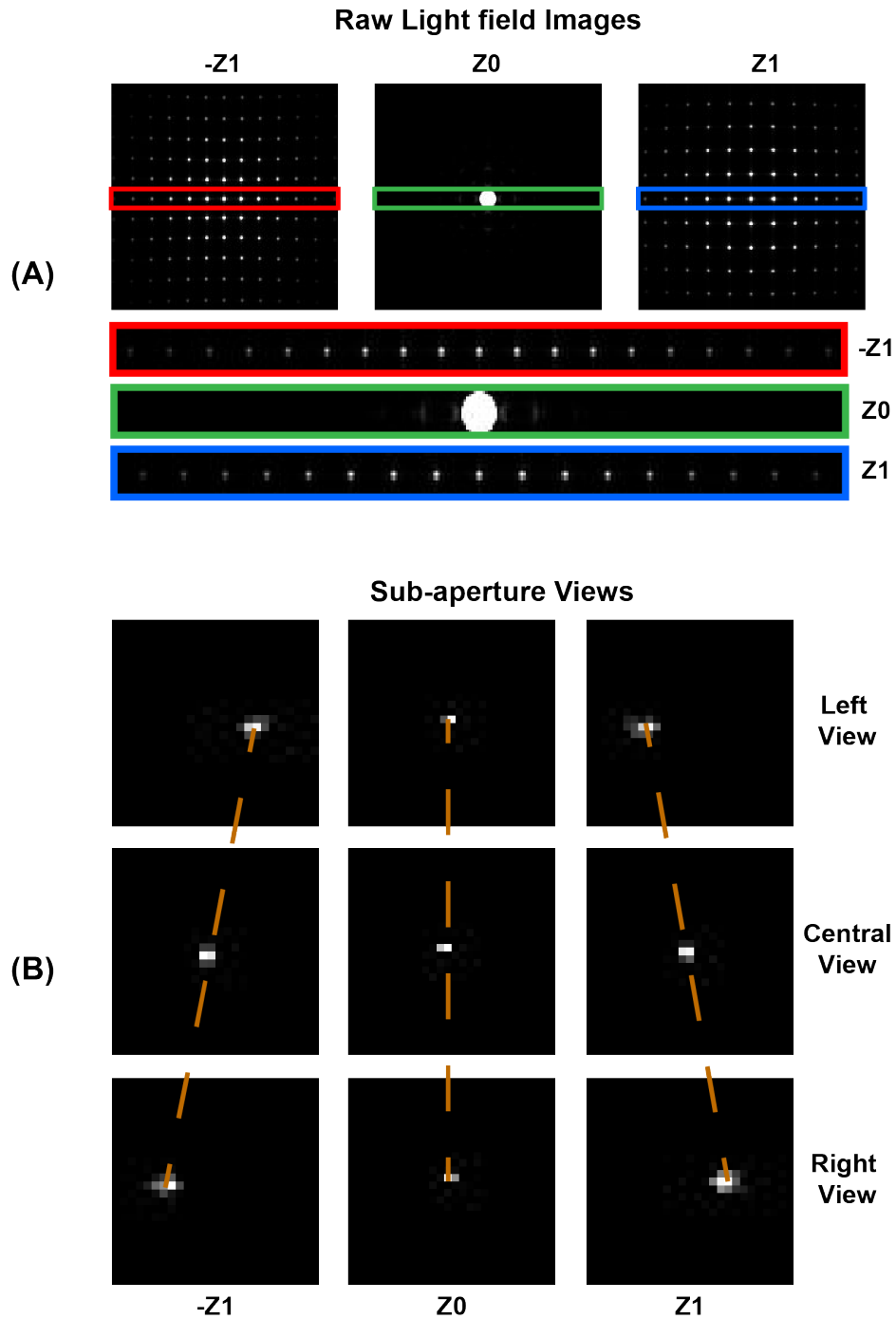
Sub-aperture Views

Fig. 5.6 (A) Light field images for an emitter in the object plane ($Z0$) and outside the object plane ($Z1$ and $-Z1$) (B) Sub-aperture views generated for images in (A). For the emitter in the object plane, signal is at the same position in different views. For emitters outside the object plane, signal is at different pixels in different views. This displacement of signal between views depends on the axial position of an emitter.

5.4   Experimental Setup and Data Analysis

In this section the experimental setup and the image analysis pipeline for localisation microscopy involving light field imaging modality are discussed.

5.4.1   Experimental Setup and Alignment of Lenslet Array

Our localisation based super-resolution microscope was modified to include the light field imaging capability by installing a lenslet array in the image plane. Focal plane of the array was imaged on the Hamamatsu Flash 4.0 camera through a $1 : 1$ relay system. See Chapter 2 for a detailed description of the experimental setup of the microscope.

   Figure 5.2B shows that for an emitter in the focal plane of the objective, image is formed at a single μ-lens and the beam expands afterwards. To avoid cross talk between neighbouring lenses, the beam size in the focal plane of the μ-lens should be smaller than (or equal to) the lens diameter. If f_{TL} and d_{BFP} is the focal length of the tube lens and the diameter of the BFP respectively, the condition of no cross talk can be calculated by using the properties of similar triangles (see Figure 5.2B).

$$\frac{f_\mu}{d_\mu} = \frac{f_{TL}}{d_{BFP}}$$
$$\frac{f_\mu}{d_\mu} = M \frac{f_{obj}}{d_{BFP}}$$

(5.4)

where, f_{obj} is the focal length of the objective, $M = f_{TL}/f_{obj}$ is the magnification of the microscope and d_μ is the diameter of the μ-lens. So, to avoid cross talk on a given microscope, f_μ and d_μ should be chosen carefully. We used a commercial lenslet array with $f_\mu = 2100\,\mu m$ and $d_\mu = 100\,\mu m$, which fulfilled the criterion presented in Eq 5.4. For our $60x$ Olympus objective, used with a 200 mm focal length tube lens, the maximum beam size in the focal plane of a μ-lens was $80.6\,\mu m$, smaller than the $100\,\mu m$ diameter μ-lenses.

   To install the lenslet array in the microscope, collimated light was directed through the microscope objective. The lenslet array was translated about the approximate location of the image plane until the square profiles of μ-lenses could be seen on the camera. Next, the camera was axially shifted to image the focal plane of the array. At this position a set of focused spots was observed on the detector due to the μ-lenses focusing the collimated beam. The axial location of the lenslet array was also verified by imaging a thin fluorescent layer on a coverslip. For a well aligned system, the corresponding image was composed of uniformly intense circles, since in this configuration each μ-lens was imaging the BFP of the microscope objective. It is important to mention that due to chromatic focal shifts in

the lenslet array, the distance between the camera and the lenslet array had to be adjusted for different emission bands i.e. one configuration could not be used to optimally perform super-resolution imaging over multiple wavelengths. Doing so could introduce significant errors in the estimation of the axial position of an emitter.

5.4.2   Data Analysis

On a light field microscope, emissions from point emitters in the imaged volume are captured by a camera placed in the focal plane of a lenslet array. In this section, the image analysis pipeline to determine the three-dimensional position of an emitter on such a microscope is discussed. This involved rectification of raw images followed by generation of sub-aperture views. Finally, the three-dimensional position of the emitter was calculated from its displaced images in these views.

Rectification of Images

Before any data analysis, rectification of raw light field images was required to correct for any angular or transnational shift between the camera chip and the lenslet array, and to precisely estimate the pitch of the array. For rectification, images of a thin fluorescent layer or collimated light directed through the microscope objective were used. Example calibration images are shown in Figure 5.7. Different rectification parameters were obtained as follows:

1. Rotation of the lenslet array was estimated by calculating the Radon transform over the calibration image. The orientation which maximised the variance of the transform gave the rotation of the array.

2. Calibration images had a periodic pattern of spots, so the pitch of the lenslet array was calculated by localising harmonics in the Fourier space with a sub-pixel resolution.

3. Translation of the lenslet array was calculated by generating a grid of points spanning the calibration image, using the estimated rotation and the pitch. This grid was translated a distance equal to the pitch of the lenslet array. At each translated position, signal was summed at all the grid points. Calculating the centroid of the summed intensities (for different translations of the grid) gave the translation of the lenslet array.

These parameters were subsequently used to rectify the light field images acquired experimentally, before generating the sub-aperture views from them. The method described above was implemented in *Python* by Ruth Sims, a former PhD student at CAIC, and described in more detail in [152].

(A)   (B)
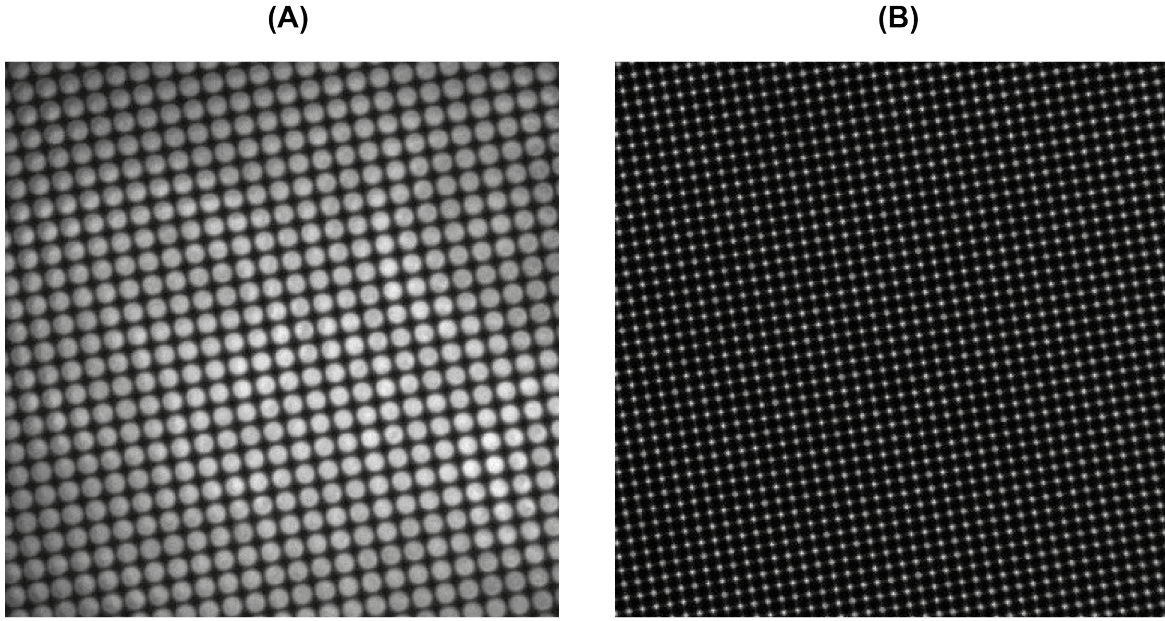
Fig. 5.7 Calibration images, to determine the rectification parameters, obtained by imaging (A) a thin fluorescent layer on a coverslip, and (B) collimated light sent through the microscope objective

Generating Sub-aperture Views

After rectification, sub-aperture views were generated from raw light field images by extracting the same pixel from all the μ-lenses in the FOV, according to Eq 5.2, as shown in Figure 5.5. If M and N are the number of pixels behind a μ-lens along the horizontal and the vertical directions respectively, $M \times N$ views can be generated from a raw image. For our system:

$$M = N = \frac{Lens\ diameter}{Pixel\ size} = \frac{100\,\mu\mathrm{m}}{6.5\,\mu\mathrm{m}} = 15.3 \tag{5.5}$$

During rectification, interpolation was performed to have 17 pixels along both the directions. Having an odd number of pixels ensured the presence of the central view, which was important to calculate the lateral position of an emitter as explained later in this section.

An example lightfield image and the corresponding sub-aperture views are shown in Figure 5.8A&B respectively. Figure 5.8B was obtained by arranging sub-aperture views according to the position of the pixel used for their generation. For example, if (u, v) is the coordinate system (of pixels) behind a μ-lens, the top left view was generated from the pixel at (8,8). Similarly the central view and the bottom right view were generated from pixels at (0,0) and (-8,-8) respectively [143].
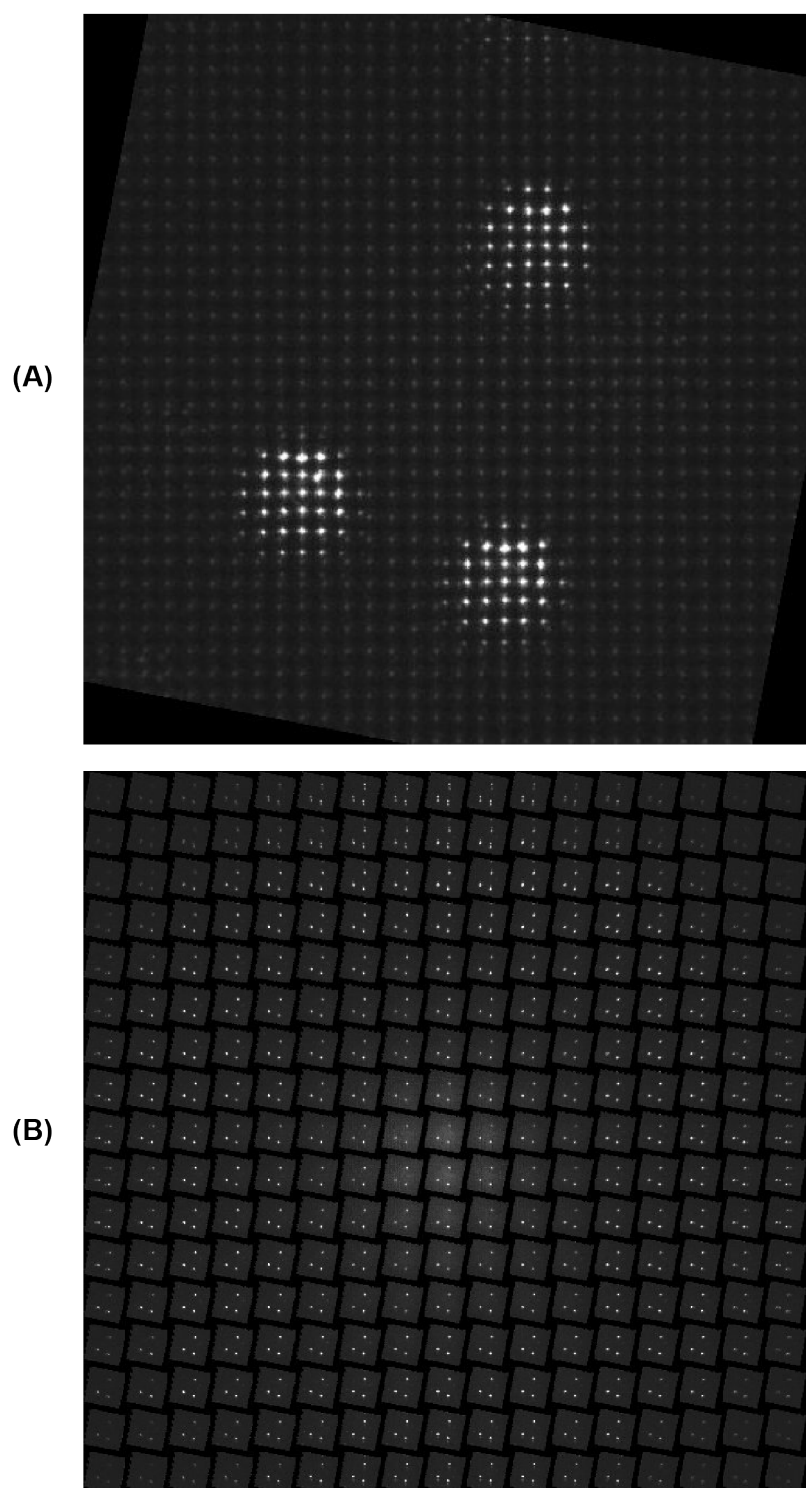
Fig. 5.8 (A) An example light field image with three 100 nm fluorescent beads in the FOV. (B) sub-aperture views generated from (A)

Localisation in the Sub-aperture Views and Tracking

Once the sub-aperture views were generated from a raw light field image, (images of the) emitters were localised in them. The difference in the position of an emitter in two sub-aperture views is called *disparity* [149] and was used as a measure of the axial position of the emitter. To calculate disparity, spots corresponding to the same emitter (in different views) had to be grouped together. For a single emitter in the FOV, this was straight forward as a single spot was present per view. However, for multiple emitters in the FOV, spot tracking over sub-aperture views was required to group localisations corresponding to the same emitter. We achieved this by combining the process of localisation and tracking as discussed below and explained in Figure 5.9:

1. Start by localising spots in the top left view. Let this be view 1.

2. Localise spots in the neighbouring view (along row or column), view 2, at a distance d_0 (which is the initial user defined value) from the localisations in view 1. This was done by finding local maximum in a 4×4 pixel region followed by fitting of a two-dimensional Gaussian function around the detected peak.

3. Calculate the distance between positions of an emitter in views 1&2. Let this distance be d_1, Its value will depend on the axial position of the emitter.

4. Search for spots in view 3 at a distance d_1 from the positions calculated in view 2 and perform spot localisation. Let the distance between positions of the emitter in views 2&3 be d_2. In the absence of aberration, we found the disparity to be the same between any two views, so $d_1 \approx d_2$ (see the next section for more details).

5. In the next view, search for spots at a distance $d_{av} = 0.5 \times (d_1 + d_2)$ and repeat the process for the entire row. Although not necessary, due to constant disparity between neighbouring views, but we updated d_{av} after spot localisation in each view.

6. Once at the end of the row, move to the next row and look for spots at a distance d_{av} from the localisations in view 1 (Figure 5.9).

7. Repeat the above mentioned steps for all the rows

By applying the above mentioned steps, we grouped localisations corresponding to the same emitter in all the sub-aperture views, when multiple emitters were present in the FOV. It is important to note that the discussed algorithm did not work for overlapping emitters in the sub-aperture views. Advanced tracking algorithms, similar to the *vbSPT*, should be used to group localisations in such a situation.
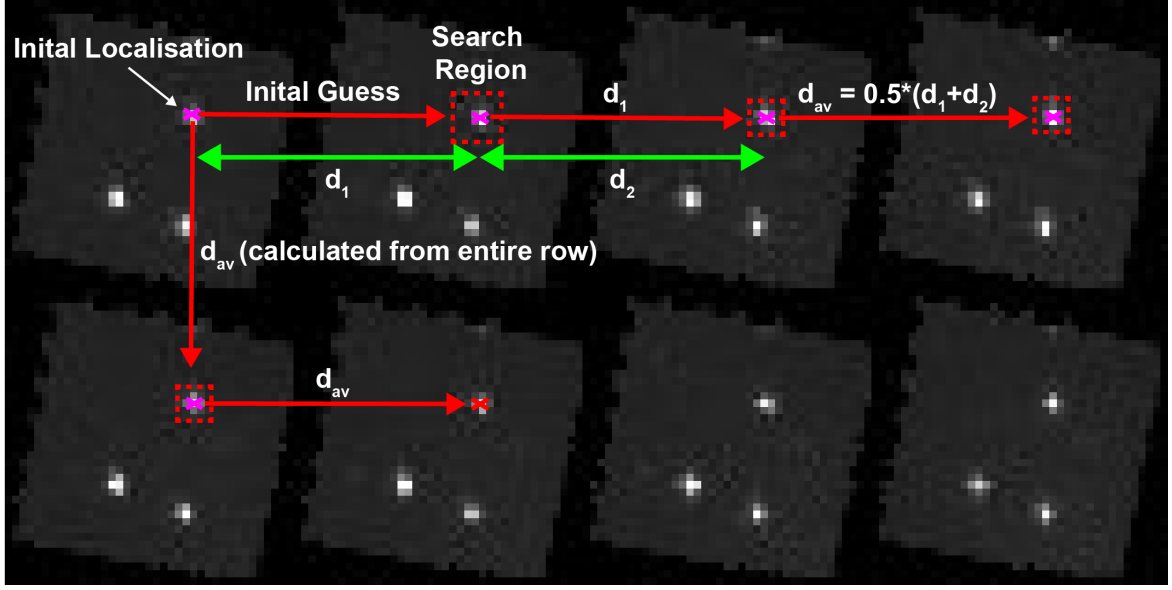
Fig. 5.9 A schematic of our method to localise and track emitters in sub-aperture views.

Three-dimensional Position from Disparity

After grouping localisations, we calculated disparity from the positions of an emitter in different views. If $(x_{u,v}, y_{u,v})$ is the position of an emitter in the sub-aperture view, $s_{u,v}$, generated from the pixel, (u,v), the disparity was calculated as follows:

$$disp_{u,v} = \sqrt{(x_{u,v} - x_{u_0,v_0})^2 + (y_{u,v} - y_{u_0,v_0})^2} \tag{5.6}$$

here, $(x_{u_0,v_0}, y_{u_0,v_0})$ is the position of the emitter in the central view, s_{u_0,v_0}. We also defined $r_{u,v}$ as the distance of a view, $s_{u,v}$, from the central view and calculated it as follows:

$$r_{u,v} = \sqrt{(u - u_0)^2 + (v - v_0)^2} \tag{5.7}$$

Disparity was calculated relative to the central view, s_{u_0,v_0}, because the position of an emitter in this view was independent of its axial position as shown in Figure 5.11A. The figure was obtained by localising signal in the central view of a simulated light field PSF over a 15 μm axial range.

Signal in the central view corresponds to the beam segment with the symmetrical wavefront over a μ-lens (symmetrical wavefront results in focusing of the beam on the central pixel behind a μ-lens). This is only true for the centre of a defocused beam, as the beam expands about its centre for an emitter outside the object plane.

Axial Position: In the absence of aberration, $disp_{u,v}$ varies linearly as a function of $r_{u,v}$. This is because for an emitter outside the focal plane of the objective, the beam has a quadratic phase curvature at the lenslet array. μ-lenses sample the beam and focus it to their focal plane, at a position dependent on the local phase gradient at a lens. For a quadratic phase curvature, the gradient varies linearly as a function of μ-lens position, resulting in different pixels behind different μ-lenses to illuminate as shown in Figure 5.10A. As the sub-aperture views are just a rearrangement of the pixels in a raw light field image, this linear relationship also exists between $disp_{u,v}$ and $r_{u,v}$, as shown in Figure 5.10B. Figure 5.11B shows $disp_{u,v}$ as a function of $r_{u,v}$ for three different axial positions of the emitter. Slope of the graph varied as a function of the axial position and we calibrated the slope over a $20\,\mu$m axial range for our experimental setup. The calibration curve was then used to determine the axial position of an arbitrary emitter.

Later Position: Lateral position of the emitter can be determined from its position in the central view. However, central view has the highest background (due to focusing of out of focus and scattered light), resulting in the worst localisation precision. Moreover, by doing so, information about the emitter in other views is not taken into account. In our experimental configuration, this corresponded to the utilisation of $1/17^2$ of the total information captured. We overcame this problem by plotting the position of the emitter in different sub-aperture views as a function of $r_{u,v}$, which resulted in a *cone*. This happened because $disp_{u,v}$ is a linear function of $r_{u,v}$, and is constant for views at the same $r_{u,v}$. In such a configuration, apex of the cone corresponded to the position of the emitter in the central view, but calculated from its positions in all the 17^2 views.

So, the lateral position of the emitter was calculated from the apex of the cone. Moreover, the slope of the cone gives the rate of change of $r_{u,v}$ as a function of the emitter position in a view at a distance $r_{u,v}$ from the central view. So, it is inversely proportional to the slope of the graph shown in Figure 5.11B. Mathematically the cone can be described as:

$$r_{u,v} = \sqrt{\frac{(x_{u,v} - x_{u_0,v_0})^2 + (y_{u,v} - y_{u_0,v_0})^2}{m^2}} \tag{5.8}$$

here, $(x_{u_0,v_0}, y_{u_0,v_0})$ is the position of the emitter in the central view, $r_{u,v}$ is given by Eq 5.7 and $1/m$ is the slope of the $disp_{u,v}$ vs $r_{u,v}$ graph. Figure 5.12B shows the cones obtained for two different axial positions of an emitter.

Figure 5.12A shows the results for calculating the lateral position of a simulated emitter ($z = 15\,\mu$m) by direct localisation in the central view and by cone fitting. As expected, the localisation precision was significantly better (around 3 times) in the latter case.
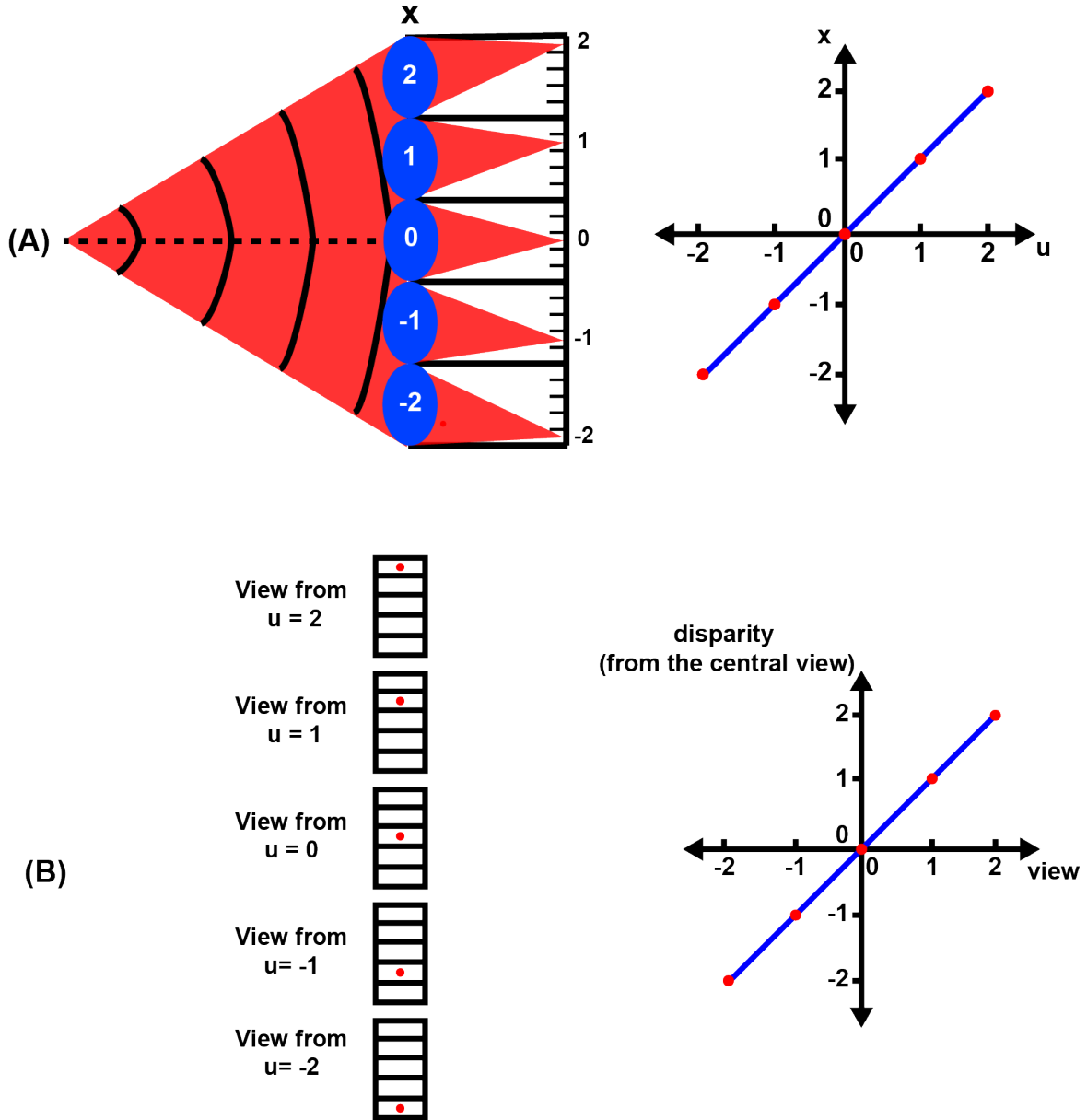
Fig. 5.10 (A) For an emitter outside the object plane, emitted beam has a quadratic phase curvature at the lenslet array. So, local phase gradient at a μ-lens varies linearly as function of its position from the centre of the beam. As a result, plotting μ-lens position, x, as function of the pixel on which it focus light, u, gives a straight line. (B) This linear relationship holds in sub-aperture view representation as well, as it is just a rearrangement of pixels in (A).
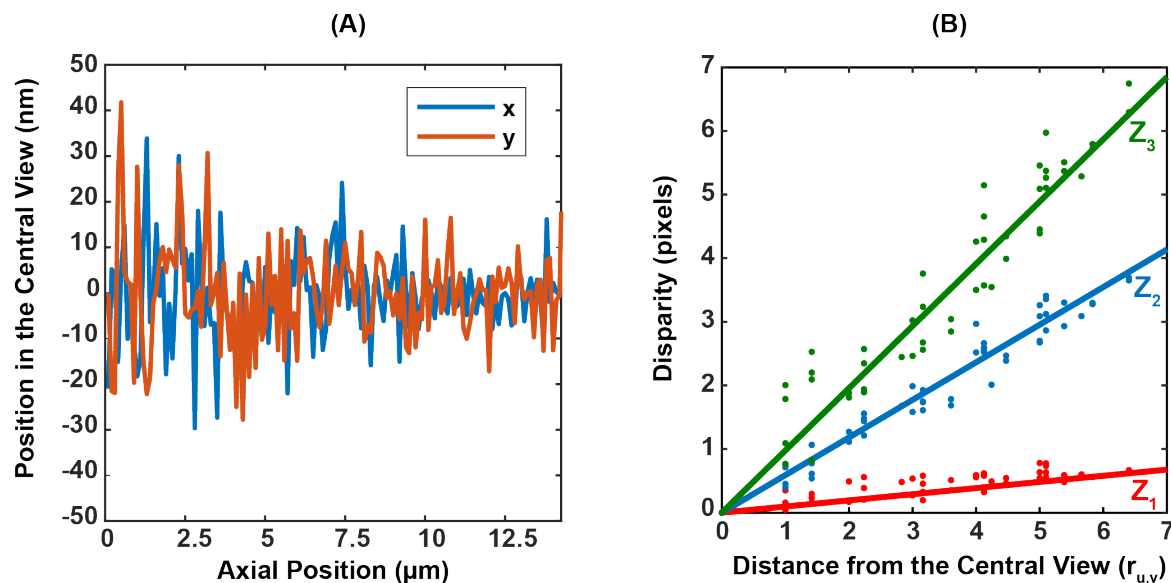
Fig. 5.11 (A) Position of a simulated emitter in the central view. (B) Disparity between sub-aperture views, for a simulated emitter at different axial positions, as a function of $r_{u,v}$. Slope of the graph varied as a function of the axial position of the emitter and we calibrated the slope over a 20μm axial range, for our experimental setup. The calibration curve was then used to determine the axial position of an arbitrary emitter

Summary of the Image Analysis Pipeline

The image processing steps for light field localisation microscopy can be summarised as follows:

1. Rectify raw light field images

2. Generate sub-aperture views

3. Localise emitters in the sub-aperture views

4. Perform tracking in between the views to group localisations corresponding to the same emitter

5. Calculate disparity between positions of an emitters in different views

6. For each emitter, fit a cone to its positions in different views

7. Apex of the cone corresponds to the lateral position of the emitter

8. Slope of the cone was related to the axial position of the emitter
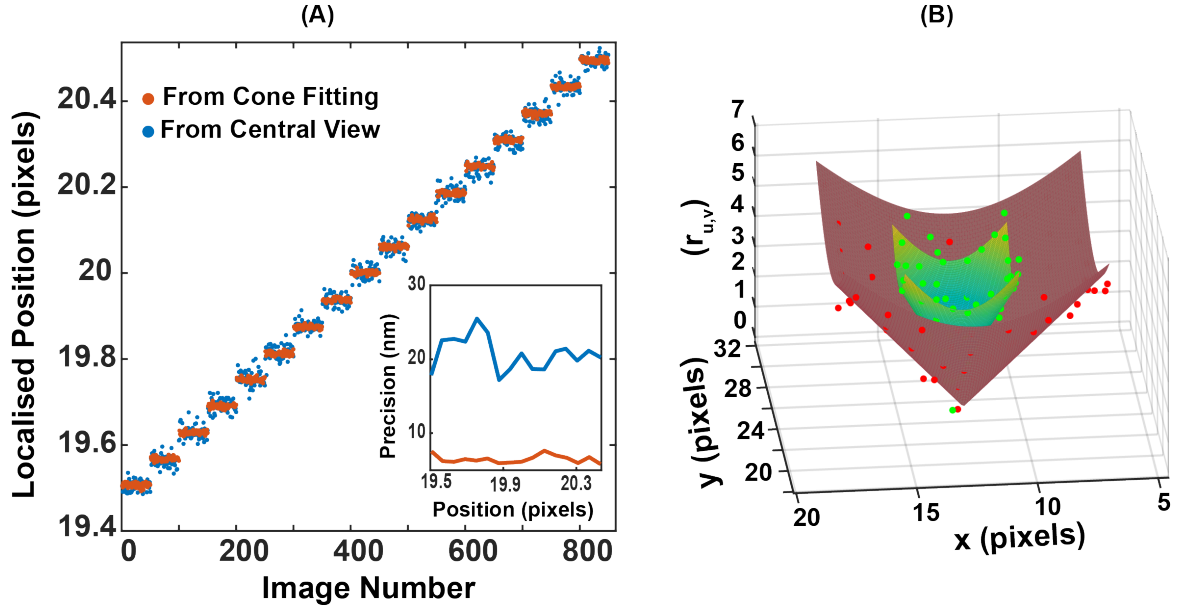
Fig. 5.12 (A) Lateral position calculations, for a simulated emitter, from the central view and by cone fitting. Position calculations from cone fitting gave three times better localisation precision. (B) Cones obtained for two axial positions of an emitter. Apex of the cone gave the lateral position of the emitter and its slope was related to the axial position of the emitter.

5.5   Simulations

This section describes the application of the proposed image analysis pipeline on the simulated data. First, a mathematical model to generate the three-dimensional light field PSF is presented. The model is then used to generate synthetic light field images for different imaging conditions. These images were analysed using our image analysis mechanism.

5.5.1   Imaging Model

To model the light field PSF, electric field in the image plane, $E(x,y)$, was calculated using the method discussed [153, 154]. For an emitter at (x_o, y_o, z_o) in the imaged volume, $E(x,y)$ is given as:

$$E(x,y) \propto \mathscr{F}\left[E_{fp}(\rho,\phi|x_0,y_0,z_0)\right] \qquad (5.9)$$

here $E_{fp}(\rho,\phi|x_0,y_0,z_0)$ is the field in the BFP of the objective with polar coordinates (ρ,ϕ). For, an aberration free system, $E_{fp}(\rho,\phi|x_0,y_0,z_0)$ is defined as follows:

$$E_{fp}(\rho,\phi,x_0,y_0,z_0) = E_{fp}(\rho,\phi,0,0,0)exp\{i(\phi_{lat}(\rho,\Phi|x_0,y_0)+\Phi_{ax}(\rho,\phi|z))\} \qquad (5.10)$$

$E_0(\rho,\phi,0,0,0)$ is the field in the BFP for an on-axis emitter in the focal plane of the objective. $\phi_{lat}(\rho,\phi|x_0,y_0)$ and $\phi_{ax}(\rho,\phi|z)$ are the phase terms dependent on the lateral displacement of the emitter from the optical axis and its axial displacement from the object plane respectively. These quantities are described as follows (according to [153, 154]):

$$E_{fp}(\rho,\phi,0,0,0) = \begin{cases} 1 & \text{if } \rho \leq 1 \\ 0 & \text{if } \rho > 1 \end{cases} \tag{5.11}$$

so, $E_0(\rho,\phi,0,0,0)$ is a circle with the radius normalised to 1 and:

$$\Phi_{ax}(\rho,\phi|z) = \frac{2\pi n}{\lambda} z_o \sqrt{1-\left(\frac{NA}{n}\rho\right)^2} \tag{5.12}$$

$$\Phi_{lat}(\rho,\phi|x_0,y_0) = \frac{2\pi NA}{\lambda \sqrt{(M^2-NA^2)}}\rho(x_0 cos\phi + y_o sin\phi) \tag{5.13}$$

The electric field in the image plane was multiplied with the phase added by the lenslet array. If $\psi(x,y)$ is the phase added by a single μ-lens, according to [155] the lenslet array can be modelled as:

$$\Psi(x,y) = \psi(x,y) * \sum_{i=-N/2}^{N/2} \sum_{j=-N/2}^{N/2} \delta(x-id,y-jd) \tag{5.14}$$

$$\psi(x,y) = A(x,y)exp\left(\frac{-ik}{2f_\mu}(x^2+y^2)\right) \tag{5.15}$$

where f_μ is the focal length of μ-lenses, d is the lenslet array pitch and:

$$\delta(x,y) = \begin{cases} 1 & \text{if x=0,y=0} \\ 0 & \text{otherwise} \end{cases}$$

$$A(x,y) = \begin{cases} 1 & \text{if } |x| \leq d/2 \text{ and } |y| \leq d/2 \\ 0 & \text{otherwise} \end{cases}$$

Finally the beam propagates from the lenslet array to the sensor placed in the focal plane of the array, where the intensity is given as [155]:

$$I(x',y') = \left| \mathscr{F}^{-1}\left\{ \mathscr{F}\left\{ E(x,y)\Psi(x,y)exp\left(-\frac{i}{4\pi}\lambda f_\mu(w_x^2+w_y^2)\right)\right\}\right\}\right|^2 \tag{5.16}$$

here (w_x, w_y) is the coordinate system of the plane containing the Fourier transform of the field after the lenslet array.

$I(x', y')$ was sampled according to the number of pixels behind a μ-lens, which for our system was 17^2. Other simulation parameters were also matched to the experimental setup. Figure 5.13 shows an example light field PSF, generated by modifying the phase of the conventional PSF of the microscope.
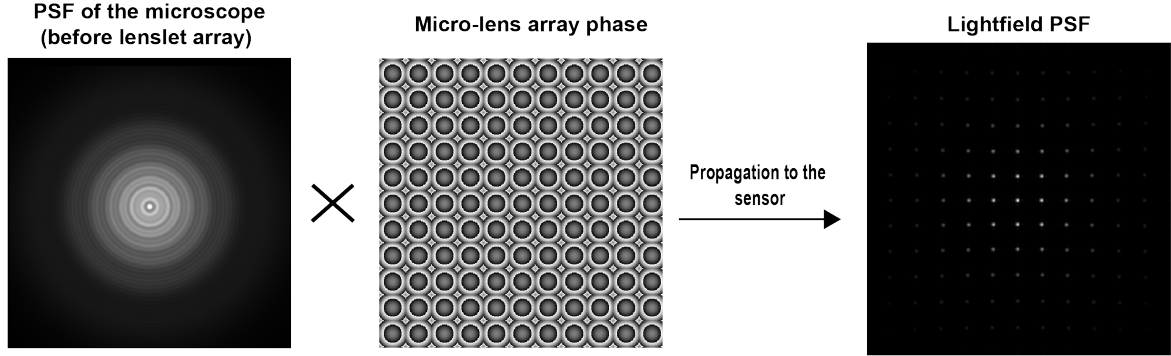
Fig. 5.13 Mechanism of simulating the light field PSF. Phase of the lenslet array was added to the beam in the image plane. Modified beam was then propagated to the focal plane of the array using Eq 5.16

5.5.2 Simulation Results

This section discusses the results for applying the proposed image analysis pipeline to the simulated images. We explore the achievable localisation precision and accuracy under different number of photons and as a function of the three-dimensional position of an emitter. Synthetic light field images were generated using Eq 5.16. Similar to the experimental setup, the simulated lenslet array had a pitch of $100\,\mu$m and a focal length of $2100\,\mu$m. Other simulation parameters were also matched to the experimental setup.

Axial Calibration Curve

We started off by generating the light field PSF over a $30\,\mu$m axial range with a step size of 100 nm. At each position, the slope of the $disp_{u,v}$ vs $r_{u,v}$ curve was calculated and the resultant calibration curve is shown in Figure 5.14A. xz projection of the simulated light field PSF is shown in Figure 5.14B.

The calibration curve shows that in a $1.2\,\mu$m region around the focal plane, slope of the graph is ~ 0, which resulted in the worst localisation accuracy for emitters close to the focal plane [155]. This was because of the beam diameter being smaller than a μ-lens

over this range as shown in Figure 5.14B. Consequently, pixels behind a single μ-lens were illuminated. So, position of the emitter did not vary in sub-aperture views, resulting in no disparity between the views. In such a situation, if positions of the emitter in different sub-aperture views were plotted as a function of $r_{u,v}$, a straight line was obtained. So, instead of fitting a cone (to this straight line), lateral position of the emitter was calculated from its average position in the sub-aperture views for $|z| < 0.6$.

Away from the beam focus (corresponding to the image of an emitter), phase curvature of the beam varies linearly as a function of z (distance from the beam focus) [8]. As the Rayleigh range of our microscope was around 380 nm (NA=1.3 and Magnification = 60 with a 180 mm focal length tube lens), we expected the calibration curve to be linear for emitters more than a micron away from the focal plane of the objective. However, for $0.6 < |z| < 5\,\mu$m, slope of the calibration curve varied significantly with z. We found this to be a consequence of the varying phase gradient of the beam over a μ-lens, which resulted in the non-linear region of the calibration curve as seen from Figure 5.14A&B. So, for the calibration curve to be linear, the phase gradient should be constant over a single μ-lens and it should vary linearly with z. Both the conditions were fulfilled for $|z| > 5\,\mu$m, as the beam was significantly large to have a constant phase gradient over a μ-lens. Hence, the calibration curve was linear over this axial range.

The calibration curve was then used to determine the axial position of a simulated emitter from the slope of the cone, obtained for that emitter.

Axial Precision

To analyse the axial precision of localising an emitter using our light filed localisation method, the light field PSF was simulated for various number of photons under the shot noise and a background of 100 photons. Images were generated over a $30\,\mu$m axial range with a step size of 300 nm and 50 repeats at each position. Axial position of the emitter was calculated by applying the calibration curve, Figure 5.14, to the slope of the $disp_{u,v}$ vs $r_{u,v}$ graph. Precision was then estimated from the standard deviation of the positions of an emitter in multiple images, generated for the same axial position of the emitter.

Figure 5.15A shows axial position of a simulated emitter as a function of the image number. The step size of 300 nm was correctly calculated over the entire $30\,\mu$m range, except in the region close to the focal plane where the beam size was smaller than a μ-lens. In Figure 5.15B localisation precision is plotted as a function of the axial position of an emitter and for different number of photons. The figure shows that for large number of photons, we achieved a precision of less than 25 nm over the entire range. However, the precision decreased as a function of z because of the spread of photons over increasing number of
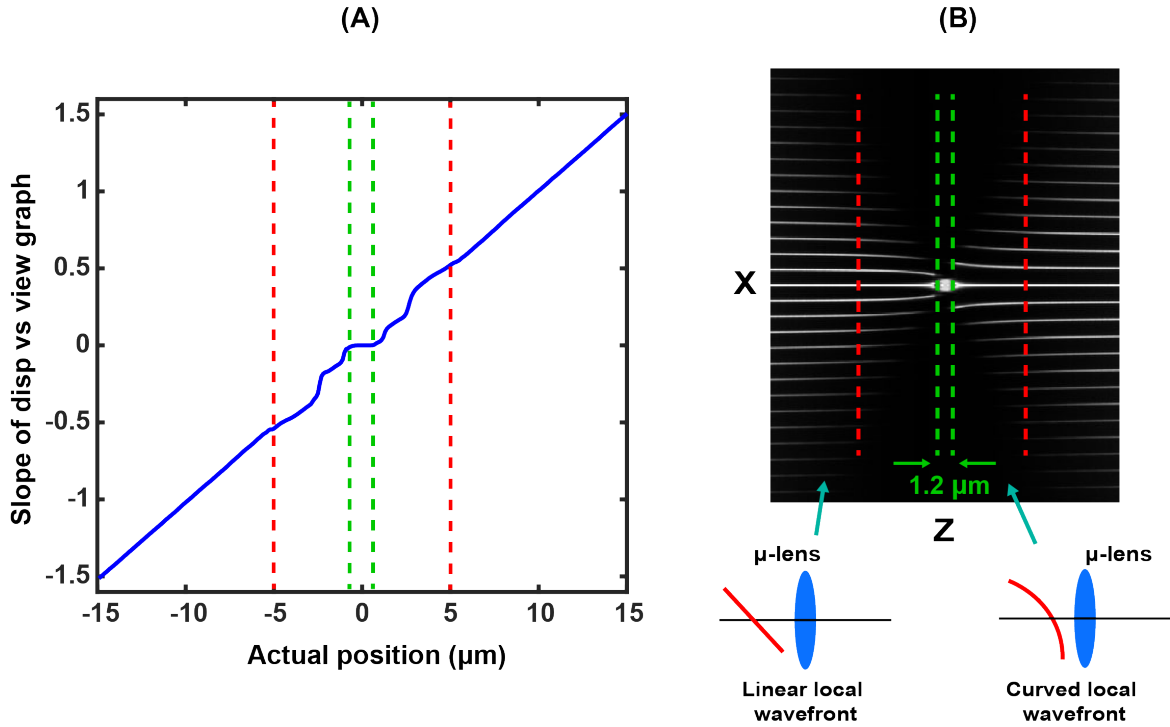
Fig. 5.14 (A) Calibration curve to determine the axial position of a simulated emitter from the slope of the cone. (B) x-z projection of the light field PSF. Over a $1.2\,\mu$m region around the focal plane, the beam covers a single μ-lens, giving the flat region in (A). For $|z| < 5\,\mu$m, the beam has a significant phase curvature over a μ-lens, resulting in the non-linear region of (A). For $|z| > 5\,\mu$m, the beam is significantly large to cover multiple μ-lenses and has a linear phase over a μ-lens, which gives the linear region of (A).

lenses. Moreover, the localisation precision also deteriorated with a decrease in the number of photons. For example, the precision decreased from $80\,$nm for 3.4×10^4 to $280\,$nm for 42×10^3 photons.

The above analysis shows that our localisation method correctly estimated the axial position of an emitter over a wide axial range and the localisation precision depended on the axial position of the emitter and the number of photons captured at the camera (for that emitter).

Lateral Precision

We also analysed the lateral precision obtained by applying our image analysis pipeline on the simulated data. Light field PSF was generated at 17 lateral positions within a μ-lens (step size = $93.8\,$nm) and over an axial range of $30\,\mu$m. 50 images were generated at each position. Precision was then estimated from the standard deviation of the positions of an emitter in
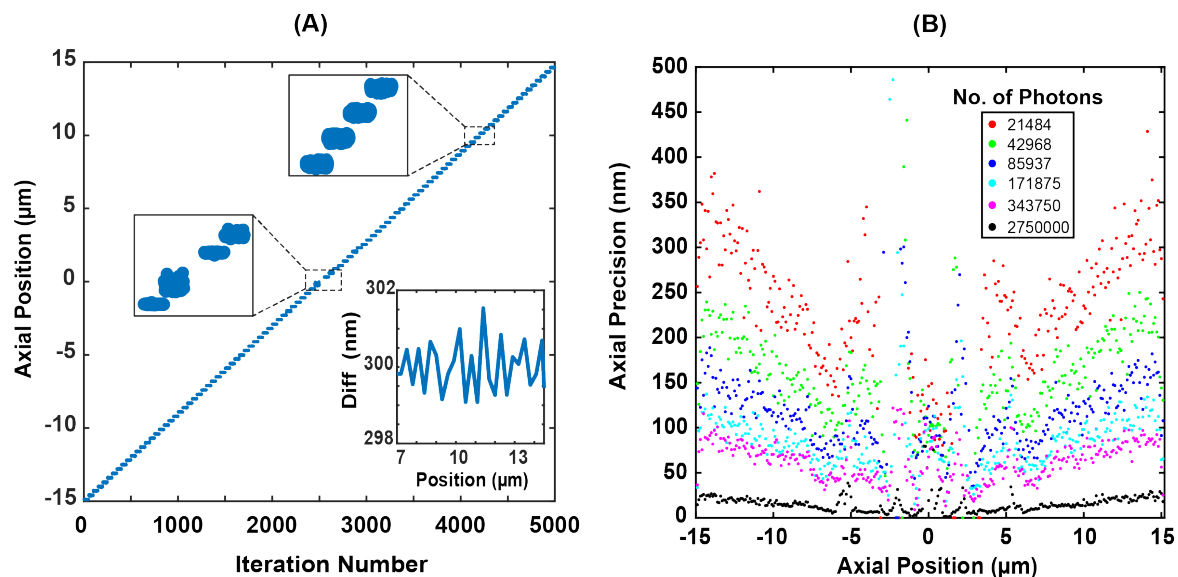
Fig. 5.15 (A) Results for localising a simulated emitter over a $30\,\mu$m axial range, with a step size of 300 nm. 50 frames were generated at each position. Our localisation method correctly estimated the axial position over the entire range, except in the region close to the focal plane where the beam size was smaller than a μ-lens. (B) Localisation precision for different number of photons, obtained from the variation in the axial position of a simulated emitter over 50 frames.

multiple images, generated for the same three-dimensional position of the emitter. Results of the analysis are shown in Figure 5.16.

Figure 5.16A shows that the lateral position of an emitter was correctly calculated throughout the diameter of a μ-lens, irrespective of its axial position (for $|z| \gg 0$). However, when the emitter was close to the focal plane of the objective ($|z| < 0.6\,\mu$m), the disparity was ~ 0 and the lateral position was estimated from its average position in the sub-aperture views. Moreover, within this axial range, the beam was detected behind a single μ-lens only. So, for a lateral step to be detectable, it had to be large enough for the signal to appear behind a neighbouring μ-lens. For example, for an emitter in the focal plane of the objective, the step size was detectable if it matched the pitch of the lenslet array (if the blur due to the diffraction limit of light is ignored). Hence, worst localisation precision and accuracy was observed for an emitter close to the focal plane of the objective. This axial range of around $1.2\,\mu$m is not shown in Figure 5.16.

Figure 5.16B shows the lateral precision of an emitter to be independent of its position within a μ-lens. However, the precision decreased with an increase in distance from the object plane, due to the spread of signal over more lenses. For example the precision was 3 nm, 4.5 nm and 6.5 nm for $z = 6\,\mu$m, $z = 9\,\mu$m and $z = 15\,\mu$m respectively. These results

also indicate that given a large number of photons, our localisation method could determine the lateral position of an emitter with a precision of less than 10 nm over a 30 μm axial range.

We also analysed the localisation precision for different number of photons and results are shown in Figure 5.16C. As expected, the precision deteriorated with a decrease in the number of photons. For example it changed from 15 nm for 1.7×10^4 to 40 nm for 2.1×10^3 photons.

In short, our localisation method correctly estimated the lateral position of an emitter over a wide axial range. Moreover, the lateral precision was independent of its position within a lens. However, it varied as a function of the axial position of the emitter and the number of photons captured at the camera.

5.6   Experimental Analysis

After testing our image analysis pipeline on simulated light field images, we applied it to the experimental data. First an axial calibration curve was generated to determine the three-dimensional position of an emitter from its positions in multiple sub-aperture views. The achievable localisation precision under different imaging conditions is also discussed. Lastly, application of the technique to track a fluorescent bead over a large DOF and its potential for single molecule imaging in labelled cells is also discussed.

5.6.1   Axial Calibration Curve

To generate the calibration curve, 100 nm fluorescent beads were scanned over a 16 μm axial range with a step size of 100 nm. 10 images were recorded at each position and the three-dimensional position of a bead was calculated by applying the analysis pipeline discussed in Section 5.4.2. The calibration curve, shown in Figure 5.17A, was calculated from the average slope of the $disp_{u,v}$ vs $r_{u,v}$ graph (as there were 10 images for each axial position). xz projection of the light filed PSF is shown in Figure 5.17A. For a better visualisation of the projection over a wide axial range, the figure was obtained by normalising the PSF at each axial position.

Shape of the experimentally calculated calibration curve and the xz projection closely matched the simulations. Different regions of the curve have been discussed in detail in Section 5.5.2 and are briefly mentioned below:

- $|\mathbf{z}| \leq \mathbf{0.6}$: In this axial range, the beam diameter was smaller than a μ-lens resulting in the slope of the calibration curve to be ~ 0. As a consequence, the localisation precision and accuracy was the worst in this region.
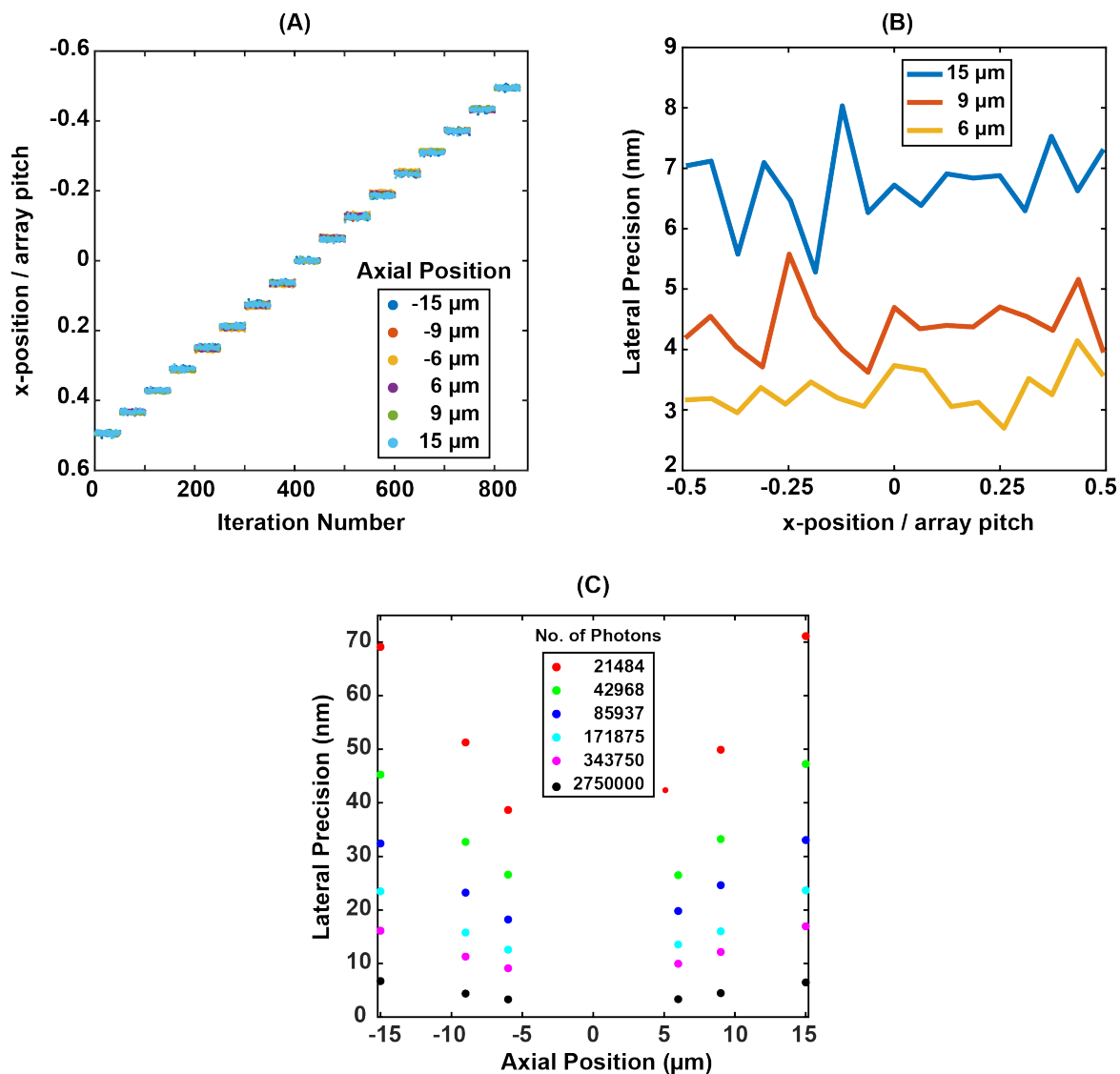
Fig. 5.16 (A) Results for localising a simulated emitter, scanned laterally over a μ-lens with a step size of $93.8\,\text{nm}$, for multiple axial positions. 50 images were generated at each position. Our localisation method correctly estimated the lateral position of the emitter. (C) Localisation precision for different number of photons, obtained from the variation in the calculated lateral position over 50 frames.

- **$0.6 < |\mathbf{z}| < 5$**: In this region, the wavefront had a significant phase curvature over the diameter of a μ-lens (see Figure 5.14). This curvature led to the variation in the slope of the calibration curve as a function of the axial position of an emitter.

- **$|\mathbf{z}| \geq 5$**: In this axial range, the emitter was significantly away from the focal plane of the objective, which resulted in an expanded beam at the lenslet array. Such a beam

had a linear wavefront over a μ-lens leading to the linear region of the calibration curve.

It is to be mentioned that although we generated the calibration curve over a $16\,\mu$m range, the linearity of the curve, for $|z| > 5$, allowed us to accurately calculate the axial position of beads over a wider axial range. This linear relationship is shown in the inset of Figure 5.17A. As in the case of simulations, the calibration curve was subsequently used to determine the axial position of an emitter from the slope of the cone obtained for that emitter.
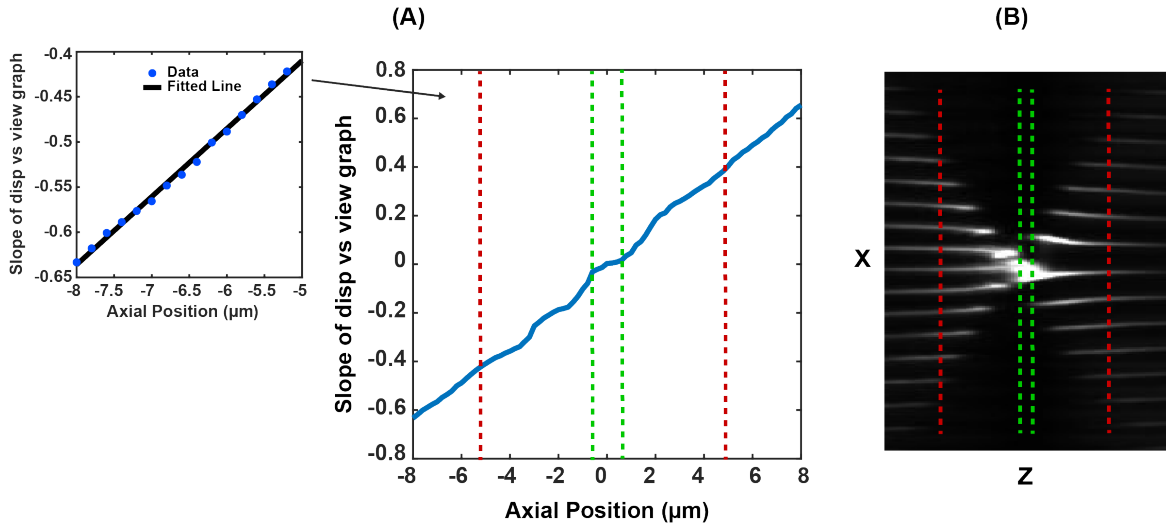
Fig. 5.17 (A) Experimental calibration curve to determine the axial position of an emitter, from the slope of the cone. (B) x-z projection of the light field PSF. Different regions, marked in (B), are explained in Figure 5.14. Linearity of the calibration for $|z| > 5$ allowed us to calculate axial positions over a wider axial range (beyond the range, for which the calibration curve is plotted).

5.6.2   Localisation Precision

Next step in the characterisation of our light filed localisation microscope was to determine the achievable axial and lateral precision using the proposed image analysis pipeline. $100\,$nm diameter fluorescent beads were scanned over a $12\,\mu$m axial range, on one side of the focal plane, with a step size of $1\,\mu$m. Only one side of the focal plane was considered because of the symmetry of the calibration curve around the focal plane and to minimise the effect of photobleaching on the precision measurements. 500 images were captured at each position and precision was calculated from the standard deviation of the positions of the localised beads over these frames. Imaging was carried out at different laser powers, which resulted in different number of photons at the camera i.e. 16×10^3, 39×10^3, 47×10^3, 16×10^3,
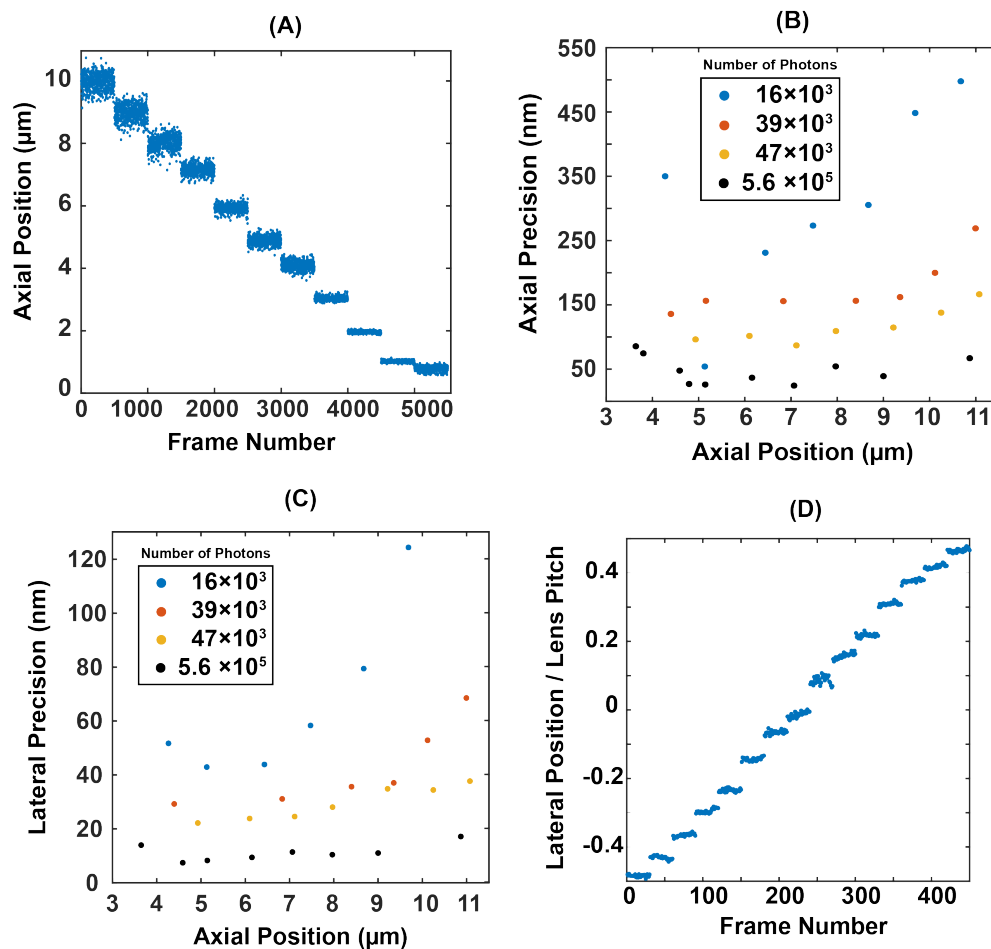
Fig. 5.18 Experimental results for characterising our light field microscope using 100 nm fluorescent beads as a test sample. (A) Calculated axial position of a bead scanned over a distance of 10 μm (on one side of the focal plane) with a step size of 1 μm. 500 images were obtained at each position. (B)&(C) Axial and lateral localisation precision, for different number of photons, obtained from the variation in the position of the bead over 500 frames. (D) Calculated lateral position of a bead scanned over a distance of 1.5 μm (equal to the lens pitch) with a step size of 100 nm.

and 2.93×10^5. The number of photons were obtained by calculating the area of the PSF when beads were in the object plane. This plane was chosen because, in this plane, the PSF consisted of a single spot covering all the pixels behind a single μ-lens (the effect of photobleaching was ignored in the analysis presented in this section). Currently, we are exploring more advanced algorithms to compute the number of photons from all the images/views of a bead in the sub-aperture view representation. Result of the analysis are shown in Figure 5.18.

Figure 5.18A shows the axial position of a bead as a function of the frame number. The figure shows that our localisation method correctly identified the axial step size of 1μm over the entire range, except when the bead was close to the focal plane of the objective. This was in accordance with the shape of the calibration curve and the simulation results discussed in the last section. Figure 5.18B shows axial precision as a function of the axial position of the bead. The figure shows that given a large number of photons, our image analysis pipeline localised emitters with a precision of less than 50 nm over the entire axial range. However, the precision decreased with an increase in z due to the spread of signal over an increasing number of μ-lenses. Moreover, a decrease in the number of photons also led to the deterioration of the localisation precision. For example it varied from below 50 nm to 200 nm at a depth of $7\,\mu$m, for 5.6×10^5 and 30×10^3 photons respectively.

Figure 5.18C shows the lateral precision as a function of the axial position and different number of photons. As expected both an increase in the axial depth and a decrease in the number of photons led to the loss of precision. For example it varied form below 20 nm to 45 nm for 5.6×10^5 and 30×10^3 photons respectively. Finally, Figure 5.18D shows results for the lateral scanning of a bead, with a step size of 100 nm. The figure shows that the positions of the bead were correctly calculated over the entire pitch of the lenslet array.

The above analysis shows that the proposed image analysis pipeline determined the three-dimensional position of fluorescent beads with significant accuracy, over a DOF of $20\,\mu$m. The localisation precision depended on the number of photons and the axial position of an emitter.

Light field and Super-resolution Imaging

Application of the proposed image analysis method on the simulated and the experimental data show that the method could determine the three-dimensional position of an emitter with high accuracy over a DOF of more than $20\,\mu$m. Moreover, given enough photons, an emitter could be localised with a precision of less than 50 nm in all three spatial dimensions. These results show the capability of light field imaging and the proposed image analysis method to localise emitters with a sub-diffraction precision over a large DOF.

The precision depended greatly on the number of photons captured for an emitter and its axial position. For the typical number of photons involved in single molecule imaging, the obtained precision was of the order of hundreds of nanometres. This was because of the use of a sub-optimal off-the-shelf lenslet array in the experiments. We anticipate that with some hardware and software modifications, the technique could be applied to perform localisation microscopy over the entire volume of a cell. These modifications are discussed in Section 5.7 and are a current topic of research at CAIC.

5.6.3   Tracking Experiment
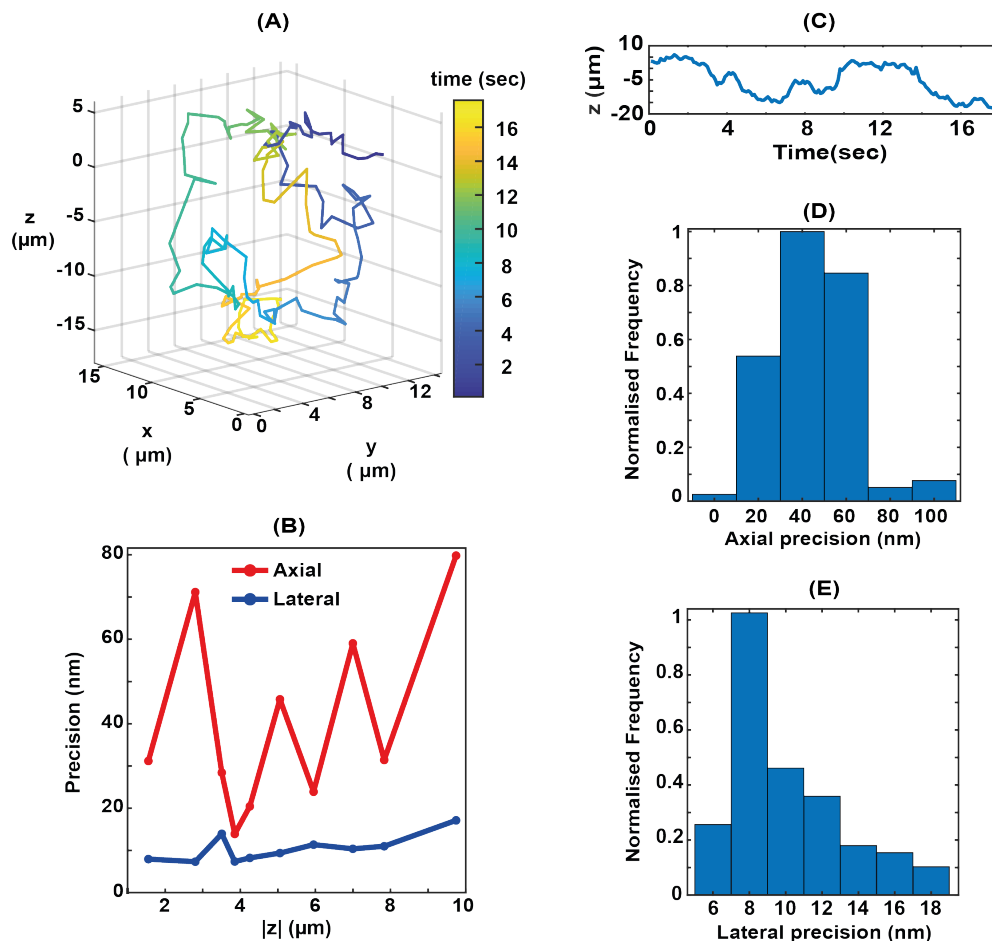
Fig. 5.19 Tracking a freely diffusing $100\,\text{nm}$ fluorescent bead over a depth of field of $25\,\mu\text{m}$ (A) Estimated $3D$ trajectory of a representative bead, using our localisation method. (C) Axial location of the bead as a function of time. (D)&(E) Histograms of lateral and axial precision respectively, throughout the depth of field. Axial and lateral precision was calculated from Figure 5.18 for comparable numbers of photons.

The capability of the system with respect to data acquisition across an extended DOF of $25\,\mu\text{m}$, was demonstrated by imaging $100\,\text{nm}$ fluorescent beads, freely diffusing in water. Data from a typical bead, tracked for $18\,\text{sec}$, at $100\,\text{msec}$ intervals is summarised in Fig. 5.19. The bead was localised in each frame using the workflow discussed in Section 5.4.2. Slope of the cone, m, was converted into z positions using the experimental calibration curve plotted in Figure 5.17F. Localisation precision in (B), (D) and (E) were obtained from Figure 5.18. For each axial position of the bead, we looked up the corresponding lateral and axial precisions in the figure.

We also performed experiments to demonstrate the feasibility of single molecule imaging using light field microscopy. Membrane (TCR) proteins labelled with cage-552 dye were imaged in fixed T-cells, using 561 nm illumination and 20 msec exposure time. Histones labelled with alexa-647 were imaged in Drosophila spermatocytes, using 638 nm illumination and 50 msec exposure time (see *Materials and Methods* section at the end of this chapter for the preparation of the imaged samples). Typical fluorescent traces from each set of experiments are plotted in Fig. 5.20. These exhibit discrete signal levels, specific to the single molecule photobleaching events [156]. This shows the potential of the technique for single molecule localisation microscopy.
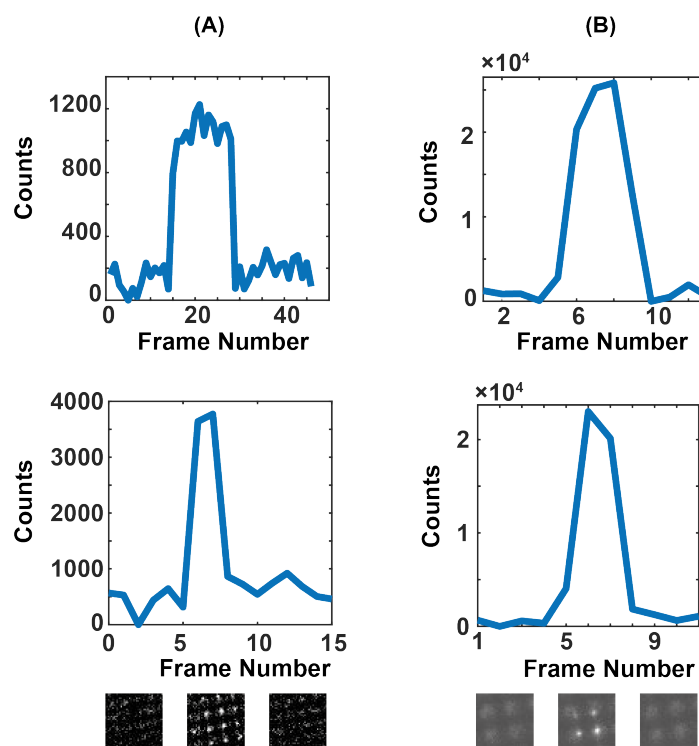
Fig. 5.20 Single molecule photobleaching events captured using light field microscopy. Photobleaching curves for (A) CAGE-552 fluorophores imaged on the surface of fixed T-cells and (B) Alexa-647 labelled histones in Drosophila spermatocytes. In each case the integrated intensity is plotted as a function of time.

5.7 Discussion and Future Work

Results presented in this chapter show that the light field based localisation microscopy has significant potential to provide extended DOF with high localisation precision in all three spatial dimensions. Through simulations and experiments we showed that the technique can

provide sub-diffraction limit precision over a DOF of more than $20\,\mu$m. While proof-of-principle experiments were carried out using fluorescent beads, which emit relatively large numbers of photons, the viability of light field microscopy as a single molecule imaging technique was demonstrated by detecting emissions from single fluorophore molecules in labelled cells.

Experiments discussed in the chapter were carried out using a sub-optimal, off-the-shelf, lenslet array. It is anticipated that modification of the array characteristics along with further development of the algorithm will facilitate the application of light field microscopy to imaging single molecules throughout the entire volume of a cell. In order to reach this goal, the localisation precision for low number of photons must be improved.

Such improvements can be readily achieved by optimising the lenslet array pitch according to the required DOF. An array with smaller lenses gives better lateral precision, particularly close to the object plane, but suffers in terms of shot noise due to the distribution of photons over large number of spots. Using an array with large lenses solves this problem but localisation accuracy and precision are affected in this case. So, the optimal lens size would give the best localisation precision over the required DOF for the typical number of photons involved in single molecule experiments. Another simple modification can be to position the array in the conjugate BFP of the objective. In this configuration, the camera directly images sub-aperture views, the number of which is dictated by the number of μ-lenses spanning the diameter of the BFP. The localisation precision is dictated by the effective camera pixel size and the number of photons similar to the case of typical 2D single molecule imaging experiments. Moreover, such a configuration can give a uniform localisation precision over the entire DOF (as light is always split into the same number of spots, irrespective of the axial position of an emitter).

Improving the image analysis pipeline will involve the application of advanced algorithms to track overlapping spots in the sub-aperture views. Moreover, localising emitters in the reconstructed volumes, obtained from deconvolution [155] or back-projections from multiple angular views [157], could also be applied . However unlike these reconstruction methods, the calibration curve involved in the discussed method absorbs the effect of systematic aberrations of the microscope. This is beneficial for high precision and accuracy requirements in localisation microscopy.

5.8   Summary

The chapter described the application of a lenslet array to obtain multiple angular views of an emitter. Disparity between these views was used to calculate the three dimensional position

of the emitter. The proposed image analysis pipeline was tested on simulated data before its application to characterise and calibrate the light field microscope. We achieved a DOF of over $20\,\mu$m with a precision of $50\,$nm in all three spatial dimensions. While proof-of-principle experiments were carried out using fluorescent beads, which emit relatively large numbers of photons, the potential of light field microscopy for single molecule imaging was shown by detecting emissions from single fluorophores in labelled cells. The prototype system incorporated a sub-optimal off-the-shelf lenslet array. It is anticipated that modification of the array characteristics along with further developments in localisation algorithms will make light field based localisation microscopy an attractive tool to image single molecules throughout the volume of a cell.

5.9 Contributions

Light field imaging modality was included in the microscope by me with inputs from Kevin O'Holleran. I also optimised the imaging conditions and carried out the experiments with the help from Ruth Sims. Simulated images of the light field PSF, under different conditions, were generated by Ruth Sims with my inputs. She also designed and implemented the script for the rectification of light field images and generation of sub-aperture views from them. I wrote the script for the localisation of emitters in the sub-aperture views, with inputs from Ruth Sims and Leila Muresan. This involved tracking of emitters over sub-aperture views and cone fitting. Simulated and experimental data was analysed by me for the localisation of emitters in the sub-aperture views. Rectification of the experimental data was performed by Ruth Sims. I also carried out the subsequent data analysis to obtain all the results presented in the chapter. Labelled T-cells and primary spermatocytes were provided by the *Lee Lab* and the *White Lab* respectively.

5.10   Materials and Methods

Sample preparation and labelling for spermatocytes is discussed in Appendix 4.10. This section covers the t-cell labelling protocol, which were (labelled and) kindly provided to us by the *Lee Lab* based in the *Department of Chemistry*.

Around 10^6 T cells were labelled with 200 nM of the labelled TCR-(CAGE552) fabs (anti CD3, UCHT-1) on ice for 25 minutes. Cells were then washed three times in filtered PBS (involving centrifugation). Labelled T cells were fixed in 4% paraformaldehyde (Sigma) and 0.2% glutaraldehyde (Sigma) for 60 minutes at room temperature. The fixed cells were washed three times in filtered PBS and suspended in filtered PBS. For imaging, cells were stuck on a glass bottom dish and imaged using 561 nm excitation, with regular bursts of 405 nm activation laser.

Chapter 6

Conclusion

6.1 Thesis Summary

The thesis described the design, development and optimisation of a multifunctional localisation based super-resolution microscope at CAIC. In Chapter 1, the origin of the resolution limit in optical microscopy from the diffraction properties of light was explained. Basics of localisation microscopy along with the methods to extend its DOF were also discussed. Chapter 2 explained the development and optimisation of a super-resolution microscope with the following functionalities:

- two-dimensional localisation microscopy

- dual-colour localisation microscopy

- three-dimensional localisation microscopy using DHPSF

- light field localisation microscopy

Calibration and characterisation of the microscope was also discussed. This involved, determining the pixel dependent characteristics (gain and read noise) of sCMOS cameras and estimating the achievable localisation precision under different number of photons. Effects of SA on localisation microscopy were explored and a method to optimally adjust the correction collar of the objective to overcome the systematic SA in the microscope was proposed. An optimal alignment method to achieve high localisation accuracy over large FOVs in three-dimensional localisation microscopy was also proposed.

After characterisation and optimisation, the microscope was applied to image challenging biological samples, in collaboration with the research groups at the *Department of Physiology Development and Neuroscience*. The first application, discussed in Chapter 3, was to

investigate the dynamics of a DNA binding transcription factor involved in the Notch signalling pathway. Imaging was carried out at a depth of more than $20\,\mu$m from the surface of coverslips, in whole salivary glands of Drosophila. Careful consideration of SA was required to capture emissions from single fluorophores at such depths. We presented the use of motion blurring analysis to determine the presence of multiple diffusion populations in the localisation data. These populations were then precisely quantified by applying single particle tracking analysis.

In Chapter 4 application of the microscope to study the architecture of dense chromatin fibres in primary spermatocytes of Drosophila was presented. Imaging conditions and data analysis software were optimised to image nuclei with varying densities of labelling dye in different regions. Clustering analysis was used to detect clusters in the localisation data and to quantify their characteristics. The chapter also included characterisation and application of dual-colour localisation microscopy to investigate the arrangement of active transcription sites in chromatin fibres.

Chapter 5 proposed the use of light field localisation microscopy to overcome some of the shortcomings of the existing 3D single molecule imaging techniques. By calculating disparity between multiple angular views of an emitter, it was localised over a DOF of more than $20\,\mu$m with high precision in all three spatial dimensions. The image analysis pipeline was tested on simulated data before its application to calibrate the microscope using fluorescent beads. Effectiveness of the technique to image single fluorophore molecules was also discussed.

6.2   Optimisations and Novel Developments

The thesis presented optimised application of localisation microscopy to answer challenging biological questions. It also proposed a novel three-dimensional single molecule imaging technique to increase the DOF in localisation microscopy. These optimisations and developments are summarised below.

Optimisations: A method to overcome the systematic SAs in a microscope was presented, to maximise the efficiency of signal collection from single fluorophore molecules. This allowed us to efficiently carry out localisation microscopy in thick biological samples. We also proposed an alignment procedure to accurately perform three-dimensional localisation microscopy, involving phase modifying optics, over large FOVs. Motion blurring analysis was extended to detect and quantify multiple diffusion populations in the localisation data. Moreover, characterisation and optimised application of single molecule tracking to extract dynamics from short tracks (5-6 frames) was also discussed. Lastly, optimisation of imaging

conditions and localisation software to super-resolve nuclei with varying densities of the labelling dye, in their different regions, was also presented.

These optimisations allowed us to successfully image challenging biological samples on the localisation microscope developed as part of the PhD.

Novel Developments: The thesis also presented the use of light field imaging to extend the DOF in localisation microscopy. An image analysis pipeline to localise point emitters in light filed images was also proposed. Through simulations and experiments, it was shown that the technique, along with the proposed localisation method, could achieve a DOF of over $20\,\mu$m with high localisation precision. Potential of the technique to detect single molecule emissions was shown by carrying out localisation microscopy in labelled cells.

It is anticipated that future hardware and software modifications will make light field based localisation microscopy an attractive tool to image single molecules throughout the volume of a cell. Some of these modifications were also discussed in the thesis.

Appendix A

Splitting of Light and Precision

Suppose N is the total number of photons in a spot of standard deviation, σ. In the presence of shot noise, its localisation precision, P_{tot}, will be given as (for each lateral axis, obtained by ignoring the pixellation effects and background in Eq 1.17):

$$P_{tot} = \frac{\sigma}{\sqrt{N}} \tag{A.1}$$

If the photons are equally split into two spots, each of size σ, the localisation precision for each spot will be:

$$P_{split} = \frac{\sigma}{\sqrt{N/2}} \tag{A.2}$$

The centre of the two spots can be calculated as :

$$\text{Centre of Spots} = \left(\frac{x_2 - x_1}{2}, \frac{y_2 - y_1}{2} \right) \tag{A.3}$$

where (x_1, y_1) and (x_2, y_2) are the localised centres of the spots with the localisation error given by Eq A.2. The precision of localising the centre will be [158]:

$$
\begin{aligned}
\text{Overall Precision} &= 0.5 \times \sqrt{\left(\frac{\sigma}{\sqrt{N/2}} \right)^2 + \left(\frac{\sigma}{\sqrt{N/2}} \right)^2} \\
&= 0.5 \times \sigma \sqrt{\left(\frac{2}{N} \right) + \left(\frac{2}{N} \right)} \\
&= 0.5 \times \sigma \sqrt{\left(\frac{2 \times 2}{N} \right)} \\
&= \frac{\sigma}{\sqrt{N}}
\end{aligned}
\tag{A.4}
$$

So, splitting of signal into two spots (with the waist matching the original spot and having equal number of photons) does not result in any loss of precision. The analysis can be extended to the splitting of light into any arbitrary number of spots as well.

Appendix B

Zernike Polynomials

Zernike polynomials form a complete and orthogonal basis set over a unit circle [42]. In localisation microscopy, electric field in the BFP of the microscope is a circle of uniform magnitude with a phase dependent on the three-dimensional position of the emitter and aberrations (local to that emitter) in the sample. Hence, Zernike polynomials are useful for representing phase of the beam in this plane. Another major advantage of Zernike polynomials is that the commonly occurring aberrations such as coma, astigmatism and spherical aberrations can be represented as its different modes (coma: Z_3^{-1}, astigmatism: Z_2^2 and spherical aberrations Z_4^0).

Zernike polynomials are given by Eq. B.1 and first fifteen modes are shown in Figure B.1.

$$Z_n^m(r, \theta) = R_n^m(r) \cos(m\theta) \qquad m \geq 0$$
$$Z_n^{-m}(r, \theta) = R_n^m(r) \sin(m\theta) \qquad m < 0$$

(B.1)

where,

$$R_n^m(r) = \sum_{k=0}^{\frac{n-m}{2}} \frac{(-1)^k (n-k)!}{k!(\frac{n+m}{2} - k)!(\frac{n-m}{2} - k)!} r^{n-2k}$$

here, m and n are integers with $n \geq 0$, $n \geq m$ and $n - |m|$ an even number.

Eq B.1 shows that the Zernike polynomials represent balanced aberrations. This means that for a certain aberration in the optical system, Zernike representation is the sum of all possible terms that maximise amplitude of the PSF in the image plane. For example, Zernike representation of spherical aberrations contains a defocus term, because combination of the two gives maximum intensity in the image plane [159]. For a detailed discussion on Zernike polynomials and their properties see [42].
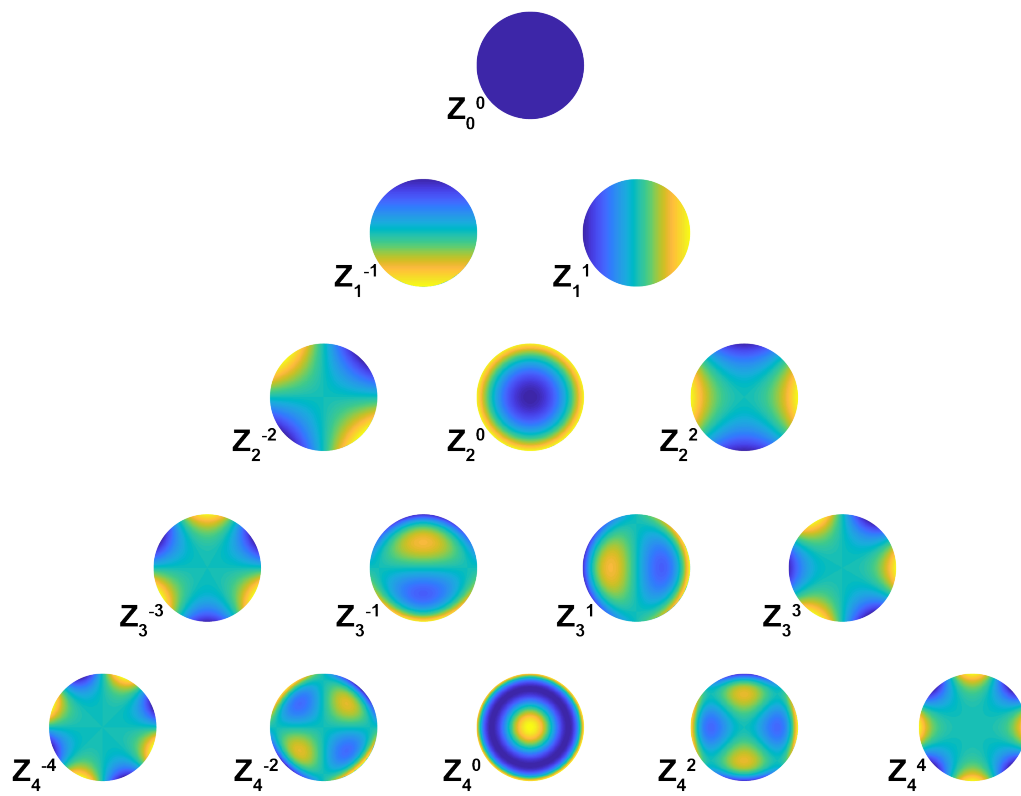
Fig. B.1 First fifteen Zernike modes

Appendix C

Beams with Rotating Intensity

In this appendix, we discuss beams with rotating intensity, which form the basis of the double helix point spread function (DHPSF). If $E(x,y,z)$ is the electric field at any point in the free space, it will be rotationally invariant if it fulfils the following equation:

$$|S(R(f[E(x,y,z_0)]))|^2 = |uE(x,y,z_0)|^2 \tag{C.1}$$

here, f is a beam propagation operator, which under the paraxial approximation is given by Eq 1.2. R and S are operators for beam rotation and scaling respectively.

Solution to C.1 can be found by representing the electric field as a superposition of Laguerre-Gaussian (LG) modes, given by Eq C.2 [160].

$$
\begin{aligned}
E(r,\phi,z_o) = &\sqrt{\frac{2p!}{\pi(p+|l|)!}} \frac{1}{w(z)} \left(\frac{r\sqrt{2}}{w(z)}\right)^{|l|} \exp\left[\frac{-r^2}{w(z)^2}\right] L_p^{|l|}\left[\frac{2r^2}{w(z)^2}\right] \exp\left[il\phi\right] \\
&\exp\left[\frac{ikr^2z}{2(z^2+z_r^2)}\right] \exp\left[-i(2p+|l|+1)\tan^-\left[\frac{z}{z_r}\right]\right]
\end{aligned}
\tag{C.2}
$$

here, l and p are azimuthal and radial components of the beam respectively, $L_p^{|l|}$ is an associated Laguerre polynomial, z_r is the Rayleigh range of the beam and w_z is its $1/e$ radius. See [160] for a detailed review of LG beams.

For such beams, operators in Eq C.1 can be defined as follows:

$$
\begin{aligned}
f[z](E(r,\phi,z_0) &= f(E(x,y,z_0+z) \\
R[\phi_0](E(r,\phi,z_0) &= E(r,\phi+\phi_0,z_0) \\
S[a](E(r,\phi,z_0) &= E(ar,\phi,z_0)
\end{aligned}
$$

If such a representation of electric field is used to solve Eq C.1, beams with rotating intensity are obtained, if LG modes are chosen along a straight line in the lp-space i.e. $\frac{\delta p}{\delta l} = V_1$ (where, V_1 is a constant). Rate of rotation of such a beam is given as:

$$\text{Rate of rotation} = \frac{V_1}{1+z^2} \tag{C.3}$$

So, the rate of rotation is maximum near the beam waist and it drops to 0 as $z \to \infty$

Another important property of these beams is that the number of rotating lobes is determined by the multiples of l superimposed to form the beam. For example, the beam has 2 lobes if the superimposed LG modes are $(0,0),(2,2),(4,4),(6,6),(8,8)$. Similarly 4 lobes are obtained for $(0,0),(4,4),(8,8)$. This is shown in Figure C.1B&E respectively.
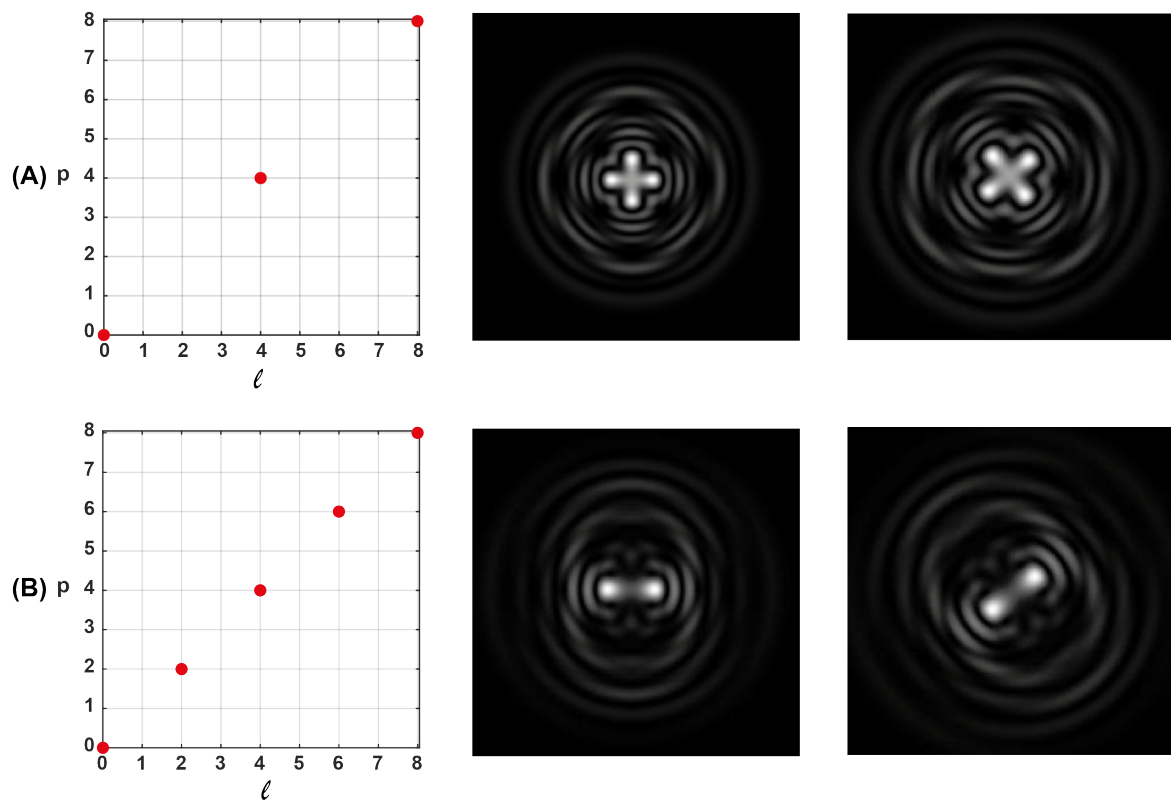
Fig. C.1 Super-position of LG modes along a straight line result in beams that rotate as a function of their propagation. Number of rotating lobes is determined by the multiples of l superimposed to form the beam. (A) Rotating beam with four lobes, (B) Rotating beam with two lobes.

Appendix D

Control of the Microscope

As discussed in Chapter 2, a LabVIEW software was written to control the microscope. The software included the following functionalities:

- Control of stages for three dimensional scanning with the required dwell time. Step size could be selected for each dimension separately.

- Simultaneous image acquisition, and subsequent storage, on two cameras (*Flash 4.0* and *Prime 95B*). Images could be acquired in all the formats supported by the cameras. The software allowed use of one camera at a time as well.

- Control of lasers in pulsed and continuous modes.

Control of different components from LabVIEW, allowed us to automate time-lapse imaging. This was especially useful for the characterisation of microscope for light field and DHPSF imaging. Layout of the software is below:
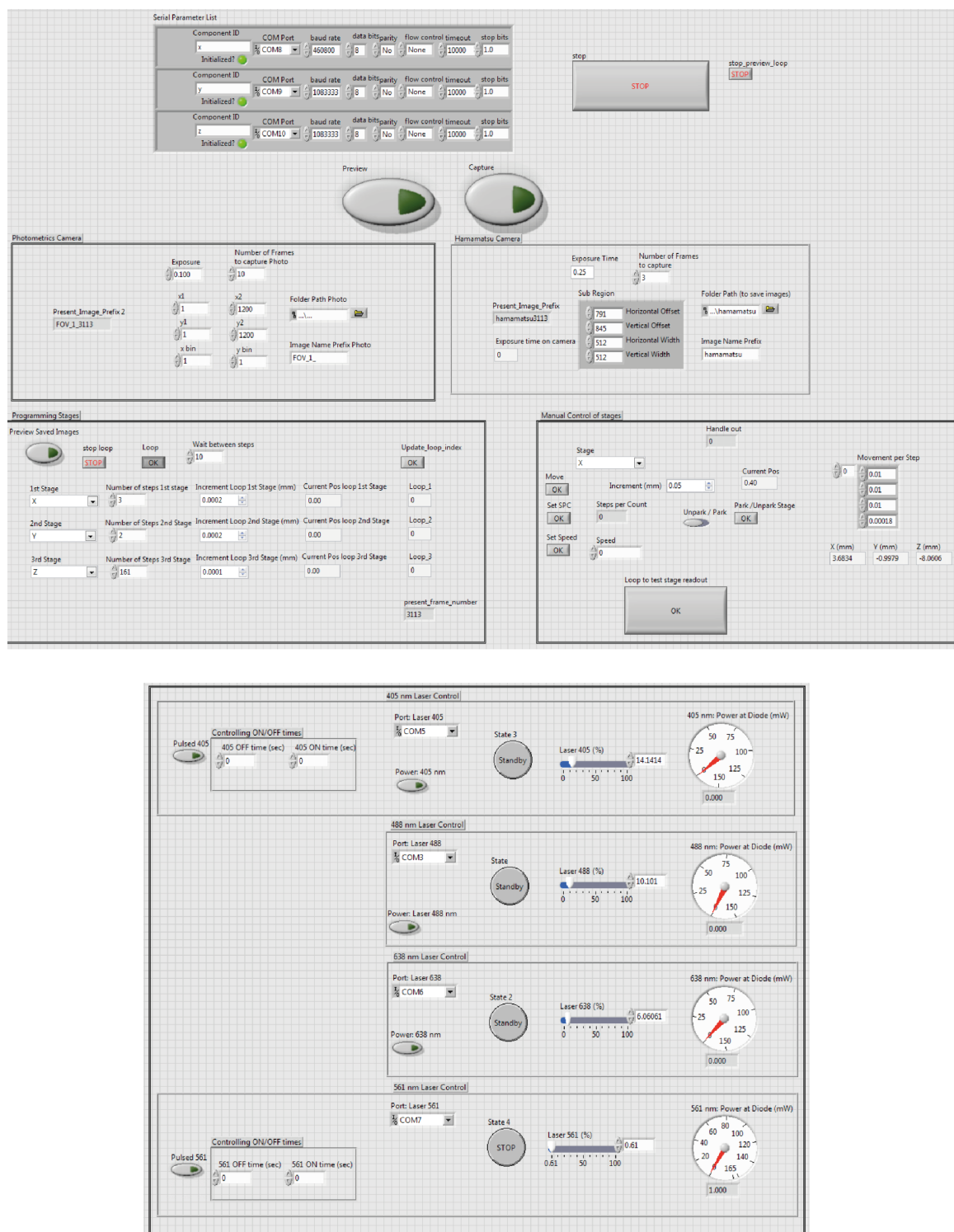
Fig. D.1 LabVIEW VI for the control of the microscope

References

[1] Howard Gest. The discovery of microorganisms by Robert Hooke and Antoni Van Leeuwenhoek, fellows of the Royal Society. *Notes and Records of the Royal Society*, 58(2):187–201, 2004.

[2] Adam JM Wollman, Richard Nudd, Erik G Hedlund, and Mark C Leake. From Animaculum to single molecules: 300 years of the light microscope. *Open biology*, 5(4):150019, 2015.

[3] Nobel Media. Popular information: Super-resolved fluorescence microscopy. *NobelPrize.org*, 2014.

[4] Nobel Media. The Nobel Prize in Chemistry 2014. *NobelPrize.org*, 2014.

[5] Bo Huang, Wenqin Wang, Mark Bates, and Xiaowei Zhuang. Three-dimensional super-resolution imaging by stochastic optical reconstruction microscopy. *Science (New York, N.Y.)*, 319(5864):810–813, February 2008.

[6] Sri Rama Prasanna Pavani, Michael A Thompson, Julie S Biteen, Samuel J Lord, Na Liu, Robert J Twieg, Rafael Piestun, and WE Moerner. Three-dimensional, single-molecule fluorescence imaging beyond the diffraction limit by using a double-helix point spread function. *Proceedings of the National Academy of Sciences*, 106(9):2995–2999, 2009.

[7] Alex von Diezmann, Yoav Shechtman, and WE Moerner. Three-dimensional localization of single molecules for super-resolution imaging and single-particle tracking. *Chemical reviews*, 117(11):7244–7275, 2017.

[8] J. Peatross and M. Ware. *Physics of Light and Optics*. optics.byu.edu, 3rd edition, 2015.

[9] Masud Mansuripur. Abbe's sine condition. *Optics and Photonics News*, 9(2):56–60, 1998.

[10] A. J. den Dekker and A. van den Bos. Resolution: a survey. *J. Opt. Soc. Am. A*, 14(3):547–557, Mar 1997.

[11] Bo Huang, Hazen Babcock, and Xiaowei Zhuang. Breaking the diffraction barrier: super-resolution imaging of cells. *Cell*, 143(7):1047–1058, 2010.

[12] Nobel Media. Scientific Background: Super-resolved fluorescence microscopy. *NobelPrize.org*, 2014.

[13] Eric Betzig, George H Patterson, Rachid Sougrat, O Wolf Lindwasser, Scott Olenych, Juan S Bonifacino, Michael W Davidson, Jennifer Lippincott-Schwartz, and Harald F Hess. Imaging intracellular fluorescent proteins at nanometer resolution. *Science (New York, N.Y.)*, 313:1642–1645, September 2006.

[14] Michael J Rust, Mark Bates, and Xiaowei Zhuang. Sub-diffraction-limit imaging by stochastic optical reconstruction microscopy (STORM). *Nature methods*, 3:793–795, October 2006.

[15] Sean A. McKinney, Christopher S. Murphy, Kristin L. Hazelwood, Michael W. Davidson, and Loren L. Looger. A bright and photostable photoconvertible fluorescent protein. *Nature Methods*, 6:131–133, February 2009.

[16] Mark Bates, Timothy R. Blosser, and Xiaowei Zhuang. Short-Range Spectroscopic Ruler Based on a Single-Molecule Optical Switch. *Phys. Rev. Lett.*, 94:108101, Mar 2005.

[17] Graham T Dempsey, Joshua C Vaughan, Kok Hao Chen, Mark Bates, and Xiaowei Zhuang. Evaluation of fluorophores for optimal performance in localization-based super-resolution imaging. *Nature methods*, 8:1027–1036, November 2011.

[18] Steven F. Lee, Quentin Vérolet, and Alexandre Fürstenberg. Improved Super-Resolution Microscopy with Oxazine Fluorophores in Heavy Water. *Angewandte Chemie International Edition*, 52(34):8948–8951, July 2013.

[19] Daria M. Shcherbakova, Prabuddha Sengupta, Jennifer Lippincott-Schwartz, and Vladislav V. Verkhusha. Photocontrollable Fluorescent Proteins for Superresolution Imaging. *Annual Review of Biophysics*, 43(1):303–329, 2014. PMID: 24895855.

[20] Alex Small and Shane Stahlheber. Fluorophore localization algorithms for super-resolution microscopy. *Nature Methods*, 11:267–279, March 2014.

[21] Sarah Frisken Gibson and Frederick Lanni. Experimental test of an analytical model of aberration in an oil-immersion objective lens used in three-dimensional light microscopy. *J. Opt. Soc. Am. A*, 9(1):154–166, Jan 1992.

[22] E. Wolf B. Richards. Electromagnetic diffraction in optical systems, ii. Structure of the image field in an aplanatic system. *Proceedings of the Royal Society of London A: Mathematical, Physical and Engineering Sciences*, 253(1274):358–379, 1959.

[23] Sjoerd Stallinga and Bernd Rieger. Accuracy of the Gaussian point spread function model in 2D localization microscopy. *Optics express*, 18(24):24461–24476, 2010.

[24] Kim I Mortensen, L Stirling Churchman, James A Spudich, and Henrik Flyvbjerg. Optimized localization analysis for single-molecule tracking and super-resolution microscopy. *Nature Methods*, 7:377, apr 2010.

[25] Michael K. Cheezum, William F. Walker, and William H. Guilford. Quantitative Comparison of Algorithms for Tracking Single Fluorescent Particles. *Biophysical Journal*, 81(4):2378 – 2388, 2001.

[26] Bo Zhang, Josiane Zerubia, and Jean-Christophe Olivo-Marin. Gaussian approximations of fluorescence microscope point-spread function models. *Appl. Opt.*, 46(10):1819–1829, Apr 2007.

[27] Daniel Sage, Thanh-An Pham, Hazen Babcock, Tomas Lukes, Thomas Pengo, Jerry Chao, Ramraj Velmurugan, Alex Herbert, Anurag Agrawal, Silvia Colabrese, et al. Super-resolution fight club: assessment of 2d and 3d single-molecule localization microscopy software. *Nature methods*, page 1, 2019.

[28] Mikael P Backlund, Matthew D Lew, Adam S Backer, Steffen J Sahl, and WE Moerner. The Role of Molecular Dipole Orientation in Single-Molecule Fluorescence Microscopy and Implications for Super-Resolution Imaging. *ChemPhysChem*, 15(4):587–599, 2014.

[29] Russell E Thompson, Daniel R Larson, and Watt W Webb. Precise nanometer localization analysis for individual fluorescent probes. *Biophysical journal*, 82(5):2775–2783, 2002.

[30] Steve Wolter, Mark Schüttpelz, Marko Tscherepanow, Sebastian Van de Linde, Mike Heilemann, and Markus Sauer. Real-time computation of subdiffraction-resolution fluorescence images. *Journal of microscopy*, 237(1):12–22, 2010.

[31] Alex Herbert. Single Molecule Light Microscopy ImageJ Plugins, 2014.

[32] Norman Brede and Melike Lakadamyali. GraspJ: an open source, real-time analysis package for super-resolution imaging. *Optical Nanoscopy*, 1(1):11, Dec 2012.

[33] Eric J Rees, Miklos Erdelyi, Gabriele S Kaminski Schierle, Alex Knight, and Clemens F Kaminski. Elements of image processing in localization microscopy. *Journal of Optics*, 15(9):094012, 2013.

[34] Leila Muresan, Jaroslaw Jacak, Erich Peter Klement, Jan Hesse, and Gerhard J Schutz. Microarray analysis at single-molecule resolution. *IEEE transactions on nanobioscience*, 9(1):51–58, 2010.

[35] Jean-Christophe Olivo-Marin. Extraction of spots in biological images using multiscale products. *Pattern recognition*, 35(9):1989–1996, 2002.

[36] I Izeddin, J Boulanger, V Racine, CG Specht, A Kechkar, D Nair, A Triller, D Choquet, M Dahan, and JB Sibarita. Wavelet analysis for single molecule localization microscopy. *Optics express*, 20(3):2081–2095, 2012.

[37] Ricardo Henriques, Mickael Lelek, Eugenio F. Fornasiero, Flavia Valtorta, Christophe Zimmer, and Musa M. Mhlanga. QuickPALM: 3D real-time photoactivation nanoscopy image processing in ImageJ. *Nature Methods*, 7:339–340, 2010.

[38] Andrew J. Berglund, Matthew D. McMahon, Jabez J. McClelland, and J. Alexander Liddle. Fast, bias-free algorithm for tracking single particles with variable size and shape. *Opt. Express*, 16(18):14064–14075, Sep 2008.

[39] CJR Sheppard. Depth of field in optical microscopy. *Journal of Microscopy*, 149(1):73–75, 1988.

[40] IT Young, R Zagers, LJ Van Vliet, J Mullikin, F Boddeke, and H Netten. Depth-of-focus in microscopy. In *8th Scandinavian Conference on Image Analysis, Tromso, Norway*. Citeseer, 1993.

[41] Yiming Li, Markus Mund, Philipp Hoess, Joran Deschamps, Ulf Matti, Bianca Nijmeijer, Vilma Jimenez Sabinina, Jan Ellenberg, Ingmar Schoen, and Jonas Ries. Real-time 3D single-molecule localization using experimental point spread functions. *Nature Methods*, 15:367–369, May 2018.

[42] Vasudevan Lakshminarayanan and Andre Fleck. Zernike polynomials: a guide. *Journal of Modern Optics*, 58(7):545–561, 2011.

[43] Rafael Piestun, Yoav Y Schechner, and Joseph Shamir. Propagation-invariant wave fields with finite energy. *JOSA A*, 17(2):294–303, 2000.

[44] Yoav Y. Schechner, Rafael Piestun, and Joseph Shamir. Wave propagation with rotating intensity distributions. *Phys. Rev. E*, 54:R50–R53, Jul 1996.

[45] Sri Rama Prasanna Pavani and Rafael Piestun. High-efficiency rotating point spread functions. *Opt. Express*, 16(5):3484–3489, Mar 2008.

[46] Alexander R Carr, Aleks Ponjavic, Srinjan Basu, James McColl, Ana Mafalda Santos, Simon Davis, Ernest D Laue, David Klenerman, and Steven F Lee. Three-dimensional super-resolution in eukaryotic cells using the double-helix point spread function. *Biophysical journal*, 112(7):1444–1454, 2017.

[47] *In vivo three-dimensional superresolution fluorescence tracking using a double-helix point spread function*, volume 7571, 2010.

[48] Matthew D Lew, Alexander R S von Diezmann, and W E Moerner. Easy-DHPSF open-source software for three-dimensional localization of single molecules with precision beyond the optical diffraction limit. *Protocol exchange*, 2013, February 2013.

[49] Yoav Shechtman, Steffen J. Sahl, Adam S. Backer, and W. E. Moerner. Optimal Point Spread Function Design for 3D Imaging. *Phys. Rev. Lett.*, 113:133902, Sep 2014.

[50] Raimund J. Ober, Sripad Ram, and E. Sally Ward. Localization Accuracy in Single-Molecule Microscopy. *Biophysical Journal*, 86(2):1185 – 1200, 2004.

[51] Yoav Shechtman, Lucien E. Weiss, Adam S. Backer, Steffen J. Sahl, and W. E. Moerner. Precise Three-Dimensional Scan-Free Multiple-Particle Tracking over Large Axial Ranges with Tetrapod Point Spread Functions. *Nano Letters*, 15(6):4194–4199, 2015. PMID: 25939423.

[52] Erdal Toprak, Hamza Balci, Benjamin H. Blehm, and Paul R. Selvin. Three-Dimensional Particle Tracking via Bifocal Imaging. *Nano Letters*, 7(7):2043–2045, 2007. PMID: 17583964.

[53] Manuel F Juette, Travis J Gould, Mark D Lessard, Michael J Mlodzianoski, Bhupendra S Nagpure, Brian T Bennett, Samuel T Hess, and Joerg Bewersdorf. Three-dimensional sub–100 nm resolution fluorescence microscopy of thick samples. *Nature methods*, 5(6):527, 2008.

[54] Sripad Ram, Dongyoung Kim, Raimund J Ober, and E Sally Ward. 3D single molecule tracking with multifocal plane microscopy reveals rapid intercellular transferrin transport at epithelial cell barriers. *Biophysical journal*, 103(7):1594–1603, 2012.

[55] Colin JR Sheppard and Min Gu. Aberration compensation in confocal microscopy. *Applied optics*, 30(25):3563–3568, 1991.

[56] Edward J Botcherby, Rimas Juskaitis, Martin J Booth, and Tony Wilson. Aberration-free optical refocusing in high numerical aperture microscopy. *Optics letters*, 32(14), 2007.

[57] Paul A Dalgarno, Heather IC Dalgarno, Aurélie Putoud, Robert Lambert, Lynn Paterson, David C Logan, David P Towers, Richard J Warburton, and Alan H Greenaway. Multiplane imaging and three dimensional nanoscale particle tracking in biological microscopy. *Optics express*, 18(2):877–884, 2010.

[58] Sara Abrahamsson, Jiji Chen, Bassam Hajj, Sjoerd Stallinga, Alexander Y Katsov, Jan Wisniewski, Gaku Mizuguchi, Pierre Soule, Florian Mueller, Claire Dugast Darzacq, et al. Fast multicolor 3D imaging using aberration-corrected multifocus microscopy. *Nature methods*, 10(1):60, 2012.

[59] Bassam Hajj, Mohamed El Beheiry, and Maxime Dahan. PSF engineering in multifocus microscopy for increased depth volumetric imaging. *Biomedical optics express*, 7(3):726–731, 2016.

[60] U. R. Dhond and J. K. Aggarwal. Structure from stereo-a review. *IEEE Transactions on Systems, Man, and Cybernetics*, 19(6):1489–1510, Nov 1989.

[61] Yujie Sun, Jennine Dawicki McKenna, John M Murray, E Michael Ostap, and Yale E Goldman. Parallax: high accuracy three-dimensional single molecule tracking using split images. *Nano letters*, 9(7):2676–2682, 2009.

[62] Yujie Sun, Osamu Sato, Felix Ruhnow, Mark E Arsenault, Mitsuo Ikebe, and Yale E Goldman. Single-molecule stepping and structural dynamics of myosin X. *Nature structural & molecular biology*, 17(4):485, 2010.

[63] Junichiro Yajima, Kana Mizutani, and Takayuki Nishizaka. A torque component present in mitotic kinesin Eg5 revealed by three-dimensional tracking. *Nature Structural and Molecular Biology*, 15(10):1119, 2008.

[64] Wesley R Legant, Lin Shao, Jonathan B Grimm, Timothy A Brown, Daniel E Milkie, Brian B Avants, Luke D Lavis, and Eric Betzig. High-density three-dimensional localization microscopy across large volumes. *Nature methods*, 13(4):359, 2016.

[65] Sohaib Abdul Rehman, Alexander R Carr, Martin O Lenz, Steven F Lee, and Kevin O'Holleran. Maximizing the field of view and accuracy in 3D Single Molecule Localization Microscopy. *Optics express*, 26(4):4631–4637, 2018.

[66] Charles D. Howard Travis Goulette and Michael W. Davidson. Infinity Optical Systems. https://www.microscopyu.com/microscopy-basics/infinity-optical-systems.

[67] Saumya Saurabh, Suvrajit Maji, and Marcel P Bruchez. Evaluation of sCMOS cameras for detection and localization of single Cy5 molecules. *Optics express*, 20(7):7338–7349, 2012.

[68] Fang Huang, Tobias MP Hartwich, Felix E Rivera-Molina, Yu Lin, Whitney C Duim, Jane J Long, Pradeep D Uchil, Jordan R Myers, Michelle A Baird, Walther Mothes, et al. Video-rate nanoscopy using sCMOS camera–specific single-molecule localization algorithms. *Nature methods*, 10(7):653, 2013.

[69] M Newberry. Tech note: pixel response effects on CCD camera gain calibration. *Mirametrics Inc., Copy right*, 1998.

[70] Zhen-Li Huang, Hongyu Zhu, Fan Long, Hongqiang Ma, Lingsong Qin, Yongfeng Liu, Jiuping Ding, Zhihong Zhang, Qingming Luo, and Shaoqun Zeng. Localization-based super-resolution microscopy with an sCMOS camera. *Optics Express*, 19(20):19156–19168, 2011.

[71] Abbas El Gamal and Helmy Eltoukhy. CMOS image sensors. *IEEE Circuits and Devices Magazine*, 21(3):6–20, 2005.

[72] Steve Ross. Correcting for Spherical Aberration with a Correction Collar. https://www.ibiology.org/talks/spherical-aberattion/, March 2012.

[73] Jun Zeng, Pierre Mahou, Marie-Claire Schanne-Klein, Emmanuel Beaurepaire, and Delphine Débarre. 3D resolved mapping of optical aberrations in thick tissues. *Biomedical optics express*, 3:1898–1913, August 2012.

[74] P. Török, P. Varga, Z. Laczik, and G. R. Booker. Electromagnetic diffraction of light focused through a planar interface between materials of mismatched refractive indices: an integral representation. *Journal of the Optical Society of America A. Optics, Image Science, and Vision*, 12(2):325–332, 1995.

[75] P Török and P Varga. Electromagnetic diffraction of light focused through a stratified medium. *Applied optics*, 36:2305–2312, April 1997.

[76] Martin J Booth. Adaptive optics in microscopy. *Philosophical Transactions of the Royal Society of London A: Mathematical, Physical and Engineering Sciences*, 365(1861):2829–2843, 2007.

[77] Virendra N. Mahajan. Zernike Polynomials and Optical Aberrations. *Appl. Opt.*, 34(34):8060–8062, Dec 1995.

[78] Akifumi Yoshida. Spherical aberration in beam optical systems. *Applied optics*, 21(10):1812–1816, 1982.

[79] T. D. Milster and E. P. Walker. Figures of merit for laser beam quality. In J. M. Darchuk, editor, *Laser Energy Distribution Profiles: Measurement and Applications*, volume 1834 of *procspie*, pages 79–85, April 1993.

[80] J. P. Mills and B. J. Thompson. Effect of aberrations and apodization on the performance of coherent optical systems. i - The amplitude impulse response. ii - Imaging. *Journal of the Optical Society of America A*, 3:694–716, May 1986.

[81] Majid Badieirostami, Matthew D Lew, Michael A Thompson, and WE Moerner. Three-dimensional localization precision of the double-helix point spread function versus astigmatism and biplane. *Applied physics letters*, 97(16):161103, 2010.

[82] Matthew D Lew, Michael A Thompson, Majid Badieirostami, and WE Moerner. In vivo three-dimensional superresolution fluorescence tracking using a double-helix point spread function. In *Single Molecule Spectroscopy and Imaging III*, volume 7571, page 75710Z. International Society for Optics and Photonics, 2010.

[83] Alex von Diezmann, Maurice Y Lee, Matthew D Lew, and WE Moerner. Correcting field-dependent aberrations with nanoscale accuracy in three-dimensional single-molecule localization microscopy. *Optica*, 2(11):985–993, 2015.

[84] Bo Shuang, Wenxiao Wang, Hao Shen, Lawrence J Tauzin, Charlotte Flatebo, Jianbo Chen, Nicholas A Moringo, Logan DC Bishop, Kevin F Kelly, and Christy F Landes. Generalized recovery algorithm for 3D super-resolution microscopy using rotating point spread functions. *Scientific reports*, 6:30826, 2016.

[85] Yoav Shechtman, Anna-Karin Gustavsson, Petar N Petrov, Elisa Dultz, Maurice Y Lee, Karsten Weis, and WE Moerner. Observation of live chromatin dynamics in cells via 3d localization microscopy using tetrapod point spread functions. *Biomedical optics express*, 8(12):5735–5748, 2017.

[86] Yoav Shechtman, Lucien E Weiss, Adam S Backer, Maurice Y Lee, and WE Moerner. Multicolour localization microscopy by point-spread-function engineering. *Nature photonics*, 10(9):590, 2016.

[87] Maria J Gomez-Lamarca, Julia Falo-Sanjuan, Robert Stojnic, Sohaib Abdul Rehman, Leila Muresan, Matthew L Jones, Zoe Pillidge, Gustavo Cerda-Moya, Zhenyu Yuan, Sarah Baloul, et al. Activation of the Notch Signaling Pathway In Vivo Elicits Changes in CSL Nuclear Dynamics. *Developmental cell*, 44(5):611–623, 2018.

[88] Craig S Nowell and Freddy Radtke. Notch as a tumour suppressor. *Nature reviews. Cancer*, 17:145–159, March 2017.

[89] Panagiotis Ntziachristos, Jing Shan Lim, Julien Sage, and Iannis Aifantis. From fly wings to targeted cancer therapies: a centennial for notch signaling. *Cancer cell*, 25:318–334, March 2014.

[90] Sarah J Bray. Notch signalling: a simple pathway becomes complex. *Nature reviews Molecular cell biology*, 7(9):678, 2006.

[91] Sarah J Bray. Notch signalling in context. *Nature reviews. Molecular cell biology*, 17:722–735, November 2016.

[92] Raphael Kopan and Maria Xenia G Ilagan. The canonical Notch signaling pathway: unfolding the activation mechanism. *Cell*, 137:216–233, April 2009.

[93] Scott Barolo, Tammie Stone, Anne G Bang, and James W Posakony. Default repression and Notch signaling: Hairless acts as an adaptor to recruit the corepressors Groucho and dCtBP to Suppressor of Hairless. *Genes & development*, 16:1964–1976, August 2002.

[94] V Morel, M Lecourtois, O Massiani, D Maier, A Preiss, and F Schweisguth. Transcriptional repression by suppressor of hairless involves the binding of a hairless-dCtBP complex in Drosophila. *Current biology : CB*, 11:789–792, May 2001.

[95] T Borggrefe and F Oswald. The Notch signaling pathway: transcriptional regulation at Notch target genes. *Cellular and molecular life sciences : CMLS*, 66:1631–1646, May 2009.

[96] Kelly J Collins, Zhenyu Yuan, and Rhett A Kovall. Structure and function of the CSL-KyoT2 corepressor complex: a negative regulator of Notch signaling. *Structure (London, England : 1993)*, 22:70–81, January 2014.

[97] Bradley D VanderWielen, Zhenyu Yuan, David R Friedmann, and Rhett A Kovall. Transcriptional repression in the Notch pathway: thermodynamic characterization of CSL-MINT (Msx2-interacting nuclear target protein) complexes. *The Journal of biological chemistry*, 286:14892–14902, April 2011.

[98] Zhenyu Yuan, Heiko Praxenthaler, Nassif Tabaja, Rubben Torella, Anette Preiss, Dieter Maier, and Rhett A Kovall. Structure and Function of the Su(H)-Hairless Repressor Complex, the Major Antagonist of Notch Signaling in Drosophila melanogaster. *PLoS biology*, 14:e1002509, July 2016.

[99] Alena Krejcí and Sarah Bray. Notch activation stimulates transient and selective binding of Su(H)/CSL to target enhancers. *Genes & development*, 21:1322–1327, June 2007.

[100] Hongfang Wang, Chongzhi Zang, Len Taing, Kelly L Arnett, Yinling Joey Wong, Warren S Pear, Stephen C Blacklow, X Shirley Liu, and Jon C Aster. NOTCH1-RBPJ complexes drive target gene expression through dynamic interactions with superenhancers. *Proceedings of the National Academy of Sciences of the United States of America*, 111:705–710, January 2014.

[101] David Castel, Philippos Mourikis, Stefanie J J Bartels, Arie B Brinkman, Shahragim Tajbakhsh, and Hendrik G Stunnenberg. Dynamic binding of RBPJ is determined by Notch signaling status. *Genes & development*, 27:1059–1071, May 2013.

[102] Experimental tool: mEos3.2. FlyBase 2.0: the next generation.

[103] Philip Gröger, Nicole Poulsen, Jennifer Klemm, Nils Kröger, and Michael Schlierf. Establishing super-resolution imaging for proteins in diatom biosilica. *Scientific reports*, 6:36824, 2016.

[104] Hideaki Mizuno, Tapas Kumar Mal, Kit I Tong, Ryoko Ando, Toshiaki Furuta, Mitsuhiko Ikura, and Atsushi Miyawaki. Photo-induced peptide cleavage in the green-to-red conversion of a fluorescent protein. *Molecular cell*, 12(4):1051–1058, 2003.

[105] Douglas Cromey. The importance of #1.5 thickness coverslips for Microscopy. Technical report, The University of Arizona, 2017.

[106] Chanho Kim, Fuxin Li, Arridhana Ciptadi, and James M Rehg. Multiple hypothesis tracking revisited. In *Proceedings of the IEEE International Conference on Computer Vision*, pages 4696–4704, 2015.

[107] Nicolas Chenouard. Spot Detection Import and Export. icy Plugin List.

[108] Nicolas Chenouard, Isabelle Bloch, and Jean-Christophe Olivo-Marin. Multiple hypothesis tracking for cluttered biological image sequences. *IEEE transactions on pattern analysis and machine intelligence*, 35(11):2736–3750, 2013.

[109] Michael J Saxton. Lateral diffusion in an archipelago. Single-particle diffusion. *Biophysical journal*, 64(6):1766–1780, 1993.

[110] Laura Weimann, Kristina A Ganzinger, James McColl, Kate L Irvine, Simon J Davis, Nicholas J Gay, Clare E Bryant, and David Klenerman. A quantitative comparison of single-dye tracking analysis tools using Monte Carlo simulations. *PLoS One*, 8(5):e64287, 2013.

[111] Michael J Saxton and Ken Jacobson. Single-particle tracking: applications to membrane dynamics. *Annual review of biophysics and biomolecular structure*, 26(1):373–399, 1997.

[112] Michael J Saxton. Single-particle tracking: the distribution of diffusion coefficients. *Biophysical journal*, 72(4):1744–1753, 1997.

[113] Fredrik Persson, Martin Lindén, Cecilia Unoson, and Johan Elf. Extracting intracellular diffusive states and transition rates from single-molecule tracking data. *Nature methods*, 10(3):265, 2013.

[114] Thomas J Etheridge, Rémi L Boulineau, Alex Herbert, Adam T Watson, Yasukazu Daigaku, Jem Tucker, Sophie George, Peter Jönsson, Matthieu Palayret, David Lando, et al. Quantification of DNA-associated proteins inside eukaryotic cells using single-molecule localization microscopy. *Nucleic acids research*, 42(19):e146–e146, 2014.

[115] John T Lis. Imaging Drosophila gene activation and polymerase pausing in vivo. *Nature*, 450(7167):198, 2007.

[116] Jonathan B Grimm, Brian P English, Jiji Chen, Joel P Slaughter, Zhengjian Zhang, Andrey Revyakin, Ronak Patel, John J Macklin, Davide Normanno, Robert H Singer, et al. A general method to improve fluorophores for live-cell and single-molecule microscopy. *Nature methods*, 12(3):244, 2015.

[117] Silvia Aldaz, Luis M Escudero, and Matthew Freeman. Live imaging of Drosophila imaginal disc development. *Proceedings of the National Academy of Sciences*, 107(32):14217–14222, 2010.

[118] Andrea H Brand and Norbert Perrimon. Targeted gene expression as a means of altering cell fates and generating dominant phenotypes. *development*, 118(2):401–415, 1993.

[119] James Fraser, Iain Williamson, Wendy A Bickmore, and Josée Dostie. An overview of genome organization and how we got there: from FISH to Hi-C. *Microbiology and Molecular Biology Reviews*, 79(3):347–372, 2015.

[120] D. Seemungal and G. Newton. Human Genome Project. In Sydney Brenner and Jefferey H. Miller, editors, *Encyclopedia of Genetics*, pages 980 – 981. Academic Press, New York, 2001.

[121] Bruce Alberts, Alexander Johnson, Julian Lewis, Martin Raff, Keith Roberts, and Peter Walter. *Molecular Biology of the Cell, Fourth Edition.* Garland Science, 4 edition, 2002.

[122] Nathaniel C. Comfort. From controlling elements to transposons: Barbara Mcclintock and the Nobel Prize. *Trends in Biochemical Sciences*, 26(7):454 – 457, 2001.

[123] Guillaume Andrey and Stefan Mundlos. The three-dimensional genome: regulating gene expression during pluripotency and development. *Development*, 144(20):3646–3658, 2017.

[124] M. Jordan Rowley, Michael H. Nichols, Xiaowen Lyu, Masami Ando-Kuri, I. Sarahi M. Rivera, Karen Hermetz, Ping Wang, Yijun Ruan, and Victor G. Corces. Evolutionarily Conserved Principles Predict 3D Chromatin Organization. *Molecular Cell*, 67(5):837 – 852.e7, 2017.

[125] Tadasu Nozaki, Ryosuke Imai, Mai Tanbo, Ryosuke Nagashima, Sachiko Tamura, Tomomi Tani, Yasumasa Joti, Masaru Tomita, Kayo Hibino, Masato T. Kanemaki, Kerstin S. Wendt, Yasushi Okada, Takeharu Nagai, and Kazuhiro Maeshima. Dynamic Organization of Chromatin Domains Revealed by Super-Resolution Live-Cell Imaging. *Molecular Cell*, 67(2):282 – 293.e7, 2017.

[126] G. Cenci, S. Bonaccorsi, C. Pisano, F. Verni, and M. Gatti. Chromatin and microtubule organization during premeiotic, meiotic and early postmeiotic stages of Drosophila melanogaster spermatogenesis. *Journal of Cell Science*, 107(12):3521–3534, 1994.

[127] Silvia Bonaccorsi, Claudio Pisano, Francesca Puoti, and Maurizio Gatti. Y chromosome loops in Drosophila melanogaster. *Genetics*, 120(4):1015–1034, 1988.

[128] Marko Swoboda, Jörg Henig, Hsin-Mei Cheng, Dagmar Brugger, Dietmar Haltrich, Nicolas Plumeré, and Michael Schlierf. Enzymatic oxygen scavenging for photostability without pH drop in single-molecule experiments. *ACS nano*, 6:6364–6369, July 2012.

[129] Xinghua Shi, John Lim, and Taekjip Ha. Acidification of the oxygen scavenging system in single-molecule fluorescence studies: in situ sensing with a ratiometric dual-emission probe. *Analytical chemistry*, 82(14):6132–6138, 2010.

[130] Liisa M Hirvonen and Susan Cox. STORM without enzymatic oxygen scavenging for correlative atomic force and fluorescence superresolution microscopy. *Methods and Applications in Fluorescence*, 6(4):045002, 2018.

[131] Claudia Geisler, Thomas Hotz, Andreas Schönle, Stefan W Hell, Axel Munk, and Alexander Egner. Drift estimation for single marker switching based imaging schemes. *Optics express*, 20:7274–7289, March 2012.

[132] Carla Coltharp, Xinxing Yang, and Jie Xiao. Quantitative analysis of single-molecule superresolution images. *Current opinion in structural biology*, 28:112–121, 2014.

[133] Tony E. Smith. Notebook on Spatial Data Analysis. https://www.seas.upenn.edu/ ese502/, 2016.

[134] Adrian Baddeley. R Documentation: thomas.estK (Fit The Thomas Point Process By Minimum Contrast). https://www.rdocumentation.org/packages/spatstat/versions/1.55-1/topics/thomas.estK.

[135] Adrian Baddeley. R Documentation: thomas.estpcf (Fit The Thomas Point Process By Minimum Contrast). https://www.rdocumentation.org/packages/spatstat/versions/1.56-1/topics/thomas.estpcf.

[136] Leila Muresan. SpatialClusterTest. https://github.com/lemur01/SpatialClusterTest, 2018.

[137] Single-Molecule Localization Microscopy • Software Benchmarking. Web. Tubulins of various diameters.

[138] Horng D Ou, Sébastien Phan, Thomas J Deerinck, Andrea Thor, Mark H Ellisman, and Clodagh C O'shea. ChromEMT: Visualizing 3D chromatin structure and compaction in interphase and mitotic cells. *Science*, 357(6349):eaag0025, 2017.

[139] Tim J Stevens, David Lando, Srinjan Basu, Liam P Atkinson, Yang Cao, Steven F Lee, Martin Leeb, Kai J Wohlfahrt, Wayne Boucher, Aoife O'Shaughnessy-Kirwan, et al. 3D structures of individual mammalian genomes studied by single-cell Hi-C. *Nature*, 544(7648):59, 2017.

[140] Robert PJ Nieuwenhuizen, Keith A Lidke, Mark Bates, Daniela Leyton Puig, David Grünwald, Sjoerd Stallinga, and Bernd Rieger. Measuring image resolution in optical nanoscopy. *Nature methods*, 10(6):557, 2013.

[141] Joerg Schnitzbauer, Maximilian T Strauss, Thomas Schlichthaerle, Florian Schueder, and Ralf Jungmann. Super-resolution microscopy with DNA-PAINT. *Nature protocols*, 12(6):1198, 2017.

[142] Ruth R. Sims, Sohaib Abdul Rehman, Martin O. Lenz, Leila Mureşan, and Kevin O'Holleran. Super-resolving light fields in microscopy: depth from disparity. *bioRxiv*, 2019.

[143] Ren Ng. Digital light field photography. *PhD thesis, Stanford University, Stanford, CA*, 2006.

[144] Marc Levoy, Ren Ng, Andrew Adams, Matthew Footer, and Mark Horowitz. Light Field Microscopy. *ACM Trans. Graph.*, 25(3):924–934, July 2006.

[145] Ren Ng, Marc Levoy, Mathieu Brédif, Gene Duval, Mark Horowitz, Pat Hanrahan, et al. Light field photography with a hand-held plenoptic camera. *Computer Science Technical Report CSTR*, 2(11):1–11, 2005.

[146] E. H. Adelson and J. Y. A. Wang. Single lens stereo with a plenoptic camera. *IEEE Transactions on Pattern Analysis and Machine Intelligence*, 14(2):99–106, February 1992.

[147] T. E. Bishop and P. Favaro. The Light Field Camera: Extended Depth of Field, Aliasing, and Superresolution. *IEEE Transactions on Pattern Analysis and Machine Intelligence*, 34(5):972–986, May 2012.

[148] Andrew Lumsdaine and Todor Georgiev. Full resolution lightfield rendering. *Adobe Technical Report, Adobe Systems, Inc.*, January 2008.

[149] Marc Levoy and Pat Hanrahan. Light Field Rendering. In *Proceedings of the 23rd Annual Conference on Computer Graphics and Interactive Techniques*, SIGGRAPH '96, pages 31–42, New York, NY, USA, 1996. ACM.

[150] Zhou Xue, Loïc Baboulaz, Paolo Prandoni, and Martin Vetterli. Light eld panorama by a plenoptic camera. *SPIE Proceedings, Computational Imaging XII*, 9020, 2013.

[151] Joseph W Goodman. *Introduction to Fourier optics*. Roberts and Company Publishers, 2015 edition, July 2005.

[152] Ruth Rebecca Sims. *Volumetric Imaging Across Spatiotemporal Scales inBiology with Fluorescence Microscopy*. PhD thesis, University of Cambridge, 2019.

[153] Bridget M Hanser, Mats GL Gustafsson, DA Agard, and John W Sedat. Phase-retrieved pupil functions in wide-field fluorescence microscopy. *Journal of microscopy*, 216(1):32–48, 2004.

[154] Petar N Petrov, Yoav Shechtman, and WE Moerner. Measurement-based estimation of global pupil functions in 3D localization microscopy. *Optics express*, 25(7):7945–7959, 2017.

[155] Michael Broxton, Logan Grosenick, Samuel Yang, Noy Cohen, Aaron Andalman, Karl Deisseroth, and Marc Levoy. Wave optics theory and 3-D deconvolution for the light field microscope. *Optics express*, 21(21):25418–25439, 2013.

[156] Clarissa Liesche, Kristin S Grußmayer, Michael Ludwig, Stefan Wörz, Karl Rohr, Dirk-Peter Herten, Joël Beaudouin, and Roland Eils. Automated analysis of single-molecule photobleaching data by statistical modeling of spot populations. *Biophysical journal*, 109(11):2352–2362, 2015.

[157] Nicola Viganò, Henri Der Sarkissian, Charlotte Herzog, Ombeline de la Rochefoucauld, Robert van Liere, and Kees Joost Batenburg. Tomographic approach for the quantitative scene reconstruction from light field images. *Optics express*, 26(18):22574–22602, 2018.

[158] Michigan State University. Error propagation. Website: http://lectureonline.cl.msu.edu/ mmp/labs/error/e2.htm.

[159] *Zernike polynomials and aberration balancing*, volume 5173, 2003.

[160] Alison M Yao and Miles J Padgett. Orbital angular momentum: origins, behavior and applications. *Advances in Optics and Photonics*, 3(2):161–204, 2011.